

Phase Change Material Cooling for Icy Moon Exploration Robot

Thesis report

Freek Theodoor Kunz

Delft University of Technology



Phase Change Material Cooling for Icy Moon Exploration Robot

Thesis report

by

Freek Theodoor Kunz

Name	Student number
Freek Kunz	4829409

Supervisors: Dr. Stéphanie Cazaux & Dr. Jovana Jovanova
Institution: Delft University of Technology
Place: Faculty of Aerospace Engineering, Delft
Track: Space Exploration
Date: October 2023

Preface

This report is written to conclude my master's program in Space Flight and Space Exploration, at the faculty of Aerospace Engineering at the Technical University of Delft, where I spent 5 years of my life. I fell in love with this study program when I was 14 years old and got a tour of the faculty by Ricky Curran. The project described in this report is, therefore, my child's dream: Helping to find life, because I love life. This project allowed me to do experiments and to learn how to build something in the real world, that you design in your head. It was a welcome change from the many projects done with the computer alone.

I was happy to follow in the adhesion link tracks of Tom Mooijman, who thought of the system underlying this research. When I heard about this project, I knew I wanted to help build the icy moon-licking robot. During this project, I learned how to zoom in on a problem and understand how it works.

I would like to thank Stéphanie Cazaux and Jovana Jovanova, for their enthusiastic guidance with care. I enjoyed our meetings and talks. I would like to thank Tom for answering all my questions about his project and Marnix for all the 3D printing. Jule for giving me space and my mom for allowing me to 'lekker te rommelen'.

*Freek Theodoor Kunz
Delft, October 2023*

Abstract

Enceladus has all the ingredients to support life in its ocean and is therefore a good place to start looking for extraterrestrial life in our Solar System. To explore Enceladus, a probe is needed that autonomously navigates the extreme, icy and unknown environment. Multiple robotic systems are proposed to explore Enceladus. The concept to be optimised by this research is the Freezing Locomotion Integrated Chain Kinematics (FLICK). This concept uses a track of adhesion links that use state-of-the-art ice locomotion: By melting and freezing the ice with peltier modules integrated into the links, the robot can move over the ice wall. To reach subzero temperatures to freeze the ice, the hot side of the Peltier modules must be cooled. The aim of this research is to optimise the adhesion link design by the replacement of the water cooling system with a Phase Change Material (PCM) cooling system. Utilising the latent heat storage of the PCM, this research provides a solid-state cooling solution. The PCM container was made of aluminium to increase the heat transfer from the Peltier module to the PCM and enable the heat absorbed by the PCM to radiate to the environment. Furthermore, 3 heat fins were used to increase the contact area between the PCM and the container, increasing the available latent heat storage. The cooling performance of various PCMs was tested and the octadecane was found to be the best option, due to its high latent heat capacity and relatively low density. Tests on ice showed ice adhesion with PCM cooling of the Peltier modules was possible. A theoretical model was built to estimate the required octadecane volume to obtain subzero temperatures. 7.457 g of octadecane was integrated into the adhesion link of FLICK. The model of the new link obtained a minimum temperature of -1.1°C and subzero cooling time of 45 s, for an ambient temperature of 21°C without the presence of ice. Using the designed PCM cooling mechanism, the mass of FLICK's cooling system could be reduced from $>1309\text{ g}$ to 375.68 g . However, the system must be built and tested to assess its behaviour and viability. This design assumed Earth conditions. To make the system fit to the cold temperatures and low pressures of Enceladus, the adhesion mechanism should be tested in a cooled vacuum chamber.

Contents

Preface	i
Abstract	ii
Nomenclature	vi
List of Figures	vii
List of Tables	xii
1 Introduction	1
2 Exploring Enceladus	3
2.1 The Saturnian system	3
2.2 Interior of Enceladus	3
2.3 South polar region	4
2.4 Proposed Enceladus Exploration Probes	6
2.4.1 Enceladus Vent Explorer	6
2.4.2 Exobiology Extant Life Surveyor	6
2.4.3 Enceladus Explorer IceMole	7
3 FLICK and its Cooling System	8
3.1 Freezing Locomotion Integrated Chain Kinematics	8
3.2 Peltier modules	9
3.3 Water cooling system.	12
3.4 Phase change materials	14
3.4.1 Solid-liquid PCMs.	15
3.4.2 Liquid-vapour PCM	15
3.5 Conclusion and Knowledge Gap.	16
4 Ice Adhesion Test Mechanism Design	18
4.1 Test setup	18
4.1.1 Thermocouples	19
4.1.2 Power supply	19
4.2 Selected Peltier module and model	20
4.2.1 MCPF-127-14-25-E	20
4.2.2 Theoretical model	21
4.3 Solid-liquid PCM container.	23
4.3.1 Position of PCM	24
4.3.2 Container material	25
4.3.3 Contact area	25
4.3.4 Effect on temperature response	29
4.4 Adhesion pad	31
4.5 Conclusion	33
5 Phase Change Material Cooling	34
5.1 Sensible heat storage	34
5.2 Latent heat storage.	35
5.3 Combined heat storage	38
5.4 Phase change temperature	40
5.5 Thermal conductivity	41
5.6 PCM selection	41
5.7 Conclusion	42

6	Tests on Ice	44
6.1	Experiment 1 - Peltier module on ice	44
6.2	Experiment 2 - Flipping the Peltier module on ice	45
6.3	Experiment 3 - Test adhesion mechanism with coconut oil.	46
6.3.1	Experiment 3.1 - Continuous cooling	46
6.3.2	Experiment 3.2 - 5 seconds cooling	46
6.4	Experiment 4 - Test difference between water and coconut oil cooling	47
6.5	Experiment 5 - Test ice adhesion mechanism with octadecane	48
6.6	Conclusion	49
7	Integration of PCM into FLICK's Adhesion Link	50
7.1	Model FLICK link	50
7.1.1	TEC1-06308 module	50
7.1.2	Model PCM cooling.	51
7.1.3	Estimation required PCM mass	52
7.2	PCM cooling of adhesion link	55
7.2.1	PCM container design	55
7.2.2	Integration of container into link	57
8	Conclusion and Recommendations	59
8.1	Summary of findings	59
8.1.1	Ice adhesion test mechanism design	59
8.1.2	PCM selection	60
8.1.3	Tests on ice	60
8.1.4	Theoretical model	60
8.1.5	PCM cooled adhesion link	61
8.2	Recommendations	62
8.2.1	Test PCM cooled adhesion link	62
8.2.2	Calcium Chloride Hexahydrate	62
8.2.3	Model improvements	62
8.2.4	AirJet	63
8.2.5	Enceladus Conditions	63
8.2.6	Phase change actuated robot	64
	References	70
A	Overview of the Experiment Data	70
B	Model of the TEC1-06308 module with PCM cooling	81
C	Theoretical Model of the Peltier Module	89
C.1	Peltier module model	89
C.1.1	Heat pumping rate	89
C.1.2	Physical characteristics estimation	90
C.1.3	Temperature response	91
C.1.4	Effect applied voltage	93
C.1.5	Effect of temperature	94
C.1.6	Heat dissipation to surrounding air	94
C.1.7	Effect of heat flow between the sides of the Peltier module	95
C.1.8	Effect wire resistance.	96
C.1.9	Final model	97
C.2	Model ice adhesion mechanism	98
C.2.1	Model effect PCM container	98
C.2.2	Model adhesion pad response.	100
C.3	Conclusion and model limitations	101

D	Phase Change Material Tests	102
D.1	Melting PCM experiments	102
D.1.1	GCS-104-PCM	102
D.1.2	Coconut oil	104
D.1.3	Paraffin wax.	107
D.1.4	PCM selection - Octadecane	108
D.2	Vaporising PCM experiments	113
D.2.1	Acetone	113
D.2.2	NOVEC7000 Engineering Fluid	117
D.3	Conclusion	120
E	Peltier module tests	121
E.0.1	TEC1-12706	122
E.0.2	QC-127-1.4-6.0A	124
E.0.3	MCPF-127-14-25-E	125
E.1	Power supplies	126

Nomenclature

Abbreviations

Abbreviation	Definition
EELS	Exobiology Extant Life Surveyor
EVE	Enceladus Vent Explorer
FLICK	Freezing Locomotion Integrated Chain Kinematics
PCM	Phase Change Material
PEEP	Proposed Enceladus Exploration Probes
CIRS	Composite Infrared Spectrometer
RHS	Right Hand Side
RMSE	Root Mean Square Error
SPT	South Polar Terrain
VIMS	Visible and Infrared Mapping Spectrometer

Symbols

Symbol	Definition	Unit
A	Area	[m ²]
c_p	Specific heat capacity at constant pressure	[J/(gK)]
C_{latent}	Fraction of heat absorbed by the latent heat storage	[-]
e	Elementary charge	[C]
E_F	Fermi energy	[J]
E_G	Energy gap	[J]
F	Force	[N]
h	Convective heat transfer coefficient	[W/(m ² K)]
ΔH	Latent heat capacity	[kJ/kg]
I	Current	[A]
k_B	Boltzmann constant	[J/K]
K	Thermal conductivity	[W/(mK)]
L	Length	[m]
m	Mass	[kg]
M	Moment	[Nm]
p	Pressure	[Pa]
Q	Heat	[J]
Q_c	Heat pumping rate of the Peltier module	[W]
Q_h	Heat flow to hot side of the Peltier module	[W]
R	Resistance	[Ω]
t	Time	[s]
T	Temperature	[K] or [°C]
U	Voltage	[V]
v_{melt}	Melting velocity	[m/s]
V	Volume	[L] or [m ³]
W	Power	[W]
α	Seebeck coefficient	V/K
ρ	Density	[kg/m ³]

List of Figures

2.1	Saturn's system with rings and the major icy moons [50]	3
2.2	Ocean thickness of Enceladus with (a) and without (b) the spherical harmonic coefficients of the core [52].	4
2.3	Cassini image of ice blocks on Enceladus' South Polar Terrain [44]. Resolution: 8 m/pixel. Latitude: 77°S. Longitude: 86°W.	5
2.4	The tiger stripes on the South Polar Terrain. The warm colours show the distribution of 9–17 μm thermal emission seen by CIRS in the white trapezoidal outline on March 12, 2008, with a spatial resolution of about 15 km. The white circles show the locations (with uncertainties) of dust plume sources seen by ISS. The blue line indicates the surface trace of a stellar occultation observed by UVIS [66].	5
2.5	Composite VIMS images of Enceladus in the Infrared. The colours indicate the degree of crystallinity of the ice: (Red 3.1/1.65 μm , green 2.0 μm & blue 1.8 μm). (Credit: NASA/JPL-Caltech/University of Arizona/LPG/CNRS/University of Nantes/Space Science Institute)	6
2.6	Artist impression of EVE mission. Left: Robot climbing into ice vent. Middle: in-situ science. Right: sample return mechanism [55].	6
2.7	Artist impression of EELS mission. [10].	7
2.8	Technical drawing of EnEx-IceMole (top) and its head (bottom) [38].	7
3.1	Movement of the Freezing Locomotion Integrated Chain Kinematics on ice [76].	9
3.2	Phase diagram of water [13].	9
3.3	Working principle of the Peltier effect [79].	10
3.4	Schematic of the interior of a peltier module [58].	10
3.5	Effect of water cooling on the temperature response of the cold side of the TEC1-12706 Peltier module [76].	12
3.6	Water cooling components inside the FLICK frame [76].	12
3.7	Adhesion link of FLICK. (a) shows the aluminium adhesion pad. (b) shows the cooling water through the translucent link material [76].	13
3.8	Water manifold of FLICK with integrated live swivel and push-in fittings [76].	13
3.9	FLICK with flexible water tubing to cool the adhesion link climbing ice at a 45° angle [76].	13
3.10	Comparison of stored energy by liquid water and octadecane between 0 and 50 °C [53].	14
3.11	Schematic drawing of a heat pipe [23].	15
4.1	Schematic drawing of ice adhesion mechanism with PCM cooling in the test setup. The dots indicate the temperature sensors.	18
4.2	Schematic of a thermocouple [47].	19
4.3	2 amperes regulated DC power supply connected to a Peltier module.	19
4.4	Final model of the MCPF-127-14-25-E Peltier module for 3, 7.5 and 12 V and 2A.	20
4.5	Flowchart of Peltier module model.	21
4.6	Modelled heat absorbed at the cold side of the MCPF-127-14-25-E Peltier module and input voltage for 3V, 7.5 V and 12V.	23
4.7	Setup with the coconut oil PCM clay holder.	23
4.8	Partly melted coconut oil after phase change test.	24
4.9	Bubbles in paraffin after phase change test.	24
4.10	Drawing of coconut holder assembly.	24
4.11	First 3D printed design of the coconut holder loaded with solid coconut oil.	24

4.12 Performance of coconut oil PCM cooling for different test setups. The 13 g PCM was connected on top of the Peltier module with tape, the 12 g PCM was connected to the bottom of the Peltier module with the clay holder and the 18.7 g was connected to the top of the Peltier module with the PLA printed holder. All tests used the TEC1-12706 module with a 7.5 V 2 A power supply.	25
4.13 Schematic setup of performed test with coconut oil shown in Figure 4.12. (Coconut pictogram designed by Freepik)	25
4.14 Schematic of melting mechanism of PCM on Peltier module.	26
4.15 Peltier module after test showing the location where the coconut oil contacted the module.	27
4.16 Aluminium interface between Peltier and coconut oil with fins.	27
4.17 Cold side temperature response of the aluminium pad connected to the QC-127-1.4-6.0A with and without aluminium fins.	28
4.18 Solid work drawing of the theoretical aluminium container.	28
4.19 Solid work drawing of the actual aluminium container.	28
4.20 Aluminium PCM container with coconut oil.	28
4.21 Aluminium PCM container with coconut oil after 1:10 min of heating.	28
4.22 Aluminium PCM container with coconut oil after 2:50 min of heating.	28
4.23 Temperature response of the hot and cold side of the MCPF-127-14-25-E module with and without the empty aluminium container.	29
4.24 Modelled and measured temperature response of the MCPF-127-14-25-E module with the empty aluminium container.	30
4.25 Modelled temperature response of the MCPF-127-14-25-E module with a 20% reduced heat pumping power with the empty aluminium container compared to the measurements.	30
4.26 Liquid water formed during the melting phase (top), potentially causing the adhesion pad and ice sample to separate (bottom). Deformations are scaled up (3X) to visualise the effect. [76].	31
4.27 Drawing of 1 cm aluminium pad.	31
4.28 Peltier module with aluminium 1 cm pad on the bottom and 1 mm interface plate at the top.	31
4.29 Temperature response of QC-127-1.4-6.0A with a 1 mm aluminium plate at the hot side with and without a 1 cm aluminium pad. $T_{amb} = 20.7\text{ }^{\circ}\text{C}$	32
4.30 Modelled and measured temperature response of the MCPF-127-14-25-E module with the aluminium adhesion pad and the empty container. 7.5 V 2 A.	32
4.31 Top view	33
4.32 Bottom view	33
4.33 Final adhesion mechanism assembly with octadecane.	33
5.1 Modelled and measured temperature response of the MCPF module with the aluminium adhesion pad and the container filled with water.	35
5.2 Comparison of stored energy by liquid water, coconut oil and octadecane between 0 and 50 °C	35
5.3 Temperature response of the MCPF-127-14-25-E with octadecane compared to water and the empty container, supplied power: 7.5 V and 2 A.	36
5.4 Modelled and measured temperature response of the MCPF module with the aluminium adhesion pad and the container with octadecane. Where the melting time is indicated by the pink window.	37
5.5 Modelled and measured temperature response of the MCPF module with the aluminium adhesion pad and the container with coconut oil. Where the melting time is indicated by the pink window.	38
5.6 Fitted model of the temperature response of the MCPF module with the aluminium adhesion pad and the container with coconut oil. During the melting phase, 70% of heat is absorbed by sensible heat storage and 30% by latent heat storage.	39
5.7 Cold side temperature response of QC-127-1.4-6.0A with acetone for different voltages.	40
5.8 Performance of PCM cooling of TEC1-12706 for 7.5 V 2 A power supply and different PCM types.	40

5.9	Temperature between the start of operation for the MCPF-127-14-25-E Peltier module and the melting temperature of octadecane.	41
5.10	Performance of PCM cooling of the adhesion pad with the MCPF-127-14-25-E module for 7.5 V 2 A power supply and different PCM types in the aluminium container.	43
6.1	Experiment 1 - Proof working mechanism of ice adhesion with Peltier module.	45
6.2	Film of ice on Peltier module after flipping on ice (Experiment 2).	45
6.3	Simplified free body diagram of Experiment 3.1 - Test 3D printed adhesion mechanism with coconut oil, continuous cooling. $d = 5.1$ cm.	46
6.4	Experiment 3.2 - Test 3D printed adhesion mechanism with coconut oil, 5 seconds of cooling.	47
6.5	Experiment 4 - Test adhesion mechanism with aluminium container on ice.	47
6.6	Experiment 4 - Temperature response of adhesion pad cooled by MCPF-127-14-25-E with coconut oil and water on ice.	48
6.7	Experiment 5 - Test ice adhesion mechanism with octadecane.	49
7.1	Modelled temperature response of the TEC1-06308 module for 3.8 & 4.36 V.	51
7.2	Schematic drawing of the model with the PCM container, Peltier module and the adhesion pad (side view).	51
7.3	Effect of coconut oil mass on the modelled temperature response of the cooling mechanism.	52
7.4	Effect of octadecane mass on the modelled temperature response of the cooling mechanism.	52
7.5	Minimum temperature over PCM mass.	53
7.6	Effect of octadecane mass on the modelled temperature response of the adhesion pad.	53
7.7	Subzero cooling time over octadecane mass.	54
7.8	Temperature response and current for the mechanism with 13.75 and 19.39 g of octadecane.	54
7.9	Old track link with integrated adhesion effector [76].	55
7.10	Old track link bottom CAD design [76].	55
7.11	Technical drawing of the PCM container.	56
7.12	Technical drawing of the PCM container lid.	56
7.13	Temperature response and current for the final adhesion link mechanism (with octadecane PCM cooling) with and without heat fins, voltage supply of 4.35 V for 200 seconds, $T_{amb} = 21$ °C.	57
7.14	Without lid	57
7.15	With lid	57
7.16	Final adhesion mechanism assembly with PCM container.	57
7.17	Exploded view of the link with the PCM container.	58
8.1	Top view	60
8.2	Bottom view	60
8.3	Conclusion: Designed ice adhesion mechanism assembly with octadecane.	60
8.4	Without lid	61
8.5	With lid	61
8.6	Final adhesion mechanism assembly with PCM container.	61
8.7	Top left: AirJet schematic where the cold incoming air is shown with blue arrows and the hot outgoing air with red arrows. Bottom: The cross-section of the AirJet module shows images of the generated pulsating air-jets and the outflow of air [24].	63
8.8	The pumpless phase change soft actuator.	64
8.9	A schematic of the bio-inspired untethered soft robot.	64
8.10	Bioinspired untethered soft robot with pumpless phase change soft actuators by bidirectional thermoelectrics proposed by Yoon et al. 2023 [79]	64
A.1	Folder with data stored by date of test from the 14th of April.	71
A.2	Tests performed on 3 April 2023.	72
A.3	Tests performed on 4 April 2023.	72

A.4 Tests performed on 14 April 2023.	73
A.5 Tests performed on 18 April 2023.	74
A.6 Tests performed on 20 April 2023.	75
A.7 Tests performed on 8 May 2023.	75
A.8 Tests performed on 23 May 2023.	75
A.9 Tests performed on 6 June 2023.	76
A.10 Tests performed on 8 June 2023.	77
A.11 Tests performed on 15 June 2023.	77
A.12 Tests performed on 16 June 2023.	78
A.13 Tests performed on 5 July 2023.	79
A.14 Tests performed on 6 July 2023.	79
A.15 Tests performed on 14 July 2023.	80
A.16 Tests performed on 5 July 2023.	80
C.1 Flowchart of Peltier module model.	91
C.2 Model with the estimated parameters as proposed by Zhaoxia Luo 2008 [5], compared to the measured temperature responses of 3, 7.5 and 12 V.	92
C.3 Modelled voltage of MCPF-127-14-25-E module for a current of 2 A.	93
C.4 Measured and modelled temperature response of the module with power limits of 3, 7.5 and 12 V and 2 A. (h=18)	93
C.5 Thermal conductivity of Al ₂ O ₃ [12]	94
C.6 Heat dissipation of the modelled Peltier module.	95
C.7 Effect of the convective heat transfer coefficient.	95
C.8 Effect of heat flow through air on temperature response.	96
C.9 Temperature around operating MCPF-127-14-25-E Peltier module measured with a FLIR camera. The temperature in this figure ranges from 14.1 to 39.5 °C indicated by dark purple to bright orange.	96
C.10 Final model of the MCPF-127-14-25-E Peltier module for 3, 7.5 and 12 V and 2A.	97
C.11 Modelled heat absorbed at the cold side of the MCPF-127-14-25-E Peltier module and input voltage for 3V, 7.5 V and 12V.	98
C.12 Drawing of the PCM container showing the area inside the container in green.	99
C.13 Modelled and measured temperature response of the MCPF module with the empty aluminium container.	99
C.14 Modelled temperature response of the MCPF module with a 20% reduced heat pumping power with the empty aluminium container compared to the measurements.	100
C.15 Modelled and measured temperature response of the MCPF module with the aluminium adhesion pad and the empty container.	101
D.1 Peltier module with GCS-104-PCM with a thermocouple measuring the temperature.	102
D.2 Temperature response of the hot and cold side of the TEC1-12706 of KIWI electronics with and without GCS-104-PCM. Power supply: 2A, 7.5V	103
D.3 Temperature response of the cold side of the TEC1-12706 of KIWI electronics with and without GCS-104-PCM with a thickness of 1.2 mm. Power supply: 2A, 7.5V	104
D.4 Setup with 13 g coconut oil as PCM.	104
D.5 Temperature response of the Peltier cold side with and without coconut oil PCM.	105
D.6 Temperature between the start of operation for the Peltier module and the melting temperature of the coconut oil.	105
D.7 Test setup with the aluminium container with 34 g coconut oil.	106
D.8 Temperature response MCPF-127-14-25-E with 34 g coconut oil PCM.	106
D.9 Setup with 13.7 g paraffin wax as PCM.	107
D.10 Temperature response of the TEC1-12706 Peltier cold side with and without paraffin wax PCM.	107
D.11 Temperature between the start of operation for the TEC1-12706 Peltier module and the melting temperature of the paraffin wax.	108
D.12 Correlation between the start and minimum temperature of the cold side of the TEC1-12706 7.5 V 2 A, the hot side was cooled by various solid-liquid PCMs.	109

D.13 Performance of PCM cooling of TEC1-12706 for 7.5 V 2 A power supply and different PCM types.	110
D.14 Comparison of stored energy by liquid water and coconut oil between 0 and 50 °C	111
D.15 Temperature between the start of operation for the MCPF-127-14-25-E Peltier module and the melting temperature of octadecane.	111
D.16 Temperature response of the MCPF-127-14-25-E with Octadecane compared to water and the empty container, supplied power: 7.5 V and 2 A.	113
D.17 Temperature over time of TEC1-12706 peltier hot side, with acetone and GCS-104-PCM. 113	
D.18 Temperature over time of TEC1-12706 peltier cold side, with acetone and GCS-104-PCM. 113	
D.19 Balloon with acetone heated by TEC1-12706.	114
D.20 Cold side temperature response of TEC1-12706 for different PCMs.	114
D.21 Minimum temperature of TEC1-12706 for different PCMs.	115
D.22 Balloon with acetone holder heated by QC-127-1.4-6.0A.	115
D.23 Temperature between the start of operation for the QC-127-1.4-6.0A Peltier module and the boiling temperature of acetone.	116
D.24 Cold side temperature response of QC-127-1.4-6.0A with acetone for different voltages. 116	
D.25 Liquid PCM holder with NOVEC7000.	117
D.26 Liquid container with elastic membrane (balloon) clamped to the setup.	117
D.27 Inflated balloon during test of setup with NOVEC7000.	117
D.28 Temperature between the start of operation for the QC-127-1.4-6.0A Peltier module and the boiling temperature of the NOVEC7000 engineering fluid.	117
D.29 Minimum temperature cold side QC-127-1.4-6.0A with and without NOVEC7000 and water. 118	
D.30 Temperature response cold side QC-127-1.4-6.0A with and without NOVEC7000 and water.	119
D.31 Temperature response 1 cm aluminium pad connected to the cold side of QC-127-1.4-6.0A with and without NOVEC7000 and water. Tested at 15 W (7.5V 2A) and 50 W (14V).	119
D.32 Temperature response of the MCPF-127-14-25-E with NOVEC7000 engineering liquid, supplied power: 7.5 V and 2 A.	120
D.33 Performance of PCM cooling of the adhesion pad with the MCPF-127-14-25-E module for 7.5 V 2 A power supply and different PCM types in the aluminium container.	121
E.1 Set up to measure the temperatures on the hot and cold side of the TEC1-12706 Peltier module.	122
E.2 Temperature response of TEC1-12706 for different voltages, $T_{amb} = 18.5\text{ °C}$	123
E.3 Minimum temperature of TEC1-12706 for different voltages, $T_{amb} = 18.5\text{ °C}$	123
E.4 Temperature response and power consumption over time of TEC1-12706 with water cooling as shown in T. Mooijman 2023 [76]. $T_{amb} = 18\text{ °C}$	124
E.5 Temperature response of QC-127-1.4-6.0A, $T_{amb} = 20.7\text{ °C}$	124
E.6 Temperature response for the MCPF-127-14-25-E for 3, 7.5 and 12 V, $T_{amb} = 20.2\text{ °C}$. . 125	
E.7 GLPS 3003E 0-30V 0-3A power supply	126
E.8 ES015-10 power supply	126

List of Tables

3.1	Components of FLICK's water cooling system	16
4.1	Properties of the MCPF-127-14-25-E peltier module.	20
5.1	Properties of considered PCMs.	42
8.1	Comparison components and weight of water cooling system and the proposed PCM cooling system.	61
D.1	Properties of PCMs with a melting point between 17 and 33 °C.	112
D.2	Properties of tested PCMs	120
E.1	Properties of the Peltier modules.	125

1

Introduction

One of the missions of Space Exploration is understanding the origins and possibilities of life in the cosmos [48]. Water is life [21]. Our living Earth is called the blue planet due to the amount of water that covers the surface. Compared to other worlds in our universe this amount of water is small. Hidden in the vast expanse of the solar system, nestled within the mysterious rings of Saturn, orbits the moon Enceladus made of 20% water compared to the 0.12% of Earth [8]. The Cassini spacecraft observed erupting geysers from the south polar zone of Enceladus and found proof of liquid water beneath its surface [61]. As flowing water is a key ingredient for life, this icy moon is one of the few known extraterrestrial bodies that may harbour life. The results of the Cassini mission point to the possibility of hydrothermal activity on Enceladus, which would be comparable to the deep-sea vents on Earth, that can provide the necessary organic molecules and energy to cause the emergence of microbial life [14]. Enceladus has all the ingredients to support life in its ocean and is therefore a good place to start looking for extraterrestrial life in our Solar System.

To explore Enceladus, a probe is needed that autonomously navigates the extreme and unknown environment, collects scientific data, and sends it back to Earth. Multiple missions are proposed to better understand this moon, using screws [55], revolving propulsion [10], and melting [15] to navigate its icy surface. The Freezing Locomotion Integrated Chain Kinematics (FLICK), as designed by Tom Mooijman 2023 [76], utilizes the phase change of water to create ice adhesion. This robot is designed to first work in Earth conditions, before moving to the tops of the Martian poles and eventually climb down the geysers walls of Enceladus. To create ice adhesion on Earth the ice is melted and refrozen by the system with Peltier modules, these must be cooled to reach the temperatures needed for freezing. FLICK uses a water cooling system to dissipate the heat, using moving parts, increasing the risk of the mission. As this cooling system is key to the working principle of the robot and the replacement of parts is difficult during Earth exploration and close to impossible for a space exploration mission, finding a solid-state cooling solution is a must to make this system reliable.

Phase Change Material (PCM) cooling, utilizes the energy needed to change from a more ordered to a less ordered state, so melting or vaporizing, to cool a component to the transition temperature of the material [53]. This research aims to assess the performance of PCM cooling, optimize the design of FLICK by integration of a PCM, and answer the research question:

How to use phase change material cooling to create ice adhesion for an ice-climbing robot?

The main research question can be decomposed into sub-questions:

- What is the potential of using phase change material cooling instead of water cooling for an ice-climbing robot?
- How to cool a Peltier module with a phase change material?
- What is the optimal phase change material to absorb the energy from the adhesion mechanism?
- How to create ice adhesion with a PCM-cooled mechanism?

- How to integrate the PCM cooling mechanism into a robotic system?

To answer these questions, an experimental setup is designed to test the cooling effect of PCMs on the Peltier modules. An ice adhesion mechanism is created and multiple PCMs are tested. From these experiments and a theoretical model of the Peltier module and PCM cooling, the selection criteria for selecting the PCM are derived and the optimal PCM is selected. This PCM is used in the ice adhesion mechanism and tested on ice. The theoretical model is used to estimate the required amount of PCM to obtain ice adhesion. Finally, the PCM is integrated into the FLICK probe.

In Chapter 2, the environment of Enceladus is analyzed and the proposed missions to explore Enceladus are described. FLICK and the to-be-optimized adhesion mechanism are described in Chapter 3. Chapter 4 presents the setup of the experiments, the performance of the selected Peltier module and the theoretical model, and the design of the ice adhesion mechanism. In Chapter 5, the effect of different properties of PCMs is analysed using the developed adhesion mechanism and model. The tests on ice are presented in Chapter 6. The integration of PCMs into a robotic system is discussed in Chapter 7. The conclusion and recommendations for further research are presented in Chapter 8. In Appendix A, the overview of the data gathered during the experiments of this research is listed to ease the data handling for future research. The Python code of the theoretical model is shown in Appendix B and fully described in Appendix C. The tests with various PCMs and different Peltier modules are described in detail in Appendix D and Appendix E.

2

Exploring Enceladus

Enceladus, named after one of the Giants in Greek mythology, was discovered in 1789 by the British astronomer William Herschel. It is the sixth-largest moon of Saturn and is one of the smallest spherical moons in the solar system, with a diameter of roughly 500 kilometres. However, Enceladus has the potential to yield ground-breaking discoveries, despite its small size. The presence of a liquid ocean and observed organic compounds by the Cassini mission [61], hint towards extraterrestrial life. This chapter describes its place in the Saturnian System, its interior, and the South Polar Region, which is the area to be explored by the research probe. Finally, the previously proposed robotic systems to explore Enceladus are described.

2.1. The Saturnian system

The Saturnian system is shown in Figure 2.1. The seven primary rings are labelled in the order in which they were discovered. Saturn's major rings are the A, B, and C rings, which are separated by the Cassini Division. The D ring is Saturn's nearest and most faint ring. Pandora and Prometheus circle Saturn in the tight F ring. Following this ring comes the faint ring G & E. The E ring is the largest planetary ring in our solar system, stretching from Mimas' orbit to Titan's orbit and measuring 1 million kilometres in width. Enceladus is located in the E ring of Saturn. Saturn has 7 major satellites: Mimas, Enceladus, Tethys, Dione, Rhea, Titan, and Iapetus. Enceladus completes two orbits around Saturn for every one orbit completed by the moon Dione (2:1 orbital resonance). This resonance results in an orbital eccentricity of 0.0047 for Enceladus [50].



Figure 2.1: Saturn's system with rings and the major icy moons [50]

2.2. Interior of Enceladus

The majority of what is known about the interior of Enceladus comes from Doppler tracking of the Cassini spacecraft during Enceladus flybys [57]. Combining the derived quadruple gravity field and

hemispherical asymmetry [35] with the observation of Enceladus' icy crust's significant forced physical liberation of $0.120 \pm 0.014^\circ$ on the surface led to the conclusion that Enceladus' ice crust was entirely decoupled [75]. This is only possible if Enceladus has a worldwide underground liquid water ocean. The thickness of the south polar ocean is believed to be 40-50 km [9]. Figure 2.2 depicts the global ocean thickness.

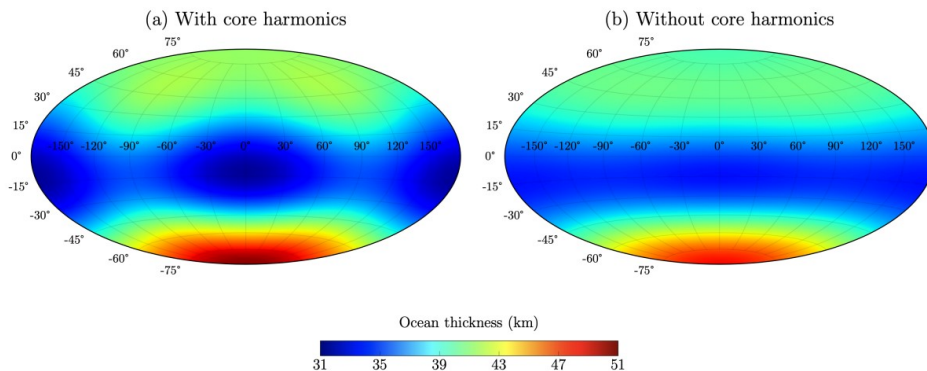


Figure 2.2: Ocean thickness of Enceladus with (a) and without (b) the spherical harmonic coefficients of the core [52].

The estimated thickness of the ice shell is 10 - 45 km and 5 - 10 km at the south polar terrain (SPT)[9]. It is unknown whether the ocean freezes and melts regularly, which would reduce the likelihood of the formation of life in the water. Variations in orbital eccentricity generate changes in ice shell thickness, which can reach the subsurface ocean and cause the observed geyser activity at the SPT. The reported eruptions from the south polar region are not driven by ocean overpressure, but rather by decompression boiling and tidal dissipation within the fissures [59].

Enceladus is not in hydrostatic equilibrium. The analysis of the plume hints towards hydrothermal activity within Enceladus. Temperatures of more than 360 K are estimated inside Enceladus [32]. These hydrothermal systems may be similar to those on Earth where life is supposed to have begun [14]. High temperatures may cause serpentinization of olivine and the formation of H_2 [31], which may be utilized by autotrophic organisms.

2.3. South polar region

The South polar terrain (SPT) is considered to be generated by subsurface tidal heating, which causes lithosphere thinning and surface deformation at the south pole [4]. Changes in tidal dissipation create changes in heat flow in the ice shell, resulting in fissures. Because of Enceladus' low gravity, these fissures could penetrate the 15 km thick ice shell [59].

The SPT shows four dominant fractures, known as the "tiger stripes." Figure 2.4 depicts the locations of the SPT and the tiger stripes: Damascus, Baghdad, Cairo, and Alexandria Sulcus. In terms of geyser activity, the later 'Sulcus' is the least active [29]. Because these tiger stripes produce eruptive jets, the fissures must go deep enough into the ice crust to reach a body of water or a CO_2 gas chamber [45]. The fissures were found to be 2 kilometres wide and 130 kilometres long [65].

The surface composition of the tiger stripes corresponds to the plume composition measured by the Cassini mission. Hence, it is expected that this area is covered by the deposition of the plume. Grain sizes of up to $100 \mu m$ were discovered due to the fallout of larger and slower plume grains near their source and the expansion of grains caused by plume gas deposition [66]. Figure 2.3 shows ice blocks with 10-100 m diameters and densities of 1500 450 blocks/ km^2 at the SPT [44].

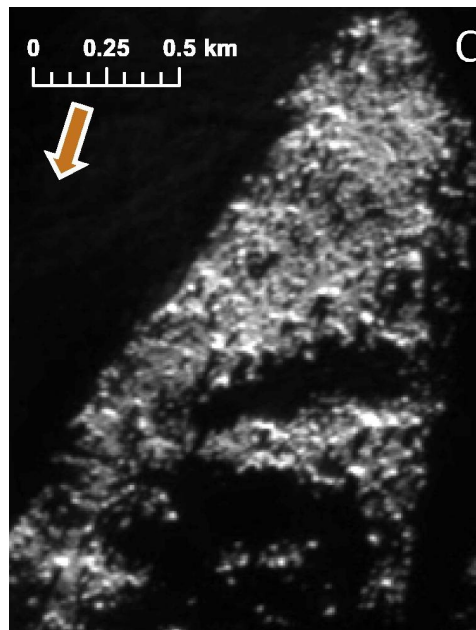


Figure 2.3: Cassini image of ice blocks on Enceladus' South Polar Terrain [44]. Resolution: 8 m/pixel. Latitude: 77°S. Longitude: 86°W.

As illustrated in Figure 2.4, the Composite Infrared Spectrometer (CIRS) on Cassini discovered that the fractures on Enceladus had a higher temperature, 197 ± 20 K [26], than their surroundings (100 K) [65]. The bottom right image in Figure 2.5 depicts the various ice morphology observed by the Visible and Infrared Mapping Spectrometer (VIMS): Amorphous ice is present outside the tiger stripes, created by condensation of water vapor below 100 K, however, the stripes are dominated by crystalline ice (red in Figure 2.5) due to ice production at high temperatures [7].

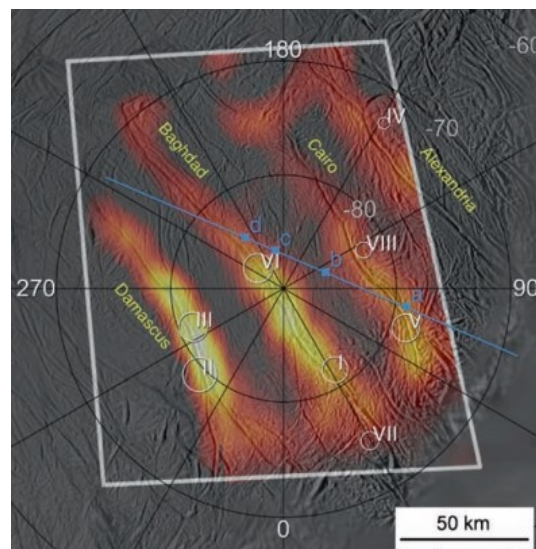


Figure 2.4: The tiger stripes on the South Polar Terrain. The warm colours show the distribution of 9–17 μm thermal emission seen by CIRS in the white trapezoidal outline on March 12, 2008, with a spatial resolution of about 15 km. The white circles show the locations (with uncertainties) of dust plume sources seen by ISS. The blue line indicates the surface trace of a stellar occultation observed by UVIS [66].

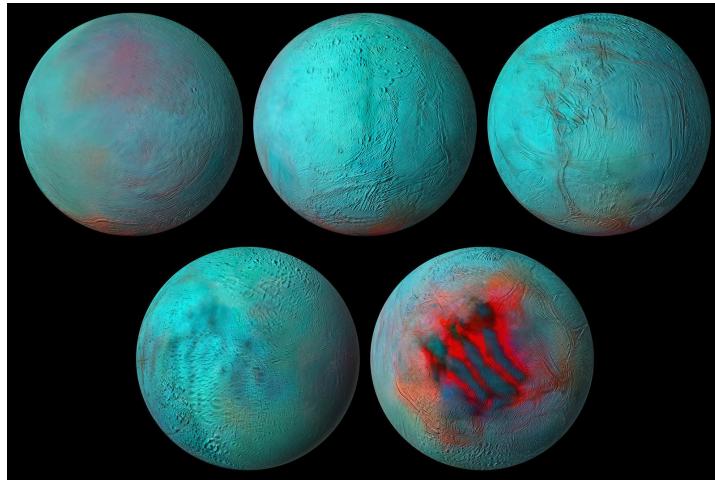


Figure 2.5: Composite VIMS images of Enceladus in the Infrared. The colours indicate the degree of crystallinity of the ice: (Red 3.1/1.65 μm , green 2.0 μm & blue 1.8 μm).

(Credit: NASA/JPL-Caltech/University of Arizona/LPG/CNRS/University of Nantes/Space Science Institute)

2.4. Proposed Enceladus Exploration Probes

So far, Enceladus exploration has been confined to observations obtained by the Cassini spacecraft, which completed its mission in 2017 by plummeting into Saturn's atmosphere [49]. The future investigation, however, has been made possible by the interesting observations of small moon [61]. Missions specifically intended for investigating Enceladus are already being considered by scientists and space organizations. The objectives of these proposed missions are to deepen our understanding of the subterranean ocean of the moon, characterize it, and look for life. In this section, the Proposed Enceladus Exploration Probes (PEEP) show possible robotic systems to search for life on Enceladus. The three described concepts are the Enceladus Vent Explorer, the Exobiology Extant Life Surveyor, and the IceMole.

2.4.1. Enceladus Vent Explorer

The Enceladus Vent Explorer (EVE) mission, proposed in 2018, will send a robot inside Enceladus vents. It will be made up of two modules: the Surface Module (the lander) and the Descent Module (the robot). The robot will descend the vents using limbs equipped with ice screws. Ice climbers utilize these hollow metal screws to create a strong anchor on ice walls, as seen in Figure 2.6 on the left. The robot will conduct scientific experiments utilizing a microscopic imager and a microfluidics chip, as depicted in Figure 2.6 on the left. As seen in Figure 2.6 on the right, it will gather samples to bring to the Surface Module for comprehensive analysis [55].

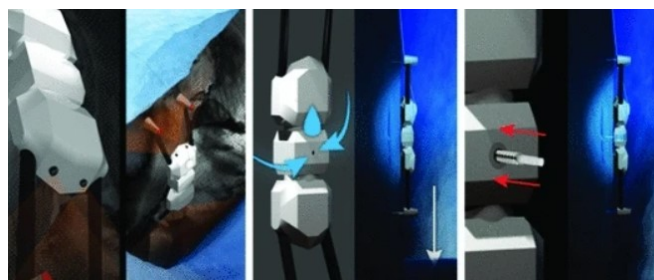


Figure 2.6: Artist impression of EVE mission. Left: Robot climbing into ice vent. Middle: in-situ science. Right: sample return mechanism [55].

2.4.2. Exobiology Extant Life Surveyor

The Exobiology Extant Life Surveyor (EELS) mission, seen in Figure 2.7, will employ a snake-like, self-propelled robot constructed from identical actuation and propulsion segments. It will use revolving

propulsion (or screw-like) devices that will cut through the ice and act as underwater propellers. This allows this concept to study both Enceladus' vents and seas [10].



Figure 2.7: Artist impression of EELS mission. [10].

2.4.3. Enceladus Explorer IceMole

The IceMole developed by Dachwald et al. [15] uses a copper heating head to melt through the ice crust. Figure 2.8 shows the technical drawing of the IceMole. This ice melting probe can steer itself through directional melting and uses a hollow icescrew to sample the ice for the presence of microorganisms and ensure proper contact between the melting head and the ice to optimize the heat transfer. The robot will be powered by a nuclear power system. For a melting rate of 1 m/hour and an ice temperature of 150 K, a cylindrical probe with a diameter of 0.1 and a length of 1 m will require 5 kW of power. The nuclear power plant would be in the surface module of this mission which will also send the data gathered by this mission to the Earth.

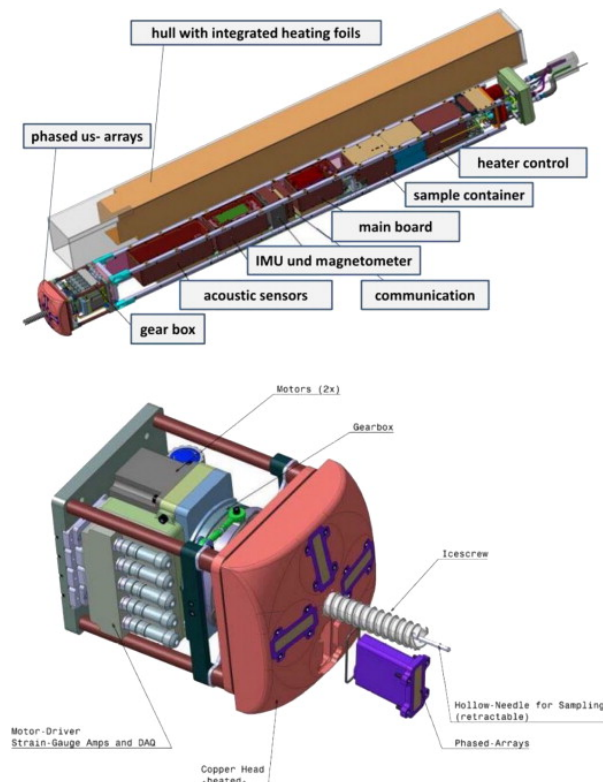


Figure 2.8: Technical drawing of EnEx-IceMole (top) and its head (bottom) [38].

Another concept using the phase change of the ice for its locomotion is the Freezing Locomotion Integrated Chain Kinematics (FLICK) as developed by Tom Mooijman 2023 [76]. As the aim of this research is to improve the adhesion mechanism of FLICK, this robot will be analyzed in more detail in the next chapter, to see how the design can be improved.

3

FLICK and its Cooling System

To explore the crevasses of the South Polar Region of Enceladus, the Freezing Locomotion Integrated Chain Kinematics (FLICK) concept was developed by Tom Mooijman 2023 [76]. This concept is first built to operate in Earth conditions, to prove the working principle, before it will be adapted to the conditions on Enceladus. To improve the adhesion links of FLICK, this section will focus on the adhesion mechanism of the design and specifically the cooling of the Peltier modules. The developed adhesion mechanism uses a Peltier module to first melt the ice and then freeze the melt water to adhere to the surface. By comparing the cooling system of this concept with phase change material cooling the following sub-question is answered:

What is the potential of using phase change material cooling instead of water cooling for an ice-climbing robot?

First, the FLICK concept is described. Then, the working principle of the Peltier modules used in the adhesion mechanism is explained. Next, the water cooling system of FLICK and phase change material cooling are described. Finally, the potential benefit of using a phase change material instead of a water cooling system is assessed by comparing the two systems.

3.1. Freezing Locomotion Integrated Chain Kinematics

The Freezing Locomotion Integrated Chain Kinematics (FLICK) was developed by Tom Mooijman during his thesis [76], to eventually explore the cracks in the ice of the South Polar region of Enceladus. FLICK is inspired by a tongue freezing to a metal pole when it is freezing outside. This concept is the first robotic system utilizing the adhesive properties of ice to climb ice. The robot uses a thermoelectric heating and cooling system (see Section 3.2) to melt and freeze the ice. By first melting the ice and refreezing the meltwater, a bond between the ice wall and the adhesion pad can be created. By heating the adhesion pad again, the bond will be broken and the pad will detach from the wall. The robot consists of 16 adhesion links integrated into a single-tracked robotic system as shown in Figure 3.1. When the link touches the ice wall at the bottom of the figure the link is first heated (red arrow), melting the ice, and then cooled (blue arrow), attaching to the ice wall by freezing the water. When the link reaches the end of the robot, it heats again to detach from the ice.

The track is supported by four sprockets of which one is driven by a planetary gear brushless DC motor. This motor is controlled with a pulse width modulated and has a RPM of 8. The output of the motor is connected with a bevel and pinion gear to the driveshaft of the drive sprocket. The gear reduction is 2:1. Two springs fitted to the non-driven sprockets ensure tension of the track. TEC1-06308 Peltier modules (40x20x3 mm) are used for the heating and cooling of the aluminium adhesion pad. The water cooling system of these modules is described in Section 3.3. The total mass of the robot is 3.8 kg [76].

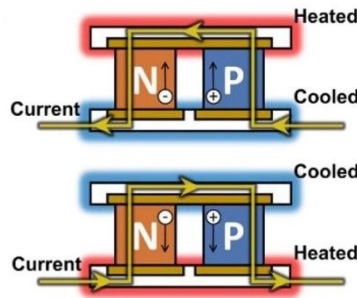


Figure 3.3: Working principle of the Peltier effect [79].

The working principle of the Peltier modules is the thermoelectric effect. This effect converts a temperature difference into an electrical current and vice versa [63]. Converting an electrical current into a temperature difference is called the Peltier effect.

This effect is shown in Figure 3.3. By running a current, the orange arrow in Figure 3.3, through a circuit of a thermocouple, one side will generate heat and one will cool. The thermocouple consists of a negative or n- and positive or p-type semiconductor, depicted by the orange square with an N and blue square with a P in Figure 3.3 respectively. The p-type has an electron deficit and the n-type conductor has an electron surplus. Therefore, when the current is flowing from the p- to the n-type (top part of Figure 3.3), and hence the electrons flow from n to p (indicated by the circles with a minus in Figure 3.3 that move up in the n-type semiconductor) the junction is heated. The circles with a plus in the p-type semiconductor in Figure 3.3 indicate the holes in the semiconductor due to the electron deficit that can absorb the electrons from the n-type semiconductor. The absorption of the free electrons of the n-type conductor by the p-type conductor results in the release of thermal energy (red glow in Figure 3.3), as the electrons can not move around freely, and hence their kinetic energy is released to the environment. When the current flows from the n- to p-type (bottom part of Figure 3.3), the absorbed electrons become free electrons. This increases their thermal energy, as the electrons are free to move again. This thermal energy is extracted from the environment (blue glow in Figure 3.3), and hence the junction is cooled [36].

In Figure 3.4 a schematic drawing of a peltier module is shown. In this figure, the connections between the n- and p-type semiconductors are indicated. These connections are often made of copper which has a high conductivity and the semiconductors are covered by ceramic plates, often alumina plates.

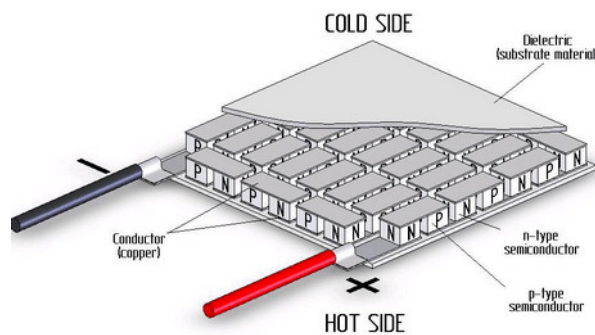


Figure 3.4: Schematic of the interior of a peltier module [58].

The total heat produced by the Peltier module and hence the input power can be calculated with Equation 3.1 [77].

$$W = (\alpha_p - \alpha_n)I\Delta T + I^2R \tag{3.1}$$

Where the first term is the heat flow generated by the Peltier module and the second term is the Joule

heating or resistance heating. The α_p and α_n denote the Seebeck coefficients of the semi-conductors in μVK^{-1} , which are related to the ratio of applied voltage and temperature gradient, I stands for the current, ΔT is the temperature difference between the hot and cold sides of the module and R is the resistivity of the module.

The Seebeck coefficient, α , of a material is defined by Equation 3.2. The Seebeck coefficient is an intrinsic property of the semiconductors that determines the amount of voltage produced by a material when a temperature gradient is applied [77].

$$\alpha = -\frac{\Delta V}{\Delta T} = -\frac{V_{top} - V_{bottom}}{T_{top} - T_{bottom}} \quad (3.2)$$

Where ΔV is the developed voltage difference and ΔT is the temperature difference between the ends of the material. Where V_{top} is the voltage at the top in Figure 3.3 and V_{bottom} is the voltage at the bottom. And similarly for the temperature. If α is positive, the end with the lower temperature has the higher voltage, and vice versa. Hence, looking at Figure 3.3, the p-type semiconductors have a positive α as the positive charge carrying holes (indicated with a +) move towards the heated side, which produces a negative compensating voltage. The n-type semiconductors have a negative α as the negative charge carrying electrons move to the heated side and a positive compensating voltage is produced. For metals, the Seebeck coefficient increases for increasing temperatures according to Equation 3.3 and decreases in semiconductors according to Equation 3.4 [77].

$$\alpha_{metal} \approx \left(\frac{k_B}{e}\right) \frac{k_B T}{E_F} \quad (3.3)$$

Where k_B is the Boltzmann constant, e the charge of an electron, $\frac{k_B}{e}$ is the constant thermopower of classical electron gas of $87 \mu\text{V}/\text{K}$, E_F is the Fermi energy which is related to the chemical potential of the material, which determines what energy levels are vacant and occupied at $T = 0 \text{ K}$.

$$\alpha_{semi-conductor} \approx \left(\frac{k_B}{e}\right) \frac{E_G}{k_B T} \quad (3.4)$$

Where, E_G is the energy gap, that the charged particles in the semiconductor must jump. The band gap determines the physical properties of semiconductors to a large extent.

The heat pumping rate at the cold side of the Peltier module, Q_c , can be calculated with Equation 3.5 [77].

$$Q_c = (\alpha_p - \alpha_n)IT_c - K\Delta T - \frac{1}{2}I^2R \quad (3.5)$$

Where T_c is the temperature of the cold side and K is the thermal conductivity of the semiconductor couple. The first term, on the RHS of the equation, describes the heat pumping by the thermoelectric effect. The 2nd term is the effect of the thermal conductivity of the couple decreasing the heat flow. The 3rd term is the Joule heating flowing to the cold side, as the other half of the total Joule heating flows to the hot side.

The maximum temperature difference achieved by Peltier modules is between 60 and 70 °C [81]. In practice the temperature difference generated by the Peltier module is often lower than 60 °C [81]. To enable the freezing of the melted ice with the Peltier modules the hot side of the module must be cooled. Theoretically, a hot side temperature of 50 °C would be enough to obtain a -10°C cold side temperature. However, in practice, the performance of the Peltier modules is influenced by the hot side temperature and temperature of the surrounding air. Hence, the hot side must be kept at a temperature around 30 °C to obtain subzero temperatures at the cold side.

To ensure this hot side temperature, the thermal energy produced by the Peltier module must be dissipated away from the system. Without cooling the whole system would heat up till the failure of the Peltier module.

3.3. Water cooling system

The effect of water flow on the cooling capacity of a Peltier module is shown in Figure 3.5. As shown water cooling of the hot side of the TEC1-12706 module results in sustained subzero temperatures at the cold side of the module. The temperature response of the Peltier without running water still obtained subzero temperatures for ~100 s. This can be explained by the absorption of heat by the copper water cooling block connected to a water body. As the specific heat capacity of water is high (4.1813 J/gK) this passive body can absorb enough energy to reach subzero temperatures, till the water is heated up and the cold side starts rising in temperature.

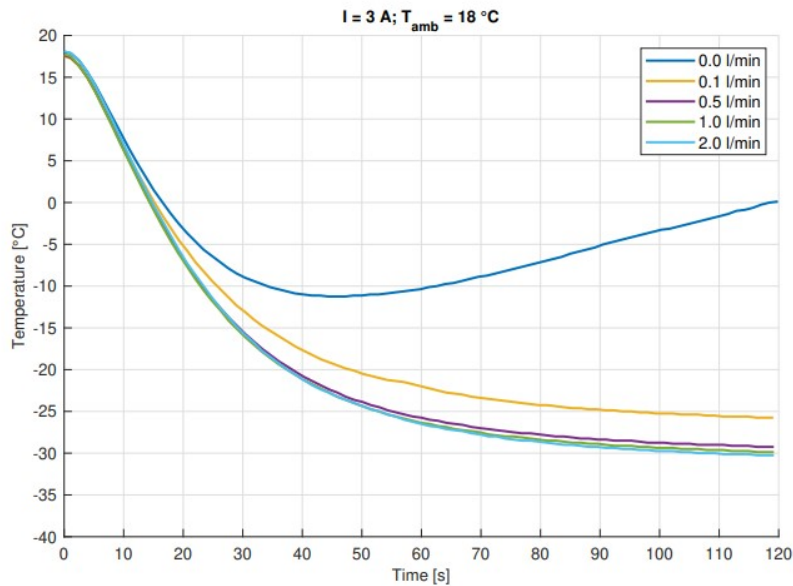


Figure 3.5: Effect of water cooling on the temperature response of the cold side of the TEC1-12706 Peltier module [76].

The Peltier modules in the adhesion links of FLICK are cooled with a water circulation system. A water circulation system uses a continuous flow of cooling water to dissipate the heat flow from the Peltier module. The water absorbs the heat and is cooled inside the robot with a 60 mm 12 V DC fan connected to a 60 mm water radiator. A Laing DDC-pump 12V DDC-1T can pump the water through flexible tubing with a flow rate of 10 L/min. The integration of the water pump and radiator is shown in Figure 3.6.

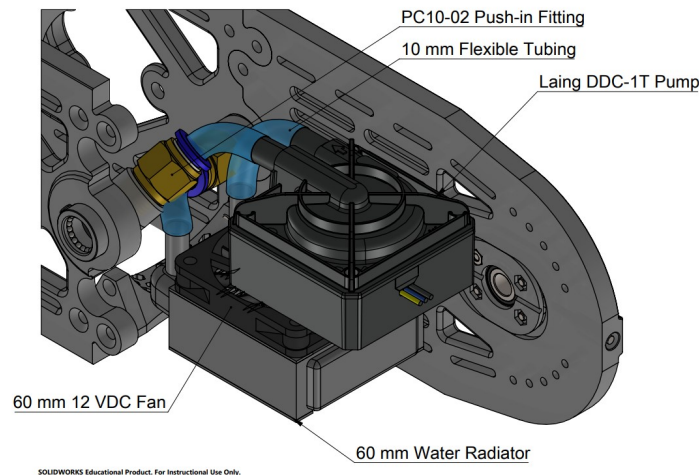


Figure 3.6: Water cooling components inside the FLICK frame [76].

The is pumped to the 16 adhesion links shown in Figure 3.7, via the 16 spout water manifold shown in Figure 3.8, resulting in a flow rate per link of 0.625 L/min. The water enters the link through a PC-04-M6 push-in fitting and runs over the 1 mm aluminium heatsink connected to the Peltier module with ProlimaTech PK-2 thermal compound to absorb the dissipated heat [76].

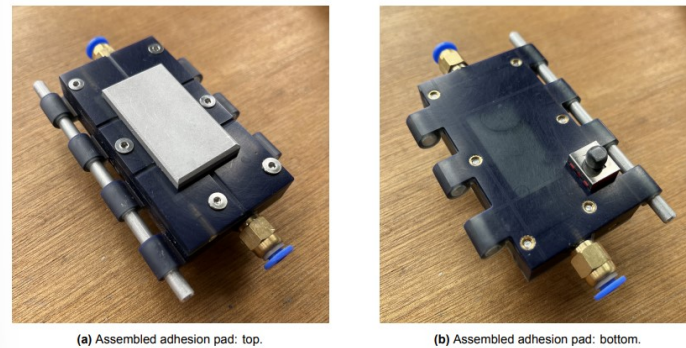


Figure 3.7: Adhesion link of FLICK. (a) shows the aluminium adhesion pad. (b) shows the cooling water through the translucent link material [76].

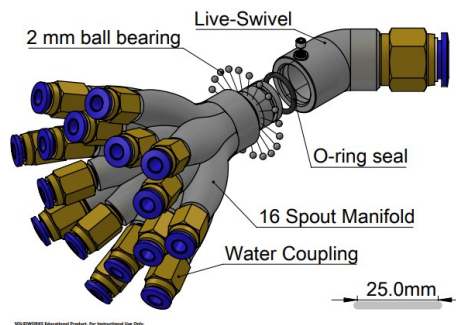


Figure 3.8: Water manifold of FLICK with integrated live swivel and push-in fittings [76].

The risk of the mission increases if the robot uses moving parts, like the fan and pump, as these can break down. The water tubes, shown in Figure 3.9, could leak or get stuck behind surface features of the environment. As this cooling system is key to the working principle of the robot and the replacement of parts is difficult during Earth exploration and close to impossible for space exploration missions, finding a solid-state cooling solution is a must to make this system reliable.

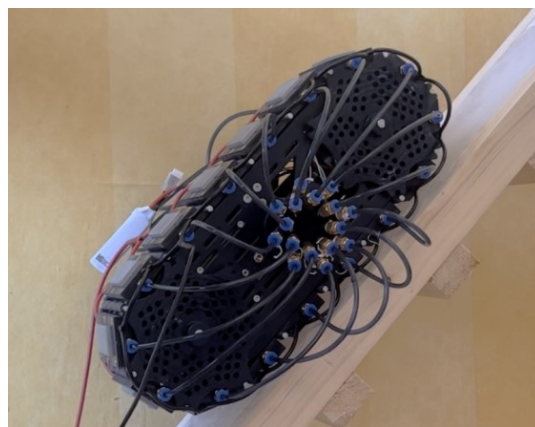


Figure 3.9: FLICK with flexible water tubing to cool the adhesion link climbing ice at a 45° angle [76].

3.4. Phase change materials

Phase change materials (PCMs) can store thermal energy by using the latent heat of the phase transition to absorb the heat. PCMs can provide a compact solid-state cooling solution [53].

Every material can store thermal energy in two ways: sensible heat storage and latent heat storage. Water cooling uses sensible heat storage. The working principle of sensible heat storage is the increase of the temperature of the material. Heating a material requires energy. The specific heat capacity of a material determines how much energy is needed to heat 1 g of material with 1 K. Hence, materials with a high specific heat capacity are most effective for sensible heat storage. The amount of sensible heat stored by a material can be calculated with Equation 3.6.

$$Q = \int_{T_1}^{T_2} m c_p T dT \quad (3.6)$$

Where Q is the stored heat in J , m the mass in kg , c_p the specific heat capacity at constant pressure in J/kgK , T_1 and T_2 the initial and final temperature respectively in K .

The working principle of latent heat storage is the phase change of the material. When a PCM is heated to its transition temperature, it changes from one phase into another. A phase change is endothermic when the material changes from a more-ordered to a less-ordered state. Hence, the change of phase of a material from solid to liquid (melting) and from liquid to vapour (evaporation) requires energy. This energy is the transition entropy change, which is called the latent heat. Before the phase change of the material, it also stores sensible heat. Hence, the amount of heat stored by a PCM over the temperature interval from T_1 to T_2 can be calculated with Equation 3.7.

$$Q = \int_{T_1}^{T_{trs}} m c_{p,1} T dT + m \Delta_{trs} H + \int_{T_{trs}}^{T_2} m c_{p,2} T dT \quad (3.7)$$

Where T_{trs} is the transition temperature, $c_{p,1}$ & $c_{p,2}$ the specific heat capacity at a constant pressure before and after the phase change, $\Delta_{trs} H$ the latent heat capacity in kJ/kg .

The latent heat capacity is often larger than the specific heat capacity over a small temperature range. Therefore, PCMs can outperform sensible heat storage materials near their transition temperature. Figure 3.10 compares the energy stored by liquid water (sensible heat storage) with the energy stored by the PCM octadecane over the temperature range between 0 and 50 °C. The dashed line shows the energy absorption by water with a specific heat capacity of 4.2 J/gK and the solid line the energy absorption of octadecane with a melting point of 28°C. When the PCM reaches this melting point the stored energy is increased while the temperature of the material stays constant. This property can be used to cool a component to a constant temperature around the melting point of the PCM.

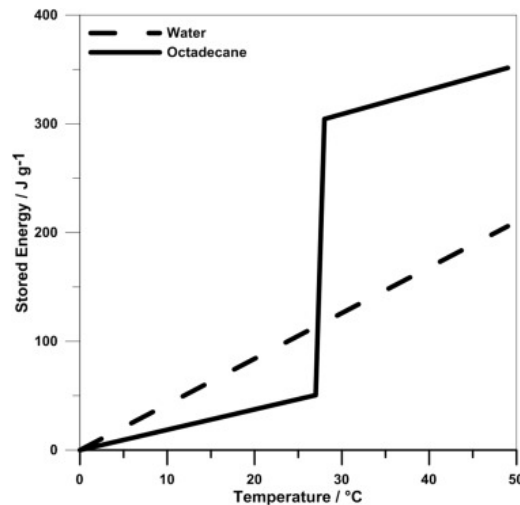


Figure 3.10: Comparison of stored energy by liquid water and octadecane between 0 and 50 °C [53].

3.4.1. Solid-liquid PCMs

Most PCMs utilize solid-liquid transitions. These transitions have high enthalpy changes (~ 200 kJ/kg) and only a small volume change ($<10\%$). However, the liquid phase needs to be contained [53].

Cooling of Peltier modules with PCMs has been done in previous research [40], where the PCM-OM37 with a power input of 3W could deliver the temperature of 10°C for 20 minutes. This PCM had a phase change temperature of 37°C and a latent heat capacity of 218 kJ/kg. The research in this report aims to obtain subzero temperatures to enable ice adhesion. Hence, a PCM with a lower transition temperature or a higher latent heat capacity must be selected. PCMs with a phase change temperature between 20 and 30°C are paraffin waxes, salt hydrates and eutectic mixtures.

Materials labelled as 'paraffin wax' are semi-refined hydrocarbon blends with many n-alkane chains of varying lengths. The melting temperature of paraffins increases with chain length. The melting temperatures of paraffin waxes range typically from 5.5 to 66°C and the latent heat between 184 to 247 kJ/kg [30].

Salt hydrates are crystalline structures formed by anhydrous salt in the presence of water. The melting temperature of salt hydrates ranges typically from 8 to 58°C and the latent heat capacity from 99 to 289 kJ/kg [30].

Eutectics are alloys of inorganics and/or organics. Eutectics can melt and freeze without phase segregation [41]. This means the solid and melted parts of the PCM do not separate from each other when the mixture is heated. By creating eutectic mixtures the desired melting temperature can be designed by selecting specific components and their proportions [64].

3.4.2. Liquid-vapour PCM

PCMs using liquid-vapour transitions are usually used less due to the high volume change between the liquid and the vapour. However, the enthalpy changes are high (>300 kJ/kg) which makes it a promising cooling option. The latent heat of evaporation is used in heat pipes. A heat pipe is a high-performance heat transfer device which is used to transfer a large amount of heat at a high rate with a small temperature difference between the two points of the heat pipe. This is achieved by evaporation of the working fluid in the evaporator section, condensing in the condenser section and return of the condensate, as shown in Figure 3.11.

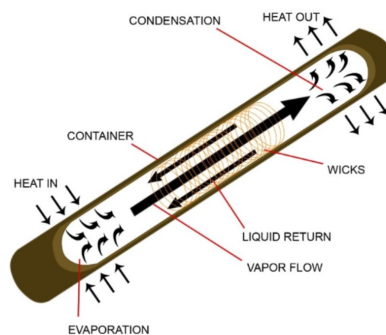


Figure 3.11: Schematic drawing of a heat pipe [23].

One easily available and cheap liquid to test the feasibility of a liquid PCM for this research is acetone. Acetone has a boiling temperature of 56°C and a latent heat of evaporation of 542 kJ/kg. Another tested liquid is the NOVEC7000 engineering fluid with a boiling point of 34°C and a latent heat of 142 kJ/kg. The volume expansion of the liquid-vapour PCMs results in the expansion of the cooling mechanism itself, as it collects the gas. As this space is not available in the current track design of FLICK, this type of PCM was discarded as a viable option to cool the FLICK link. The tests performed with liquid-vapour PCM are described in Appendix D.

3.5. Conclusion and Knowledge Gap

In conclusion, this section aimed to answer the question:

What is the potential of using phase change material cooling instead of water cooling for an ice-climbing robot?

The concept to be optimised by this research is the Freezing Locomotion Integrated Chain Kinematics (FLICK). This concept uses a track of adhesion links that use state-of-the-art ice locomotion: By melting and freezing the ice with peltier modules integrated into the links, the robot can move over the ice wall. To reach subzero temperatures to freeze the ice, the hot side of the Peltier modules must be cooled.

FLICK uses a water circulation system to provide this cooling. The components of this water cooling system are listed in Table 3.1. As shown, this system requires multiple parts (tubes, fan, pump & water manifold to divide the water), which increases the volume, weight, complexity and risk of the system. Furthermore, the pump and fan use power.

Table 3.1: Components of FLICK's water cooling system

Component	Mass [g]	Amount
Laing DDC-pump 12V DDC-1T	249	1
60 mm 12 VDC fan	40	1
60 mm water radiator	122	1
PC10-02 Push-in Fitting	19	4
PC-04-M6 Push-in Fitting	10	64
10 mm flexible tube	60/m	2
4 mm flexible tube	10/m	64
2 mm ball bearing	36	2
O-ring seal	4	2
Live-Swivel	NA	2
16 spout manifold	NA	2

Phase Change Materials use the energy needed for phase change from a more ordered to a less ordered state, or latent heat, to absorb energy and thereby cool a heating element. This results in sustained cooling around the phase change temperature. PCMs are a promising solid-state cooling technique, as the components listed in Table 3.1 could be replaced by 16 containers with PCM. This cooling system would require no power.

Previous research has been done on PCM cooling of Peltier modules. In the research of X. Li et al. 2014 [40], PCM-OM37 was used to cool the Peltier with a power input of 3 W resulting in a temperature of 10 °C for 20 min. Tan and Zhao et al. 2015 [68] studied the performance of TEC systems for space cooling applications using PCM, reaching a minimum temperature of 12.1 °C for 5.0 A over 14 hours. The experimental tests demonstrated that the average coefficient of performance of the Peltier modules increased by 56% (from 0.5 to 0.78) due to integration with PCM. These two researches focused on long-duration cooling and no subzero temperatures were obtained. The research described in this report aims to obtain subzero temperatures for the duration needed to freeze the melted ice and obtain ice adhesion.

Using pulse operation C. Selvam et al. 2019 [62] simulated subzero temperatures and the use of PCM reduced the cold side temperature from -14.5 to -17.5 °C. The research described in this report aims to find subzero temperatures with a constant DC power supply, instead of a pulse operation, to ensure the PCM can be powered with the 1S2P 8800 mAh 3.8 V LiHV battery pack as described by Tom Mooijman 2023 [76].

This research will answer the question:

How to use phase change material cooling to create ice adhesion for an ice-climbing robot?

In the next chapters, this question will be answered as follows: The test setup and the design of the ice adhesion test mechanism are described in Chapter 4. This mechanism is used in the experiments described in Chapter 5 and Chapter 6. In Chapter 5 the cooling performance of various PCMs is assessed with experiments and a theoretical model, resulting in a selected PCM. In Chapter 6 the ice adhesion of the mechanism with the selected PCM is tested on ice. Using these results and the theoretical model, PCM cooling is integrated into the FLICK's adhesion link as described in Chapter 7.

4

Ice Adhesion Test Mechanism Design

As discussed in Chapter 3, PCMs can provide a solid-state cooling solution for the FLICK robot. To cool the Peltier module with a PCM, the PCM must be integrated into the adhesion mechanism. This adhesion mechanism is needed to test the cooling behaviour of different PCMs and test the viability of using PCM cooling for ice adhesion. This chapter will answer the subquestion:

How to cool a Peltier module with a phase change material?

To answer this question, an ice adhesion mechanism is designed using PCM cooling. Figure 4.1 shows a schematic drawing of this mechanism in the test setup. Where the temperature sensors are indicated by the black dots. First, the test setup, used to assess the cooling performance of the PCMs, is described. Next, the selected Peltier module and the theoretical model are described. Then, the design of the solid-liquid PCM holder and the adhesion pad are described. Finally, the chapter concludes with the major findings of this chapter and the presentation of the final ice adhesion mechanism used in the tests in Chapter 5 and Chapter 6.

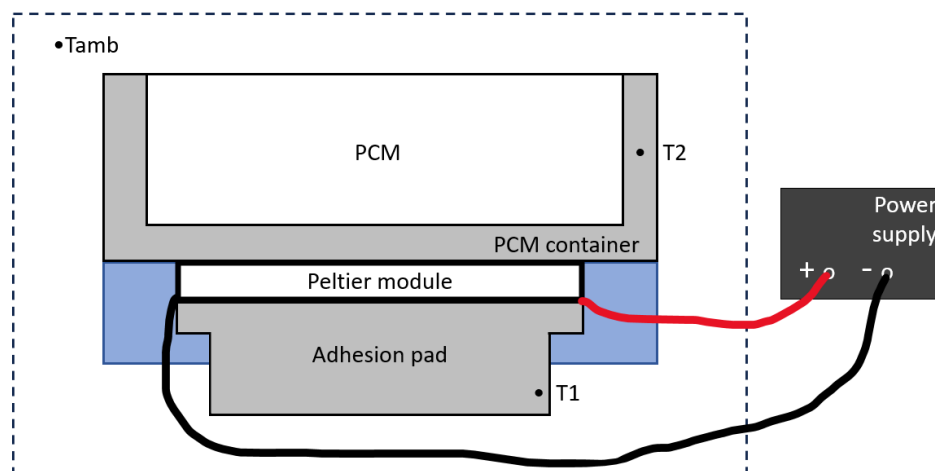


Figure 4.1: Schematic drawing of ice adhesion mechanism with PCM cooling in the test setup. The dots indicate the temperature sensors.

4.1. Test setup

The tests were performed in the wind tunnel facility of the faculty of Aerospace Engineering. In this section, the test setup is described. First, the thermocouples which will be used to measure the temperature response of the Peltier module will be described. Next, the power supplies used during the tests are described.

4.1.1. Thermocouples

T-type thermocouples, interfaced as described by S. Sklavenitis [67], were used to conduct the experiments described in this report. The t-type thermocouple uses a Copper and a Constantan (Cu & Cu-Ni) alloy wire. Type T thermocouples have high stability at sub-zero temperatures, perform well in the presence of moisture without oxidizing and can be used in atmospheres with inert pressures [69].

Thermocouples consist of two wires with different metals which connect at the measuring junction. The ends of the wires are kept at a reference temperature by submerging this reference point in a semi-frozen bath of distilled water or the temperature at this reference point is measured by another temperature sensor. The temperature at the measuring junction can be determined from the voltage between the two wires using the thermoelectric effect as explained in Section 3.2. As the Seebeck coefficient is known for both materials, the temperature can be calculated with Equation 3.2.

A thermocouple is shown in Figure 4.2. Here, two wires are connected to the object at T_{sense} while the other side is at a reference temperature T_{ref} . The ends of the wires are connected to a voltmeter (V) with copper wires. The measured volt can be converted to the T_{sense} .

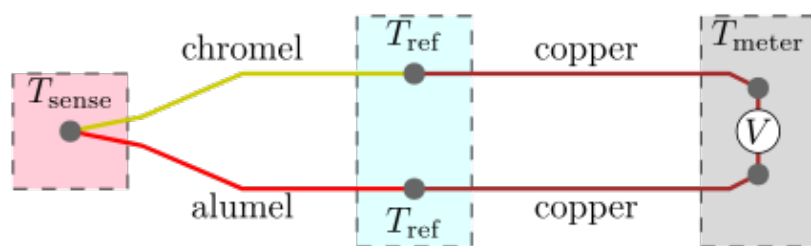


Figure 4.2: Schematic of a thermocouple [47].

The data acquisition rate of the sensors was set to measure the temperature 20 times per second. Before each test, the room temperature of the wind tunnel lab was determined by averaging the temperature output of the two thermocouples to be used in the experiment. The temperature response during the experiments was often measured with 2 sensors on the same side of the Peltier module to reduce the risk of measurement errors.

4.1.2. Power supply

A 2 amperes-regulated direct current power supply was used to control the Peltier modules used in the experiments. This power supply, shown in Figure 4.3, could supply a voltage of 3, 4.5, 6, 7.5, 9 and 12 V. To switch the polarity of the power supply the red and black wires were switched manually.



Figure 4.3: 2 amperes regulated DC power supply connected to a Peltier module.

4.2. Selected Peltier module and model

To melt and freeze the ice, Peltier modules are used as explained in Chapter 3. In this section, the selected Peltier module and the developed theoretical model of this module are described.

4.2.1. MCPF-127-14-25-E

The MCPF-127-14-25-E Peltier module from Farnell produces a large maximum temperature difference of 73 K with low power consumption and hence produces less heat than a high-power Peltier module. Table 4.1 shows the properties of the Peltier module. The MCPF-127-14-25-E is more expensive and thicker than other tested modules (see Appendix E), but reaches a larger temperature difference for less supplied power. The recommended operation current is lower than 0.7 of I_{max} , which is 2.73 A in this case.

Table 4.1: Properties of the MCPF-127-14-25-E peltier module.

name	max temperature difference	max voltage	max current	max power	price	dimensions
MCPF-127-14-25-E	73 K	15.7 V	3.9 A	37 W	65.54 EU	40x40x4.8 mm ³

Figure 4.4 shows the measured (solid line in Figure 4.4) and modelled (dashed line in Figure 4.4) temperature response of the MCPF-127-14-25 Peltier module with 3 (green line), 7.5 (blue line) and 12 V (orange line) and 2 A. The measured maximum temperature differences between the hot and cold sides of the MCPF module are 21.56 °C for 3 V, 49.11 °C for 7.5 V and 64.47 °C for 12 V.

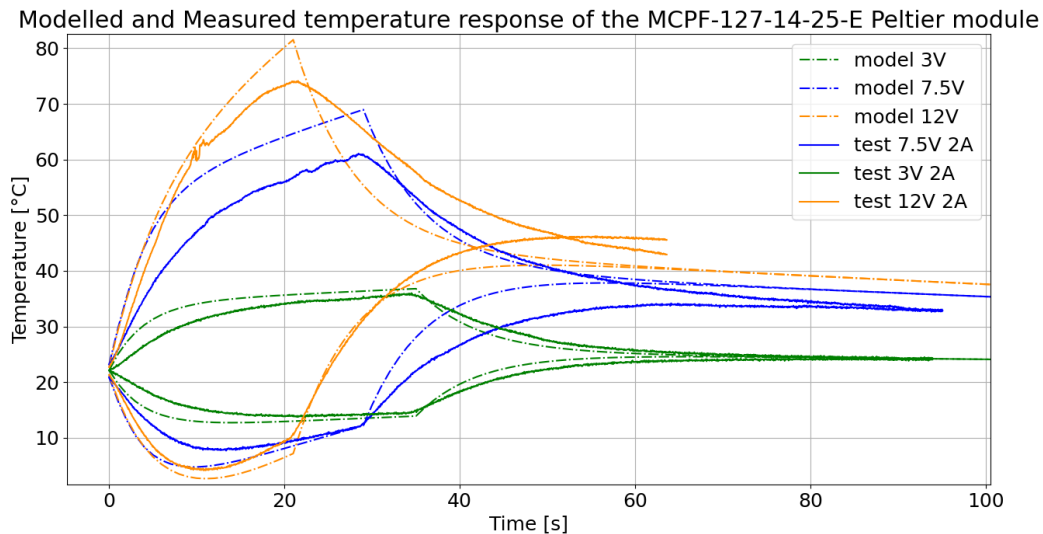


Figure 4.4: Final model of the MCPF-127-14-25-E Peltier module for 3, 7.5 and 12 V and 2A.

As shown in Figure 4.4, the model overestimates the maximum temperatures and underestimates the minimum temperatures. Hence, the model overestimates the heat-pumping capacity of the module. This is due to the assumption that the Seebeck coefficient is constant as discussed in Section C.1.5, especially for the 7.5 V run. The errors on the hot side temperature are 0.78 K for 3V, 7.90 K for 7.5 V and 7.39 K for 12V. The cold side temperature errors are 1.04 K for 3V, 2.93 K for 7.5 V and 1.49 K for 12 V. As this model will be used to estimate the amount of PCM needed to adhere to ice, this model is accurate enough to provide a first order estimation.

4.2.2. Theoretical model

The temperature response of the model was modelled with the estimation equations derived by Zhaoxia Luo 2008 [5] as described in detail in Appendix C. This method uses the parameters on the vendor sheet to estimate the resistivity, thermal conductivity and Seebeck coefficient of the module. This method ensures the developed model can be easily changed to describe a different module with the parameters provided by the developer. To create a more precise module the estimated physical characteristics should be measured as proposed by Huang et al. 2000 [34].

To model the heat pumping rate of the module, Q_c , Equation 3.5 is multiplied by the number of semiconductor couples (127 in the MCPF module) and the Seebeck coefficients of the two semiconductors are combined into the relative Seebeck coefficient to find Equation 4.1 [6]. In a measurement of the Seebeck effect, the difference in the Seebeck coefficients of the two dissimilar materials is called the relative Seebeck coefficient ($\alpha_{pn} = \alpha_p - \alpha_n$) [77].

$$Q_c = 2N \cdot \alpha_{pn} \cdot I \cdot T_c - 0.5 \cdot I^2 \cdot R - K \cdot \Delta T \quad (4.1)$$

Where, N is the number of semiconductor couples, α_{pn} the relative Seebeck coefficient of the semiconductor couple in V/K, I is the current in A, T_h the temperature of the hot side in Kelvin, R the resistance of the Peltier module in Ω , K the thermal conductivity in W/K and ΔT the temperature difference in Kelvin.

The temperature of the hot and cold sides of the Peltier module as a function of time is estimated as shown in the flowchart shown in Figure 4.5.

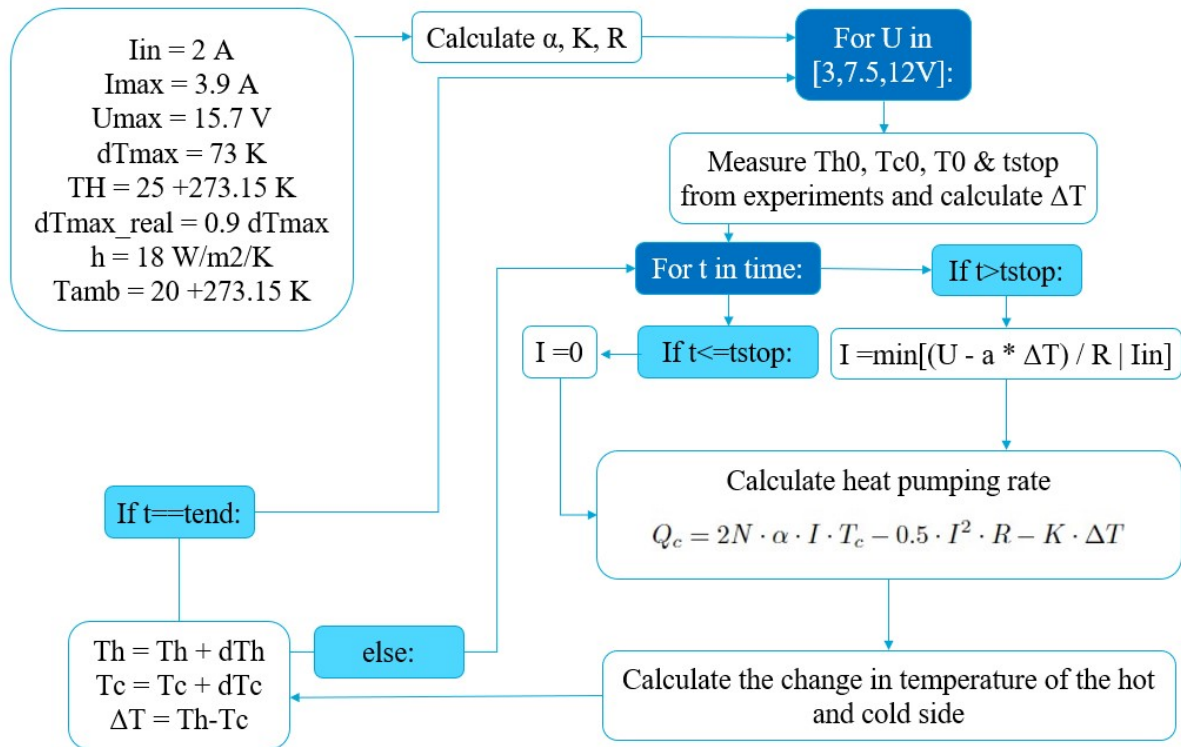


Figure 4.5: Flowchart of Peltier module model.

First, the applied current and voltage, convective heat transfer coefficient, h, and ambient temperature are set, together with the U_{max} , T_H , I_{max} and ΔT_{max} from the vendor datasheet. Next, the Seebeck coefficient, thermal conductivity and resistance are calculated (0.0002073 V/K, 0.363 W/mK & 3.1385 Ω) with the equation described in Section C.1.2. Then, for 3, 7.5 and 12 V, the start temperature and the time the Peltier module was turned off are derived from the measurements shown in Figure 4.4.

Next, the heat flow to and from the hot side is calculated with Equation 4.2.

$$Q_{hot} = 2N\alpha_{pn}IT_c + 0.5 \cdot I^2R - K\Delta T - h \cdot A_{peltier}(T_h - T_{ambh}) \quad (4.2)$$

Where T_c is the modelled temperature of the cold side of the Peltier module, h is the convective heat transfer coefficient, $A_{peltier}$ is the area of one side of the Peltier module, T_h is the modelled temperature of the hot side, ΔT is the temperature difference between the hot and cold side and T_{ambh} is the modelled temperature of the air surrounding the hot side of the Peltier module (see Section C.1.6).

Similarly, the heat flow to and from the cold side can be calculated by Equation 4.3.

$$Q_{cold} = -2N\alpha_{pn}IT_c + 0.5 \cdot I^2R + K\Delta T - h \cdot A_{peltier}(T_c - T_{ambc}) \quad (4.3)$$

Where T_c is the modelled temperature of the cold side of the Peltier module, h is the convective heat transfer coefficient, $A_{peltier}$ is the area of one side of the Peltier module and T_{ambc} is the modelled temperature of the air surrounding the cold side of the Peltier module (see Section C.1.6).

Every 20th of a second (the sampling rate of the sensor), the temperature change is calculated by Equation 4.4, which is derived from the equation of sensible heat storage (Equation 3.6) [53].

$$dT = \frac{Q}{c \cdot m} \quad (4.4)$$

Where dT is the temperature change, Q the heat at the Peltier side, including heat pumping, joule heating and dissipation, and c is the specific heat coefficient which is 0.880 J/gK for the alumina (Al_2O_3) ceramic plate covering the semiconductors. m is the mass of the plate of 6.38 g , calculated with the density of alumina (3.987 g/cm^3 [46]) and plate thickness of 1 mm .

Hence, the temperature of the hot side can be updated as shown in Equation 4.5 and the cold side temperature as shown in Equation 4.6.

$$T_h^{new} = T_h^{old} + \frac{Q_{hot}}{c \cdot m} \quad (4.5)$$

$$T_c^{new} = T_c^{old} + \frac{Q_{cold}}{c \cdot m} \quad (4.6)$$

After the cold and hot side plates and air temperature are updated, the temperature difference between the two plates is calculated. These steps are iterated over time till t_{stop} is reached. Then, the current is set to zero and the program runs till the end of the measured time.

The model was fitted to the measurements with the convective heat transfer coefficient between air and the module and the parameter reducing the ΔT_{max} . The actual ΔT_{max} is often smaller than listed on the vendor datasheet. The optimal fit was found for a ΔT_{max} of 90% of the ΔT_{max} mentioned in the vendor sheet (65.7 instead of $73 \text{ }^\circ\text{C}$) and a convective heat transfer coefficient of $18.55 \text{ W/m}^2\text{K}$.

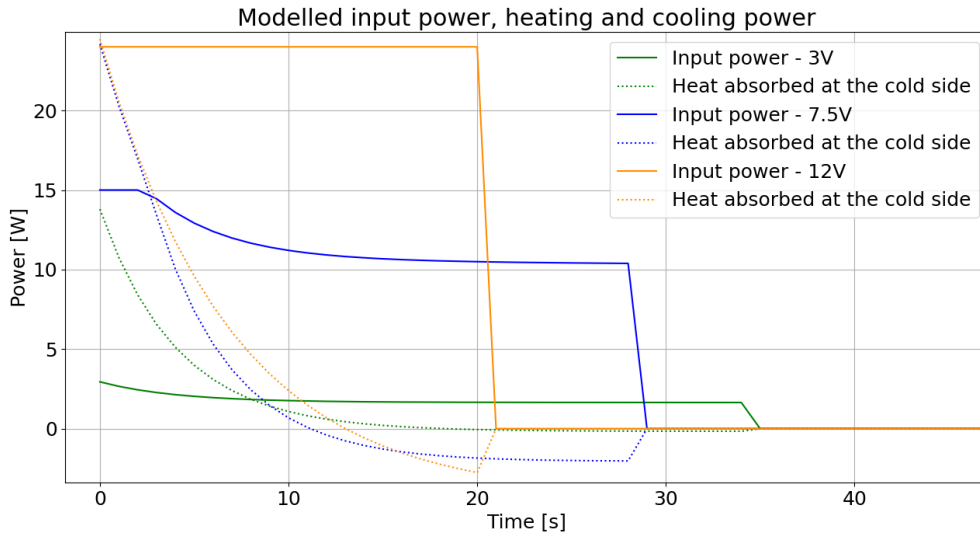


Figure 4.6: Modelled heat absorbed at the cold side of the MCPF-127-14-25-E Peltier module and input voltage for 3V, 7.5 V and 12V.

In Figure 4.6 the heat absorbed at the cold side of the Peltier module and the input power is modelled for the different power levels. The coefficient of performance (COP) of a Peltier module is described by Equation 4.7 [77].

$$COP = \frac{Q_c}{W} = \frac{2N \cdot \alpha_{pn} \cdot I \cdot T_c - 0.5 \cdot I^2 \cdot R - K \cdot \Delta T}{I[2N \cdot \alpha_{pn} \cdot \Delta T + I \cdot R]} \quad (4.7)$$

The COP is larger than 1 (dashed line above solid line in Figure 4.6) for 8s with 3 V, 2.6 s with 7.5 V and 0.1 s with 12 V. When the temperature difference between the hot and cold sides becomes significantly large, the heat flowing to the cold side is larger than the heat pumping. This results in a negative absorbed heat in Figure 4.6 after 18.5 s for 3 V, 11 s for 7.5 V and 13 s for 12 V.

4.3. Solid-liquid PCM container

To cool the hot side of the Peltier module, it must be connected to the PCM. However, as the PCM absorbs the heat of the module, it starts to melt. To contain the liquid PCM, a container is needed to hold the PCM. In Figure 4.7 the test setup used in this section is shown for the clay PCM holder. 2 thermocouples are placed on the cold side of the Peltier module to measure the temperature response. In this section, the effect of the PCM position, material of the PCM holder and contact area between the PCM and the Peltier module is described.

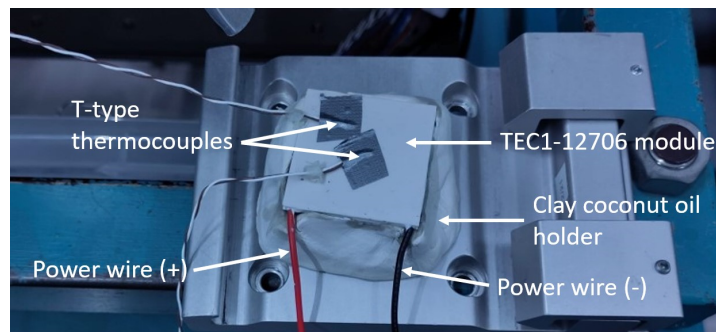


Figure 4.7: Setup with the coconut oil PCM clay holder.

4.3.1. Position of PCM

To test the effect of the position of the PCM, a PCM holder was made from clay as shown in Figure 4.7, holding the PCM under the Peltier module. However, not all the coconut oil melted during this test, as shown in Figure 4.8 by the white solid coconut oil in the middle under the melted transparent oil.

This is caused by the position of the PCM. As the PCM in the clay holder touches the bottom of the Peltier module, the oil is not pressed onto the Peltier module by gravity and the pressure of the atmosphere. When the PCM is on top of the Peltier module, the weight of the PCM increases the contact force between the PCM and the module.

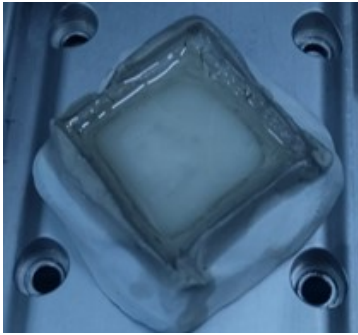


Figure 4.8: Partly melted coconut oil after phase change test.



Figure 4.9: Bubbles in paraffin after phase change test.

Similarly, the air pressure (weight of the atmosphere above the PCM) increases the contact force by pressing the PCM onto the module. As shown in Figure 4.14 the contact force ensures proper melting of the PCM, instead of partial or no melting when the contact force is negative. Furthermore, due to the orientation of the holder, the air bubbles in the PCM would rise towards the Peltier module during the melting (as shown in Figure 4.9, limiting the cooling capacity of the PCM as these air bubbles on the hot side of the Peltier module easily rise in temperature).

Therefore, the coconut oil holder was redesigned to place the coconut oil on top of the Peltier module. This assembly was 3D printed with PLA, shown in Figure 4.10 and Figure 4.11, and could hold 18.7 g of coconut oil. The blue rubber band shown in Figure 4.11 prevented leakage of the coconut oil.

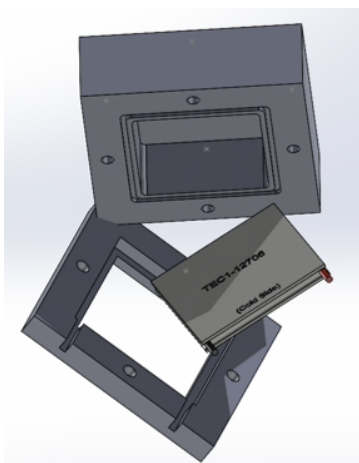


Figure 4.10: Drawing of coconut holder assembly.

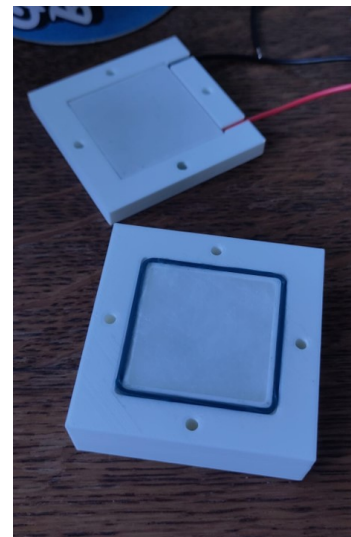


Figure 4.11: First 3D printed design of the coconut holder loaded with solid coconut oil.

Plotting the difference between the start and minimum temperature over the minimum temperature of the temperature response of the TEC1-12706 module with 12 g (clay holder) and 18.7 g (PLA holder) of coconut oil results in Figure 4.12. The minimum temperature of the mechanism must be minimised as subzero temperatures are needed for the ice adhesion. However, the larger the difference between the minimum temperature and the start temperature, the better the cooling mechanism performs. This ensures the ambient temperature during the test is taken into consideration. The PLA holder on top of the Peltier module outperforms the clay holder assembly in terms of this parameter. The test with 13 g of coconut oil taped on top of the Peltier module outperforms both concepts as described in detail in Section 4.3.3.

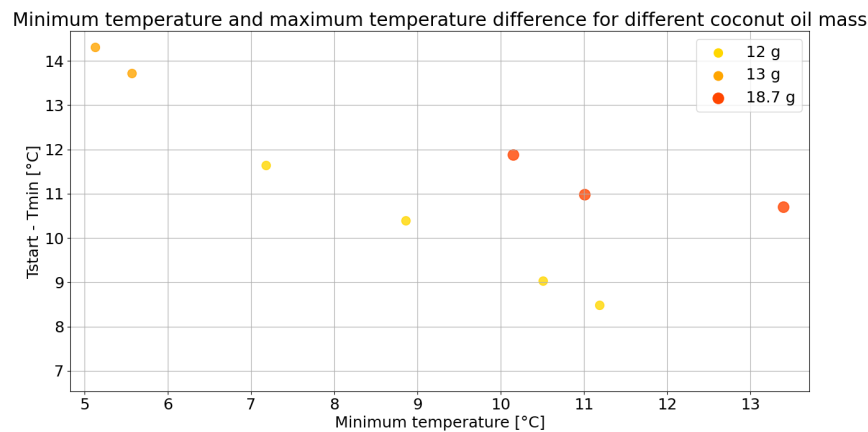


Figure 4.12: Performance of coconut oil PCM cooling for different test setups. The 13 g PCM was connected on top of the Peltier module with tape, the 12 g PCM was connected to the bottom of the Peltier module with the clay holder and the 18.7 g was connected to the top of the Peltier module with the PLA printed holder. All tests used the TEC1-12706 module with a 7.5 V 2 A power supply.

4.3.2. Container material

Due to the high ambient temperature (± 21 °C) during the tests, the coconut oil would not solidify after the test with the 3D printed holder due to the isolating nature of the PLA material [42]. This shows one of the issues of using a PCM to cool a Peltier module, as the heat needs to be released to the environment to be transferred away from the system. Therefore, the coconut holder is made from aluminium, which ensures a high heat flow to the surroundings due to the high thermal conductivity of aluminium (237 W/mK [72]).

4.3.3. Contact area

The effect of the contact area was tested by comparing the PLA printed container and with PCM taped to the Peltier module. The PLA container does not cover the complete area of the module with PCM while the taped test does.

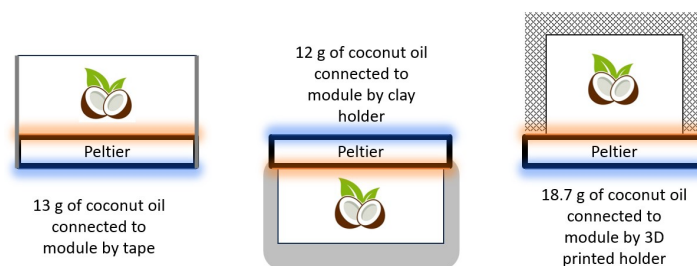


Figure 4.13: Schematic setup of performed test with coconut oil shown in Figure 4.12. (Coconut pictogram designed by Freepik)

In Figure 4.13 the three different test setups resulting in the Figure 4.12 are shown. The first test with coconut oil taped to the top of the Peltier module (see Figure D.4), the second with a clay coconut oil holder (see Figure 4.7) and the third with a 3D printed coconut oil holder (see Figure 4.11).

With Equation 4.8 the time it takes to melt a PCM can be calculated.

$$t_{melt} = m \cdot \Delta H / Q \quad (4.8)$$

Where t_{melt} is the melt time, m is the mass of the PCM, ΔH is the latent heat capacity and Q is the heat produced by the Peltier.

If all the thermal energy (15W) would be absorbed by the coconut oil during melting, it would theoretically maintain a constant temperature on the hot side of the Peltier module for 2 min and 11s for 18.7 g, 1 min and 31s for 13 g and 1 min and 24 s for 12 g. With increasing mass, lower minimum temperatures are reached, as the hot side is kept at a constant temperature for longer. However, this is not observed in Figure 4.12 as the taped PCM test performs the best.

In reality, the hot side of the Peltier module is not kept constant but is heated together with the melted coconut oil. The heat from the Peltier module must travel through the melted coconut oil to melt more of the solid heat, which is described by the thermal conductivity of 0.165 W/mK [18]. The higher the thermal conductivity the easier heat flows through the material. This heat flow causes the melted oil to heat up by sensible heating, dictated by the specific heat capacity of liquid coconut oil of 2.71 J/gK [18].

All the tests reached the minimum temperature 50 seconds after the module was turned on, which is lower than the time needed to melt all the coconut oil. Therefore, the cooling performance is likely determined by the mass of coconut oil touching the ceramic plate instead of the total PCM mass, as shown in Figure 4.14.

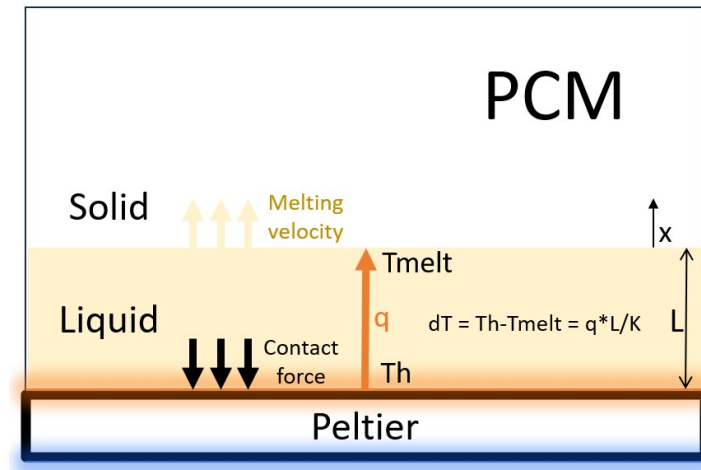


Figure 4.14: Schematic of melting mechanism of PCM on Peltier module.

Fourier's law of thermal conduction shown in Equation 4.9 describes how heat flows through a material in all directions. Assuming the heat flow is constant over the Peltier module, the temperature of the hot side of the Peltier module can be estimated by reducing Equation 4.9 to one dimension resulting in Equation 4.10.

$$q = -K \nabla T \quad (4.9)$$

$$T_h = dT + T_{melt} = \frac{qL}{K} + T_{melt} \quad (4.10)$$

Where T_h is the hot side temperature, ∇T the temperature gradient, dT the difference between the hot side and melting temperature, T_{melt} the melting temperature, q the heat flux in W/m^2 , L the thickness of the melted coconut oil and K the thermal conductivity. This method does not take into account the heat absorbed by sensible heat storage of the melted PCM, which would heat the top side more as not all power is absorbed by the latent heat of the PCM. Hence, this results in an underestimation of the hot side temperature.

The melting velocity can be calculated by dividing the thickness of the melted coconut oil, x , by the melt time calculated by Equation 4.8 resulting in Equation 4.11.

$$V_{melt} = \frac{x}{t_{melt}} = \frac{q \cdot A_{peltier}}{A_{PCM} \cdot \rho \cdot \Delta H} \quad (4.11)$$

Where, A_{PCM} is the area of PCM touching the Peltier module, $A_{peltier}$ the area of the hot side of the Peltier module and ρ the density of the PCM. Here, the Q is replaced by $q \cdot A_{peltier}$.

The smaller the A_{PCM} , the larger the melting velocity which results in a higher thickness of melted coconut oil and hence a larger temperature on the hot side of the Peltier. This would explain the differences observed in Figure 4.12, as the test with 13 g of coconut oil had the largest contact area with the Peltier module. For the test with 18.7 g the coconut oil does not cover the complete Peltier module, as shown in Figure 4.15, and hence the sides can heat up without the heat being absorbed by the PCM. The performance of the 12 g coconut cooling is also influenced by the coconut oil being on the bottom instead of on the top, decreasing the contact force, as described in Section 4.3.1.

Hence, the PCM holder must increase the contact area with the PCM to enable the maintained cooling needed for ice adhesion. The contact area with the PCM can be increased by using heat fins that transport the heat of the Peltier module into the PCM as shown in Figure 4.16.

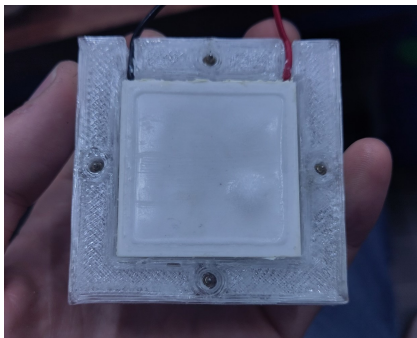


Figure 4.15: Peltier module after test showing the location where the coconut oil contacted the module.

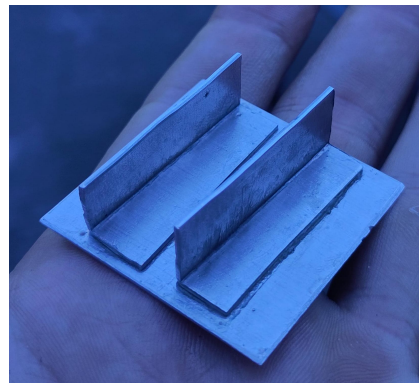


Figure 4.16: Aluminium interface between Peltier and coconut oil with fins.

These 1 mm thick aluminium fins will ensure the generated heat will be absorbed by the complete PCM and not only by the bottom layer, increasing the cooling effect of the setup. Testing the temperature response of the 1 cm aluminium pad connected to the Peltier with a current of 3A resulted in Figure 4.17.

As expected the fins increase the performance of the PCM assembly as indicated by the smaller heating rate of the cold side. However, only one of the temperature sensors shows a lower minimum temperature for the test with fins while the other shows a higher temperature (in grey) compared to the test without fins (in orange). This could be due to the connection between the fins and the aluminium plate made with 2-component epoxy. To further increase the performance the next design iteration of the container will incorporate these fins with a better thermal connection.

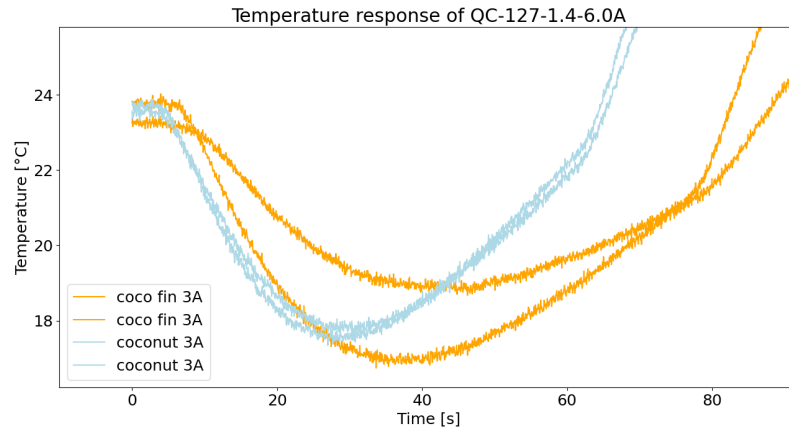


Figure 4.17: Cold side temperature response of the aluminium pad connected to the QC-127-1.4-6.0A with and without aluminium fins.

The final aluminium container was milled from 60 x 50 x 23 mm aluminium, ensuring unobstructed heat flow to the fins, as the container is made from one part. The initial design of the container is shown in Figure 4.18. Where the heat fins are thin to optimise the amount of surface area and contained PCM volume. The thickness of the aluminium between the PCM and Peltier module is 3 mm. During the production of this part, the heat fins started to break during the milling process, due to their small thickness, and the heat fin configuration was altered to ensure easy production. The new design is shown in Figure 4.19, weights 71.5 g and can hold 39.51 cm³ of PCM.

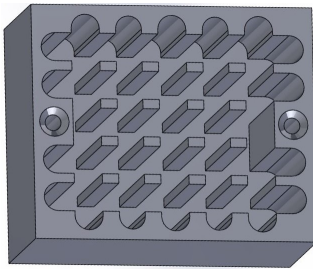


Figure 4.18: Solid work drawing of the theoretical aluminium container.

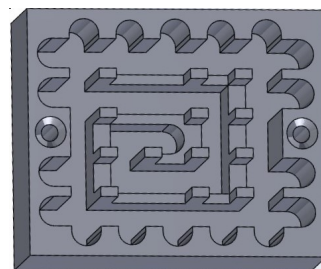


Figure 4.19: Solid work drawing of the actual aluminium container.

Figure 4.20 shows the container filled with coconut oil, Figure 4.21 the coconut oil after 1:10 min of heating and Figure 4.22 after 2:50 min of heating. These images show the heat fins ensure the heat from the Peltier module is transferred into the PCM.

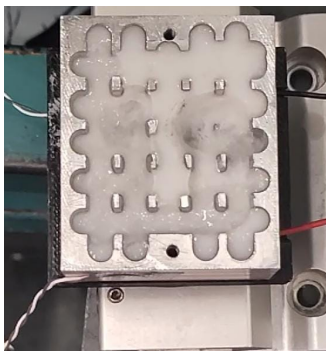


Figure 4.20: Aluminium PCM container with coconut oil.

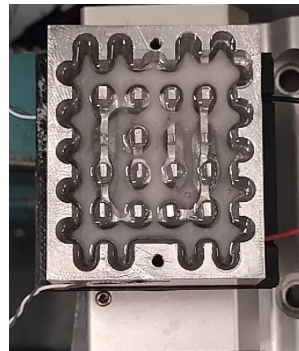


Figure 4.21: Aluminium PCM container with coconut oil after 1:10 min of heating.

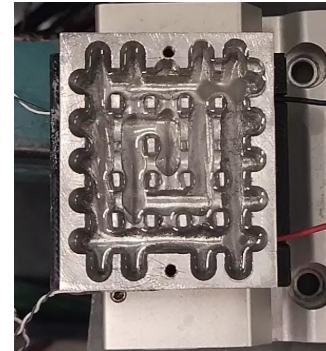


Figure 4.22: Aluminium PCM container with coconut oil after 2:50 min of heating.

4.3.4. Effect on temperature response

Connecting this container to the MCPF-127-14-25-E Peltier module with the Prolimatech PK-3 thermal paste with a thermal conductivity of 11.2 W/mK^1 and testing the temperature response with the empty container resulted in Figure 4.23.

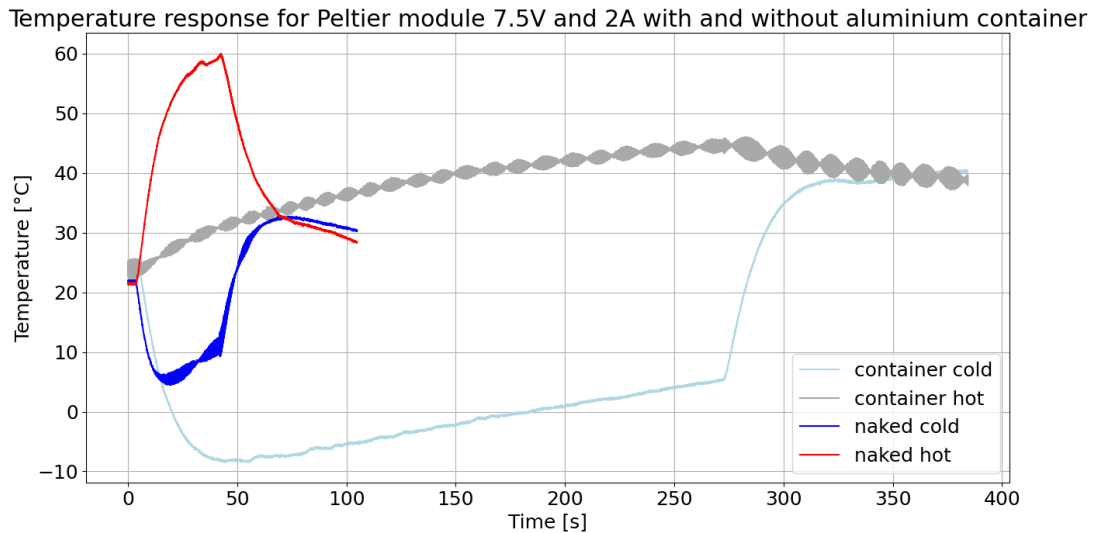


Figure 4.23: Temperature response of the hot and cold side of the MCPF-127-14-25-E module with and without the empty aluminium container.

As shown the module reaches subzero temperatures when the empty container is connected. This is due to the large surface area of the container, which radiates the heat to the surrounding air. Hence, the container works as a heat sink in this experiment.

In Figure 4.24 the results of the measurements of the MCPF module with the empty container (green solid lines) and the model (dashed lines) described in this section are plotted. This model does not consider a temperature gradient across the container. However, due to the high thermal conductivity of aluminium, the difference between the temperatures can be neglected [2]. Furthermore, the air in the container is assumed to be heated up together with the container, without modelling the heat transfer from the container to the air. This is justified by the large area of the aluminium in contact with the air due to the heat fins.

¹https://www.bo1.com/nl/nl/p/prolimatech-pk-3-5g-heat-sink-compound-11-2-w-m-k/9200000034871734/?bltgh=tPAVIQuwtXy9XYqrte1Cgw.2_22.26.ProductTitle, retrieved on 19-08-2023.

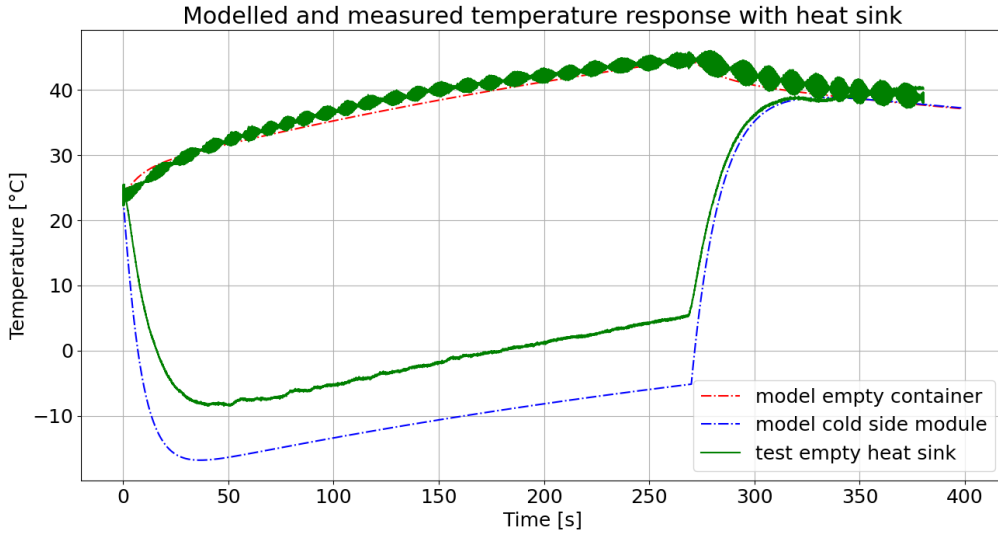


Figure 4.24: Modelled and measured temperature response of the MCPF-127-14-25-E module with the empty aluminium container.

As shown in Figure 4.24, the model provides a good fit, especially for the temperature of the container as shown by the red line. However, the temperature of the cold side is underestimated by the model as shown by the blue line. As mentioned in Section 4.2, the model overestimates the heat pumping, due to the assumption of a constant Seebeck coefficient as described in Appendix C. As this model will be used to estimate the amount of PCM needed to create ice adhesion, the cold side temperature must fit the experimental data well. The cold side must obtain subzero temperatures to freeze the adhesion pad to the ice. Hence, the model is fitted to the data by reducing the heat pumping capacity, calculated by $2N \cdot \alpha \cdot I \cdot T_c$. The best fit was found for a heat pump reduction of 20%. The resulting model is shown in Figure 4.25.

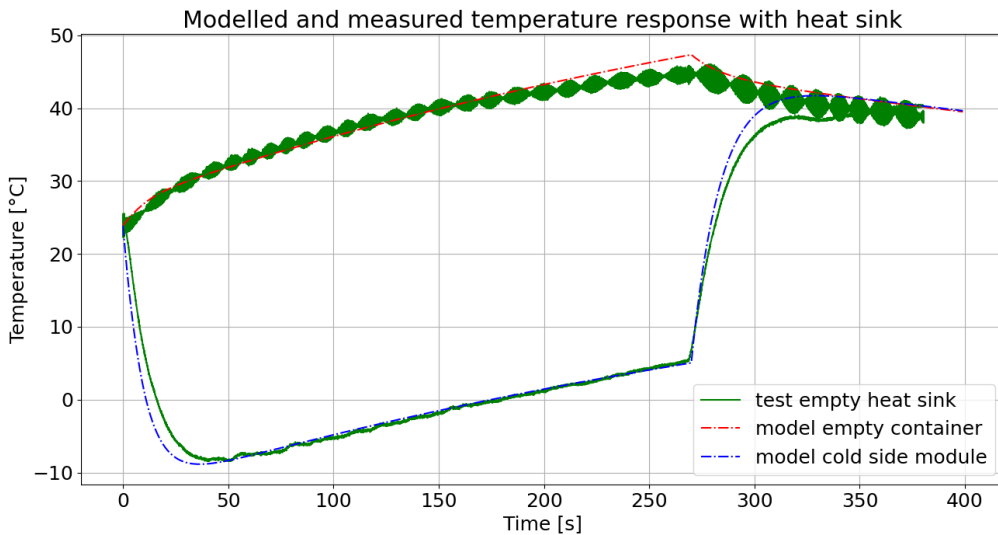


Figure 4.25: Modelled temperature response of the MCPF-127-14-25-E module with a 20% reduced heat pumping power with the empty aluminium container compared to the measurements.

4.4. Adhesion pad

As the ceramic plates of the Peltier module are brittle, applying loads should be avoided as they are sensitive to brittle fractures [16]. Therefore, to adhere to an icy surface, an adhesion pad is used to transfer the heat from the Peltier module to the ice. Previous research found aluminium to be the best material choice for the adhesion pad, due to its high thermal diffusivity (237 W/mK) and low density (2.70 g/cm³) resulting in a lightweight solution [76]. The thermal diffusivity determines the time it takes for the heat of the Peltier module to reach the ice.

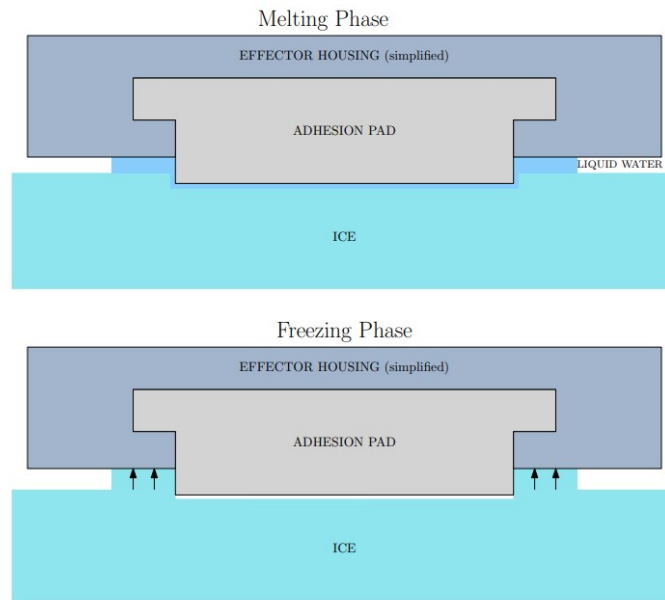


Figure 4.26: Liquid water formed during the melting phase (top), potentially causing the adhesion pad and ice sample to separate (bottom). Deformations are scaled up (3X) to visualise the effect. [76]

The thickness of the pad influences the rate of cooling and heating of the ice by the pad as well. The smaller the thickness, the faster the transfer of heat. The thickness of the pad was chosen to be 1 cm which ensures proper ice adhesion. Previous research found that reducing the thickness further could result in the separation of the pad from the ice, by the expansion of the water trapped between the ice and effector housing as shown in Figure 4.26 [76]. Figure 4.27 shows the drawing of the adhesion pad.

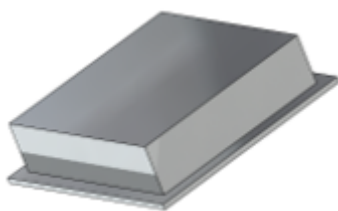


Figure 4.27: Drawing of 1 cm aluminium pad.

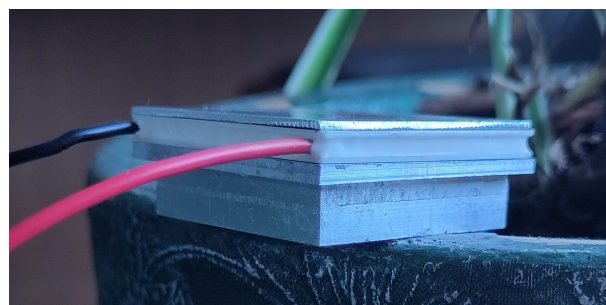


Figure 4.28: Peltier module with aluminium 1 cm pad on the bottom and 1 mm interface plate at the top.

In Figure 4.28 the 1 cm thick aluminium pad on the cold side and a 1 mm aluminium plate on the hot side connected with FCT-730 thermal conductive tape is shown. In Figure 4.29 the temperature response of this setup is plotted. Here the temperature response is shown till the Peltier module is turned off.

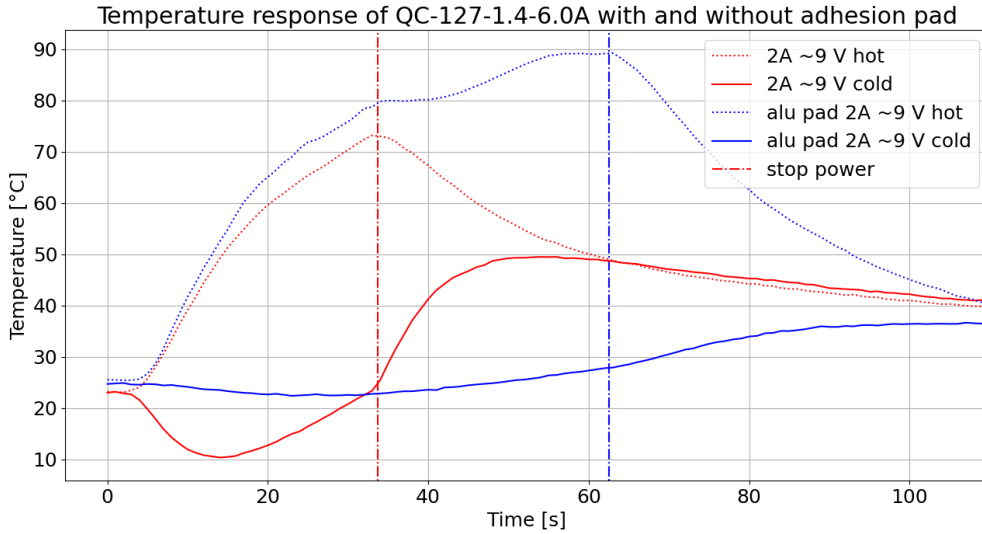


Figure 4.29: Temperature response of QC-127-1.4-6.0A with a 1 mm aluminium plate at the hot side with and without a 1 cm aluminium pad. $T_{amb} = 20.7\text{ }^{\circ}\text{C}$.

As expected the pad reaches higher temperatures on the cold side, than the measurements without the pad. This is because the heat of the Peltier module needs to be conducted through the aluminium pad. This takes time during which the system and hence the cold side of the Peltier module heat up. The specific heat capacity of aluminium is 902 J/kgK [72].

The adhesion pad is connected to the Peltier module with thermal paste and the PETG effector housing (black in Figure 4.33) is screwed to the container. In Figure 4.30, the modelled and measured temperature response of the final adhesion mechanism with an empty container is shown. The empty adhesion mechanism does not reach subzero temperatures and therefore the adhesion mechanism must be filled with a PCM to reach the desired temperatures.

Modelled and measured temperature response of adhesion pad with heat sink

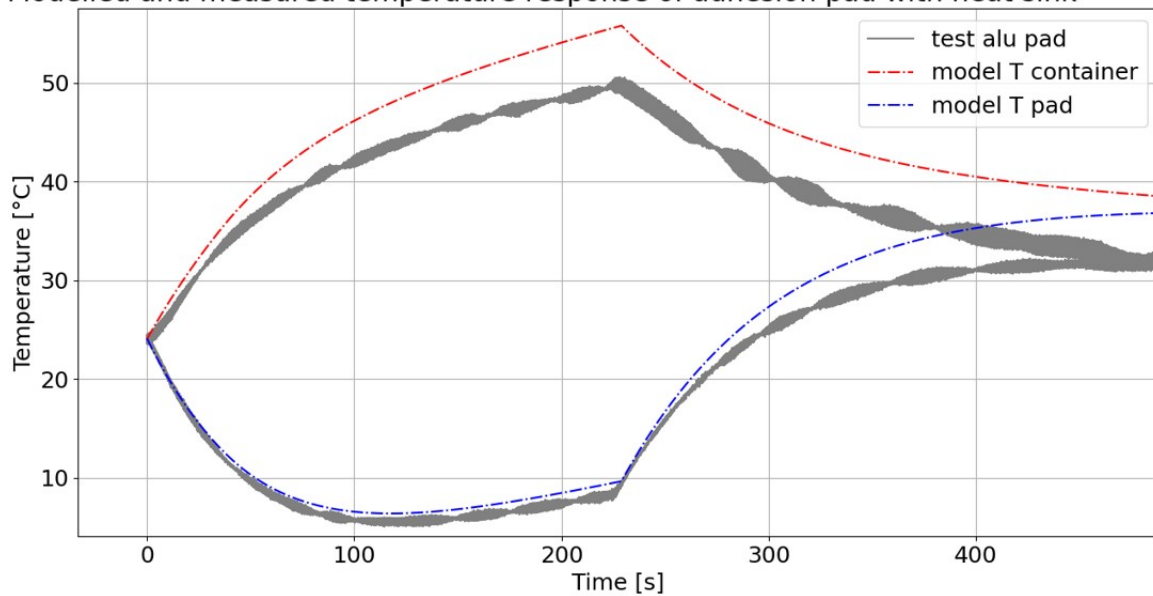


Figure 4.30: Modelled and measured temperature response of the MCPF-127-14-25-E module with the aluminium adhesion pad and the empty container. $7.5\text{ V } 2\text{ A}$.

As shown the model fits the measurement results well, especially for the adhesion pad temperatures, which determine if ice adhesion is possible or not. The slight overestimation of the adhesion pad temperature will result in a more conservative estimate for the required PCM mass (more mass, less risk of no adhesion).

4.5. Conclusion

This chapter aimed to answer the question:

How to cool a Peltier module with a phase change material?

. The important findings presented in this chapter are:

- **The PCM must be located on top of the Peltier module during melting.** This was shown by the tests with clay containers. When the PCM is placed under the module the air inside the solid PCM rises to the module when the PCM melts. This results in reduced heat absorption by the PCM.
- **The material of the PCM container should have a high thermal conductivity to ensure the PCM can radiate the absorbed heat to the environment.** During the test in this chapter, the downside of PCM cooling was observed: after the coconut oil was melted it remained melted for a long time, as the absorbed heat during melting must be dissipated to solidify the oil. Due to the isolating properties of the 3D-printed PLA, this dissipation time is large.
- **The total area of the Peltier module must be covered by the PCM or PCM container.** The first 3D-printed coconut holders did not cover the total area of the Peltier module, resulting in less heat transfer between the module and the coconut oil.
- **The contact area between the PCM and the container must be as large as possible to increase the available latent heat storage.** Aluminium heat fins were tested to decrease the heating rate of the Peltier module, as available PCM is increased with the increase in contact area between the PCM and the container.

The final assembly is shown in Figure 4.33. This assembly was used to perform the tests to select a PCM as described in Chapter 5 and tested on ice as described in Chapter 6. The holder could be closed by a 1 mm thick aluminium lid. The lid was connected by 2 screws allowing for the testing of multiple PCM. However, to prevent leaking this lid must be connected to the assembly with liquid gasket² when integrated into a robotic system.



Figure 4.31: Top view

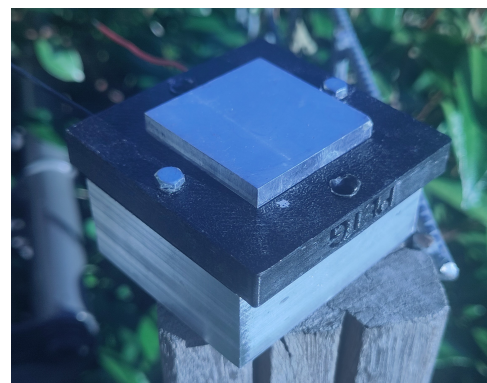


Figure 4.32: Bottom view

Figure 4.33: Final adhesion mechanism assembly with octadecane.

A theoretical model is developed to estimate the temperature response of the MCPF-127-14-25-E and the adhesion mechanism described in this chapter. This model can be used to assess the cooling performance of different PCMs, as described in Chapter 5, and estimate the amount of PCM needed to cool the FLICK links, as described in Chapter 7.

²<https://www.permabond.com/resource-center/comparison-of-fip-liquid-gaskets-to-conventional-gaskets/>, retrieved on 26-08-2023.

5

Phase Change Material Cooling

To optimise the cooling mechanism of FLICK [76], the water cooling system should be replaced by a static solution as explained in Chapter 3. Phase change materials store the thermal energy from the heat source. This energy is released as the material cools. This means that the material can absorb the generated heat, which keeps the desired component cool. Using the ice adhesion test mechanism and theoretical model described in Chapter 4 the following subquestion is answered in this chapter:

What is the optimal phase change material to absorb the energy from the adhesion mechanism?

In this chapter, sensible and latent heat storage cooling are analysed by tests with the developed adhesion mechanism and various PCM (described in detail in Appendix D) and the theoretical model (described in detail in Appendix C). Based on this analysis, a PCM is selected to use in the ice adhesion mechanism designed in Chapter 4. In Appendix A the short descriptions of the raw measurement files of the experiments are listed.

5.1. Sensible heat storage

As described in Chapter 3, the sensible heat storage can be calculated by Equation 5.1. The model uses this equation to estimate the effect of the PCM container and the adhesion pad on the temperature response.

$$Q = \int_{T_{start}}^{T_{end}} m c_p T dT \quad (5.1)$$

Where Q is the stored heat in J , m the mass in kg , c_p the specific heat capacity at constant pressure in J/kgK , T_{start} and T_{end} , the initial and final temperature respectively in K .

The effect of sensible heat storage by water can be modelled by replacing the air inside the container with water in Equation C.21 resulting in Equation 5.2.

$$dT_h = \frac{Q_h - Q_{dissipation}}{c_{alumina} * m_{plate} + c_{alu} * V_{container} * \rho_{alu} + c_{water} * V_{water} * \rho_{water}} \quad (5.2)$$

Where, Q_h is the heat flow to the hot side, $Q_{dissipation}$ the heat dissipating from the container to the surrounding air, $c_{alumina}$, c_{alu} & c_{water} are the specific heat coefficient for alumina (880 J/kgK [46]), aluminium (900 J/kgK [72]) and water (4200 J/kgK [53]), m_{plate} is the mass of the hot side plate and $V_{container}$ and V_{water} are the volume of the container (29.49 cm³) and the water inside the container (39.51 cm³). ρ_{alu} and ρ_{water} are the densities of aluminium and water.

Using this equation, the effect of the sensible heat storage of water on the temperature response to the adhesion pad can be compared to the measurements. This comparison is shown in Figure 5.1.

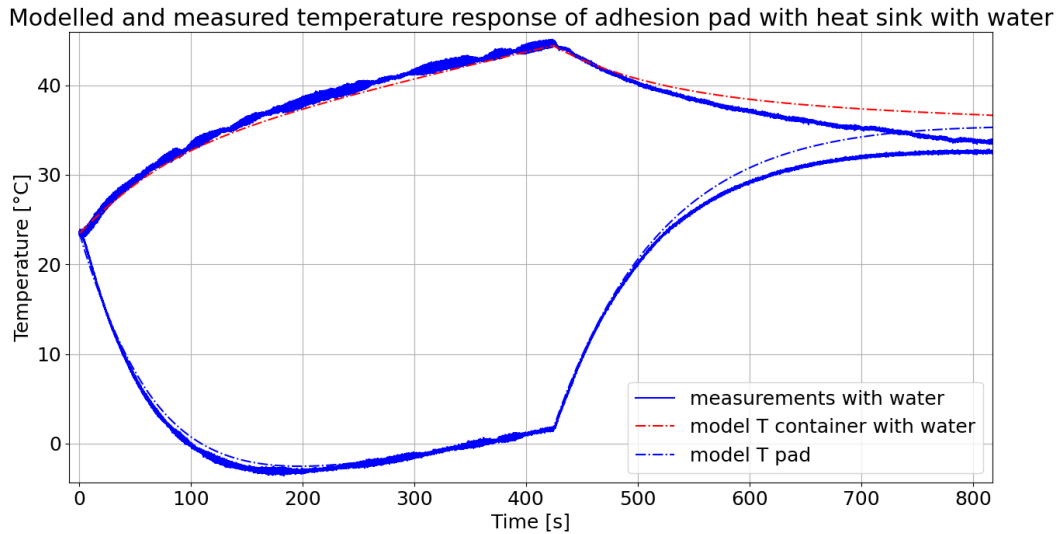


Figure 5.1: Modelled and measured temperature response of the MCPF module with the aluminium adhesion pad and the container filled with water.

As shown in Figure 5.1, the model provides a good estimation of the temperature response of the container filled with water and its effect on the temperature of the adhesion pad. Due to the higher latent heat capacity of 4200 J/kgK of water, the adhesion mechanism reaches subzero temperatures as shown in Figure 5.1.

In conclusion, sensible heat storage can be used to obtain subzero temperatures with a Peltier module. The larger the specific heat capacity, the larger the available sensible heat storage. Hence, the selected PCM must have a high specific heat capacity.

5.2. Latent heat storage

Latent heat is the amount of energy needed for a material to change phase from an ordered to a less ordered state. Figure 5.2 show the stored energy of water (blue dashed line), coconut oil (orange line) and octadecane (pink line) over the temperature range between 0 and 50 °C.

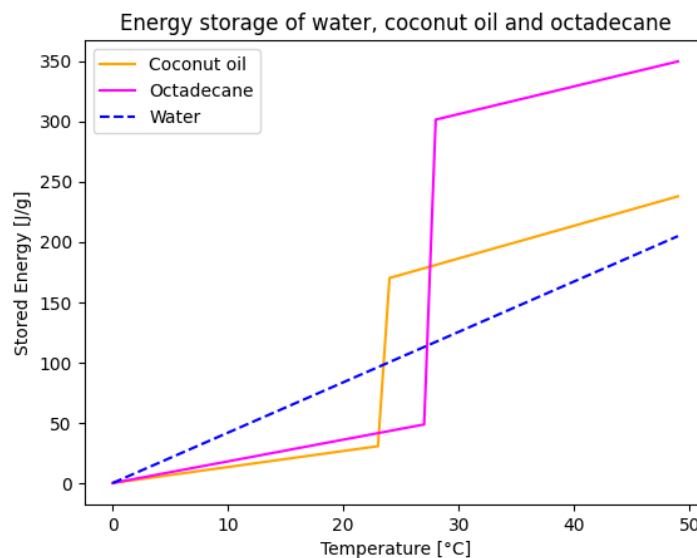


Figure 5.2: Comparison of stored energy by liquid water, coconut oil and octadecane between 0 and 50 °C

Before the melting point of the coconut oil or octadecane, the water can store more energy due to its high specific heat capacity. When the melting temperature is reached (24 °C for coconut oil and 28 °C for octadecane), the stored energy by the PCM increases due to the needed energy to melt the PCM. After this point, the PCMs outperform the water, which agrees with the notion in Chapter 3 that PCMs can outperform sensible heat storage materials near their transition temperature. Hence, both the specific and the latent heat capacity of the PCM must be high, as these determine how much heat can be absorbed before and after the point of phase change and how much energy the PCM can absorb during phase change.

In Figure 5.3 the temperature response of the MCPF-127-14-25-E with 25 g of Octadecane as PCM is compared to the empty container and the container filled with water. The bottom lines show the temperature of the adhesion pad and the top lines show the temperature of the wall of the container.

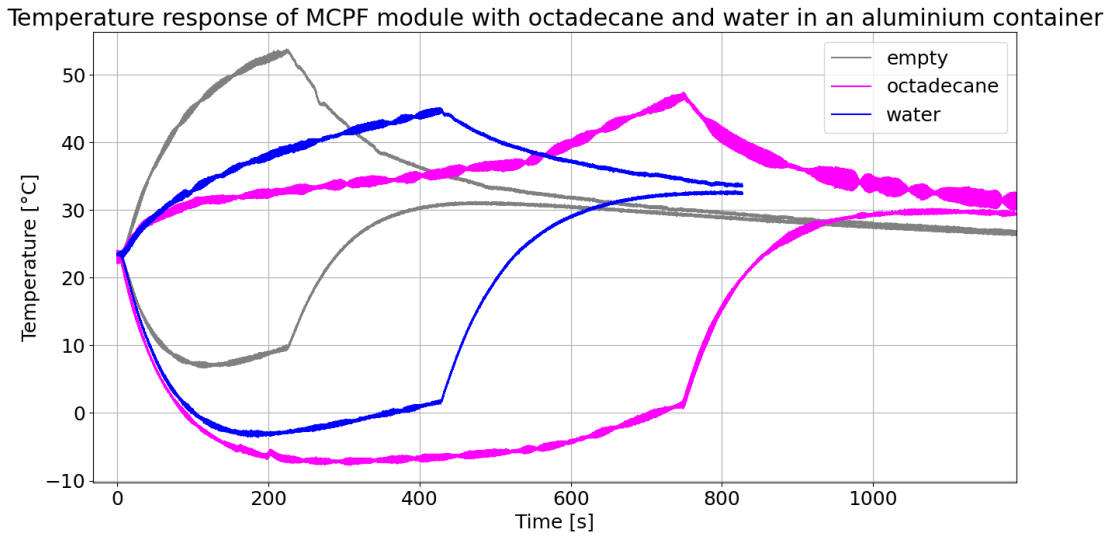


Figure 5.3: Temperature response of the MCPF-127-14-25-E with octadecane compared to water and the empty container, supplied power: 7.5 V and 2 A.

As expected from Figure 5.2 the use of octadecane as PCM results in lower temperatures that are sustained for longer as shown in Figure 5.3. A minimum temperature of -7.71 °C of the adhesion pad and sustained subzero cooling over 10 minutes and 15 seconds was obtained. These results show that the latent heat storage of octadecane outperforms the sensible heat storage of water and is therefore a good choice to use in the adhesion mechanism of the ice climbing robot at room temperature.

To model the PCM cooling, the sensible and latent heat storage of the PCM must be calculated as described in Chapter 3 with Equation 5.3.

$$Q = \int_{T_{start}}^{T_{melt}} m c_{p,s} T dT + m \Delta_{melt} H + \int_{T_{melt}}^{T_{end}} m c_{p,l} T dT \quad (5.3)$$

Where T_{melt} is the melting temperature, $c_{p,s}$ & $c_{p,l}$ the specific heat capacity at a constant pressure of the solid and liquid PCM, $\Delta_{melt} H$ the latent heat capacity in kJ/kg.

The first part of the right-hand side (RHS) of the equation describes the sensible heat storage of the PCM before it starts to melt. During this time the change in temperature of the container with PCM is calculated by plugging the specific heat capacity, volume and density of the solid PCM into Equation C.21 resulting in Equation 5.4.

$$dT_h = \frac{Q_h - Q_{dissipation}}{c_{aluminum} * m_{plate} + c_{alu} * V_{container} * \rho_{alu} + c_{PCM} * V_{PCM} * \rho_{PCM}} \quad (5.4)$$

When the temperature of the PCM container reaches the melting temperature of the PCM, the total absorbed heat by the melting of the complete PCM is calculated by the 2nd term in the RHS of Equation 5.3. However, the PCM in the container melts over time, as explained in Section 4.3. The melting velocity, v_{melt} is calculated with Equation 5.5 can be calculated while the hot side of the peltier module and hence the container heat up further.

$$v_{melt} = \frac{Q_h}{A_{PCM} \cdot \rho \cdot \Delta H} \quad (5.5)$$

Where A_{PCM} is the surface area inside the PCM container of 126.88 cm². The larger this area the slower the melting velocity, as more PCM is melted with the same heat flux.

With the melting velocity the length of melted PCM above the melting area can be calculated with Equation 5.6.

$$L = v_{melt} \cdot (t - t_{meltstart}) \quad (5.6)$$

Where t is the time and $t_{meltstart}$ is the time when the melting starts.

With this length and Figure 4.14 the temperature of the container, T_h , can be estimated with Equation 5.7

$$T_h = T_{melt} + \frac{Q_h \cdot L}{K \cdot A_{peltier} \cdot \rho_{PCM} \cdot \Delta_{melt} H} \quad (5.7)$$

When L is equal to $L_{max} = V_{pcm} / A_{pcm}$, all PCM is melted and the heat of the module is absorbed by the sensible heat storage of the melted PCM. This is described by the last term in Equation 5.3. The temperature of the container is modelled by Equation 5.4 using the specific heat capacity of the liquid PCM.

To model the temperature response of the PCM container with octadecane, the following characteristic parameters of octadecane were used [22]:

- Specific heat capacity: solid: 1800 J/kgK, liquid: 2300 J/kgK
- Latent heat capacity: 237 kJ/kg
- Thermal conductivity: 0.335 W/mK
- Density: 868 kg/m³
- Melting temperature: 28 °C

The measured and modelled temperature responses are shown in Figure 5.4.

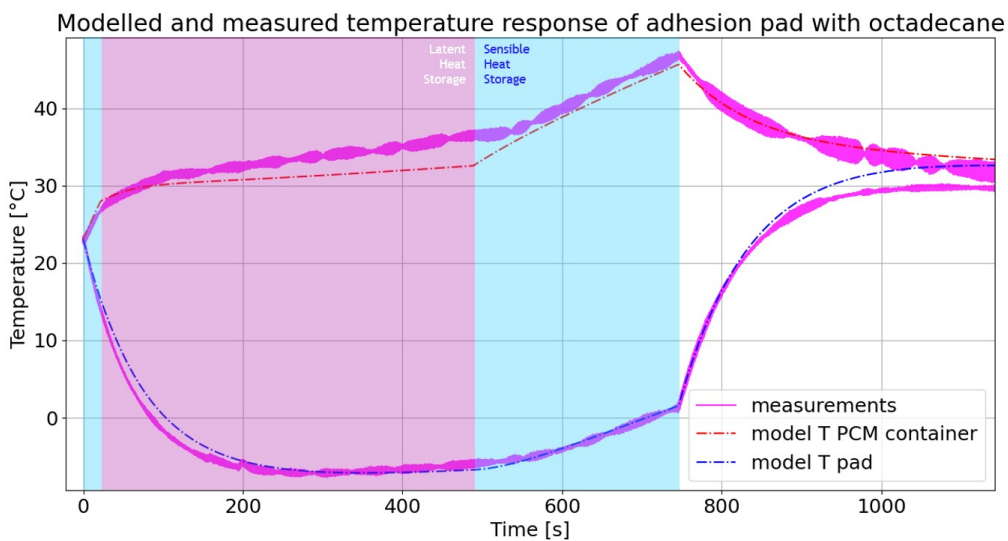


Figure 5.4: Modelled and measured temperature response of the MCPF module with the aluminium adhesion pad and the container with octadecane. Where the melting time is indicated by the pink window.

As shown the model fits the measurements well. The adhesion pad temperature response between 0 and $t_{stop} = 746$ s has an RMSE of 0.9 and the minimum temperature is overestimated by 0.56 °C. Therefore, during the melting time of octadecane (466 s), all the heat is assumed to be absorbed by the latent heat storage of octadecane and the contribution of the sensible heat storage is discarded in this model. This assumption can be made due to the high latent heat capacity of octadecane of 237 kJ/kg [22].

The phases of sensible and latent heat storage in the octadecane model are shown in Figure 5.4. The periods of sensible heat storage are indicated by the blue windows and the latent heat storage by the pink window. The heat is absorbed by the sensible heat storage of the solid octadecane between 0 and 22 s, by the latent heat storage of the melting octadecane between 22 and 488 s and by the liquid octadecane between 488 and 746 s when the Peltier is turned off.

5.3. Combined heat storage

The assumption that all heat is absorbed by the latent heat storage during the melting period of the PCM, was valid in the previous section due to the high latent heat capacity of octadecane. In reality, the container with PCM will absorb the heat with a combination of sensible and latent heat storage: While the PCM melts (latent heat storage), the container and melted PCM are heated up further (sensible heat storage). This effect must be considered for PCMs with a smaller latent heat capacity, like coconut oil, as shown in this section.

To model the temperature response of the PCM container with coconut oil, the following characteristic parameters of coconut oil were used:

- Specific heat capacity: solid: 1330 J/kgK, liquid: 2710 J/kgK [18]
- Latent heat capacity: 105 kJ/kg [37]
- Thermal conductivity: 0.165 W/mK [18]
- Density: 900 kg/m³ [37]
- Melting temperature: 24 °C [37]

The measured and modelled temperature responses are shown in Figure 5.5. As shown by the pink window in Figure 5.5, coconut oil starts melting after 6 s and is fully melted after 205 s. The heat of the Peltier module is absorbed by the sensible heat storage of the container with the solid oil till $t_{meltstart}$ and by the liquid oil between the end of melting and the end of power ($Q_h = 0$ W) indicated by the vertical red dotted line at $t_{stop} = 301$.

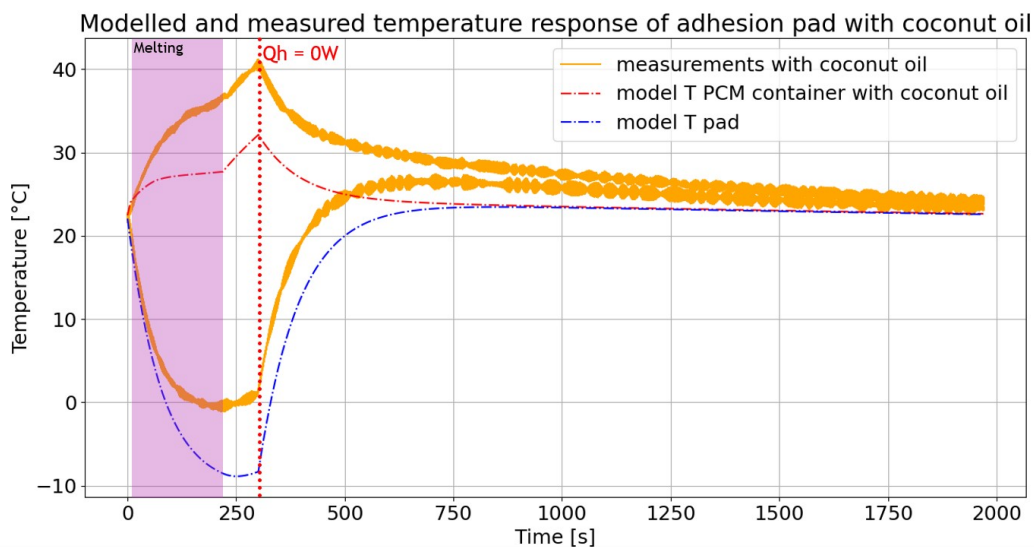


Figure 5.5: Modelled and measured temperature response of the MCPF module with the aluminium adhesion pad and the container with coconut oil. Where the melting time is indicated by the pink window.

However, as shown in Figure 5.5, the model underestimates the temperatures compared to the measurements. The minimum temperature of the model is 7.5 °C lower than the measured minimum temperature. This is due to the assumption that the coconut oil absorbs all the heat from the module during the melting time. However, part of this heat will be used to heat the container with the half-melted coconut oil, according to Equation 5.8.

$$dT_h = \frac{Q_h - Q_{dissipation}}{c_{alumina} * m_{plate} + c_{alu} * V_{container} * \rho_{alu} + \rho_{PCM} * (c_{PCM,s} * V_{PCM,s} + c_{PCM,l} * V_{PCM,l})} \quad (5.8)$$

Where, $c_{PCM,s}$ & $c_{PCM,l}$ and $V_{PCM,s}$ & $V_{PCM,l}$ are the specific heat capacity and volume of the solid and liquid coconut oil.

To estimate the fraction of the heat absorbed by the latent heat storage of the coconut oil and the sensible heat storage of the container, the model is fitted to the temperature of the adhesion pad during cooling, as this temperature determines whether ice adhesion can be obtained. The models best fit between the modelled pad temperature, between start and t_{stop} , and the measured pad temperature is found for 70% Q_h absorbed by sensible heat storage and 30% by latent heat storage. This resulted in the model shown in Figure 5.6.

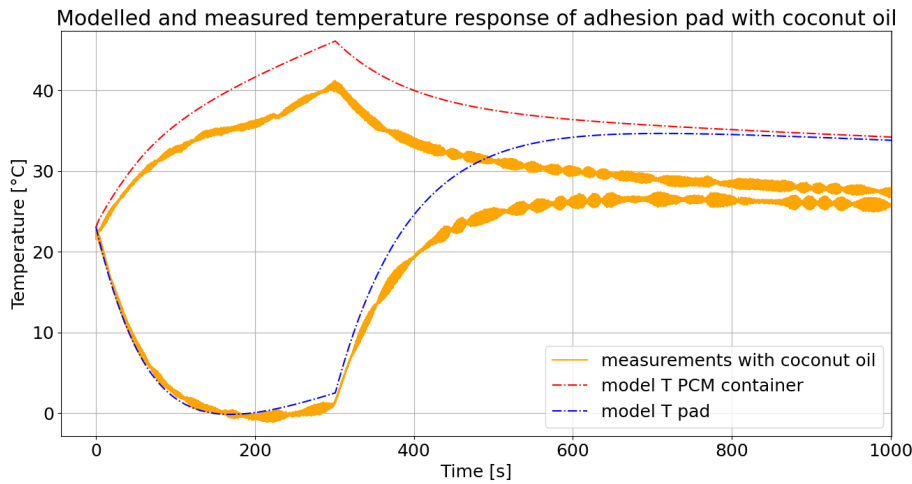


Figure 5.6: Fitted model of the temperature response of the MCPF module with the aluminium adhesion pad and the container with coconut oil. During the melting phase, 70% of heat is absorbed by sensible heat storage and 30% by latent heat storage.

The model overestimates the minimum temperature by 0.97 °C and the pad temperature, between start and t_{stop} , has a root mean square error (RMSE) of 0.72.

The temperature of the container with melting PCM can be calculated with Equation 5.9.

$$T_h = T_{melt} + C_{latent} * \frac{Q_h \cdot L}{K \cdot A_{peltier} \cdot \rho_{PCM} \cdot \Delta_{melt} H} + (1 - C_{latent}) * dTh_{sens} * dt \quad (5.9)$$

Where dTh_{sens} is the change in temperature due to the sensible heat storage of the container as estimated by Equation 5.8. C_{latent} is the coefficient that determines the fraction of heat absorbed by latent heat capacity.

The C_{latent} for coconut oil is 0.3 and 1 for octadecane, due to the increase in latent heat capacity. This validates the assumption made in Section 5.2 to discard the sensible heat storage during the melting of octadecane. To determine the relation between the latent heat capacity and the C_{latent} , more PCMs must be tested to see when and how the C_{latent} starts decreasing with decreasing latent heat capacity. Furthermore, the thermal conductivity of the material might also influence this coefficient, as this reduces the heating rate as shown in Equation 5.9.

5.4. Phase change temperature

From the previous sections, it became clear a PCM with a large latent and specific heat capacity must be selected, as this results in the most available energy storage. The PCM with the largest latent heat capacity tested in this research was acetone. This liquid has a latent heat capacity of vaporization of 542 kJ/kg.

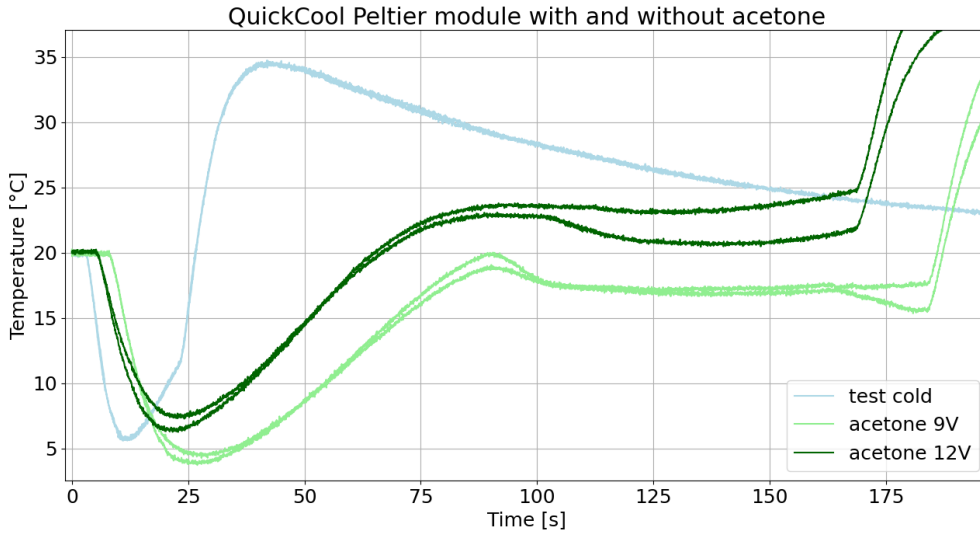


Figure 5.7: Cold side temperature response of QC-127-1.4-6.0A with acetone for different voltages.

Figure 5.7 clearly shows the working principle of the PCM. The green lines indicate the tests with acetone and the blue line the temperature response of the Peltier module without acetone. As the top side touching the acetone reaches the boiling temperature of acetone after 90 seconds, the thermal energy is absorbed by the boiling process and hence the temperature stays constant which results in a constant cold side temperature. However, to obtain a constant subzero temperature, the boiling point of the cooling liquid should be lower.

In Figure 5.8, the performance of PCM cooling of coconut oil, GCS-104-PCM and paraffin wax are compared, where the energy ranges from blue (low) to yellow (high). These tests are described in detail in Appendix D. The dotted lines indicate the mean minimum temperature and temperature difference for all measurements. The closer the data points are to the top left corner the better the performance.

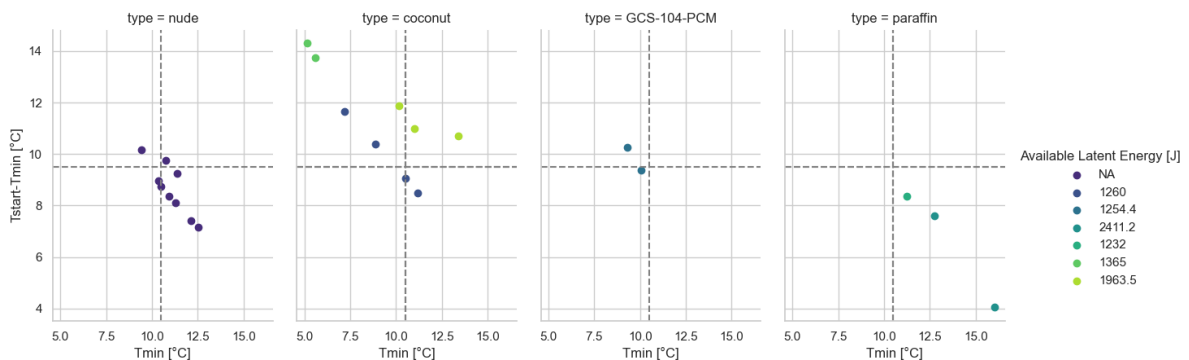


Figure 5.8: Performance of PCM cooling of TEC1-12706 for 7.5 V 2 A power supply and different PCM types.

Figure 5.8 shows the coconut oil results in the best cooling and the paraffin was in the worst cooling. This is expected as the boiling point of coconut oil is around 24 °C compared to 54 °C. Hence, a PCM

should be selected with a boiling point between 20 and 30 °C.

The melting point of octadecane is 28 °C. As shown in Figure 5.9 the time between the activation of the MCPF-127-14-25-E module and when the module reaches the melting point of octadecane is around 2.5 seconds. This together with the high latent heat capacity makes this material a good fit to use in the PCM cooling mechanism.

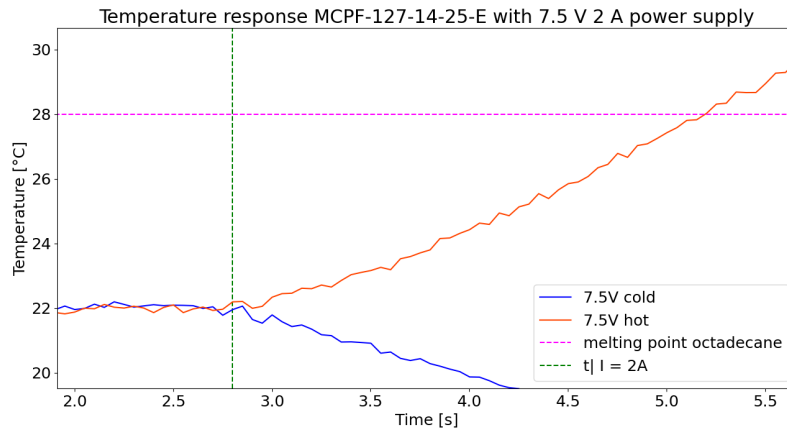


Figure 5.9: Temperature between the start of operation for the MCPF-127-14-25-E Peltier module and the melting temperature of octadecane.

5.5. Thermal conductivity

The thermal conductivity determines how far heat is conducted through a material, as described by Fourier's law of thermal conduction (Equation 4.9). The GCS-104-PCM has a melting point between 50-55 °C but shows better performance than the paraffin wax with a similar melting point (54 °C), as shown in Figure 5.8. This can be explained by the thermal conductivity of the PCM. The higher the thermal conductivity the lower the temperature of the hot side of the Peltier module as described by Equation 4.10. As the thermal conductivity of the GCS PCM is 4 W/mK compared to 0.21 W/mK for paraffin wax, this explains the observed results. Hence, the larger thermal conductivity of the PCM the better the cooling performance.

5.6. PCM selection

As described by Equation 5.5 the melting velocity of the PCM and hence the hot side temperature is influenced by the density and the latent heat capacity of the PCM. The more mass and higher the latent heat capacity the slower the PCM will melt, and the lower the temperature of the Peltier module's hot side and hence the cold side. However, as this cooling mechanism is developed for an icy moon exploration robot, the mass must be as low as possible. The mass of space mission probes must be minimised, to reduce the cost of launching the mission into space. Furthermore, a large thermal conductivity results in a lower heating rate. Therefore, a PCM must be selected with a large latent heat capacity, large thermal conductivity and a low density.

The considered PCMs are listed in Table 5.1 and octadecane was found to be the best option for this project because it had the highest latent heat capacity of the PCMs with a melting temperature between 20 and 30 °C and the lowest density of all considered solid-liquid PCMs in Table 5.1. Octadecane ($\text{CH}_3(\text{CH}_2)_{16}\text{CH}_3$) is a paraffin wax with a melting temperature of 28 °C and a latent heat capacity of 237 kJ/kg [22]. Octadecane is comparable to the commercially available HS24 PCM, which has a lower melting point and might be less toxic. However, as octadecane outperforms HS24 PCM for most selection criteria, and is more easily available, it was chosen as the PCM for this research.

Table 5.1: Properties of considered PCMs.

PCM Type	T _{melt} [°C]	Latent heat capacity [kJ/kg]	Specific heat capacity [kJ/kgK]	Thermal Conductivity [W/mK]	Density [kg/m ³]	Corrive/ Toxic	Price (on Merck)
Coconut oil [18] [37]	24	105	2.7	0.165	900	no/no	80.70 EU/kg
Octadecane [22]	28	237	1.8 solid 2.3 liquid	0.335	868	no/ irritating to eyes, respiratory system and skin	76.60 EU/100 g
Lauric acid/ Methyl Palmitrate (40:60) [60]	25.6	205.4	1.5	0.1802	888	no/ yes no/ toxic to fish	LA: 29.20 EU/100g MP: 62.50 EU/100g 43.90 EU/100ml
Glycerol [51]	17.8	200	2.43	0.285	1261	no/no	31 EU/kg
Potassium Fluoride Tetrahydrate [30]	18.7	200-246	1.5 solid 2.47 liquid	0.49	1440	yes/yes [74]	NA
Calcium Chloride Hexahydrate [30]	29	140-172	2.78 [80]	3.359 [80]	1567	no/irritating to eyes	31 EU/kg
HS24 PCM [56]	24	218	2.07 solid 2.42 liquid	1.05 solid 0.55 liquid	1621 solid 1510 liquid	no/no	NA
GCS-104-PCM [25]	50-55	200-280	NA	4	2800	No/No	24.55 EU/ 33.75 g (RS)
Paraffin Wax [3][11][19]	54	176	2.14-2.9	0.21	930	No/No	13.99 EU/ kg (Amazon)
Coconut Oil [18] [37]	24	105	1.33 solid 2.71 liquid	0.165	900	No/No	80.70 EU/kg
NOVEC7000 [1]	34	142	1.3	0.075	1400	No/No	173 EU/ 500 ml
Acetone [19] [70]	56	542	2.21	0.18	785	Yes/Yes	52.10 EU/L

5.7. Conclusion

In conclusion, this chapter aimed to answer the question:

What is the optimal phase change material to absorb the energy from the adhesion mechanism?

To answer this question both solid-liquid (melting) and liquid-vapour (vaporising) PCMs were tested. The important findings presented in this chapter are:

- **PCMs can outperform sensible heat storage materials near their transition temperature [53]** As shown in Figure 5.3 by comparing the cooling performance of water and octadecane.
- **When the latent heat capacity is low, the heat is absorbed by both the latent heat storage and sensible heat storage.** This was shown by the experiment with coconut oil. 30% of the heat was absorbed by latent heat storage and 70% by sensible heat storage during melting. For octadecane, all heat was absorbed by latent heat storage during melting.

- **Depending on the desired application, the PCM with the right transition temperature must be found.** For this research, where subzero temperatures are desired with a Peltier module operating at room temperature, this range was found to be between 20 and 30 °C.
- **The larger the thermal conductivity, the better the cooling effect.** The small amount of GCS-104-PCM outperformed the paraffin wax with the same melting point, due to the thermal conductivity.

The selected PCM material for this project is octadecane, because of its high latent heat capacity and low melting point, which resulted in a minimum temperature of -7.71 °C of the adhesion pad and sustained subzero cooling for 10 minutes and 15 seconds (see Figure 5.3).

In Figure 5.10 the temperature difference between the start and minimum temperature of the cold side is plotted over the minimum temperatures of the adhesion pad cooled by the MCPF-127-14-25-E module cooled by different PCMs in an aluminium container. The further in the top left corner of the graph, the better the performance of the PCM cooling.

As expected the octadecane, indicated by the pink star, outperforms all other tested PCMs. Furthermore, the temperature of the PCM influences its cooling performance as the cold coconut oil (~12 °C) resulted in a lower minimum temperature than the coconut oil at room temperature (~21 °C). Therefore, the mechanism should allow the PCM to dissipate its heat to the surroundings and cool down. All tests shown in Figure 5.10 are described in detail in Appendix D.

PCM cooling performance with MCPF-127-14-25-E module, aluminium holder and adhesion pad

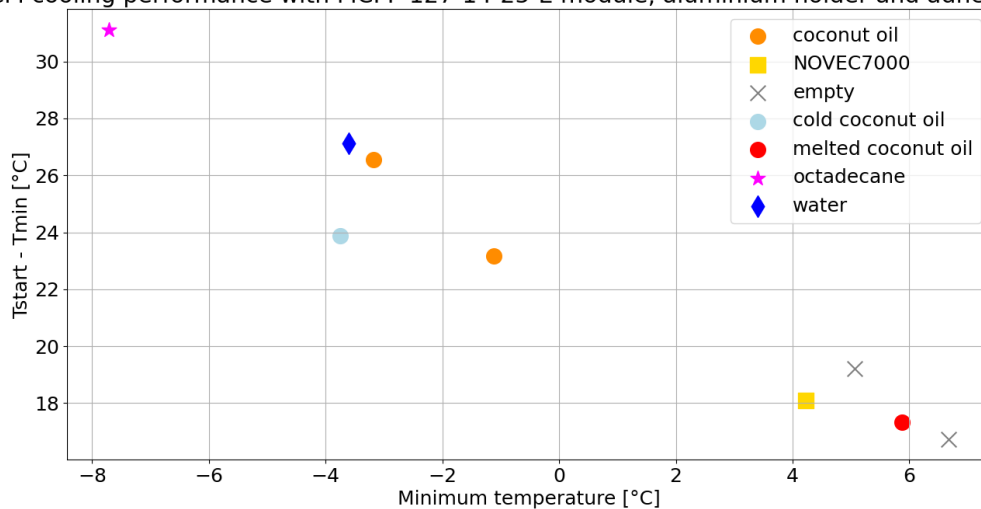


Figure 5.10: Performance of PCM cooling of the adhesion pad with the MCPF-127-14-25-E module for 7.5 V 2 A power supply and different PCM types in the aluminium container.

The tests on ice with the adhesion mechanism with octadecane are described in Chapter 6. The required octadecane mass for ice adhesion is estimated and integrated into the link design of FLICK as described in Chapter 7.

6

Tests on Ice

After the selection of octadecane in Chapter 5, it is integrated into the ice adhesion mechanism developed in Chapter 4. In this chapter, the adhesion mechanism is tested on ice to answer the question:

How to create ice adhesion with a PCM-cooled mechanism?

The experiments described in this chapter, test the performance of the PCM cooled ice adhesion mechanism. First, experiment 1 tests the adhesion of an uncooled Peltier module on ice. Experiment 2 tests the effect of flipping the Peltier module on the ice. Experiment 3 adhesion of the adhesion mechanism with coconut oil and experiment 4 compares the cooling capacity of water and coconut oil. Finally, experiment 5 tests the adhesion mechanism designed in Section 4.3 with octadecane on ice. All ice was made in a freezer, with a temperature of $-11\text{ }^{\circ}\text{C}$.

6.1. Experiment 1 - Peltier module on ice

The response of the MCPF-127-14-25-E Peltier module on ice was tested, to test the working principle of the mechanism of FLICK [76]. This test is shown in Figure 6.1, which showed that the Peltier module could be used to lift an ice block of 702 g. The ambient temperature during experiment 1 was $24.5\text{ }^{\circ}\text{C}$ and performed as follows:

1. The Peltier module is placed on the ice and a voltage of 7.5 V and a current of 2 A are applied to the Peltier modules, heating the face and touching the ice for 8 seconds.
2. The power supply is turned off and the polarity is switched in 4 seconds.
3. After switching the polarity, the power supply is turned on and the face touching the ice is cooled for 8 seconds.
4. The ice is lifted, by lifting the peltier module, as shown in Figure 6.1.

This resulted in adhesion strong enough to lift the ice block from the ground as shown in Figure 6.1. Hence, the Peltier module without cooling achieved an adhesion that could withstand a force of 6.9 N. However, the maximum adhesion strength is likely higher, but not tested here as this test was done in previous research [76].



Figure 6.1: Experiment 1 - Proof working mechanism of ice adhesion with Peltier module.

As explained in Section 3.2 the system must be cooled to enable multiple cooling cycles reaching sub-zero temperatures. As the Peltier module creates a temperature difference the temperature on the cold side depends on the temperature on the hot side. Without the removal of heat from the system, the whole system (both the hot and cold sides) will heat up due to Joule heating and not provide the necessary subzero temperatures to create adhesion by phase change. Therefore, the hot side of the Peltier module must be cooled.

6.2. Experiment 2 - Flipping the Peltier module on ice

One way of cooling is flipping the MCPF-127-14-25-E Peltier module to cool the hot side with the ice itself. This method uses the ice as a PCM to absorb the heat of the Peltier module. The ambient temperature during experiment 2 was 24.5 °C and performed as follows:

1. The Peltier module is placed on the ice and a voltage of 7.5 V and a current of 2 A are applied to the Peltier module, cooling the top side till subzero temperatures (after 12 seconds)
2. The Peltier module is flipped, creating ice adhesion after 4 seconds.
3. The Peltier module power is turned off and the module separates from the ice.

After flipping the Peltier the adhesion is created faster than in experiment 1, as the cold side already reached subzero temperatures. After the Peltier is turned off the cold side directly heats and separates from the ice, due to the heat flow from the hot to the cold side. Repeating this experiment resulted in less strong adhesion after some time, due to the bigger body of meltwater resulting in only a film of ice around the Peltier, as shown in Figure 6.2, instead of adhesion to the ice block. This highlights the importance of the right timing of melting and cooling. Due to the complexity of the integration of a flipping mechanism into the exploration probe, this method is not further explored.

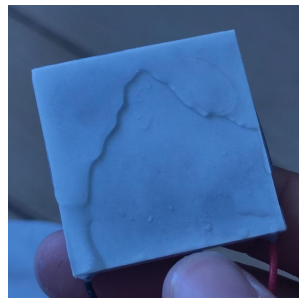


Figure 6.2: Film of ice on Peltier module after flipping on ice (Experiment 2).

6.3. Experiment 3 - Test adhesion mechanism with coconut oil

As mentioned in Section 4.4 the ceramic plates of the Peltier module are brittle, applying loads to these plates should be avoided. Therefore, the aluminium pad described in Section 4.4 is tested on ice using the QC-127-1.4-6.0A Peltier module together with the 3D printed PLA as shown in Figure 4.11. This mechanism used 18.7 g of coconut oil. The ambient temperature during experiment 3 was 20 °C and parted into experiments 3.1 and 3.2.

6.3.1. Experiment 3.1 - Continuous cooling

This experiment tests the adhesion time of the adhesion mechanism with coconut oil and continuous cooling. Experiment 3.1 is shown in Figure 6.4 and performed as follows:

1. The adhesion mechanism is placed on the ice and a voltage of 7.5 V and a current of 2 A are applied to the Peltier module, heating the adhesion pad for 5 seconds.
2. The adhesion mechanism is turned off.
3. After the 4 seconds the adhesion mechanism is turned on to cool the pad.
4. The active adhesion mechanism is lifted with the 0.7 kg of ice.

The ice dropped down after 1:08 minutes, due to the heating of the adhesion mechanism. As explained in Section 4.3, as the coconut oil melts, the hot side temperature becomes larger because of the applied power. As the Peltier module creates a temperature difference, when the hot side reaches a temperature of 71 K (the maximum temperature difference of the QC module), the cold side temperature is above zero. This results in the separation from the ice before all coconut oil is melted (which would theoretically happen after 2:11 min).

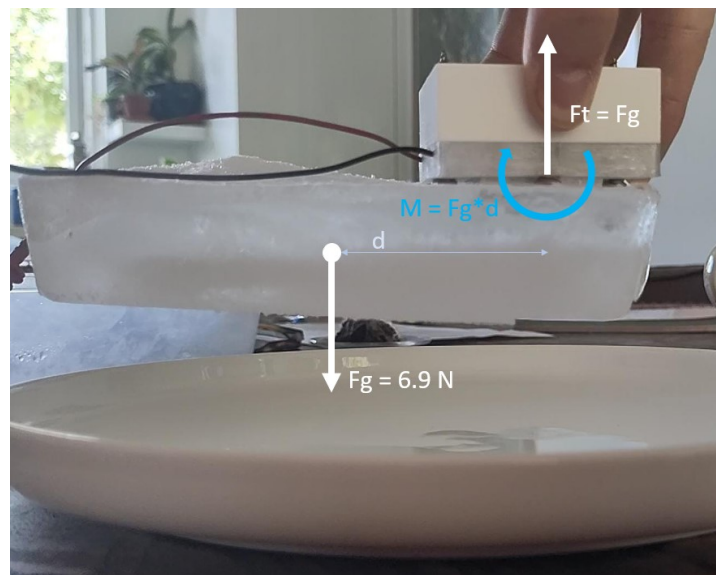


Figure 6.3: Simplified free body diagram of Experiment 3.1 - Test 3D printed adhesion mechanism with coconut oil, continuous cooling. $d = 5.1$ cm.

As shown in Figure 6.4 the adhesion mechanism supports both a tensile load of 6.9 N (indicated by the red arrow) and a momentum of 0.35 Nm (indicated by the blue arrow).

6.3.2. Experiment 3.2 - 5 seconds cooling

This experiment tests the adhesion time of the adhesion mechanism with coconut oil and 5 seconds of cooling. Experiment 3.2 is shown in Figure 6.4 and performed as follows:

1. The adhesion mechanism is placed on the ice and a voltage of 7.5 V and a current of 2 A are applied to the Peltier module, heating the adhesion pad for 5 seconds.
2. The adhesion mechanism is turned off.

3. After the 4 seconds the adhesion mechanism is turned on to cool the pad for 5 seconds.
4. The turned-off adhesion mechanism is lifted with the 0.7 kg of ice.

The ice dropped down after 14 seconds. This is due to the heating of the adhesion mechanism by the ambient temperature of 20 °C. Furthermore, the heat absorbed by the coconut oil during the 5 seconds of cooling cannot dissipate to the surroundings, due to the isolating property of the 3D printed PLA (0.13 W/mK [42]). Hence, this heat flows to the adhesion pad when the mechanism is turned off, resulting in a shorter adhesion time.

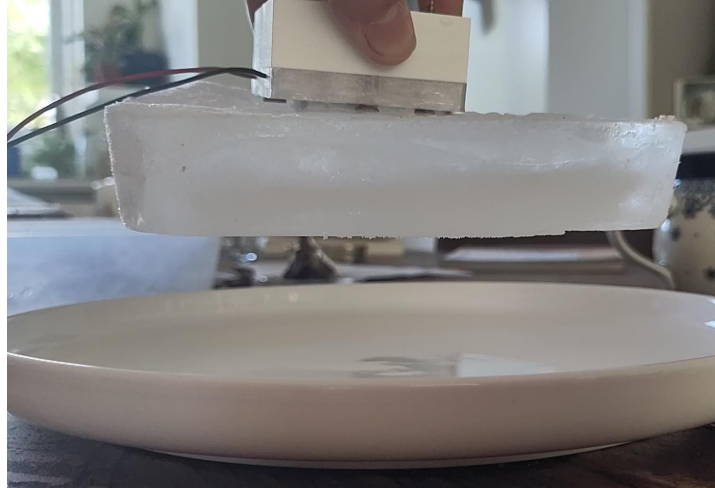


Figure 6.4: Experiment 3.2 - Test 3D printed adhesion mechanism with coconut oil, 5 seconds of cooling.

6.4. Experiment 4 - Test difference between water and coconut oil cooling

Using the aluminium container designed Section 4.3 the heat from the MCPF-127-14-25-E Peltier module and the absorbed heat by the PCM can flow to the surroundings. Experiment 4 was performed to test the cooling effect of the empty container, the container with water and coconut oil. The setup of experiment 4 is shown in Figure 6.5. One thermocouple measures the temperature of the aluminium container and the other couple the temperature of the side of the adhesion pad on ice.

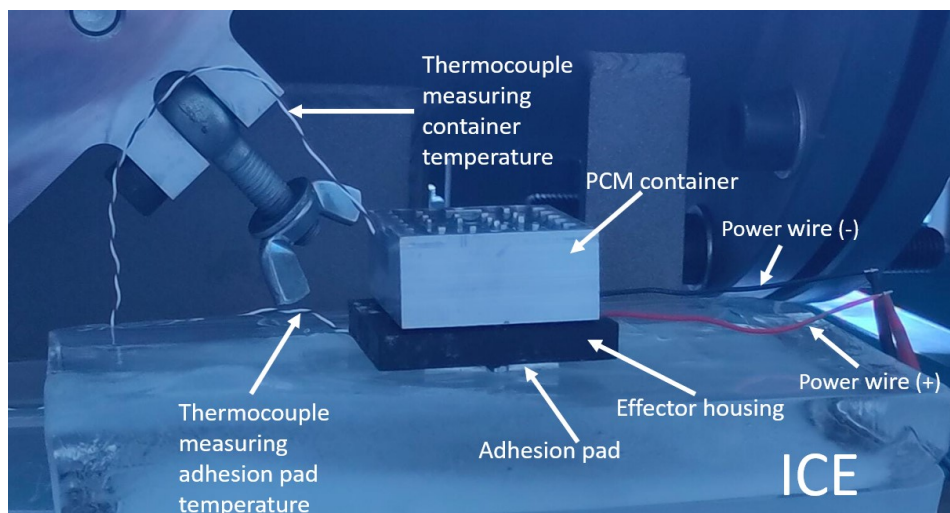


Figure 6.5: Experiment 4 - Test adhesion mechanism with aluminium container on ice.

The ambient temperature during experiment 4 was 21 °C and performed as follows:

1. The adhesion mechanism is placed on the ice and a voltage of 7.5 V and a current of 2 A are applied to the Peltier module, cooling the adhesion pad.
2. When the temperature adhesion pad rises above zero after the subzero cooling, the power is turned off.
3. Repeat steps 1) and 2) with an empty container, water and coconut oil inside the container.

The results are shown in Figure 6.6. With Figure 6.6 the results of the test with the container with coconut oil (orange line) and the container with water (blue) can be compared. The grey line indicates the empty container. As shown the water and coconut oil have a similar cooling effect. This is due to the low latent heat capacity of 105 J/g of coconut oil and the high specific heat capacity of water 4.18 J/gK, resulting in the energy storage capacity shown in Figure D.14. The mechanism maintains a subzero adhesion pad temperature for 6 min and 8 seconds with the empty container, 11 min 17 seconds with water and 10 min 42 seconds with coconut oil.

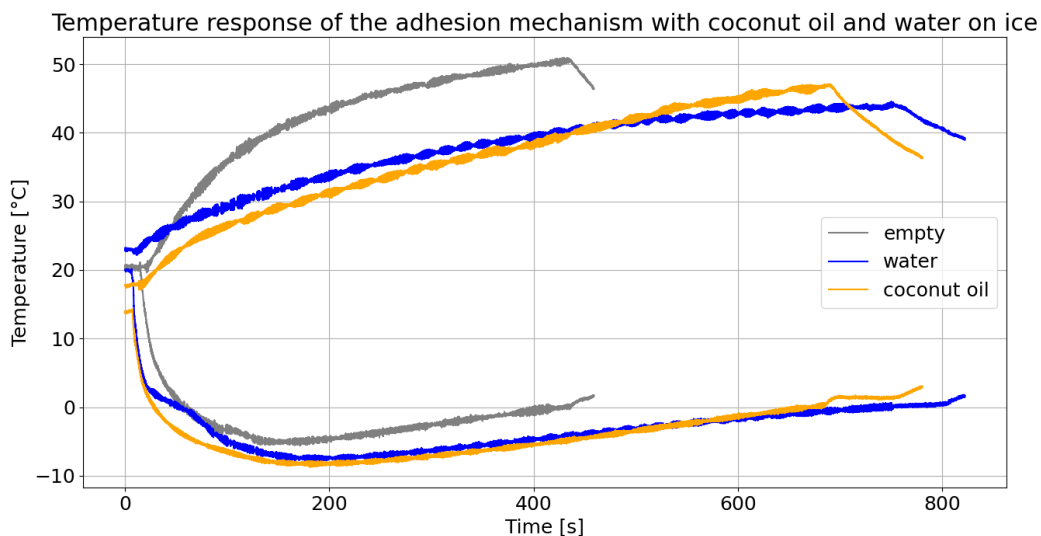


Figure 6.6: Experiment 4 - Temperature response of adhesion pad cooled by MCPF-127-14-25-E with coconut oil and water on ice.

6.5. Experiment 5 - Test ice adhesion mechanism with octadecane

To optimise the design compared to water cooling, octadecane with a latent heat capacity of 237 kJ/kg was selected (see Section D.1.4). Experiment 5 was performed to test how to create ice adhesion with the final adhesion mechanism with 25 g octadecane as described in Section 4.3, using the MCPF-127-14-25-E module. The ambient temperature during experiment 5 was 20.5 °C and performed as follows:

1. The adhesion pad is placed on the ice.
2. After 5s, a voltage of 7.5 V and a current of 2 A are applied to the Peltier module, cooling the adhesion pad for 4 seconds.
3. Lift the block of ice of 1 kg with the adhesion mechanism as shown in Figure 6.7.
4. Record the time the adhesion holds the ice block.
5. Repeat for 6, 8, 10 & 20 seconds of cooling.

The adhesion pad was not heated during this test. However, due to the high conductivity of aluminium, the ice melts when the aluminium pad touches the ice. This is the operational mode of FLICK and therefore tested in this section. The results of these tests are:

- 4 seconds of cooling: no adhesion
- 6 seconds of cooling: 5s of adhesion

- 8 seconds of cooling: 8s of adhesion
- 10 seconds of cooling: 22s of adhesion
- 20 seconds of cooling: 30s of adhesion
- Continuous cooling: 18 min and 2 s of adhesion

The results show the downside of using PCM cooling for ice adhesion: As the PCM absorbs the heat while the adhesion pad is cooled, this heat is slowly dissipated away and heats the Peltier module and adhesion pad after the heat pumping of the Peltier module is stopped. The adhesion stops due to this effect and the heating of the ambient temperature, while water cooling transfers the heat away from the adhesion link to the fan where it is dissipated.

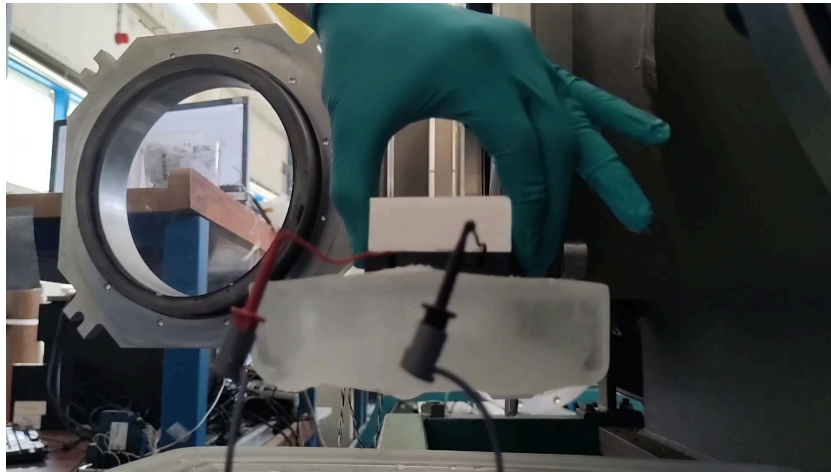


Figure 6.7: Experiment 5 - Test ice adhesion mechanism with octadecane.

The continuous cooling was tested to hold the ice for 18 min and 2s. Looking at Figure 5.3, the adhesion mechanism achieved subzero adhesion pad temperatures for 10 minutes and 15 seconds. Hence, the subzero cooling time achieved without ice is an underestimation of the ice adhesion time, due to the cooling effect of the ice itself.

6.6. Conclusion

This chapter aimed to answer the question:

How to create ice adhesion with a PCM-cooled mechanism?

The important findings presented in this chapter are:

- **Ice adhesion with a PCM-cooled mechanism is possible.**
- **Ice adhesion is possible for a system that does not obtain subzero temperatures without ice.** The assembly with coconut oil does not obtain subzero temperatures as shown in Chapter 4, but does result in ice adhesion in experiment 3.
- **Water and coconut oil have a similar cooling performance on ice and are outperformed by octadecane.** Shown by experiment 4. Octadecane outperforms both materials as shown by the continuous cooling, resulting in an adhesion time of 1082 s.
- **The ice adhesion time is longer than the subzero cooling time without ice.** As shown by comparing experiment 5 and Figure 5.3.
- **The heat flow from the hot side and PCM to the cold side and adhesion pad seems to cause the detaching of the adhesion mechanism from the ice.** This effect is the downside of PCM-cooling as the absorbed heat is not dissipated away from the system like with water cooling. This heat influences the ice adhesion.

Now that the experiments in this chapter proved ice adhesion can be achieved with a PCM-cooled mechanism, octadecane with an aluminium container can be integrated into the link design of FLICK [76] as described in Chapter 7.

7

Integration of PCM into FLICK's Adhesion Link

To use phase change material cooling to create ice adhesion for an ice climbing robot, the PCM must be integrated into a robot. This chapter will answer the question:

How to integrate the PCM cooling mechanism into a robotic system?

The theoretical model, described in the previous chapters, is used to estimate the required amount of octadecane to achieve ice adhesion. This amount is integrated into the existing FLICK link design.

7.1. Model FLICK link

In this section, the temperature response of the link of FLICK (as described in Section 3.1) will be modelled and the required PCM needed for ice adhesion will be estimated. First, the model of the MCPF-104-14-25-E is modified to the TEC1-06308 module. Next, the PCM cooling of this module is modelled. Finally, the required PCM mass and volume are estimated.

7.1.1. TEC1-06308 module

To model the temperature response of the TEC1-06308 model. The physical characteristics, R , $2N\alpha_{pn}$ & K are estimated, as described in Section C.1.2, with the following parameters from the vendor datasheet¹:

- $I_{max} = 8 \text{ A}$
- $U_{max} = 7.6 \text{ V}$
- $\Delta T_{max} = 63 \text{ }^\circ\text{C}$
- $T_H = 25 \text{ }^\circ\text{C}$

The temperature of the hot side was not given by the manufacturer but was assumed to be equal to the one of the MCPF Peltier module.

The following assumptions are used in the model as found in Chapter 4:

- $\frac{\Delta T_{max_real}}{\Delta T_{max_vendor}} = 0.9$
- $h = 18.55 \text{ W/m}^2\text{K}$
- Heat pump reduction: 0.8 Optimal heat pumping power

¹<https://www.tme.com/us/en-us/details/pm-40x40-32/peltier-modules/stonecold/tec1-06308/>, retrieved on 26-08-2023.

The TEC1-06308 modules in the FLICK links are powered by the 1S2P 8800 mAh 3.8 V LiHV battery pack, which delivers a voltage of 4.35 V when fully charged. The model of the TEC1 module is shown in Figure 7.1 for 3.8 and 4.36 V. The voltage increase results in a higher heating rate of the system and a slightly lower minimum temperature. The rest of this section will use the model with a fully charged battery (4.36 V).

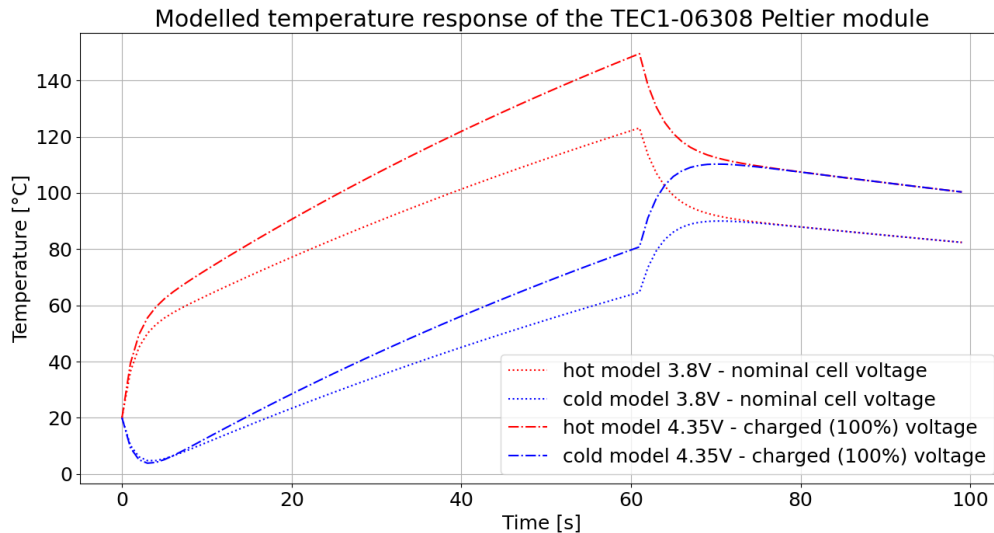


Figure 7.1: Modelled temperature response of the TEC1-06308 module for 3.8 & 4.36 V.

7.1.2. Model PCM cooling

To model the cooling of the adhesion pad with the TEC1-06308 cooled by a PCM, Figure 7.2 was used.

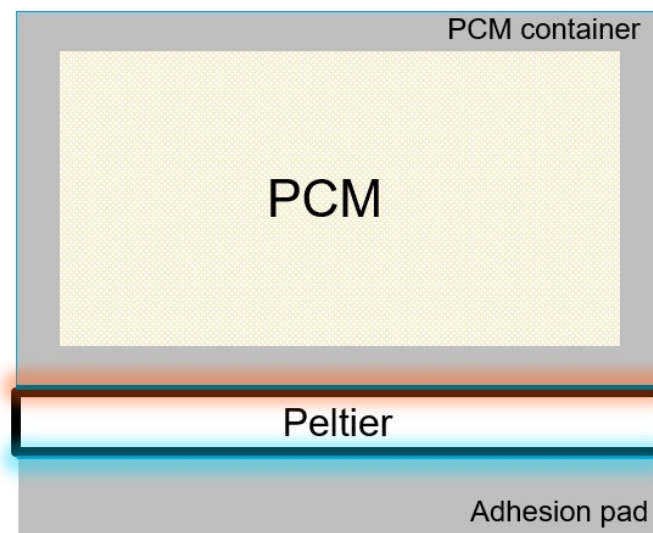


Figure 7.2: Schematic drawing of the model with the PCM container, Peltier module and the adhesion pad (side view).

Here, the PCM is considered to be contained in a rectangular container with a length of 40 mm, a width of 20 mm and a wall thickness of 2 mm. The height of the container depends on the volume of PCM. The dimensions of the TEC1-06308 module are 40 x 20 x 3.9 mm and the adhesion pad dimensions are 40 x 20 x 10 mm.

Using the method described in Section 5.2, the temperature response of the mechanism cooled by different quantities of coconut oil, shown in Figure 7.3, and octadecane, shown in Figure 7.4, can be modelled. As shown in the figures, larger PCM masses result in lower temperatures.

Modelled temperature response of the TEC1-06308 Peltier module with 4.35 V - coconut oil PCM

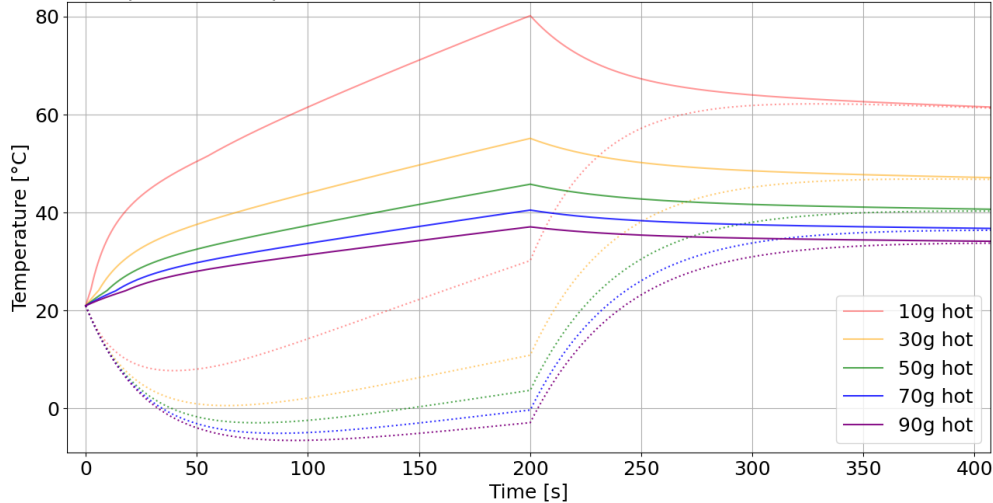


Figure 7.3: Effect of coconut oil mass on the modelled temperature response of the cooling mechanism.

Modelled temperature response of the TEC1-06308 Peltier module with 4.35 V - octadecane PCM

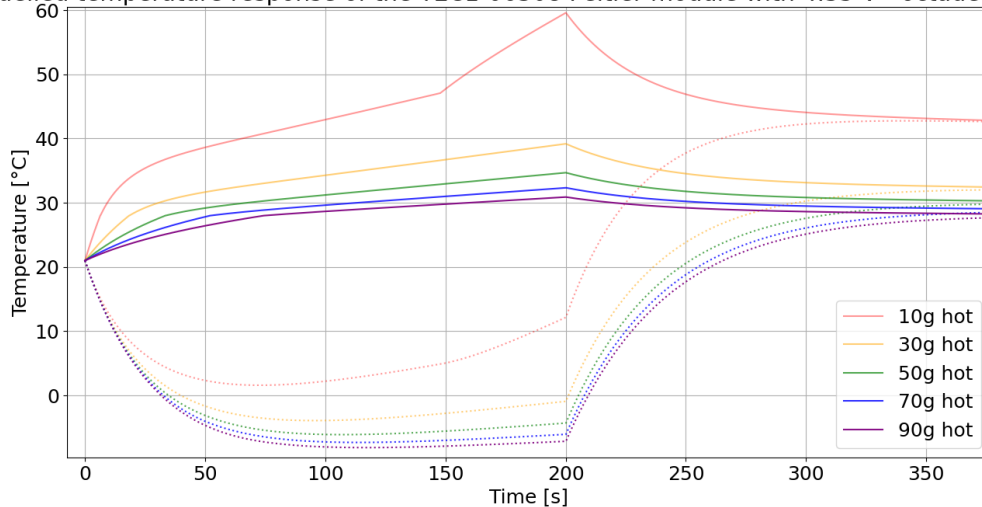


Figure 7.4: Effect of octadecane mass on the modelled temperature response of the cooling mechanism.

7.1.3. Estimation required PCM mass

To estimate the required PCM mass to obtain ice adhesion, the required mass to obtain subzero adhesion pad temperatures must be found. Plotting the minimum temperatures over the PCM mass for coconut oil and octadecane results in Figure 7.5. As shown the minimum temperatures decrease exponentially with increasing PCM mass. As expected, the octadecane (stars in Figure 7.5), outperforms the coconut oil (circles in Figure 7.5), due to the different latent heat capacities. Therefore, the mass estimation is made with the octadecane.

Minimum modelled adhesion pad temperature over PCM mass with TEC1-06308 module (4.34 V)

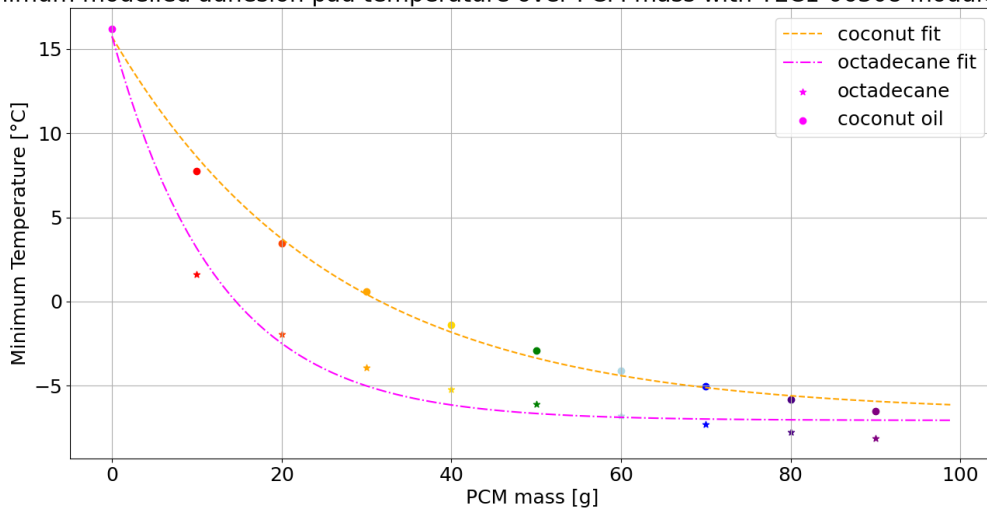


Figure 7.5: Minimum temperature over PCM mass.

To see how long the adhesion pad can be cooled to subzero temperatures for different masses of octadecane, the temperature response of the adhesion pad is shown in Figure 7.6.

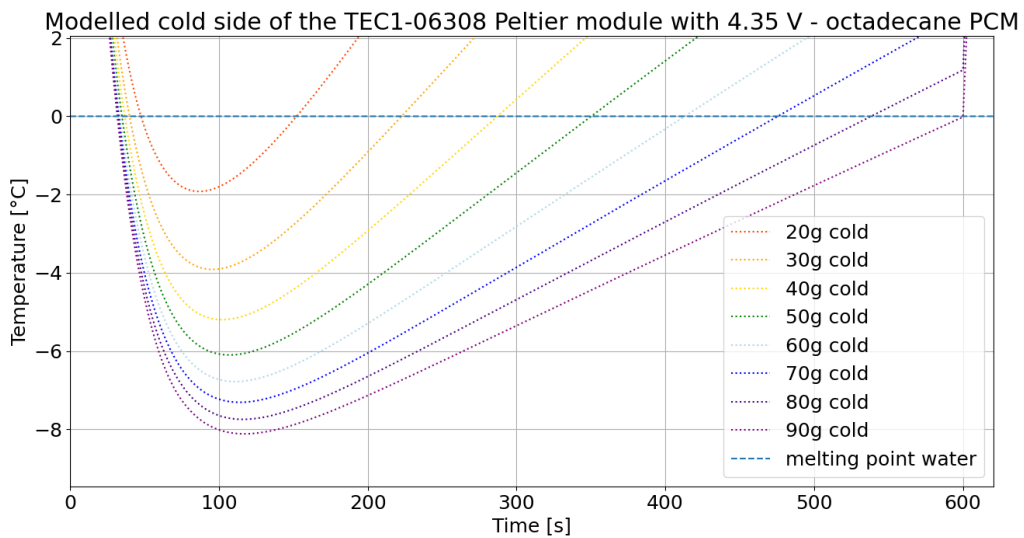


Figure 7.6: Effect of octadecane mass on the modelled temperature response of the adhesion pad.

Measuring the time of the subzero temperatures in Figure 7.6 and plotting these over the octadecane mass results in Figure 7.7.

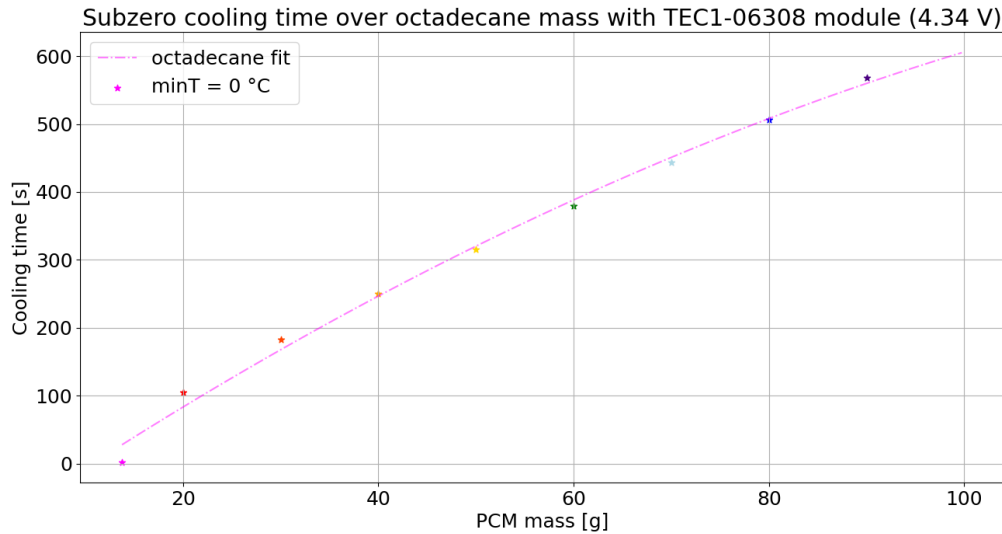


Figure 7.7: Subzero cooling time over octadecane mass.

However, during the operation of the adhesion link, the link will be in contact with the ice. This cools the adhesion pad; hence, less cooling power is needed to refreeze the ice after melting. Therefore, the required PCM mass is chosen to be the mass required to reach a minimum temperature of $0\text{ }^{\circ}\text{C}$, which means a cooling of $21\text{ }^{\circ}\text{C}$ (ambient temperature in the model). As shown in Section 6.3, ice adhesion is even possible for mechanisms that do not reach subzero temperatures without the ice. However, to ensure the PCM can keep absorbing heat by latent heat storage over multiple heating cycles, the mass is not further reduced for the estimate in this research. The mass required for a minimum temperature of $0\text{ }^{\circ}\text{C}$, was found to be 13.75 g and 19.39 g for a minimum temperature of $-1\text{ }^{\circ}\text{C}$. In Figure 7.8 the modelled temperature response and current through the Peltier module are shown.

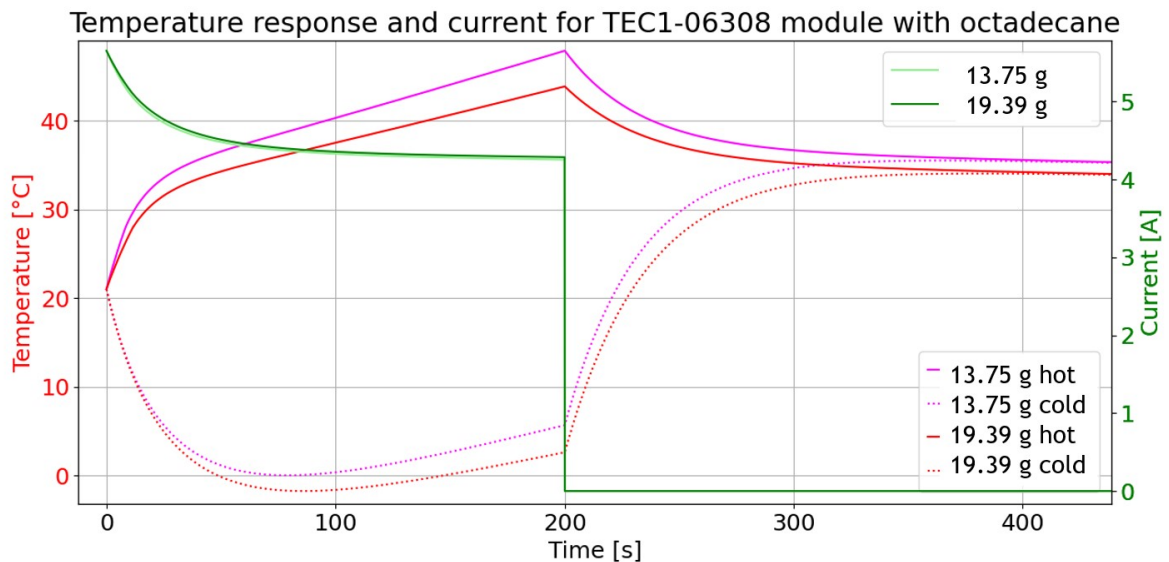
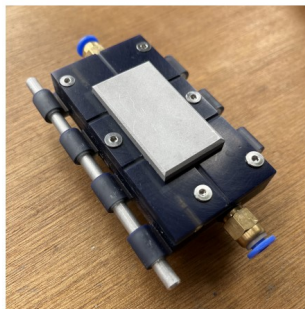


Figure 7.8: Temperature response and current for the mechanism with 13.75 and 19.39 g of octadecane.

The model with 13.75 g of octadecane (pink lines) reaches $0\text{ }^{\circ}\text{C}$ and $-1\text{ }^{\circ}\text{C}$ with 19.39 g. The current through the Peltier module is slightly lower for the 13.75 g (light green line) compared to the 19.39 g (dark green line), due to the larger temperature difference between the hot and cold side in the 13.75 g model.

7.2. PCM cooling of adhesion link

To integrate the required amount of octadecane into the link shown in Figure 7.9, a PCM container is designed. To absorb the heat radiated by the hot side of the Peltier module, this container must be in contact with the Peltier module. In this section, the container is designed and integrated into the link.



(a) Assembled adhesion pad: top.



(b) Assembled adhesion pad: bottom.

Figure 7.9: Old track link with integrated adhesion effector [76].

7.2.1. PCM container design

The aluminium container must be integrated into the bottom part of the link shown in Figure 7.10. To ensure the link can slide over the frame of the robot and the track sliding guide, shown in the middle of Figure 7.9 (b), can be attached to the track link, the PCM container must not increase the height of the link.

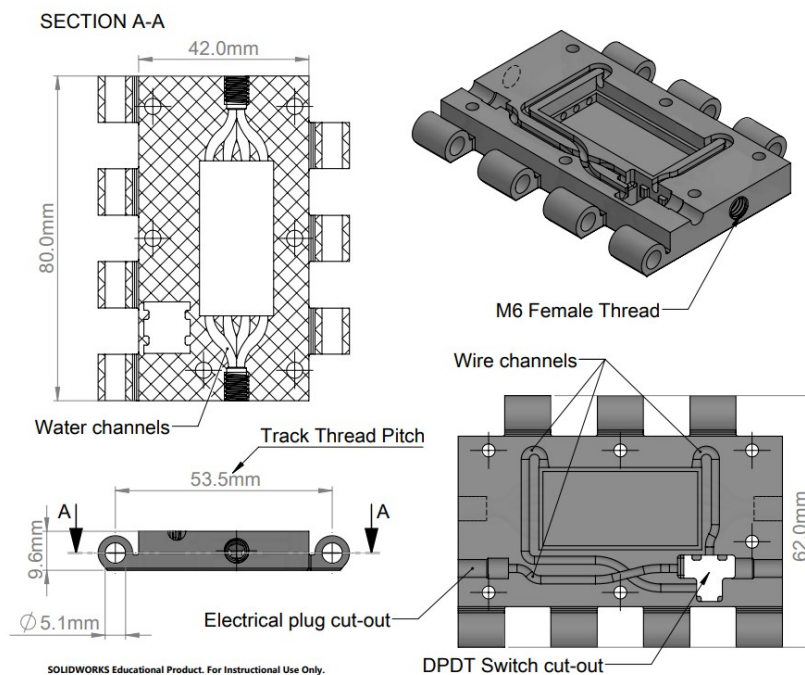


Figure 7.10: Old track link bottom CAD design [76].

Looking at Figure 7.10 the space available in the bottom part, the container must not interfere with the DPDT switch and the brass inserts keeping the link together. To increase the volume of the container the thickness of the container was changed to 1 mm. 3 heat fins (20, 53 & 62 mm) were added to improve the cooling performance. This resulted in a final PCM mass of 7.457 g of octadecane. The technical drawing of the PCM container is shown in Figure 7.11 and the container has a mass of 10.16 g.

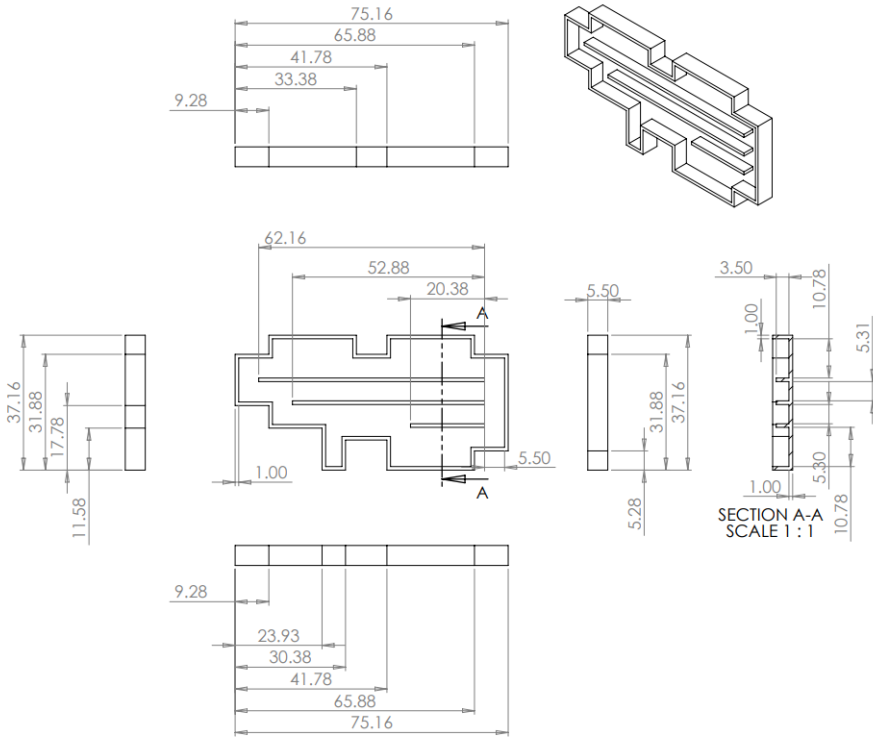


Figure 7.11: Technical drawing of the PCM container.

The container is closed by the lid shown in Figure 7.12. This lid has a mass of 5.86 g and will be sealed to the container with an anaerobic liquid gasket².

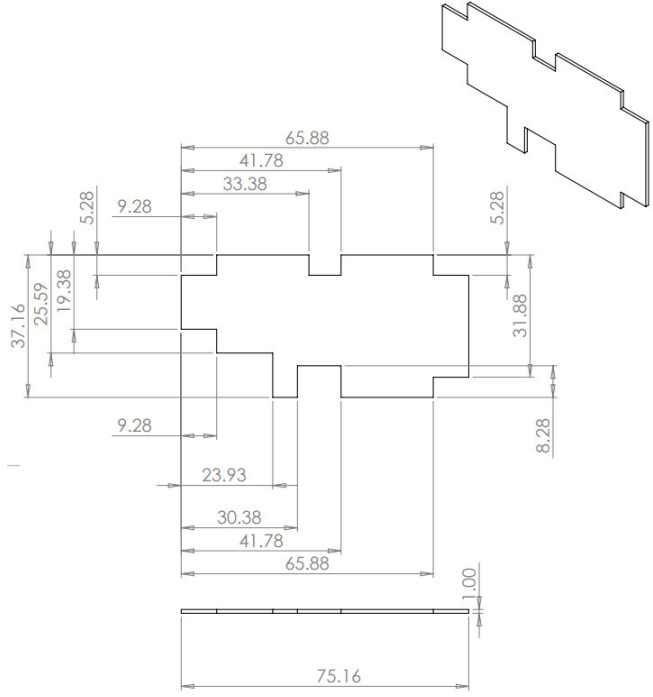


Figure 7.12: Technical drawing of the PCM container lid.

²<https://www.permabond.com/resource-center/comparison-of-fip-liquid-gaskets-to-conventional-gaskets/>

Using the model described in Section 7.1, the temperature response of the adhesion mechanism with and without the heat fins and the current through the Peltier module for an ambient temperature of 21 °C can be estimated and plotted as shown in Figure 7.13. The model reaches a minimum temperature of -0.2 °C and has a subzero cooling time of 24 s without heat fins and 7.518 g of octadecane. The model reaches a minimum temperature of -1.1 °C and has a subzero cooling time of 45 s with heat fins and 7.457 g of Octadecane. Hence, the heat fins improve the cooling performance of the system. According to the model, the link will result in adhesion to the ice, as shown by the obtained subzero temperatures.

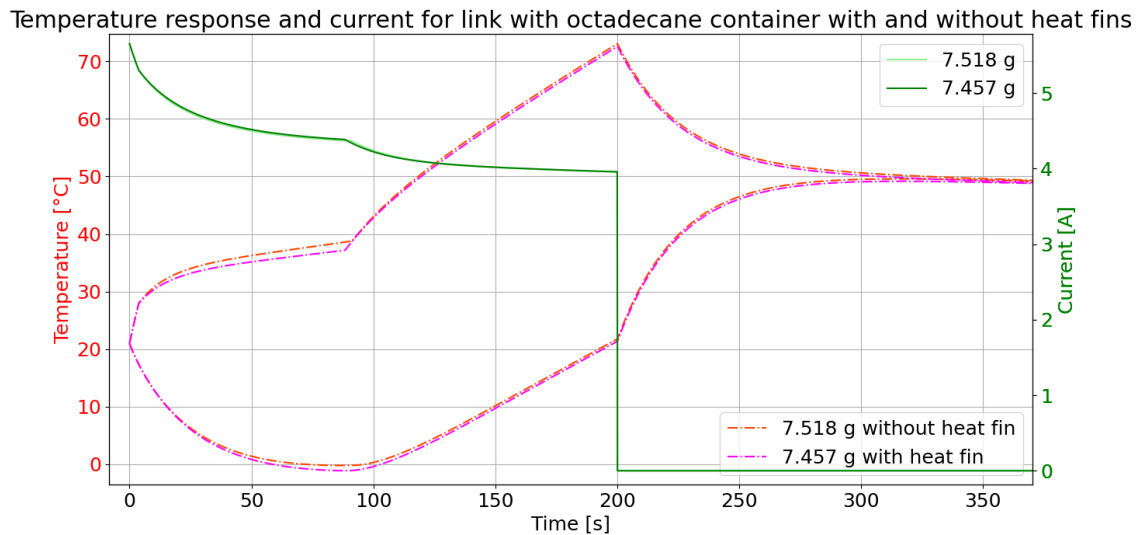


Figure 7.13: Temperature response and current for the final adhesion link mechanism (with octadecane PCM cooling) with and without heat fins, voltage supply of 4.35 V for 200 seconds, $T_{amb} = 21$ °C.

7.2.2. Integration of container into link

To integrate the container into the link, the design shown in Figure 7.10 is altered in the following ways:

- The water channels are removed.
- A cut of 6.5 mm deep is made in the bottom to the track link, to ensure contact between the PCM container and the Peltier module.

This results in the final design of the adhesion link shown in Figure 7.16. The module and container will be connected by the Prolimatech PK-3 thermal paste³.

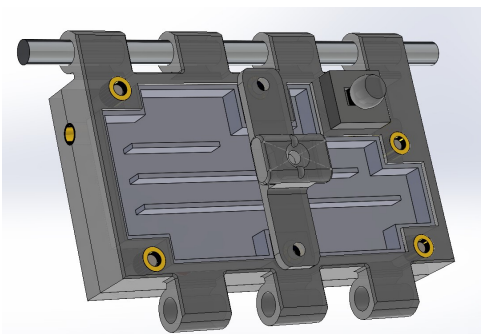


Figure 7.14: Without lid

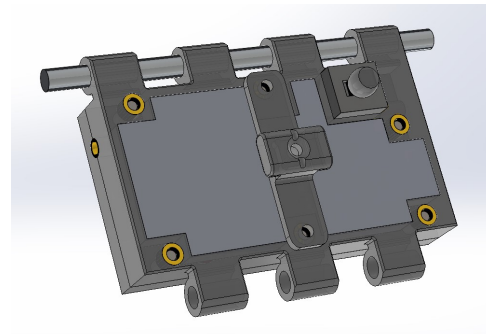


Figure 7.15: With lid

Figure 7.16: Final adhesion mechanism assembly with PCM container.

³https://www.bol.com/nl/nl/p/prolimatech-pk-3-5g-heat-sink-compound-11-2-w-m-k/9200000034871734/?bltgh=tPAVIQuwtXy9XYqrte1Cgw.2_22.26.ProductTitle, retrieved on 19-08-2023.

The exploded view of the final link design with the PCM container is shown in Figure 7.17.

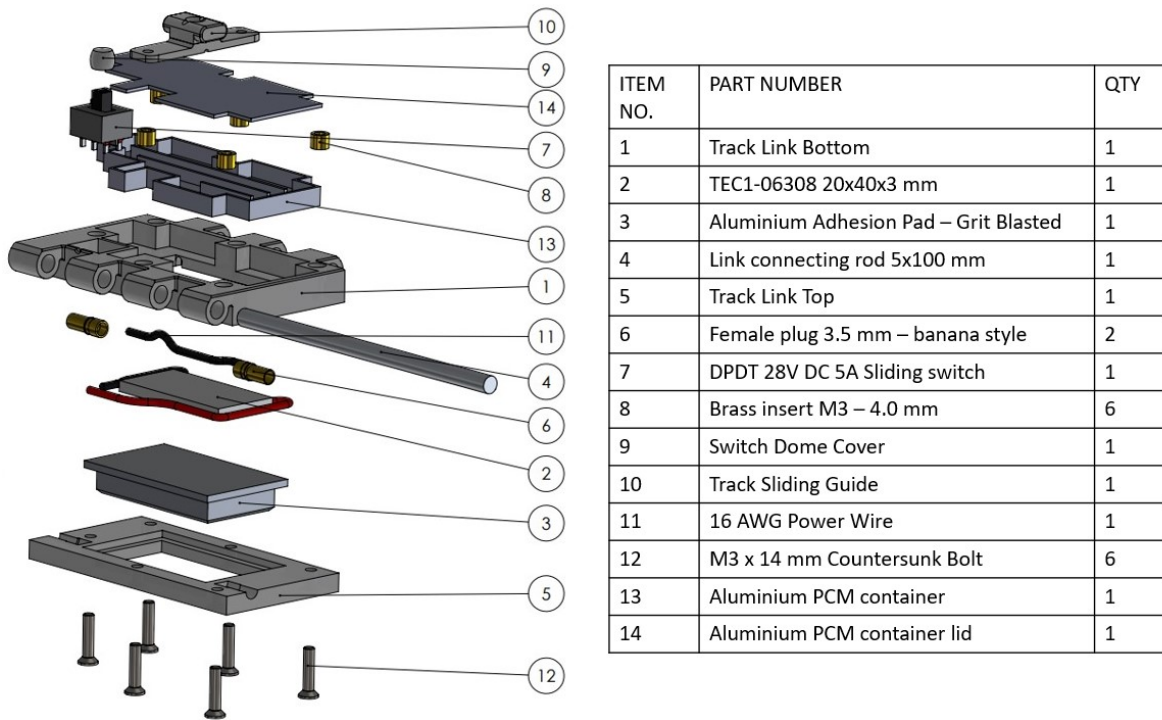
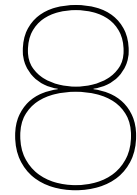


Figure 7.17: Exploded view of the link with the PCM container.

In conclusion, this section described how to integrate the required volume of octadecane into the link design of FLICK [76]. This link must be tested on ice to assess its performance during the operation of the robotic system.



Conclusion and Recommendations

This research aimed to assess the performance of PCM cooling, optimise the design of FLICK (proposed by Tom Mooijman 2023 [76]) by integration of a PCM and answer the research question:

How to use phase change material cooling to create ice adhesion for an ice-climbing robot?

To answer the main research question it was decomposed into the following sub-questions:

- What is the potential of using phase change material cooling instead of water cooling for an ice climbing robot?
- How to cool a Peltier module with a phase change material?
- What is the optimal phase change material to absorb the energy from the adhesion mechanism?
- How to create ice adhesion with a PCM-cooled mechanism?
- How to integrate the PCM cooling mechanism into a robotic system?

To answer these questions, an experimental set-up and an ice adhesion test mechanism were designed to test the cooling effect of PCMs on the Peltier modules. From these experiments and a theoretical model, the selection criteria to select the PCM were derived and the optimal PCM was selected to be octadecane. Next, the adhesion mechanism was tested on ice, to prove ice adhesion was possible with PCM-cooling. Finally, using the developed model, the PCM was integrated into the FLICK probe. In this chapter, the findings of this research are presented together with recommendations for future research.

8.1. Summary of findings

To improve the cooling mechanism design of FLICK, the water cooling system, increasing the risk of failure due to moving parts, should be replaced by a static cooling solution. Phase change materials absorb energy by latent heat storage. The latent heat is the energy needed to change a material from a more ordered state to a less ordered state (melting or vaporising). Therefore, PCMs offer a solid-state solution to cool the hot side of the Peltier module, resulting in subzero temperatures on the cold side to freeze the melted ice and adhere to the ice. In this section, the final adhesion mechanism, optimal PCM, tests on ice and the integration of the PCM into the robotic system are described.

8.1.1. Ice adhesion test mechanism design

The adhesion mechanism designed in this research to test the PCMs, shown in Figure 8.3, used a 1 cm thick aluminium adhesion pad, 3D printed PETG housing connected with 2 screws to an aluminium container with heat fins containing a maximum of 39.51 cm³ PCM. The selected Peltier module was MCPF-127-14-25-E and was connected to the pad and container with Prolimatech PK-3 thermal paste. During the design of this container, the following points became clear:

- The maximum temperature difference should be as big as possible while keeping the maximum power as low as possible for the selected Peltier module. This results in the biggest temperature

differences with the least heat production. Therefore, the MCPF-127-14-25-E was selected with a maximum temperature difference of 73 °C and a maximum power of 37 W.

- The contact area between the PCM and the container must be as large as possible to increase the available latent heat storage. Therefore, the heat fins were added to the container design.
- The material of the PCM container should have a high thermal conductivity to ensure the PCM can radiate the absorbed heat to the environment. Therefore, the container is made of aluminium with a thermal conductivity of 237 W/mK [72].



Figure 8.1: Top view

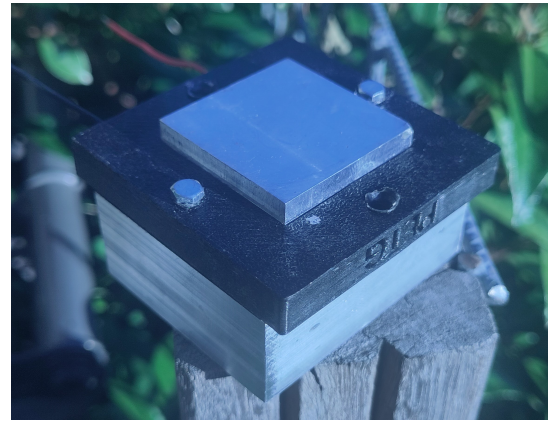


Figure 8.2: Bottom view

Figure 8.3: Conclusion: Designed ice adhesion mechanism assembly with octadecane.

8.1.2. PCM selection

To select the optimal PCM, the following parameters must be optimised:

- High latent heat capacity
- High specific heat capacity
- High thermal conductivity
- Low density

The selected PCM material for this project is octadecane, because of its high latent heat capacity of 237 kJ/kg, melting temperature of 28 °C and relatively low density of 868 kg/m³. Testing the octadecane in the adhesion mechanism, resulted in a minimum temperature of -7.71 °C of the adhesion pad and sustained subzero cooling over 10 minutes and 15 seconds.

8.1.3. Tests on ice

The performed tests proved ice adhesion with a PCM-cooled mechanism was possible. However, the heat flow from the hot side and PCM to the cold side and adhesion pad seems to cause the detaching of the adhesion mechanism from the ice after some time. This occurs when the adhesion mechanism is turned off after cooling the adhesion pad.

These tests on ice showed the downside of PCM cooling: As the absorbed heat is not dissipated away from the adhesion link it interferes with the ice adhesion mechanism. This makes the system less flexible as every link can only be cooled for a limited amount of time. When the PCM is melted it takes time to cool down, before it can absorb more heat.

8.1.4. Theoretical model

The developed theoretical model used the estimation method of the resistivity, Seebeck coefficient and thermal conductivity as proposed by Zhaoxia Luo 2008 [5] (described in detail in Appendix C), to model the temperature response of the MCPF-127-14-25-E. To obtain subzero temperatures and thereby ice

adhesion, with the TEC1-06308 module and the fully charged 1S2P 8800 mAh 3.8 V LiHV battery pack (4.35 V), 7.457 g of octadecane was required according to the model. The model of the TEC1-06308 with PCM cooling can be found in Appendix B and here:

<https://colab.research.google.com/drive/1TNSZa6nxz-4LL3EtUq4GW15tNpZGsMis?usp=sharing>

8.1.5. PCM cooled adhesion link

The required amount of octadecane was integrated into the adhesion link of FLICK as shown in Figure 8.6. The aluminium container (10.16 g) has a wall thickness of 1 mm and 3 heat fins with a height of 3.5 mm. These heat fins increase the contact area between the container and the PCM, resulting in more available latent heat storage. The lid of the container (5.86 g) is permanently sealed with an anaerobic liquid gasket, preventing leakage of the octadecane during operation. As the container was designed to fit under the track sliding guide, it can be integrated into the link without the need to redesign the FLICK track. The container holds 7.457 g of octadecane. According to the model, this assembly obtains a minimum temperature of $-1.1\text{ }^{\circ}\text{C}$ and has a subzero cooling time of 45 s for an ambient temperature of $21\text{ }^{\circ}\text{C}$ and without the presence of ice.

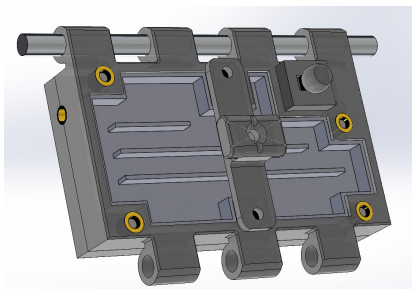


Figure 8.4: Without lid

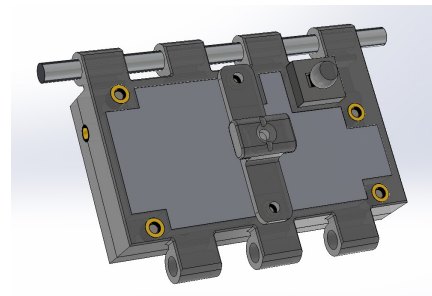


Figure 8.5: With lid

Figure 8.6: Final adhesion mechanism assembly with PCM container.

In Table 8.1 the water cooling system of FLICK is compared to the proposed PCM-cooling system. As shown the PCM-cooling system needs fewer components and has a lower total mass than the water cooling system. Furthermore, the PCM cooling requires no power and does not use moving parts which increases the reliability of the system. Hence, PCM cooling can improve the design of FLICK. However, it is yet unclear how this system will perform on ice. Therefore, the system must first be built and tested as described in Section 8.2, to assess its performance.

Table 8.1: Comparison components and weight of water cooling system and the proposed PCM cooling system.

FLICK's water cooling			PCM cooling		
Component	Mass [g]	Amount	Component	Mass [g]	Amount
Laing DDC-pump	249	1	Container	10.16	16
12V DDC-1T			Lid	5.86	16
60 mm 12 VDC fan	40	1	Octadecane	7.46	16
60 mm water radiator	122	1			
PC10-02	19	4			
Push-in Fitting					
PC-04-M6	10	64			
Push-in Fitting					
10 mm flexible tube	3	2			
4 mm flexible tube	1.5	64			
2 mm ball bearing	36	2			
O-ring seal	4	2			
Live-Swivel	NA	2			
16 spout manifold	NA	2			
Total	>1309		Total	375.68	

8.2. Recommendations

This section will present the recommendations to continue this research. First, the next steps for the adhesion mechanism with the PCM cooling are described. Then, a promising PCM not tested in this research is described. Next, the proposed improvements to the model are listed. Next, a promising air-cooling solution is described. Then, the system's implementation on Enceladus is discussed. Finally, the use of phase change in the locomotion of soft robotics is discussed.

8.2.1. Test PCM cooled adhesion link

To test the designed PCM-cooled adhesion link, it must be built. The following test could be performed with 1 adhesion link:

- **Test if ice adhesion is possible with the PCM-cooled mechanism.** Test how long the Peltier module in the link must be activated to create ice adhesion and how long it takes for the adhesion to stop when the module is turned off.
- **Test how long it takes till a complete melt of the PCM.** Test the adhesion mechanism on ice till all the octadecane is melted.
- **Test how cooling heating cycles affect the PCM.** Test how the heating and cooling of the PCM during the ice adhesion and melting affect the PCM.

When the system can obtain ice adhesion for multiple cycles without complete melt of the PCM, all 16 links can be built and integrated into the existing robotic frame of FLICK and the locomotion on ice of the new PCM-cooled FLICK 2.0 can be tested.

8.2.2. Calcium Chloride Hexahydrate

One promising hydrated salt is Calcium Chloride Hexahydrate, due to its high thermal conductivity of 3.359 W/mK [80]. It was not investigated in this research due to the high density compared to octadecane. However, in further research, it might be interesting to investigate this material to understand the exact effect of thermal conductivity on the PCM cooling performance.

8.2.3. Model improvements

To further improve the model the following limitations must be addressed:

- **Variable power function** The model can only estimate the behaviour of the PCM container for one power mode (power on and then off). Adding different power functions to the model (adding heating/cooling cycles or switching polarity), would allow for a better estimation of the behaviour of the link during operation and might influence the required PCM mass.
- **Temperature of the PCM** The model assumes the container with PCM as one mass that heats up. However, the PCM temperature remains constant around its melting temperature while melting. Hence, the container and the PCM temperature differ. Incorporation of this into the model will result in a more accurate description of the cooling effect of the PCM.
- **Solidification of PCM** The model does not consider solidification and assumes the PCM stays melted till the container cools to a temperature of less than the melting temperature. At this point, it instantaneously changes into a solid. In reality, the latent heat stored in the PCM will be released at this point.
- **Validation of the TEC1-06308 module model** The model of the TEC1-06308 uses the calibration parameters found for the MCPF-127-14-25-E module. The temperature response of TEC1-06308 must be measured, to calibrate the model to the measurements.
- **Model of ice** The model does not provide a definitive answer as to when ice adhesion will occur, as the ice is not included in the model. The temperature of the ice will influence the temperature of the adhesion pad and hence the adhesion itself. As shown by experiment 3 in Chapter 6 ice adhesion also occurs for a mechanism that does not reach subzero temperatures without the ice.

8.2.4. AirJet

One promising concept for this robot is AirJet Mini developed by Frore Systems [24]. This active cooling chip, shown in Figure 8.7, is a solid-state thermal solution. It uses tiny membranes to generate high-velocity pulsating jets by vibrating at ultrasonic frequency. These jets of air remove the heat from the heat sources and thereby cool it. The system can dissipate 5.25 W of heat and use 1 W of power. It weighs 11 g and its dimensions are 27.2 x 41.5 x 2.8 mm, which would be big enough to cool the TEC1-06308 modules used by FLICK with dimensions of 40 x 20 x 3.9 mm.

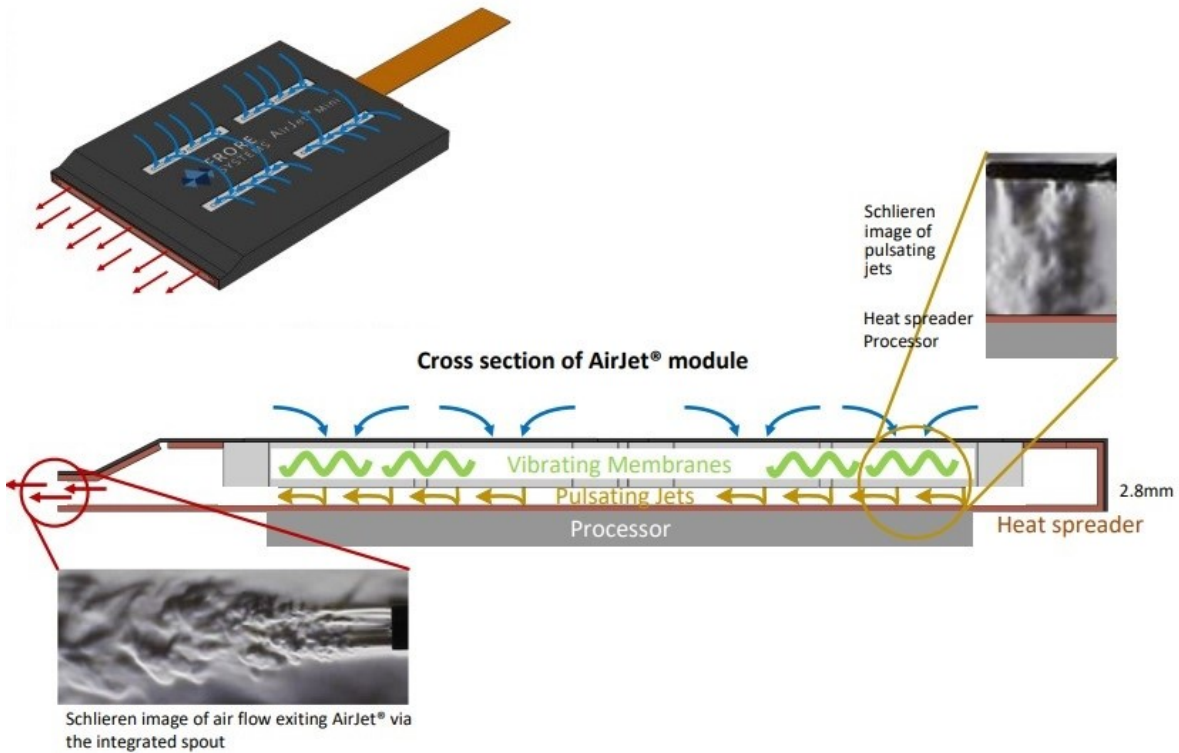


Figure 8.7: Top left: AirJet schematic where the cold incoming air is shown with blue arrows and the hot outgoing air with red arrows. Bottom: The cross-section of the AirJet module shows images of the generated pulsating air-jets and the outflow of air [24].

8.2.5. Enceladus Conditions

The robot was designed for Earth conditions and this research aimed to find a PCM to a Peltier module sufficiently to create ice adhesion at room temperature. On Enceladus the expected temperatures are below 0 °C in the cracks [26]. Hence, melting into the ice with a heating element and refreezing by the environment might be sufficient to adhere to the ice on Enceladus. To make the robot work on Enceladus where the temperatures are lower than -70 °C, the Peltier modules must be used to melt the ice. Therefore, a PCM could be used to keep the cold side warm enough to obtain temperatures above 0 °C at the hot side (The TEC1-06308). By heating the side touching the PCM heat can be stored in the PCM by latent heat storage, which can be used during the melt phase. However, materials with a melting point around -30 °C are often corrosive and toxic. Furthermore, these PCMs might be gaseous at Earth temperatures, resulting in required cooling of the robot during launch.

Joule heating might be needed to achieve the temperature differences needed to melt the ice on Enceladus. The re-freezing will not be a driving requirement, as the environment temperature will refreeze the ice. Joule heating requires a large amount of power increasing the power budget of the robotic system. The Joule heating could be digitally controlled by MOSFETs, which requires a small input current to control the load current [33]. However, the cam track solution with a manual switch will suffice in the track link locomotion [76].

Furthermore, the conditions in the vents on Enceladus must be investigated further to understand to temperature gradient along the crevasse length and the effect of the gusts in the vent on the temperature must be understood. As the working principle of the adhesion mechanism of FLICK is the phase change of water, it is important to understand the expected temperatures to ensure the system will not fail due to the unexpected melting of the ice wall.

For the lower pressures expected at Enceladus, the system must create a local pressure of 1 kPa to enable the melting of the ice instead of sublimation. However, due to the low pressure on Enceladus, the ice might sublime without the formation of liquid water. The adhesion mechanism must be tested under these low-pressure conditions to see if the pressure required to form liquid water can be produced locally.

Before making the system work for Enceladus, it could be built for the Martian north poles. The south pole is covered in an 8 m thick layer of CO_2 ice, while the northern pole only has CO_2 ice during its winter [17]. As CO_2 has a triple point at 5.11 bar [73], it is hard to obtain adhesion to the CO_2 by heating because the CO_2 ice will sublime. The Martian environment might be more suitable for ice adhesion through melting and freezing of ice than on Enceladus, as the pressures on Mars might be sufficient to create liquid water when the ice is heated. The average atmospheric pressure at the surface is 610 Pa [28], which is 10 Pa above the triple point of water (see Figure 3.2).

8.2.6. Phase change actuated robot

Soft robots are less precise and harder to control, but can be ideally made of one part, achieve complex motion, absorb impacts, have an adaptable shape and are usually made of low-cost materials [78]. Rigid wall-climbing robots have been developed with good performances in applications such as inspection, but generally use complex mechanisms composed of rigid actuators (such as electromagnetic or electrostatic motors) and transmission components (such as pulleys, wheels, or belts). Hence these robots are heavy and inflexible, unlike animals. Soft wall-climbing robots based on muscle-like actuators in flexible bodies yield higher flexibility, better adaptability, and simpler design compared to rigid robots [27].

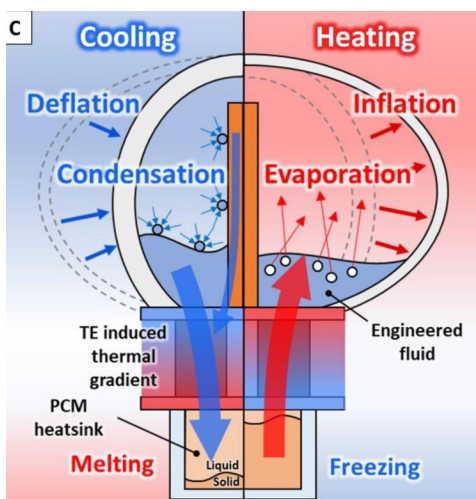


Figure 8.8: The pumpless phase change soft actuator.

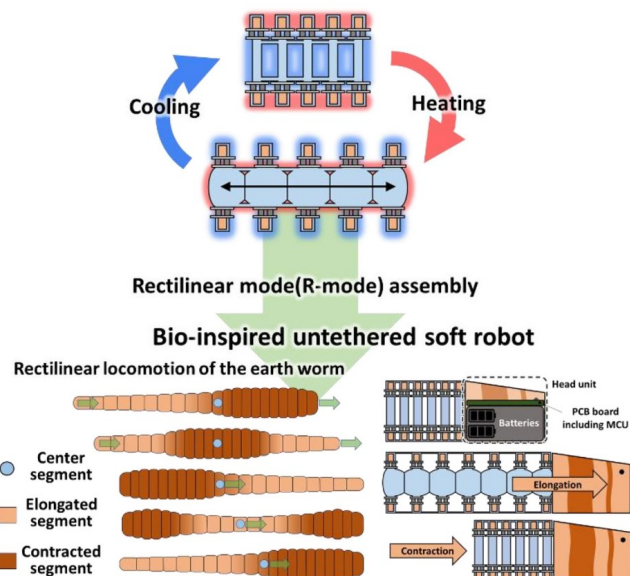


Figure 8.9: A schematic of the bio-inspired untethered soft robot.

Figure 8.10: Bioinspired untethered soft robot with pumpless phase change soft actuators by bidirectional thermoelectrics proposed by Yoon et al. 2023 [79]

The observed expansion of the liquid-vapour PCMs (shown in Appendix D) can be used for locomotion as proposed by Yoon et al. 2023 [79] shown in Figure 8.8 and Figure 8.9. The pumpless phase change soft actuators must be activated so that the robot moves forward while keeping a point of ice adhesion at all times. To make the rubber conductive it is mixed with boron nitride micro-powder. However, to create ice adhesion, a coating of aluminium might be needed between the ice and the rubber, due to the low surface energy of polymers which makes ice adhesion more difficult [43].

The chosen liquid should be non-corrosive to silicone and Ecoflex. This is the case for NOVEC7000. However, its tests only resulted in a slightly better performance compared to the empty aluminium container (yellow square in Figure 5.10). Therefore, another fluid with a higher thermal conductivity and latent heat capacity should be selected or engineered to obtain subzero temperatures.

The lack of atmosphere and the cold temperatures on Enceladus make this type of system infeasible for icy moon exploration with the current technology. However, an ice-climbing soft robot to climb ice on Earth might offer interesting solutions to exploration problems in icy environments.

References

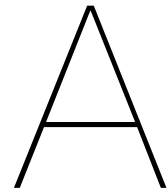
- [1] 3M NOVEC. *3M™ Novec™ 7000 Engineered Fluid*. 2021. URL: <https://multimedia.3m.com/mws/media/1213720/3m-novec-7000-engineered-fluid-tds.pdf>.
- [2] Maryam Abdollahpour. "Design of an experiment to calibrate a peltier element and measuring thermal conductivity". In: 2014. URL: <https://api.semanticscholar.org/CorpusID:33444659>.
- [3] Ashish Agarwal and R.M. Sarviya. "Characterization of Commercial Grade Paraffin wax as Latent Heat Storage material for Solar dryers". In: *Materials Today: Proceedings* 4.2, Part A (2017). 5th International Conference of Materials Processing and Characterization (ICMPC 2016), pp. 779–789. ISSN: 2214-7853. DOI: <https://doi.org/10.1016/j.matpr.2017.01.086>. URL: <https://www.sciencedirect.com/science/article/pii/S221478531730086X>.
- [4] Marie Běhouňková et al. "Tidally-induced melting events as the origin of south-pole activity on Enceladus". In: *Icarus* 219.2 (2012), pp. 655–664. ISSN: 0019-1035. DOI: <https://doi.org/10.1016/j.icarus.2012.03.024>. URL: <https://www.sciencedirect.com/science/article/pii/S0019103512001170>.
- [5] Ivaylo Belovski et al. "A Simple Method to Estimate the Physical Characteristics of a Thermoelectric Cooler from Vendor Datasheets". In: *Electronics Cooling Magazine* 14 3 (2008), pp. 22–27. URL: <https://www.electronics-cooling.com/2008/08/a-simple-method-to-estimate-the-physical-characteristics-of-a-thermoelectric-cooler-from-vendor-datasheets/>.
- [6] Ivaylo Belovski et al. "Mathematical Model of Thermoelectric Peltier Module". In: *Journal of Communication and Computer* 14 (Feb. 2017). DOI: 10.17265/1548-7709/2017.02.002.
- [7] Robert H. Brown et al. "Composition and Physical Properties of Enceladus' Surface". In: *Science* 311.5766 (2006), pp. 1425–1428. DOI: 10.1126/science.1121031.
- [8] Business Insider. *Earth is a desert planet compared to these ocean worlds in the solar system*. 2018. URL: <https://www.businessinsider.nl/water-space-volume-planets-moons-2016-10?international=true&r=US>.
- [9] Ondřej Čadek et al. "Long-term stability of Enceladus' uneven ice shell". In: *Icarus* 319 (2019), pp. 476–484. ISSN: 0019-1035. DOI: <https://doi.org/10.1016/j.icarus.2018.10.003>. URL: <https://www.sciencedirect.com/science/article/pii/S0019103518303762>.
- [10] Kalind Carpenter et al. "Exobiology Extant Life Surveyor (EELS)". In: *Earth and Space* 2021, pp. 328–338. DOI: 10.1061/9780784483374.033. eprint: <https://ascelibrary.org/doi/pdf/10.1061/9780784483374.033>. URL: <https://ascelibrary.org/doi/abs/10.1061/9780784483374.033>.
- [11] Miqdam Chaichan, Shaimaa Hilal Kamel, and Al-Ajeely M. "Thermal Conductivity Enhancement by using Nano-material in Phase Change Material for Latent Heat Thermal Energy Storage Systems". In: *SAUSSUREA* 5 (Aug. 2015), pp. 48–55.
- [12] Clemens J. M. Lasance. *The thermal conductivity of aluminum oxide*. 1999. URL: <https://www.electronics-cooling.com/1999/05/the-thermal-conductivity-of-aluminum-oxide/>.
- [13] Cmglee - Own work, CC BY-SA 3.0. *File:Phase diagram of water.svg*. URL: <https://commons.wikimedia.org/w/index.php?curid=14939155>.
- [14] Hemingway D. et al. "The Interior of Enceladus". In: *Enceladus and the Icy Moons of Saturn* (2018), pp. 57–77. DOI: 10.2458/azu_uapress_9780816537075-ch004s://doi.org/10.1029/2010JE003718.
- [15] Bernd Dachwald et al. "IceMole: a maneuverable probe for clean in situ analysis and sampling of subsurface ice and subglacial aquatic ecosystems". In: *Annals of Glaciology* 55.65 (2014), pp. 14–22. DOI: 10.3189/2014A0G65A004.

- [16] R. Danzer et al. "Fracture of Ceramics". In: *Advanced Engineering Materials* 10.4 (2008), pp. 275–298. DOI: <https://doi.org/10.1002/adem.200700347>. URL: <https://onlinelibrary.wiley.com/doi/abs/10.1002/adem.200700347>.
- [17] David Darling. *polar caps of Mars*. URL: <https://www.daviddarling.info/encyclopedia/M/Marspoles.html>.
- [18] P. Dhamodharan and A.K. Bakthavatsalam. "Experimental investigation on thermophysical properties of coconut oil and lauryl alcohol for energy recovery from cold condensate". In: *Journal of Energy Storage* 31 (2020), p. 101639. ISSN: 2352-152X. DOI: <https://doi.org/10.1016/j.est.2020.101639>. URL: <https://www.sciencedirect.com/science/article/pii/S2352152X20314766>.
- [19] Dirac Delta Science & Engineering Encyclopedia. *Specific Heat Capacity*. 2007. URL: <https://web.archive.org/web/20070804192935/http://www.diracdelta.co.uk/science/source/s/p/specific%5C%20heat%5C%20capacity/source.html> (visited on 02/06/2023).
- [20] Engineers Edge. *Convective Heat Transfer Coefficients Table Chart*. URL: https://www.engineersedge.com/heat_transfer/convective_heat_transfer_coefficients__13378.htm.
- [21] European Environment Agency. *Signals 2018 – Water is life*. 2018. URL: <https://www.eea.europa.eu/signals/signals-2018-content-list>.
- [22] Moritz Faden et al. "Review of Thermophysical Property Data of Octadecane for Phase-Change Studies". In: *Materials* 12 (Sept. 2019), p. 2974. DOI: 10.3390/ma12182974.
- [23] Ehsan Firouzfar et al. "Application of heat pipe heat exchangers in heating, ventilation and air conditioning (HVAC) systems". In: *Scientific Research and Essays* 6 (Apr. 2011), pp. 1900–1908.
- [24] Frore Systems. *AirJet® Mini*. 2022. URL: https://global-uploads.webflow.com/6387c57559192a648478384e/6387c57559192af14978394a_AirJet%5C%20Mini%5C%20Data%5C%20Sheet.pdf (visited on 02/06/2023).
- [25] GCS Thermal. *GCSP-104-PCM*. 2020. URL: <https://www.gcsthermal.com/product/gcsp-104-pcm/> (visited on 02/06/2023).
- [26] Jay D. Goguen et al. "The temperature and width of an active fissure on Enceladus measured with Cassini VIMS during the 14 April 2012 South Pole flyover". In: *Icarus* 226.1 (2013), pp. 1128–1137. ISSN: 0019-1035. DOI: <https://doi.org/10.1016/j.icarus.2013.07.012>. URL: <https://www.sciencedirect.com/science/article/pii/S0019103513003138>.
- [27] Guoying Gu et al. "Soft wall-climbing robots". In: *Science Robotics* 3.25 (2018), eaat2874. DOI: 10.1126/scirobotics.aat2874. eprint: <https://www.science.org/doi/pdf/10.1126/scirobotics.aat2874>. URL: <https://www.science.org/doi/abs/10.1126/scirobotics.aat2874>.
- [28] R.M. Haberle. "SOLAR SYSTEM/SUN, ATMOSPHERES, EVOLUTION OF ATMOSPHERES | Planetary Atmospheres: Mars". In: *Encyclopedia of Atmospheric Sciences (Second Edition)*. Ed. by Gerald R. North, John Pyle, and Fuqing Zhang. Second Edition. Oxford: Academic Press, 2015, pp. 168–177. ISBN: 978-0-12-382225-3. DOI: <https://doi.org/10.1016/B978-0-12-382225-3.00312-1>. URL: <https://www.sciencedirect.com/science/article/pii/B9780123822253003121>.
- [29] Paul Helfenstein and Carolyn C. Porco. "ENCELADUS' GEYSERS: RELATION TO GEOLOGICAL FEATURES". In: *The Astronomical Journal* 150.3 (2015). DOI: 10.1088/0004-6256/150/3/96.
- [30] Jason Hirschey et al. "Review of Inorganic Salt Hydrates with Phase Change Temperature in Range of 5°C to 60°C and Material Cost Comparison with Common Waxes". In: (). URL: <https://www.osti.gov/biblio/1468092>.
- [31] N.G. Holm et al. "Serpentinization and the Formation of H₂ and CH₄ on Celestial Bodies (Planets, Moons, Comets)". In: *Astrobiology* 15.7 (2015), pp. 587–600. DOI: 10.1089/ast.2014.1188.
- [32] HW. Hsu et al. "Ongoing hydrothermal activities within Enceladus". In: *Nature* 519 (2015), pp. 207–210. DOI: <https://doi.org/10.1038/nature14262>.

- [33] <https://www.electronicsforu.com/>. *What is a MOSFET? It's Types, Working, Circuit, and Applications*. 2023. URL: <https://www.electronicsforu.com/technology-trends/learn-electronics/mosfet-basics-working-applications>.
- [34] B.J Huang, C.J Chin, and C.L Duang. "A design method of thermoelectric cooler". In: *International Journal of Refrigeration* 23.3 (2000), pp. 208–218. ISSN: 0140-7007. DOI: [https://doi.org/10.1016/S0140-7007\(99\)00046-8](https://doi.org/10.1016/S0140-7007(99)00046-8). URL: <https://www.sciencedirect.com/science/article/pii/S0140700799000468>.
- [35] L. less et al. "The Gravity Field and Interior Structure of Enceladus". In: *Science* 344.6179 (2014), pp. 78–80. DOI: 10.1126/science.1250551.
- [36] Yehea Ismail and Ahmed Alaskalany. *Thermoelectric Devices: Cooling and Power Generation*. 2014. arXiv: 1403.3836 [cond-mat.mtrl-sci].
- [37] Samer Kahwaji and Mary White. "Edible Oils as Practical Phase Change Materials for Thermal Energy Storage". In: *Applied Sciences* 9 (Apr. 2019), p. 1627. DOI: 10.3390/app9081627.
- [38] Konstantinos Konstantinidis et al. "A lander mission to probe subglacial water on Saturn's moon Enceladus for life". In: *Acta Astronautica* 106 (2015), pp. 63–89.
- [39] Philip Kosky et al. "Chapter 12 - Mechanical Engineering". In: *Exploring Engineering (Third Edition)*. Ed. by Philip Kosky et al. Third Edition. Boston: Academic Press, 2013, pp. 259–281. ISBN: 978-0-12-415891-7. DOI: <https://doi.org/10.1016/B978-0-12-415891-7.00012-1>. URL: <https://www.sciencedirect.com/science/article/pii/B9780124158917000121>.
- [40] X. Li et al. "Thermoelectric Cooling Device Integrated with PCM Heat Storage for MS Patients". In: *Energy Procedia* 61 (2014). International Conference on Applied Energy, ICAE2014, pp. 2399–2402. ISSN: 1876-6102. DOI: <https://doi.org/10.1016/j.egypro.2014.12.014>. URL: <https://www.sciencedirect.com/science/article/pii/S1876610214030434>.
- [41] Lingai Luo and Nolwenn Le Pierrès. "Chapter 3 - Innovative Systems for Storage of Thermal Solar Energy in Buildings". In: *Solar Energy Storage*. Ed. by Bent Sørensen. Boston: Academic Press, 2015, pp. 27–62. ISBN: 978-0-12-409540-3. DOI: <https://doi.org/10.1016/B978-0-12-409540-3.00003-7>. URL: <https://www.sciencedirect.com/science/article/pii/B9780124095403000037>.
- [42] MakeltFrom.com. *Polylactic Acid (PLA, Polylactide)*. 2020. URL: <https://www.makeitfrom.com/material-properties/Polylactic-Acid-PLA-Polylactide/>.
- [43] Lasse Makkonen. "Ice Adhesion —Theory, Measurements and Countermeasures". In: *Journal of Adhesion Science and Technology* 26.4-5 (2012), pp. 413–445. DOI: 10.1163/016942411X574583.
- [44] Hilary R. Martens et al. "Spatial distribution of ice blocks on Enceladus and implications for their origin and emplacement". In: *Icarus* 245 (2015), pp. 162–176. ISSN: 0019-1035. DOI: <https://doi.org/10.1016/j.icarus.2014.09.035>. URL: <https://www.sciencedirect.com/science/article/pii/S0019103514005016>.
- [45] Dennis L. Matson et al. "Enceladus' near-surface CO₂ gas pockets and surface frost deposits". In: *Icarus* 302 (2018), pp. 18–26. ISSN: 0019-1035. DOI: <https://doi.org/10.1016/j.icarus.2017.10.025>. URL: <https://www.sciencedirect.com/science/article/pii/S0019103517302506>.
- [46] MatWeb. *Overview - Alumina, 98%, Al₂O₃*. 2023. URL: <https://www.matweb.com/search/DataSheet.aspx?MatGUID=38cd8590a98f457a8f4bea462fe91cfa&ckck=1>.
- [47] Nanite. *Thermocouple circuit Ktype including voltmeter temperature*. URL: https://commons.wikimedia.org/wiki/File:Thermocouple_circuit_Ktype_including_voltmeter_temperature.svg.
- [48] NASA Exoplanet Exploration. *The Search For Life*. 2020. URL: <https://exoplanets.nasa.gov/search-for-life/are-we-alone/>.
- [49] NASA Solar System Exploration. *Cassini*. 2021. URL: <https://solarsystem.nasa.gov/missions/cassini/overview/>.

- [50] NASA Solar System Exploration. *Saturn's Rings*. 2018. URL: <https://solarsystem.nasa.gov/resources/12669/saturns-rings/>.
- [51] National Center for Biotechnology Information. *PubChem Compound Summary for CID 753, Glycerin*. 2023. URL: <https://pubchem.ncbi.nlm.nih.gov/compound/GLYCERIN>.
- [52] Jeffrey Nederend, Marc Rovira-Navarro, and Tiago Pestana. "Thermal convection in subsurface oceans with variable thickness: Application to Enceladus." In: *Earth and Space Science Open Archive* (2020), p. 13. DOI: 10.1002/essoar.10505266.1.
- [53] John A. Noël et al. "22 - Phase change materials". In: *Storing Energy (Second Edition)*. Ed. by Trevor M. Letcher. Second Edition. Elsevier, 2022, pp. 503–535. ISBN: 978-0-12-824510-1. DOI: <https://doi.org/10.1016/B978-0-12-824510-1.00005-2>. URL: <https://www.sciencedirect.com/science/article/pii/B9780128245101000052>.
- [54] Victor Nunez et al. "Tissue cryopreservation using the 3M™ Novec™ 7000 freezing coolant offers a comparable and safe alternative to customary coolants". In: *Journal of Histotechnology* 45.2 (2022), pp. 85–91. DOI: 10.1080/01478885.2021.1993528.
- [55] Masahiro Ono et al. "Enceladus Vent Explorer Concept". In: *Outer Solar System: Prospective Energy and Material Resources*. Ed. by Viorel Badescu and Kris Zacny. Cham: Springer International Publishing, 2018, pp. 665–717. ISBN: 978-3-319-73845-1. DOI: 10.1007/978-3-319-73845-1_13. URL: https://doi.org/10.1007/978-3-319-73845-1_13.
- [56] PLUS. *TECHNICAL DATA SHEET OF save HS24*. 2022. URL: https://pluss.co.in/wp-content/uploads/2022/03/Doc-075_PCM_HS24_TDS.pdf.
- [57] Nicole J. Rappaport et al. "Mass and interior of Enceladus from Cassini data analysis". In: *Icarus* 190.1 (2007), pp. 175–178. ISSN: 0019-1035. DOI: <https://doi.org/10.1016/j.icarus.2007.03.025>. URL: <https://www.sciencedirect.com/science/article/pii/S0019103507001492>.
- [58] Sonal Renge, Yashika Barhaiya, and Shikhar Pant. "A Review on Generation of Electricity using Peltier Module". In: *International Journal of Engineering Research and V6* (Jan. 2017). DOI: 10.17577/IJERTV6IS010308.
- [59] Maxwell L. Rudolph et al. "Cooling Crusts Create Concomitant Cryovolcanic Cracks". In: *Geophysical Research Letters* 49.5 (2022), e2021GL094421. DOI: <https://doi.org/10.1029/2021GL094421>. URL: <https://agupubs.onlinelibrary.wiley.com/doi/abs/10.1029/2021GL094421>.
- [60] Rami M. Saeed et al. "Preparation and thermal performance of methyl palmitate and lauric acid eutectic mixture as phase change material (PCM)". In: *Journal of Energy Storage* 13 (2017), pp. 418–424. DOI: 10.1016/j.est.2017.08.005. URL: <https://www.scopus.com/inward/record.uri?eid=2-s2.0-85029130192&doi=10.1016%5C%2Fj.est.2017.08.005&partnerID=40&md5=26dfb587c8c3f2980b66ff06d731ed43>.
- [61] Paul Schenk et al. *Enceladus and the Icy Moons of Saturn*. Jan. 2018. ISBN: 9780816537075. DOI: 10.2458/azu_uapress_9780816537075.
- [62] C. Selvam et al. "Transient performance of a Peltier super cooler under varied electric pulse conditions with phase change material". In: *Energy Conversion and Management* 198 (2019). DOI: 10.1016/j.enconman.2019.111822. URL: <https://www.scopus.com/inward/record.uri?eid=2-s2.0-85069041162&doi=10.1016%2Fj.enconman.2019.111822&partnerID=40&md5=419e31ca37d2f453910b4c5168d805b9>.
- [63] N. Shalsam et al. "A STUDY ON THE POTENTIAL OF PELTIER IN GENERATING ELECTRICITY USING HEAT LOSS AT ENGINE SYSTEM". In: Mar. 2016. DOI: 10.13140/RG.2.1.2098.0882.
- [64] P. Singh et al. "A comprehensive review on development of eutectic organic phase change materials and their composites for low and medium range thermal energy storage applications". In: *Solar Energy Materials and Solar Cells* 223 (2021), p. 110955. ISSN: 0927-0248. DOI: <https://doi.org/10.1016/j.solmat.2020.110955>. URL: <https://www.sciencedirect.com/science/article/pii/S0927024820305493>.
- [65] J. R. Spencer et al. "Cassini Encounters Enceladus: Background and the Discovery of a South Polar Hot Spot". In: *Science* 311.5766 (2006), pp. 1401–1405. DOI: 10.1126/science.1121661.

- [66] John R. et al. Spencer. "Enceladus: An Active Cryovolcanic Satellite". In: *Saturn from Cassini-Huygens*. Dordrecht: Springer Netherlands, 2009, pp. 683–724.
- [67] Stavros Sklavenitis. *Experimental simulation and assessment of the geysers of icy moons in the laboratory*. 2022. URL: <http://resolver.tudelft.nl/uuid:3af2e6ad-4dc2-4acc-9cbf-a9afc15cebd9> (visited on 02/06/2023).
- [68] Gang Tan and Dongliang Zhao. "Study of a thermoelectric space cooling system integrated with phase change material". In: *Applied Thermal Engineering* 86 (2015), pp. 187–198. URL: <https://api.semanticscholar.org/CorpusID:109644990>.
- [69] TEMSENS. *TYPE T THERMOCOUPLE*. URL: <https://tempsens.com/blog/type-t-thermo-couple>.
- [70] The Engineering ToolBox. *Acetone - Thermophysical Properties*. 2018. URL: https://www.engineeringtoolbox.com/acetone-2-propanone-dimethyl-ketone-properties-d_2036.html.
- [71] The Engineering ToolBox. *Air - Specific Heat vs. Temperature at Constant Pressure*. 2004. URL: https://www.engineeringtoolbox.com/air-specific-heat-capacity-d_705.html.
- [72] The Engineering ToolBox. *Aluminum - Thermophysical Properties*. 2023. URL: https://www.engineeringtoolbox.com/aluminum-specific-heat-density-thermal-conductivity-temperature-d_2220.html.
- [73] The Engineering ToolBox. *Carbon Dioxide - Thermophysical Properties*. 2018. URL: https://www.engineeringtoolbox.com/CO2-carbon-dioxide-properties-d_2017.html.
- [74] ThermoFisher Scientific. *SAFETY DATA SHEET Potassium fluoride hydrate*. 2021. URL: <https://www.fishersci.com/store/msds?partNumber=AC206400050&productDescription=POTASSIUM+FLUORIDE+HYDRA+5GR&vendorId=VN00032119&countryCode=US&language=en>.
- [75] P.C. Thomas et al. "Enceladus's measured physical libration requires a global subsurface ocean". In: *Icarus* 264 (2016), pp. 37–47. ISSN: 0019-1035. DOI: <https://doi.org/10.1016/j.icarus.2015.08.037>. URL: <https://www.sciencedirect.com/science/article/pii/S0019103515003899>.
- [76] Tom Mooijman. *Bio-Inspired Ice Adhesion Robot for Exploring Icy Moons*. 2023. URL: <http://resolver.tudelft.nl/uuid:784b1427-2a6c-4553-a0e7-d86305991fd0> (visited on 07/08/2023).
- [77] T.M. Tritt. "Thermoelectric Materials: Principles, Structure, Properties, and Applications". In: *Encyclopedia of Materials: Science and Technology*. Ed. by K.H. Jürgen Buschow et al. Oxford: Elsevier, 2002, pp. 1–11. ISBN: 978-0-08-043152-9. DOI: <https://doi.org/10.1016/B0-08-043152-6/01822-2>. URL: <https://www.sciencedirect.com/science/article/pii/B0080431526018222>.
- [78] Wilfried Sire and Guilhem Velvé Casquillas. *Soft Robot: A Review*. 2019. URL: <https://www.elveflow.com/microfluidic-reviews/general-microfluidics/soft-robot/> (visited on 03/03/2023).
- [79] Yeosang Yoon et al. "Bioinspired untethered soft robot with pumpless phase change soft actuators by bidirectional thermoelectrics". In: *Chemical Engineering Journal* 451 (2023), p. 138794. ISSN: 1385-8947. DOI: <https://doi.org/10.1016/j.cej.2022.138794>. URL: <https://www.sciencedirect.com/science/article/pii/S1385894722042759>.
- [80] Yongyichuan Zhang and Xuelai Zhang. "Thermal properties of a new type of calcium chloride hexahydrate-magnesium chloride hexahydrate/expanded graphite composite phase change material and its application in photovoltaic heat dissipation". In: *Solar Energy* 204 (2020), pp. 683–695. ISSN: 0038-092X. DOI: <https://doi.org/10.1016/j.solener.2020.05.037>. URL: <https://www.sciencedirect.com/science/article/pii/S0038092X20305235>.
- [81] Dongliang Zhao and Gang Tan. "A review of thermoelectric cooling: Materials, modeling and applications". In: *Applied Thermal Engineering* 66.1 (2014), pp. 15–24. ISSN: 1359-4311. DOI: <https://doi.org/10.1016/j.applthermaleng.2014.01.074>. URL: <https://www.sciencedirect.com/science/article/pii/S1359431114000854>.



Overview of the Experiment Data

All the measurement data is saved on the computer next to the high speed wind tunnel in the wind tunnel facility of the faculty of Aerospace Engineering as shown in Figure A.1. The test before the 14th of April are stored in This PC/Desktop/Freek/Experiments. In this appendix the different experiments are summarised.

Name	Date modified
5jul	5-7-2023 12:05
6jul	5-7-2023 14:19
6juni	5-6-2023 16:07
8 mei	8-5-2023 14:52
8juni	7-6-2023 14:26
14april	1-4-2023 00:05
14jul-testsonice	13-7-2023 14:43
15juni	14-6-2023 14:28
16jun	15-6-2023 17:40
18april	5-4-2023 02:37
18jul-octadecane	16-7-2023 17:33
20 april	5-4-2023 06:01
23mei	23-5-2023 15:42

Figure A.1: Folder with data stored by date of test from the 14th of April.

31/03/2023 module: TEC1-12706 module (KIWI electronics), T_{amb} : 19 °C, 7.5 V 2 A power supply, sampling rate of 40 measurements/second compared to 20 for all the other tests.

- **pcm1** Test of 0.12 mm GSC-104-PCM on TEC1-12706 module.
- **peltier40** Test of TEC1-12706 module.

03/04/2023 module: TEC1-12706 module (KIWI electronics), T_{amb} : 16.7 °C, 7.5 V 2 A power supply, Figure A.2.

Name	Date modified	Type	Size
 20f	05/04/2023 12:23	Microsoft Excel W...	119 KB
 20fhf	05/04/2023 12:23	Microsoft Excel W...	157 KB
 20hfhf	05/04/2023 12:22	Microsoft Excel W...	181 KB
 20hftime	05/04/2023 12:23	Microsoft Excel W...	326 KB
 20hftime2	05/04/2023 12:23	Microsoft Excel W...	445 KB
 pcm20f	05/04/2023 12:27	Microsoft Excel W...	165 KB
 pcm20fhf	05/04/2023 12:29	Microsoft Excel W...	233 KB
 pcm20hfhf	31/03/2023 18:14	Microsoft Excel W...	329 KB
 pcm20hftime	05/04/2023 12:27	Microsoft Excel W...	545 KB
 pcm20hftime2	05/04/2023 12:29	Microsoft Excel W...	381 KB

Figure A.2: Tests performed on 3 April 2023.

- **20f** test on ice: cooling the ice.
- **20fhf** test on ice: cooling, heating, cooling cycle.
- **20hfhf** test on ice: heating, cooling, heating, cooling cycle.
- **20hftime** test on ice: timed heating, cooling cycles with rest in between. (4s heat, 4s cool, rest, 4s heat, 6s cool, rest, 4s heat, 8s cool, rest)
- **20hftime2** test on ice: timed heating, cooling cycles with rest in between.
- **pcm20f** test on ice with PCM: cooling the ice. (4s heat, 4s cool, rest, 4s heat, 6s cool, rest, 4s heat, 8s cool, rest)
- **pcm20fhf** test on ice with PCM: cooling, heating, cooling cycle.
- **pcm20hfhf** test on ice with PCM: heating, cooling, heating, cooling cycle.
- **pcm20hftime** test on ice with PCM: timed heating, cooling cycles with rest in between. (4s heat, 4s cool, rest, 4s heat, 6s cool, rest, 4s heat, 8s cool, rest)
- **pcm20hftime2** test on ice with PCM: timed heating, cooling cycles with rest in between. (4s heat, 4s cool, rest, 4s heat, 6s cool, rest, 4s heat, 8s cool, rest)

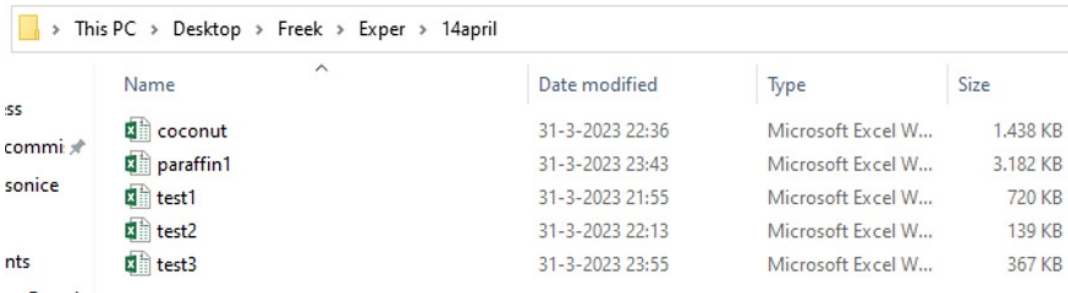
04/04/2023 module: TEC1-12706 module (KIWI electronics), T_{amb} : 16.4 °C, variable power supply, Figure A.3.

Name	Date modified	Type	Size
 2acetone7.5A2	09/04/2023 15:08	Microsoft Excel W...	474 KB
 2peltier9V2A	05/04/2023 13:13	Microsoft Excel W...	906 KB
 acetone7.5v2a	05/04/2023 12:04	Microsoft Excel W...	875 KB
 pcm7.5V2A	05/04/2023 12:04	Microsoft Excel W...	1,096 KB
 peltier7.5V2A	05/04/2023 12:04	Microsoft Excel W...	1,021 KB
 peltier7.5V2A18C	05/04/2023 12:04	Microsoft Excel W...	1,078 KB
 peltier9VA2	05/04/2023 13:13	Microsoft Excel W...	945 KB

Figure A.3: Tests performed on 4 April 2023.

- **2acetone7.5A2** 2nd test of drops of acetone on the peltier module. 7.5 V 2 A power supply.
- **2peltier9V2A** 2nd test of peltier module. 9 V 2 A power supply.
- **acetone7.5A2** test of drops of acetone on the peltier module. 7.5 V 2 A power supply.
- **pcm7.5V2A** Test of 0.12 mm GSC-104-PCM on TEC1-12706 module. 7.5 V 2 A power supply.
- **peltier7.5V2A** Test of TEC1-12706 module. T_{start} : 17.4 °C. 7.5 V 2 A power supply.
- **peltier7.5V2A18C** Test of TEC1-12706 module. T_{start} : 18 °C. 7.5 V 2 A power supply.
- **peltier9V2A** 2nd test of peltier module. 9 V 2 A power supply.

14/04/2023 module: TEC1-12706 module (KIWI electronics), T_{amb} : 18.6 °C, 7.5 V 2 A power supply, Figure A.4.



Name	Date modified	Type	Size
coconut	31-3-2023 22:36	Microsoft Excel W...	1.438 KB
paraffin1	31-3-2023 23:43	Microsoft Excel W...	3.182 KB
test1	31-3-2023 21:55	Microsoft Excel W...	720 KB
test2	31-3-2023 22:13	Microsoft Excel W...	139 KB
test3	31-3-2023 23:55	Microsoft Excel W...	367 KB

Figure A.4: Tests performed on 14 April 2023.

- **coconut** test with 13.057 g coconut oil.
- **paraffin1** test with 13.722 g paraffin wax.
- **test1** test of TEC1-12706 module.
- **test2** test of TEC1-12706 module.
- **test3** test of TEC1-12706 module.

18/04/2023 module: TEC1-12706 module (KIWI electronics), T_{amb} : 18.5 °C, variable power supply, using clay PCM holders, Figure A.5.

Name	Date modified	Type	Size
alu7.5V	5-4-2023 00:16	Microsoft Excel W...	540 KB
cntr3V	5-4-2023 00:50	Microsoft Excel W...	1.333 KB
cntr4.5V	5-4-2023 00:57	Microsoft Excel W...	358 KB
cntr6V	5-4-2023 01:05	Microsoft Excel W...	232 KB
cntr7.5V	5-4-2023 01:14	Microsoft Excel W...	160 KB
cntr9V	5-4-2023 01:22	Microsoft Excel W...	173 KB
cntr12V	5-4-2023 01:30	Microsoft Excel W...	201 KB
coco3V	4-4-2023 22:55	Microsoft Excel W...	1.198 KB
coco4.5V	4-4-2023 22:55	Microsoft Excel W...	494 KB
coco6V	4-4-2023 23:29	Microsoft Excel W...	295 KB
coco7.5V	4-4-2023 23:42	Microsoft Excel W...	185 KB
coco9V	4-4-2023 23:54	Microsoft Excel W...	150 KB
coco12V	5-4-2023 00:05	Microsoft Excel W...	220 KB
paraffin3V	4-4-2023 22:01	Microsoft Excel W...	549 KB
pcm3V	5-4-2023 01:46	Microsoft Excel W...	479 KB
pcm4.5V	5-4-2023 01:56	Microsoft Excel W...	578 KB
pcm6V	5-4-2023 02:05	Microsoft Excel W...	443 KB
pcm7.5V	5-4-2023 02:15	Microsoft Excel W...	187 KB
pcm9V	5-4-2023 02:24	Microsoft Excel W...	251 KB
pcm12V	5-4-2023 02:33	Microsoft Excel W...	278 KB

Figure A.5: Tests performed on 18 April 2023.

- **alu7.5V** test with 1cm aluminium cylinder on the hot side of the module, while cooled by coconut oil PCM.
- **cntr3V** test with 3 V 2 A power supply.
- **cntr4.5V** test with 4.5 V 2 A power supply.
- **cntr6V** test with 6 V 2 A power supply.
- **cntr7.5V** test with 7.5 V 2 A power supply.
- **cntr9V** test with 9 V 2 A power supply.
- **cntr12V** test with 12 V 2 A power supply.
- **coco3V** test with 3 V 2 A power supply and 12 g coconut oil.
- **coco4.5V** test with 4.5 V 2 A power supply and 12 g coconut oil.
- **coco6V** test with 6 V 2 A power supply and 12 g coconut oil.
- **coco7.5V** test with 7.5 V 2 A power supply and 12 g coconut oil.
- **coco9V** test with 9 V 2 A power supply and 12 g coconut oil.
- **coco12V** test with 12 V 2 A power supply and 12 g coconut oil.
- **paraffin3V** test with 3 V 2 A power supply and 7 g paraffin wax.
- **pcm3V** test with 3 V 2 A power supply and 1.92 cm³ GSC-104-PCM.
- **pcm4.5V** test with 4.5 V 2 A power supply and 1.92 cm³ GSC-104-PCM.
- **pcm6V** test with 6 V 2 A power supply and 1.92 cm³ GSC-104-PCM.
- **pcm7.5V** test with 7.5 V 2 A power supply and 1.92 cm³ GSC-104-PCM.
- **pcm9V** test with 9 V 2 A power supply and 1.92 cm³ GSC-104-PCM.
- **pcm12V** test with 12 V 2 A power supply and 1.92 cm³ GSC-104-PCM.

20/04/2023 module: TEC1-12706 module (KIWI electronics), T_{amb} : 19 °C, 7.5 V 2 A power supply, using clay PCM holders and balloon for acetone, Figure A.6.

Name	Date modified	Type	Size
acetone7.5	5-4-2023 06:01	Microsoft Excel W...	693 KB
coconut7.5	5-4-2023 05:59	Microsoft Excel W...	1.246 KB
coconutlong7.5	5-4-2023 06:01	Microsoft Excel W...	1.257 KB
control7.5	5-4-2023 03:56	Microsoft Excel W...	378 KB
paraffin7.5	5-4-2023 06:01	Microsoft Excel W...	2.739 KB

Figure A.6: Tests performed on 20 April 2023.

- **acetone7.5** test with <50 ml acetone.
- **coconut7.5** test with 12 g coconut oil.
- **coconutlong7.5** test with 12 g coconut oil.
- **control7.5** test of peltier module.
- **paraffin7.5** test with 7 g paraffin wax.

08/05/2023 TEC1-12706 module (KIWI electronics), T_{amb} : 19.6 °C, 7.5 V 2 A power supply, using first 3D printed coconut holder, Figure A.7.

Name	Date modified	Type	Size
coconut1	8-5-2023 14:47	Microsoft Excel W...	872 KB
coconut2	8-5-2023 14:52	Microsoft Excel W...	301 KB

Figure A.7: Tests performed on 8 May 2023.

- **coconut1** test with the 3D printed holder with 18.7 g coconut oil.
- **coconut2** test with the 3D printed holder with 18.7 g coconut oil.

23/05/2023 QC-127-1.4-6.0A, T_{amb} : 18.5 °C, variable power supply, using 2nd 3D printed coconut oil holder and 1st 3d printed acetone holder with balloon, Figure A.8.

Name	Date modified	Type	Size
acetone7.5	23-5-2023 11:44	Microsoft Excel W...	826 KB
acetone9	23-5-2023 12:09	Microsoft Excel W...	692 KB
acetone12	23-5-2023 12:45	Microsoft Excel W...	416 KB
coconut7.5	23-5-2023 13:23	Microsoft Excel W...	510 KB
iceacetone	23-5-2023 15:41	Microsoft Excel W...	1.515 KB
icecoco3	23-5-2023 15:12	Microsoft Excel W...	1.117 KB
icecoco7.5	23-5-2023 14:45	Microsoft Excel W...	1.787 KB
icecoco12V	23-5-2023 14:53	Microsoft Excel W...	458 KB
pad1	23-5-2023 13:53	Microsoft Excel W...	553 KB
test1	23-5-2023 11:11	Microsoft Excel W...	195 KB
test2	23-5-2023 11:16	Microsoft Excel W...	297 KB

Figure A.8: Tests performed on 23 May 2023.

- **acetone7.5** test with acetone and 7.5 V 2 A power supply.
- **acetone9** test with acetone and 9 V 2 A power supply.

- **acetone12** test with acetone and 12 V 2 A power supply.
- **coconut7.5** test with 18.7 g of coconut oil and 7.5 V 2A power supply.
- **iceacetone** test on ice with acetone and 12 V 2 A power supply and 1 cm aluminium pad.
- **icecoco3** test on ice with coconut oil and 3 V 2 A power supply and 1 cm aluminium pad.
- **icecoco7.5** test on ice with coconut oil and 7.5 V 2 A power supply and 1 cm aluminium pad.
- **icecoco12V** test on ice with coconut oil and 12 V 2 A power supply and 1 cm aluminium pad.
- **pad1** test of QC-127-1.4-6.0A with 1 cm aluminium pad and 7.5 V 2A power supply.
- **test1** test of QC-127-1.4-6.0A with 7.5 V 2A power supply.
- **test2** test of QC-127-1.4-6.0A with 7.5 V 2A power supply.

06/06/2023 QC-127-1.4-6.0A, T_{amb} : 20.7 °C, variable power supply, using 3rd 3D printed coconut oil holder with 1 mm aluminium interface, Figure A.9.

Name	Date modified	Type	Size
2.04amp	5-6-2023 14:18	Microsoft Excel W...	398 KB
2.06nude	5-6-2023 15:07	Microsoft Excel W...	590 KB
3.04nude	5-6-2023 15:07	Microsoft Excel W...	521 KB
3.07amp	5-6-2023 14:28	Microsoft Excel W...	169 KB
3A5V	5-6-2023 14:40	Microsoft Excel W...	196 KB
3A5Vnude	5-6-2023 15:08	Microsoft Excel W...	369 KB
3coco	5-6-2023 15:54	Microsoft Excel W...	420 KB
3fin	5-6-2023 15:19	Microsoft Excel W...	189 KB

Figure A.9: Tests performed on 6 June 2023.

- **2.04amp** Test with 2.04 A (\sim 9 V) power supply and 1 cm aluminium pad.
- **2.06nude** Test with 2.06 A (\sim 9 V) power supply.
- **3.04nude** Test with 3.04 A (\sim 13 V) power supply.
- **3.07amp** Test with 3.07 A (\sim 13 V) power supply and 1 cm aluminium pad.
- **3A5V** Test with 5 V 3 A power supply and 1 cm aluminium pad.
- **3A5Vnude** Test with 5 V 3 A power supply.
- **3coco** Test with coconut oil with 1 mm aluminium interface between module and PCM and 3 A power supply and 1 cm aluminium pad.
- **3fin** Test with coconut oil and aluminium heat fins on the interface between the peltier module and the coconut oil PCM and 3 A power supply and 1 cm aluminium pad.

08/06/2023 QC-127-1.4-6.0A, T_{amb} : 20.6 °C, variable power supply, using 2nd 3D printed liquid pcm holder with balloon, 1 cm aluminium pad and 1 mm aluminium interface, Figure A.10.

This PC > Desktop > Freek > Exper > 8juni

Name	Date modified	Type	Size
2Anovec	7-6-2023 13:18	Microsoft Excel W...	681 KB
2Atest	7-6-2023 12:09	Microsoft Excel W...	627 KB
2Awater	7-6-2023 13:02	Microsoft Excel W...	636 KB
3.26novec	7-6-2023 14:03	Microsoft Excel W...	275 KB
3A5Vnono	7-6-2023 13:55	Microsoft Excel W...	115 KB
3Anovec1	7-6-2023 13:31	Microsoft Excel W...	293 KB
3Anovec2	7-6-2023 13:48	Microsoft Excel W...	707 KB
3Atest	7-6-2023 12:19	Microsoft Excel W...	693 KB
3Awater	7-6-2023 12:40	Microsoft Excel W...	1.310 KB

Figure A.10: Tests performed on 8 June 2023.

- **2Anovec** test with 20 ml NOVEC7000 engineering fluid and 2A applied current.
- **2Atest** test with the empty container and 2A applied current.
- **2Awater** test with 20 ml water and 2A applied current.
- **3.26Anovec** test with 20 ml NOVEC7000 engineering fluid and 3.26 A applied current.
- **3A5Vnono** test with NOVEC7000 engineering fluid and 5 V 3 A power supply. During this test the NOVEC vaporised away.
- **3Anovec1** test with 20 ml NOVEC7000 engineering fluid and 3A applied current.
- **3Anovec2** test with 20 ml NOVEC7000 engineering fluid and 3A applied current.
- **3Atest** test with the empty container and 3A applied current.
- **3Awater** test with 20 ml water and 3A applied current.

15/06/2023 QC-127-1.4-6.0A, T_{amb} : 20.9 °C, 14 V (\sim 3.5 A) power supply, using 2nd 3D printed liquid pcm holder with balloon, 1 cm aluminium pad and 1 mm aluminium interface, Figure A.11.

This PC > Desktop > Freek > Exper > 15juni

Name	Date modified	Type	Size
litnowa14V	14-6-2023 13:17	Microsoft Excel W...	260 KB
novec14V	14-6-2023 12:33	Microsoft Excel W...	1.015 KB
nowa14V	14-6-2023 14:26	Microsoft Excel W...	488 KB
setup14V	14-6-2023 13:36	Microsoft Excel W...	150 KB
test	14-6-2023 14:26	Microsoft Excel W...	1.256 KB
test14V	14-6-2023 14:26	Microsoft Excel W...	486 KB
water14V	14-6-2023 14:04	Microsoft Excel W...	655 KB

Figure A.11: Tests performed on 15 June 2023.

- **litnowa14V** Test of QC module with 20 ml water and a bit of NOVEC7000.
- **novec14V** Test of QC module with 20 ml NOVEC7000.
- **nowa14V** Test of QC module with 20 ml water and 2 ml NOVEC7000.
- **setup14V** Test of QC module with empty container.
- **test** Test run to see how the power supply worked.
- **test14V** Test of QC module.
- **water14V** Test of QC module with 20 ml water.

16/06/2023 QC-127-1.4-6.0A, T_{amb} : 21 °C, variable power supply, using 2nd 3D printed liquid pcm holder with balloon, and 1 mm aluminium interface, Figure A.12.

Name	Date modified	Type	Size
heatonice2a	15-6-2023 15:40	Microsoft Excel W...	262 KB
novec2A75	15-6-2023 15:19	Microsoft Excel W...	589 KB
novec14	15-6-2023 14:45	Microsoft Excel W...	268 KB
novecice2a	15-6-2023 15:35	Microsoft Excel W...	236 KB
novecice2a2	15-6-2023 15:44	Microsoft Excel W...	222 KB
novecring14	15-6-2023 14:57	Microsoft Excel W...	165 KB
nudenovvec	15-6-2023 17:38	Microsoft Excel W...	295 KB
nudetest	15-6-2023 17:14	Microsoft Excel W...	129 KB
nudewater	15-6-2023 17:28	Microsoft Excel W...	364 KB
test2A75	15-6-2023 16:49	Microsoft Excel W...	225 KB
test14	15-6-2023 17:00	Microsoft Excel W...	266 KB
water2A75	15-6-2023 16:35	Microsoft Excel W...	337 KB
water14	15-6-2023 15:53	Microsoft Excel W...	193 KB
wateragain14	15-6-2023 16:11	Microsoft Excel W...	202 KB

Figure A.12: Tests performed on 16 June 2023.

- **heatonice2a** test of module on ice with empty container, 1 cm aluminium pad and 7.5 V 2 A power supply.
- **novec2A75** test with 20 ml NOVEC, 1 cm aluminium pad and 7.5 V 2 A power supply.
- **novec14** test with 20 ml NOVEC, 1 cm aluminium pad and 14 V power supply.
- **novecice2a** test on ice with 20 ml NOVEC, 1 cm aluminium pad and 7.5 V 2 A power supply.
- **novecice2a2** test with 20 ml NOVEC, 1 cm aluminium pad and 7.5 V 2 A power supply.
- **novecring14** test with 20 ml NOVEC, 1 cm aluminium pad and 14 V 2 A power supply.
- **nudenovvec** test with 20 ml NOVEC and 7.5 V 2 A power supply.
- **nudetest** test with empty container and 7.5 V 2 A power supply.
- **nudewater** test with 20 ml water and 7.5 V 2 A power supply. T5 sensor separated from the model.
- **test2A75** test with empty container, 1 cm aluminium pad and 7.5 V 2 A power supply.
- **test14** test with empty container, 1 cm aluminium pad and 14 V power supply.
- **water2A75** test with 20 ml water, 1 cm aluminium pad and 7.5 V 2 A power supply.
- **water14** test with 20 ml water, 1 cm aluminium pad and 14 V power supply.
- **wateragain14** test with 20 ml water, 1 cm aluminium pad and 7.5 V 2 A power supply.

05/07/2023 MCPF-127-14-25-E, T_{amb} : 20.2 °C, variable power supply, using aluminium PCM holder, Figure A.13.

Name	Date modified	Type	Size
3v2a	4-7-2023 13:00	Microsoft Excel W...	177 KB
3vwithoutheatsink	4-7-2023 13:40	Microsoft Excel W...	131 KB
4.5v2a	4-7-2023 13:03	Microsoft Excel W...	131 KB
6v2a	4-7-2023 13:10	Microsoft Excel W...	172 KB
7.5v2a	4-7-2023 13:14	Microsoft Excel W...	142 KB
7.5vcoconut	4-7-2023 15:38	Microsoft Excel W...	668 KB
7.5vempty	4-7-2023 14:13	Microsoft Excel W...	487 KB
7.5vnovec	4-7-2023 15:17	Microsoft Excel W...	350 KB
7.5vpad	4-7-2023 14:42	Microsoft Excel W...	617 KB
7.5vwithoutheatsink	4-7-2023 13:46	Microsoft Excel W...	134 KB
9v2a	4-7-2023 13:19	Microsoft Excel W...	132 KB
12v2a	4-7-2023 13:24	Microsoft Excel W...	108 KB
12vwithoutheatsink	4-7-2023 13:56	Microsoft Excel W...	95 KB

Figure A.13: Tests performed on 5 July 2023.

- **3v2a** test of MCPF-127-14-25-E with 3 V 2 A power supply. The module was laying on metal acting like a heatsink.
- **3withoutheatsink** test of MCPF-127-14-25-E with 3 V 2 A power supply.
- **4.5v2a** test of MCPF-127-14-25-E with 4.5 V 2 A power supply. The module was laying on metal acting like a heatsink.
- **6v2a** test of MCPF-127-14-25-E with 6 V 2 A power supply. The module was laying on metal acting like a heatsink.
- **7.5v2a** test of MCPF-127-14-25-E with 7.5 V 2 A power supply. The module was laying on metal acting like a heatsink.
- **7.5coconut** test with aluminium container with 34.46 g coconut oil, 1 cm aluminium pad and 7.5 V 2 A power supply.
- **7.5empty** test with empty aluminium container and 7.5 V 2 A power supply.
- **7.5novec** test with aluminium container with 20 ml NOVEC7000 engineering fluid, 1 cm aluminium pad and 7.5 V 2 A power supply.
- **7.5pad** test with empty aluminium container, 1 cm aluminium pad and 7.5 V 2 A power supply.
- **7.5v2awithoutheatsink** test of MCPF-127-14-25-E with 7.5 V 2 A power supply.
- **9v2a** test of MCPF-127-14-25-E with 9 V 2 A power supply. The module was laying on metal acting like a heatsink.
- **12v2a** test of MCPF-127-14-25-E with 12 V 2 A power supply. The module was laying on metal acting like a heatsink.
- **12v2awithoutheatsink** test of MCPF-127-14-25-E with 12 V 2 A power supply.

06/07/2023 MCPF-127-14-25-E, T_{amb} : 20 °C, 7.5 V 2 A power supply, using aluminium PCM holder and 1 cm aluminium pad, Figure A.14.

Name	Date modified	Type	Size
coconut7.5V	5-7-2023 12:39	Microsoft Excel W...	2.432 KB
coldcoco7.5V	5-7-2023 13:38	Microsoft Excel W...	1.008 KB
meltedcoco7.5V	5-7-2023 12:55	Microsoft Excel W...	1.169 KB

Figure A.14: Tests performed on 6 July 2023.

- **coconut7.5V** test with 34 g of coconut oil.
- **coldcoco7.5V** test with 34 g cold coconut oil.
- **meltedcoco7.5V** test with 34 g melted coconut oil.

14/07/2023 MCPF-127-14-25-E, T_{amb} : 21 °C, 7.5 V 2 A power supply, using aluminium PCM holder and 1 cm aluminium pad, Figure A.15.

Name	Date modified	Type	Size
coco4scycles	13-7-2023 12:18	Microsoft Excel W...	417 KB
cocolong	13-7-2023 12:34	Microsoft Excel W...	975 KB
empty4scycles	13-7-2023 12:57	Microsoft Excel W...	241 KB
empty4scycles2	13-7-2023 13:09	Microsoft Excel W...	267 KB
emptyfirst	13-7-2023 12:52	Microsoft Excel W...	127 KB
emptylong	13-7-2023 13:04	Microsoft Excel W...	500 KB
emptylong2	13-7-2023 13:36	Microsoft Excel W...	579 KB
water4scycles	13-7-2023 14:15	Microsoft Excel W...	307 KB
waterlong	13-7-2023 13:57	Microsoft Excel W...	1.026 KB

Figure A.15: Tests performed on 14 July 2023.

- **coco4scycles** test heating cooling cycles on ice with 34 g of coconut oil in aluminium holder. (cool 4s, rest 4s, heat 4s, rest 20s)
- **cocolong** test cooling on ice with 34 g of coconut oil in aluminium holder.
- **empty4scycles** test heating cooling cycles on ice with empty aluminium holder. (cool 4s, rest 4s, heat 4s, rest 20s).
- **empty4scycles2** test heating cooling cycles on ice with empty aluminium holder. (cool 4s, rest 4s, heat 4s, rest 20s).
- **emptyfirst** test run with empty container.
- **emptylong** test cooling on ice with empty aluminium holder.
- **emptylong2** test cooling on ice with empty aluminium holder.
- **water4scycles** test heating cooling cycles on ice with 30 ml of water in aluminium holder. (cool 4s, rest 4s, heat 4s, rest 20s)
- **waterlong** test cooling on ice with 30 ml of water in aluminium holder.

18/07/2023 MCPF-127-14-25-E, T_{amb} : 21 °C, 7.5 V 2 A power supply, using aluminium PCM holder and 1 cm aluminium pad, Figure A.16.

Name	Date modified	Type	Size
empty	16-7-2023 16:45	Microsoft Excel W...	1.501 KB
in_octadecane	17-7-2023 14:29	Microsoft Excel W...	1.267 KB
octadecane	17-7-2023 14:09	Microsoft Excel W...	2.651 KB
water	16-7-2023 16:01	Microsoft Excel W...	1.033 KB

Figure A.16: Tests performed on 5 July 2023.

- **empty** Test of peltier module with aluminium adhesion pad and empty container.
- **in_octadecane** One of the sensors measures the temperature inside the octadecane PCM and the other the temperature of the container.

- **octadecane** Test of peltier module with aluminium adhesion pad and container with 25 g octadecane.
- **water** Test of peltier module with aluminium adhesion pad and container with 30 ml water.

B

Model of the TEC1-06308 module with PCM cooling

```
1 import numpy as np
2 import matplotlib.pyplot as plt
3 import pandas as pd
4 from scipy.optimize import minimize
5
6 plt.rc('font', size=18)
7
8 #constants
9 sb = 5.670374419*10**(-8)
10
11 # aluminium
12 cal = 900 # j/kgK
13 rhoal = 2700 # kg/m3
14 Kal = 237
15
16 # air
17 cair = 1006 # j/kgK
18 rhoair = 1.204 # kg/m3
19
20 # #water
21 cwater = 4180
22 rhowater = 1000
23
24 #peltier
25 lpel = 0.04
26 bpel = 0.02
27 Apel = lpel*bpel
28
29 #plate material - alumina Al2O3
30 rho = 3987 #[g/cm3]
31 m = Apel*0.001*rho# [kg]
32 c = 880 #[J/kg.K] https://www.matweb.com/search/datasheet.aspx?matguid=0654701067d147e88e8a38c646dda195&ckck=1
33
34 #vendor datasheet
35 TH = 25+273.15
36 Imax = 8
37 Umax = 7.6
38 dTmax = 63
39 Tmax = 138
40
41 #fitted parameters from MCPF measurements
42 fitDT = 0.90 #dTmax_real/dTmax_vendor
```

```

43 h = 18.55 #convective heattransfer coefficient air
44 Heat_pump_reduction = 0.8 #reduction in heatpumping applied in model with pcm
45
46
47 #estimate parameters
48 a = (Umax) / TH
49
50 R = (TH - fitDT*dTmax) * Umax / (TH * Imax)
51
52 K = (TH - fitDT*dTmax) * Umax * Imax / (2 * TH *fitDT* dTmax)
53
54 #input parameters
55 # Iinput = 2 #[A]
56 Tamb = 21 + 273.15
57
58 #time
59 dt = 0.1
60 t = np.arange(0,1000,dt)
61 tstop = 615
62 U = 4.5
63
64
65 naked = False
66 if naked == True:
67     for U in [3.8,4.35]:
68
69         listTh = []
70         listTc = []
71         Th = Tamb
72         Tc = Tamb
73         Tambh = Tamb
74         Tambc = Tamb
75
76         for i in t:
77
78             listTh.append(Th-273.15)
79             listTc.append(Tc-273.15)
80             dT = Th - Tc
81
82             I = (U - a * dT) / (R)
83
84             if i <= tstop:
85                 Qh = a * I * Tc + 0.5 * I ** 2 * R - K * dT
86                 dTh = (Qh -h*Apel*(Th-Tambh)) / (c * m)
87                 dTc = (-a * I * Tc + K * dT -h*Apel*(Tc-Tambc) + 0.5 * I ** 2 * R) / (c * m)
88
89                 Th = Th + dTh
90                 Tc = Tc +dTc
91
92
93             else:
94                 dTh = (-h*Apel*(Th-Tambh) - K * dT) / (c * m)
95                 dTc = (-h*Apel*(Tc-Tambc) + K * dT) / (c * m)
96
97                 Th = Th + dTh
98                 Tc = Tc +dTc
99
100             dThot =h * Apel * (Th - Tambh)
101             dTcold =h * Apel * (Tc - Tambc)
102
103
104             T4c = (Tambc * Tambc * Tambc * Tambc - Tamb * Tamb * Tamb * Tamb)
105             T4h =(Tambh*Tambh*Tambh*Tambh -Tamb*Tamb*Tamb*Tamb)
106             radcold = sb * (Apel+lpel*0.1*2+bpel*0.1*2) * T4c
107             radhot = sb * (Apel+lpel*0.1*2+bpel*0.1*2) * T4h
108             Tambh = Tambh + ((dThot - radhot) / (1005 * Apel *0.1 * 1.225))
109             Tambc = Tambc + ((dTcold - radcold) / (1005 * Apel * 0.1 * 1.225))
110
111         if U ==3.8:
112             line = ':'
113             label = str(U)+'V - nominal cell voltage'

```

```

114     if U == 4.35:
115         line = '-.'
116         label = str(U) + 'V - charged (100%) voltage'
117
118
119     plt.plot(t, listTh, color='red', linestyle='-', label= 'hot model ' + label )
120     plt.plot(t,listTc,color='blue',linestyle='.', label='cold model ' + label)
121
122
123     plt.title('Modelled temperature response of the TEC1-06308 Peltier module')
124     plt.xlabel('Time [s]')
125     plt.ylabel('Temperature [°C]')
126     plt.legend()
127     plt.grid()
128     plt.show()
129
130 pcmmodel = True
131 Tmincoco = []
132 Tminoct = []
133 tcooloct = []
134 tccolcoc = []
135 legend_labels_ax2=[]
136
137 pcm = 'octadecane'
138 for pcm in ['octadecane']:
139     c = 0
140     fig, ax1 = plt.subplots()
141     for mpcm in [7.518,7.457]:
142         U = 4.35
143
144         fin = False
145         if mpcm ==7.457:
146             fin = True
147
148
149         if pcm == 'coconut oil':
150             cpcms = 1330
151             cpcml = 2710
152             Tmelt = 24 + 273.15
153             Kpcm = 0.165
154             rhopcm = 900
155             dH = 105000
156             colh = 'orangered'
157             colc = 'gold'
158             mark = 'o'
159             sensible_heat_when_melting = 0.66845693 #fitted contribution of sensible heat
storage during melting
160
161         if pcm=='octadecane':
162             cpcms = 1800
163             cpcml = 2300
164             Tmelt = 28 + 273.15
165             Kpcm = 0.335
166             rhopcm = 868 #[kg/m3]
167             dH = 237000
168             mark = '*'
169             sensible_heat_when_melting = 0 #contribution of sensible heat storage during
melting is ignored for octadecane
170
171             colh = 'maroon'
172             colc = 'magenta'
173
174
175             Abot = 0.00192492 #m2
176             twall = 0.001 #[m]
177
178
179             mpcm =mpcm/1000
180             Vpcm = mpcm/rhopcm
181
182

```



```

251         dThsensible = sensible_heat_when_melting * (Qh) / (
252             c * m + cal * rhoal * Vhs + Vl * rhopcm * cpcml + Vs *
rhopcm * cpcms) *dt
253
254         dTc = (Heat_pump_reduction * (-a * I * Tcold) + K * dT + 0.5 * I ** 2
* R - h * (Apad) * (Tcold - Tambc)) / (c * m + cal * Vpad * rhoal)
255         dThsens = dThsens + dThsensible
256         Th = Tmelt + dTh + dThsens
257         Tc = Tcold + dTc *dt
258
259
260     else:
261         I=0
262         listI.append(I)
263         dTh = (-h * (Ahs) * (Thold - Tambh) - K * dT) / (c * m + cal * rhoal * Vhs +
Vpcm * rhopcm * cpcml)
264         dTc = ((K * dT) - h * Apad * (Tcold - Tambc)) / (c * m + cal * Vpad * rhoal)
265
266         Th = Thold + dTh *dt
267         Tc = Tcold + dTc *dt
268
269         dThot = h * Ahs * (Thold - Tambh)
270         dTcold = h * Apad * (Tcold - Tambc)
271
272         radcold = sb * (Apad) * (Tambc ** 4 - Tamb ** 4)
273         radhot = sb * (Ahs) * (Tambh ** 4 - Tamb ** 4)
274         Tambh = Tambh + (dThot - radhot) / (cair * Ahs*0.1 * rhoair) *dt
275         Tambc = Tambc + (dTcold - radcold) / (cair * Apad*0.1*rhoair) *dt
276
277     if U == 3.8:
278         line = ':'
279         label = str(U) + 'V - nominal cell voltage'
280     if U == 4.35:
281         line = '-.'
282         label = str(U) + 'V - charged (100%) voltage'
283
284     cmap = ['magenta', 'red', 'orangered', 'orange', 'gold', 'green', 'lightblue', 'blue', '
indigo', 'purple']
285     # cmap = ['red', 'orange', 'green', 'blue', 'purple']
286     # cmap = ['orangered', 'orange', 'gold', 'green', 'lightblue', 'blue', 'indigo', '
purple']
287     ccur = ['lightgreen', 'green', 'darkgreen', 'brown']
288     cmap = ['orangered', 'magenta']
289     if c==0:
290         label='7.518 g without heat fin'
291         cur = '7.518 g'
292     if c==1:
293         cur = '7.457 g'
294         label='7.457 g with heat fin'
295
296     ax1.set_xlabel('Time [s]')
297     ax1.set_ylabel('Temperature [°C]', color='red')
298     # ax1.plot(t, listTh, color='red', linestyle='-', label='hot model')
299     # ax1.plot(t, listTc, color='blue', linestyle=':', label='cold model')
300     ax1.plot(t, listTh, color=cmap[c], linestyle=line, label=label)
301     ax1.plot(t, listTc, color=cmap[c], linestyle=line)
302     ax1.tick_params(axis='y', labelcolor = 'red')
303     ax2 = ax1.twinx()
304     ax2.set_ylabel('Current [A]', color='green')
305     ax2.plot(t, listI, color=ccur[c])
306     ax2.tick_params(axis='y', labelcolor='green')
307     legend_labels_ax2.append(cur)
308
309
310     if pcm == 'octadecane':
311         Tminoct.append(min(listTc))
312
313     count = 0
314     for item in listTc:
315         if item < 0:
316             count += 1

```

```

317         tcooloct.append(count*dt)
318
319     if pcm == 'coconut oil':
320         Tmincoco.append(min(listTc))
321         count = 0
322         for item in listTc:
323             if item < 0:
324                 count += 1
325         tcoolcoc.append(count*dt)
326     # if c==0:
327     #     plt.scatter(mpcm * 1000, min(listTc), color=cmap[c], marker=mark,label=str(pcm)
328 )
329     # else:
330     #     plt.scatter(mpcm*1000,min(listTc),color=cmap[c],marker=mark)
331     # if c==0:
332     #     plt.scatter(mpcm * 1000, count*dt, color=cmap[c], marker=mark,label='minT = 0
333 °C')
334     # else:
335     #     plt.scatter(mpcm*1000,count*dt,color=cmap[c],marker=mark)
336     print('Subzero cooling time: ',count*dt,' s, Min temperature: ',min(listTc),' °C')
337     c = c+1
338
339 from scipy.optimize import curve_fit
340 mrange = [13.74718275,20,30,40,50,60,70,80,90]
341 # Define exponential functions
342 def coconut_exp(m, a, b, c):
343     return a* np.exp(-b*m) + c
344
345 def octa_exp(m, a, b, c):
346     return a * np.exp(-b*m) + c
347
348 def octa_poly(m, a, b,c):
349     return a *m**2+b*m+c
350
351 # Fit exponential functions to the data
352 # popt_coconut, _ = curve_fit(coconut_exp, mrange, Tmincoco)
353 # popt_octa, _ = curve_fit(octa_exp, mrange, Tminoc)
354 # print(popt_coconut)
355 # print(popt_octa)
356 # # Create arrays for the fitted curves
357 # a,b,c = np.polyfit(mrange,tcooloct,2)
358 # x_fit = np.arange(13.74718275, 100, 1)
359 #
360 # coconut_fit = coconut_exp(x_fit, *popt_coconut)
361 # octa_fit = octa_poly(x_fit, a,b,c)
362
363 # Plot the data and fitted curves
364 # plt.plot(x_fit, coconut_fit, color='orange', linestyle='--', label='coconut fit')
365 # plt.plot(x_fit, octa_fit, alpha=0.5,color='magenta', linestyle='-.', label='octadecane fit
366 ')
367 # plt.plot(t,np.zeros(len(t)),linestyle='--',label='melting point water')
368 # plt.title('Modelled temperature response of the TEC1-06308 Peltier module with 4.35 V - '+'
369 str(pcm)+' PCM')
370 # plt.title('Minimum modelled adhesion pad temperature over PCM mass with TEC1-06308 module
371 (4.34 V)')
372 # plt.title('Subzero cooling time over octadecane mass with TEC1-06308 module (4.34 V)')
373 # plt.xlabel('Time [s]')
374 # plt.ylabel('Temperature [°C]')
375 # plt.xlabel('PCM mass [g]')
376 # plt.ylabel('Cooling time [s]')
377 # plt.ylabel('Minimum Temperature [°C]')
378 # plt.xticks(np.arange(0,100,10))
379 # plt.legend(loc="upper right")
380
381 ax1.legend(loc="lower right")
382 for i, label in enumerate(legend_labels_ax2):
383     ax2.plot([], [], color=ccur[i], label=label)
384
385 # Combine all legends for ax2 into one
386 ax2.legend(loc="upper right")

```

```

383 ax1.grid()
384 # ax1.set_title('Temperature response and current for link with 8.458 g octadecane')
385 ax1.set_title('Temperature response and current for link with octadecane container with and
    without heat fins')
386 plt.show()
387
388 from scipy.optimize import minimize
389 def cost_function(params):
390     mpcm = params
391     U = 4.35
392     pcm = 'octadecane'
393
394
395     if pcm == 'coconut oil':
396         cpcms = 1330
397         cpcml = 2710
398         Tmelt = 24 + 273.15
399         Kpcm = 0.165
400         rhopcm = 900
401         dH = 105000
402         colh = 'orangered'
403         colc = 'gold'
404         mark = 'o'
405         sensible_heat_when_melting = 0.66845693 # fitted contribution of sensible heat
    storage during melting
406
407     if pcm == 'octadecane':
408         cpcms = 1800
409         cpcml = 2300
410         Tmelt = 28 + 273.15
411         Kpcm = 0.335
412         rhopcm = 868 # [kg/m3]
413         dH = 237000
414         mark = '*'
415         sensible_heat_when_melting = 0 # contribution of sensible heat storage during
    melting is ignored for octadecane
416
417         colh = 'maroon'
418         colc = 'magenta'
419
420     l = lpel
421     b = bpel
422     l = 0.06808
423     b = 0.01979
424     twall = 0.001 # [m]
425
426     mpcm = mpcm / 1000
427     Vpcm = mpcm / rhopcm
428     hpcm = Vpcm/((1-4*twall)*(b-2*twall))
429     hhs = hpcm+2*twall
430     lfin = np.sqrt((1-2*twall)**2+(b-2*twall)**2)
431     Vhs = l*b*hhs-Vpcm+twall*hpcm*lfin
432     Ahs = 2*l*hhs+Apel+2*b*hhs
433     Apcm = (1-2*twall)*(b-2*twall)*2+2*hpcm*((1-2*twall)+(b-2*twall))+2*lfin*hpcm
434
435
436
437     tpad = 0.01
438     Apad = Apel + 2 * tpad * (lpel + bpel)
439     Vpad = Apel * tpad
440
441     L = Vpcm / Apcm
442
443     x = 0
444     dThsens = 0
445     listTh = []
446     listTc = []
447     Th = Tamb
448     Tc = Tamb
449     Tambh = Tamb
450     Tambc = Tamb

```

```

451 tstop = 200
452
453
454
455 for i in t:
456     listTh.append(Th - 273.15)
457     listTc.append(Tc - 273.15)
458     dT = Th - Tc
459     Thold = Th
460     Tcold = Tc
461
462     I = (U - a * dT) / (R)
463
464
465     if i <= tstop:
466
467         Qh = Heat_pump_reduction * (a * I * Tcold) + 0.5 * I ** 2 * R - K * dT
468
469         if Thold < Tmelt:
470             dTh = (Qh - h * (Ahs) * (Th - Tambh)) / (c * m + cal * rhoal * Vhs + Vpcm *
rhopcm * cpcms)
471
472             dTc = (Heat_pump_reduction * (-a * I * Tc) + K * dT + 0.5 * I ** 2 * R - h *
(
473                 Apad) * (Tc - Tambc)) / (c * m + cal * Vpad * rhoal)
474             Th = Thold + dTh * dt
475             Tc = Tcold + dTc * dt
476
477         if Thold >= Tmelt:
478             vmelt = Qh / (Apcm * rhopcm * dH)
479             x = x + vmelt * dt
480             if x < L:
481
482                 Vl = Apcm * x
483                 if Vl >= Vpcm:
484                     Vl = Vpcm
485                 Vs = Vpcm - Vl
486                 dTh = (Qh * x / Apel * Kpcm)
487                 dThsensible = sensible_heat_when_melting * (Qh) / (
488                     c * m + cal * rhoal * Vhs + Vl * rhopcm * cpcml + Vs * rhopcm *
cpcms) * dt
489
490                 dTc = (Heat_pump_reduction * (-a * I * Tcold) + K * dT + 0.5 * I ** 2 * R
- h * (Apad) * (
491                     Tcold - Tambc)) / (c * m + cal * Vpad * rhoal)
492                 dThsens = dThsens + dThsensible
493                 Th = Tmelt + dTh + dThsens
494                 Tc = Tcold + dTc * dt
495
496
497             if x >= L:
498                 dTh = (Qh - h * (Ahs) * (Thold - Tambh)) / (
499                     c * m + cal * rhoal * Vhs + Vpcm * rhopcm * cpcml)
500
501                 dTc = (Heat_pump_reduction * (-a * I * Tcold) + K * dT + 0.5 * I ** 2 * R
- h * (
502                     Apad) * (Tcold - Tambc)) / (c * m + cal * Vpad * rhoal)
503                 Th = Thold + dTh * dt
504                 Tc = Tcold + dTc * dt
505
506
507         else:
508             dTh = (-h * (Ahs) * (Thold - Tambh) - K * dT) / (c * m + cal * rhoal * Vhs + Vpcm
* rhopcm * cpcml)
509             dTc = ((K * dT) - h * Apad * (Tcold - Tambc)) / (c * m + cal * Vpad * rhoal)
510
511             Th = Thold + dTh * dt
512             Tc = Tcold + dTc * dt
513
514             dThot = h * Ahs * (Thold - Tambh)
515             dTcold = h * Apad * (Tcold - Tambc)

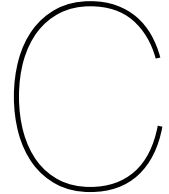
```

```

516     radcold = sb * (Apad) * (Tambc ** 4 - Tamb ** 4)
517     radhot = sb * (Ahs) * (Tambh ** 4 - Tamb ** 4)
518     Tambh = Tambh + (dTthot - radhot) / (cair * Ahs * 0.1 * rhoair) * dt
519     Tambc = Tambc + (dTcold - radcold) / (cair * Apad * 0.1 * rhoair) * dt
520
521     return abs(min(listTc))
522
523
524
525 op = False
526 if op == True:
527     initial_params = [10]
528
529     bounds = [(5, 40)]
530     result = minimize(cost_function, initial_params, method='L-BFGS-B', bounds=bounds)
531     optimal_params = result.x
532     optimal_m = optimal_params
533
534     print(optimal_m)

```

Listing B.1: TEC1-06308.py



Theoretical Model of the Peltier Module

To estimate the effect of different PCMs, PCM containers and Peltier modules on the performance of the ice adhesion mechanism without performing tests, a theoretical model is developed in this chapter. Next, the effect of the ice adhesion mechanism designed in Chapter 4 with different content is modelled and compared to the measurements in Appendix D.

C.1. Peltier module model

To understand the underlying equations to describe the heating and cooling by the Peltier module, a theoretical model is developed to simulate the expected temperature response of the MCPF-127-14-25-E module. This model can be used in the analysis to estimate the hot side temperature of the Peltier modules, which could not always be measured. In Table E.1 the properties of the MCPF-127-14-25-E are listed, hereafter referred to as the Peltier module in this section.

C.1.1. Heat pumping rate

To model the heat pumping rate of the module, Q_c , Equation 3.5 is multiplied by the number of semiconductor couples (127 in the MCPF module) and the Seebeck coefficients of the two semiconductors are combined into the relative Seebeck coefficient to find Equation C.1 [6]. In a measurement of the Seebeck effect, the difference in the Seebeck coefficients of the two dissimilar materials is called the relative Seebeck coefficient ($\alpha_{pn} = \alpha_p - \alpha_n$) [77].

$$Q_c = 2N \cdot \alpha_{pn} \cdot I \cdot T_c - 0.5 \cdot I^2 \cdot R - K \cdot \Delta T \quad (\text{C.1})$$

Where, N is the number of semiconductor couples, α_{pn} the relative Seebeck coefficient of the semiconductor couple in V/K, I is the current in A, T_h the temperature of the hot side in Kelvin, R is the

resistance of the Peltier module in Ohm, K the thermal conductivity in W/K and ΔT the temperature difference in Kelvin.

C.1.2. Physical characteristics estimation

To estimate the Seebeck coefficient, resistance and thermal conductivity of the Peltier module, Equation C.8, Equation C.9, Equation C.11 from Zhaoxia Luo 2008 are used [5] and reported below. These equations were developed to estimate these physical characteristics (α_{pn} , R & K) with the parameters commonly provided in the vendor datasheet from the manufacturer (For MCPF-10=27-14-25-E: $\Delta T_{max} = 73$ °C, $U_{max} = 15.7$ V, $T_H = 25$ °C and $I_{max} = 3.9$ A, where U_{max} , T_H and I_{max} are measured at ΔT_{max}). As the maximum temperature difference is measured at I_{max} , V_{max} and $Q = 0$ W. Equation C.1 can be rewritten to Equation C.1.2 to calculate the temperature difference when the heat pumping rate is 0 W.

$$\Delta T = \frac{1}{K} \left(2N\alpha_{pn}T_c I - \frac{1}{2} I^2 R \right) \quad (C.2)$$

Where, T_c is the cold side temperature at ΔT_{max} .

To estimate the characteristics, the derivative of Equation C.1.2 with respect to I is taken and the root of Equation C.3 is taken to estimate the parameters at ΔT_{max} , as shown below:

$$\frac{d\Delta T}{dI} = \frac{1}{K} (2N\alpha_{pn}T_c - IR) = 0 \quad (C.3)$$

Resulting in Equation C.4, where T_c can

$$I_{max} = \frac{2N\alpha_{pn}}{R} T_c = \frac{2N\alpha_{pn}}{R} (T_H - \Delta T_{max}) \quad (C.4)$$

Plugging this into results in Equation C.5:

$$\begin{aligned} \Delta T_{max} &= \frac{1}{K} \left(2N\alpha_{pn}T_c \frac{2N\alpha_{pn}}{R} T_c - \frac{1}{2} \left(\frac{2N\alpha_{pn}}{R} T_c \right)^2 R \right) \\ &= \frac{1}{K} \left(\frac{4N^2\alpha_{pn}^2}{R} T_c^2 - \frac{1}{2} \frac{4N^2\alpha_{pn}^2}{R} T_c^2 \right) \\ &= \frac{1}{2K} \left(\frac{(2N\alpha_{pn})^2}{R} T_c^2 \right) \\ &= \frac{1}{2K} \left(\frac{(2N\alpha_{pn})^2}{R} (T_H - \Delta T_{max})^2 \right) \end{aligned} \quad (C.5)$$

The voltage over a Peltier module can be calculated with Equation C.6 [6].

$$U = IR + 2N\alpha_{pn}\Delta T \quad (C.6)$$

Where ΔT is the temperature difference between the hot and cold sides. The U_{max} can be calculated by plugging Equation C.4 and Equation C.5 into Equation C.6, resulting in Equation C.7.

$$U_{max} = I_{max}R + 2N\alpha_{pn}\Delta T_{max} = 2N\alpha_{pn}T_H \quad (C.7)$$

Using Equation C.7, the Seebeck coefficient can be estimated with Equation C.8.

$$2N\alpha_{pn} = \frac{U_{max}}{T_H} \quad (C.8)$$

Next, by plugging Equation C.8 into Equation C.7, the resistance can be estimated with Equation C.9.

$$R = \frac{U_{max} - \frac{U_{max}}{T_H} \Delta T_{max}}{I_{max}} = \frac{(T_H - \Delta T_{max})U_{max}}{T_H I_{max}} \quad (C.9)$$

Combining Equation C.5, Equation C.8, Equation C.9 and Equation C.7 results in Equation C.10. The thermal conductivity can be estimated by rewriting Equation C.10 into Equation C.11.

$$U_{max} = I_{max} \frac{(T_H - \Delta T_{max})U_{max}}{T_H I_{max}} + \frac{U_{max}}{T_H} \frac{1}{2K} \left(\frac{\left(\frac{U_{max}}{T_H}\right)^2}{\frac{(T_H - \Delta T_{max})U_{max}}{T_H I_{max}}} (T_H - \Delta T_{max})^2 \right) = \frac{(T_H - \Delta T_{max})U_{max}}{T_H} + \frac{U_{max}^2 I_{max} (T_H - \Delta T_{max})}{2T_H^2 K} \quad (C.10)$$

$$K = \frac{(T_h - \Delta T_{max})U_{max}I_{max}}{2T_h \Delta T_{max}} \quad (C.11)$$

C.1.3. Temperature response

Using Equation C.1, Equation C.8, Equation C.9 and Equation C.11, the temperature of the hot and cold side of the Peltier module as a function of time can be estimated as shown in the flowchart shown in Figure C.1.

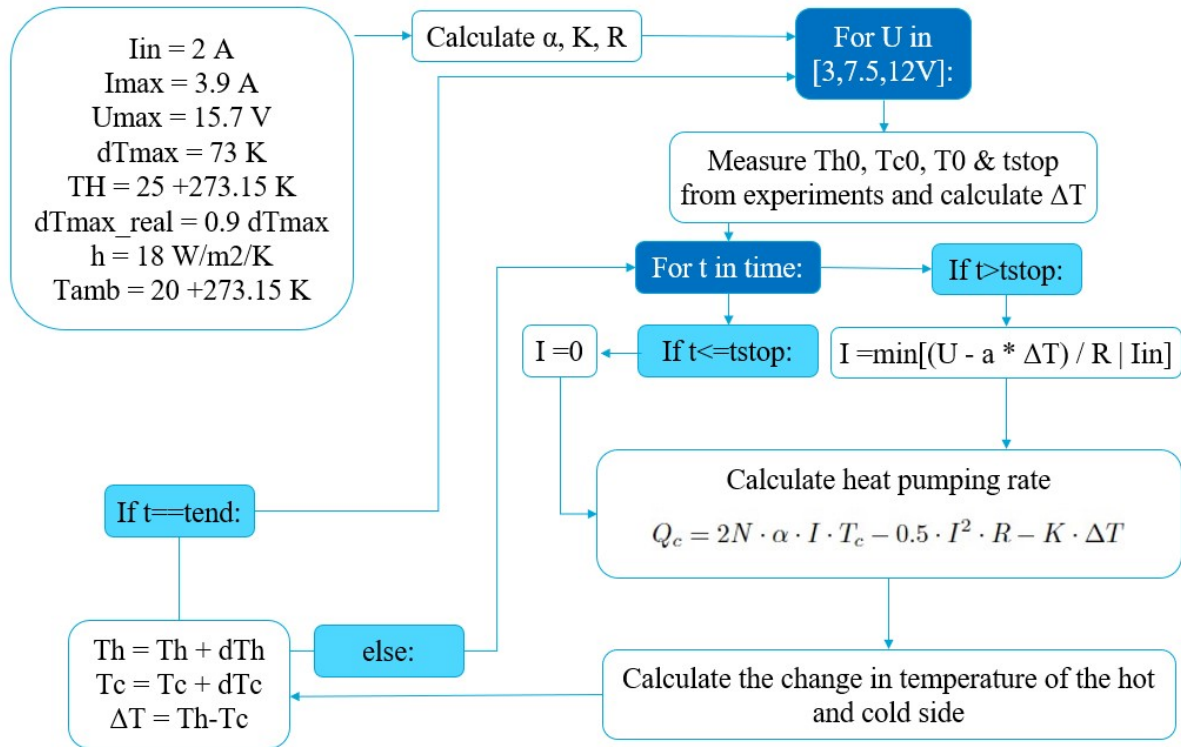


Figure C.1: Flowchart of Peltier module model.

First, the applied current and voltage, convective heat transfer coefficient, h , and ambient temperature are set, together with the U_{max} , T_H , I_{max} and ΔT_{max} from the vendor datasheet. Next, the Seebeck coefficient, thermal conductivity and resistance are calculated (0.0002073 V/K, 0.363 W/mK & 3.1385 Ω) with the equation described in Section C.1.2. Then, for 3, 7.5 and 12 V, the start temperature and the time the peltier was turned off are derived from the measurements shown in Figure E.6. Next, the heat flow to and from the hot side is calculated with Equation C.12.

$$Q_{hot} = 2N\alpha_{pn}IT_c + 0.5 \cdot I^2 R - K\Delta T - h \cdot A_{peltier}(T_h - T_{ambh}) \quad (C.12)$$

Where T_c is the modelled temperature of the cold side of the Peltier module, h is the convective heat transfer coefficient, $A_{peltier}$ is the area of one side of the Peltier module, T_h is the modelled temperature of the hot side, ΔT is the temperature difference between the hot and cold side and T_{ambh} is the modelled temperature of the air surrounding the hot side of the Peltier module (see Section C.1.6). Similarly, the heat flow to and from the cold side can be calculated by Equation C.13.

$$Q_{cold} = -2N\alpha_{pn}IT_c + 0.5 \cdot I^2R + K\Delta T - h \cdot A_{peltier}(T_c - T_{ambc}) \quad (C.13)$$

Where T_c is the modelled temperature of the cold side of the Peltier module, h is the convective heat transfer coefficient, $A_{peltier}$ is the area of one side of the Peltier module and T_{ambc} is the modelled temperature of the air surrounding the cold side of the Peltier module (see Section C.1.6).

Every 20th of a second (the sampling rate of the sensor), the temperature change is calculated by Equation C.14, which is derived from the equation of sensible heat storage (Equation 3.6) [53].

$$dT = \frac{Q}{c \cdot m} \quad (C.14)$$

Where dT is the temperature change, Q the heat at the Peltier side, including heat pumping, joule heating and dissipation as described by Figure C.6, c is the specific heat coefficient which is 0.880 J/gK for the alumina (Al_2O_3) ceramic plate covering the semiconductors. m is the mass of the plate of 6.38 g , calculated with the density of alumina (3.987 g/cm^3 [46]) and plate thickness of 1 mm .

Hence, the temperature of the hot side can be updated as shown in Equation C.15 and the cold side temperature as shown in Equation C.16.

$$T_h^{new} = T_h^{old} + \frac{Q_{hot}}{c \cdot m} \quad (C.15)$$

$$T_c^{new} = T_c^{old} + \frac{Q_{cold}}{c \cdot m} \quad (C.16)$$

After the cold and hot side plates and air temperature are updated, the temperature difference between the two plates is calculated. These steps are iterated over time till t_{stop} is reached. Then, the current is set to zero and the program runs till the end of the measured time. Running this model for 3, 7.5 and 12 V results in Figure C.2. As shown in Figure C.2, the three models describe the same response except for the different end times, explaining the highest temperature for the 3V test. This is expected as the model describes the behaviour when 2 A is applied to the module without a limit on the voltage. The effect of the applied voltage is explained in the next subsection.

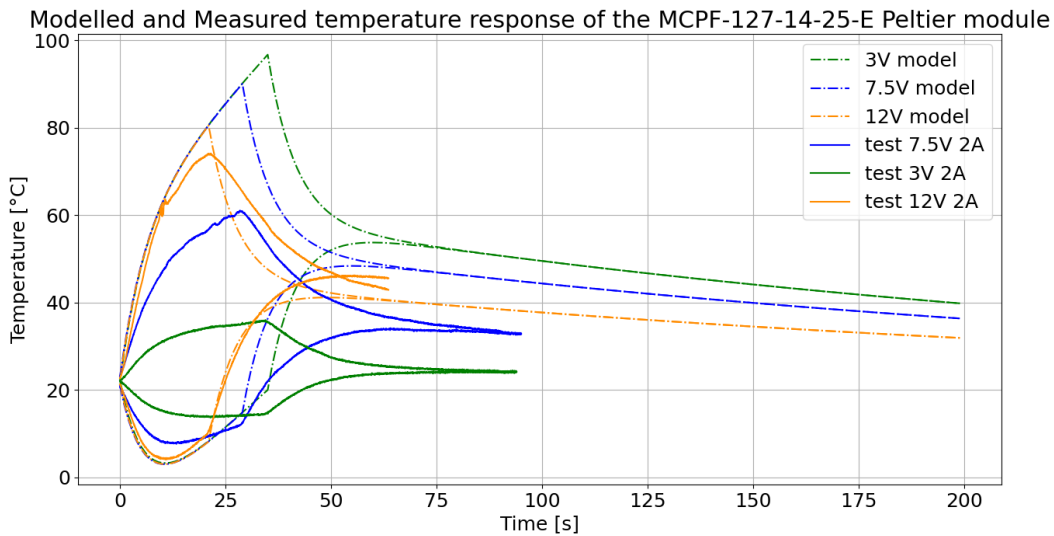


Figure C.2: Model with the estimated parameters as proposed by Zhaoxia Luo 2008 [5], compared to the measured temperature responses of 3, 7.5 and 12 V.

C.1.4. Effect applied voltage

The effect of the applied voltage can be added to the model with Equation C.6. In Figure C.3 the modelled voltage when 2 A is supplied to the Peltier module.



Figure C.3: Modelled voltage of MCPF-127-14-25-E module for a current of 2 A.

As shown in Figure C.3, the voltage exceeds the applied voltage for the run with 3 and 7.5 V. This voltage limit can be added to the model by calculating the current with Equation C.17.

$$I = (U_{input} - 2N\alpha_{pn}\Delta T)/R \quad (C.17)$$

This new current ensures the voltage over the Peltier module does not exceed the input voltage, U_{max} . When Equation C.17 exceeds the input current of 2 A, the current is set to this current, to ensure the current through the module does not exceed the current of the power supply. The modelled temperature responses with these power limits are shown in Figure C.4.

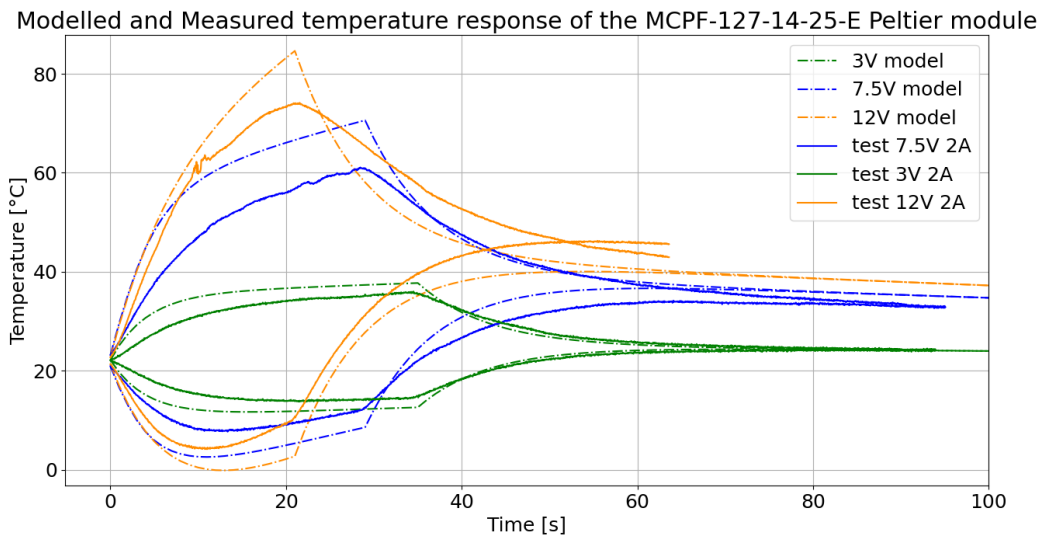


Figure C.4: Measured and modelled temperature response of the module with power limits of 3, 7.5 and 12 V and 2 A. ($h=18$)

As shown in Figure C.4, the model of the effect of the input voltage is successfully implemented, as the model provides a reasonable fit. The errors on the maximum hot side temperature are 1.77 K for 3V,

9.74 K for 7.5 V and 10.48 K for 12V. The minimum cold side temperature errors are 2.11 K for 3V, 5.15 K for 7.5 V and 4.29 K for 12 V. The errors are likely because the model describes an ideal module with the module parameters (α_{pn} , R and K) as constants.

C.1.5. Effect of temperature

In reality, α_{pn} , R and K depend on temperature. In semiconductors, the resistance decreases with increasing temperature, as more charge-carrying particles are created. This effect also decreases the Seebeck coefficient with increasing temperature as described by Equation 3.4. The thermal conductivity increases with increasing temperature [77]. However, as the thermal conductivity decreases with increasing temperature for the aluminium oxide (Al_2O_3) plates as shown in Figure C.5 [12], these changes in thermal conductivity are assumed to balance each other out. Furthermore, as these relations depend on the semiconductor material used in the Peltier module, which is not supplied by the manufacturer, the temperature dependence is not considered in the model.

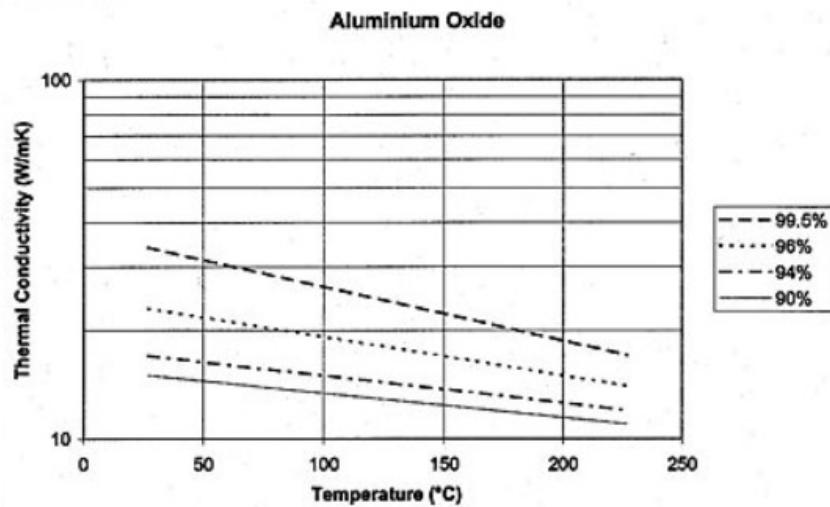


Figure C.5: Thermal conductivity of Al_2O_3 [12]

C.1.6. Heat dissipation to surrounding air

The heat from the Peltier module is assumed to first heat a pocket of air of 40 x 40 x 100 mm according to Equation C.18 [39] as shown in Figure C.6. The heated pocket of air radiates the heat to the ambient air according to the Stefan–Boltzmann law shown in Equation C.19.

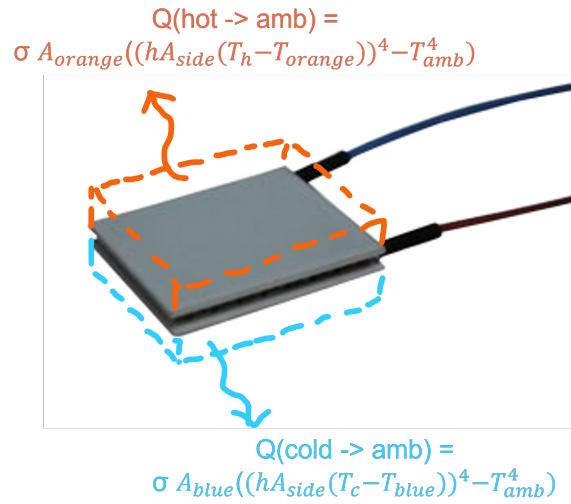


Figure C.6: Heat dissipation of the modelled Peltier module.

$$Q_{\text{airpocket}} = h A_{\text{peltier}} (T_h - T_{\text{airpocket}}) \tag{C.18}$$

Where A_{peltier} is the area of one side of the Peltier module, h is the convective heat transfer coefficient which is usually between 10 and 100 W/m^2K [20]. Figure C.7 shows the effect of h , where the lighter lines indicate a smaller coefficient. The smaller the coefficient the higher the temperature especially after the module is turned off. This is expected as the smaller the coefficient the smaller the heat transfer to the air and hence the module stays warmer for longer.

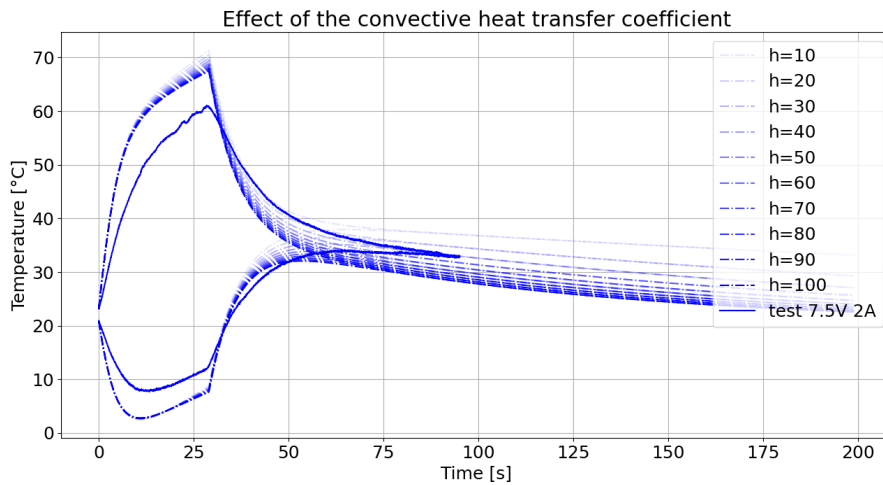


Figure C.7: Effect of the convective heat transfer coefficient.

$$Q = \sigma A_{\text{airpocket}} (T_{\text{airpocket}}^4 - T_{\text{amb}}^4) \tag{C.19}$$

Where σ is the Stefan–Boltzmann coefficient of $5.67e-8 W/m^2K^4$, $A_{\text{airpocket}}$ the area of the air-pocket touching the surrounding air and T_{amb} the ambient temperature of 20 °C.

C.1.7. Effect of heat flow between the sides of the Peltier module

Some heat is flowing from the air heated by the hot side to the cold side and vice versa. Adding this heat flow via the air, results in the temperature responses plotted in Figure C.8. Where the temperature response is modelled for 0 to 100 % of the heat of one side flowing to the other.

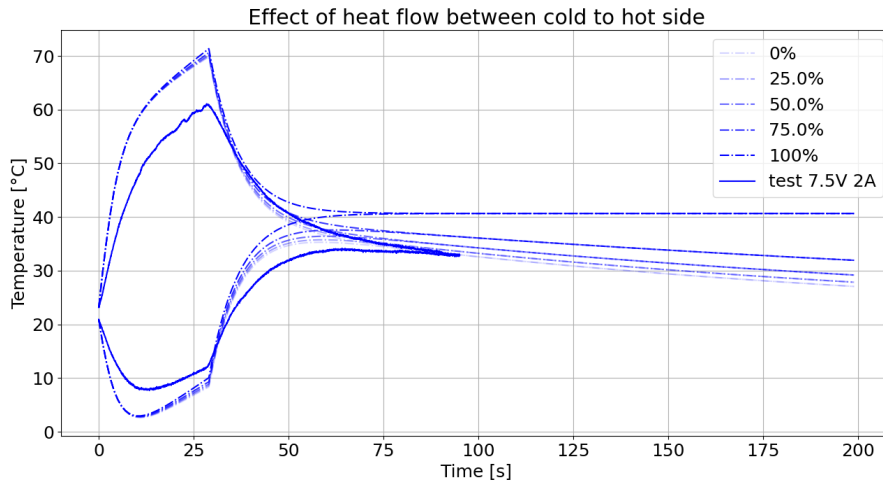


Figure C.8: Effect of heat flow through air on temperature response.

As shown the effect of this heat flow only becomes prominent after the Peltier module is turned off and not considering this effect gives the best fit. Measuring the temperature of a Peltier module insulated from the surrounding air with styrofoam with an HD thermal imaging FLIR camera as shown in Figure C.9 did not show any prominent heat flow through the air. Therefore, this effect is not considered in this model.

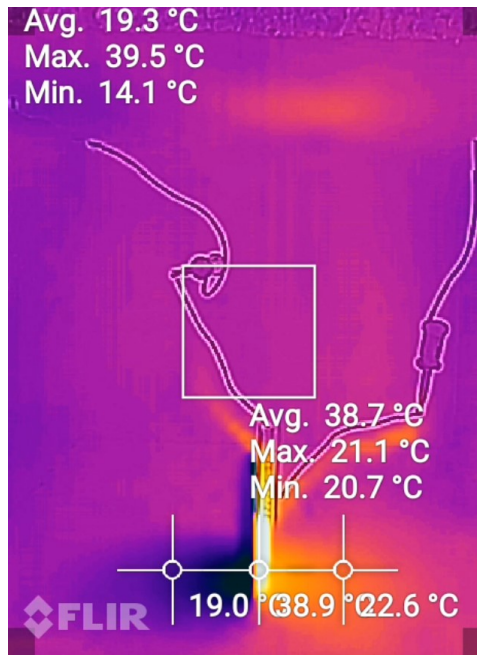


Figure C.9: Temperature around operating MCPF-127-14-25-E Peltier module measured with a FLIR camera. The temperature in this figure ranges from 14.1 to 39.5 °C indicated by dark purple to bright orange.

C.1.8. Effect wire resistance

As shown in Figure C.9 the wires lose heat, which shows these add resistance which could explain the lower calculated resistance. The resistance of the two 10 cm stranded tinned copper wires with a resistance of $94.2 \Omega/km^1$. This explains the observed heat losses by the wires as shown in Figure C.9 by the orange lines under the wires, captured with an infrared camera. Adding this resistance of 0.01884Ω to the model, resulted in the following improvement for errors on the hot side temperature: 1.70 K

¹<https://www.farnell.com/datasheets/2719479.pdf>, retrieved on 15-08-2023.

(was 1.77) for 3 V, 9.52 (was 9.74 K) for 7.5 V and 10.48 K (no improvement) for 12 V. The cold side temperature errors are 2.09 K (was 2.11) for 3V, 5.11 K (was 5.15) for 7.5 V and 4.29 K (no improvement) for 12 V. As shown including the effect of the wire losses slightly improves the model. As expected no improvements in the 12 V model were found, as the module does not use all the applied voltage for the run with 12 V as shown in Figure C.3.

C.1.9. Final model

To conclude the model a best fit is made with the convective heat transfer coefficient and the parameter reducing the ΔT_{max} . As mentioned before this model assumes an ideal module. However, in reality, the ΔT_{max} is often smaller than listed on the vendor datasheet. Reducing the least square error between the measurements and the model results in the final model shown in Figure C.10. The optimal fit was found for a ΔT_{max} of 90% of the ΔT_{max} mentioned in the vendor sheet (instead of 73 °C) and a convective heat transfer coefficient of 18.55 W/m²K. These parameters were found by the Limited-memory BFGS minimization of SciPy².

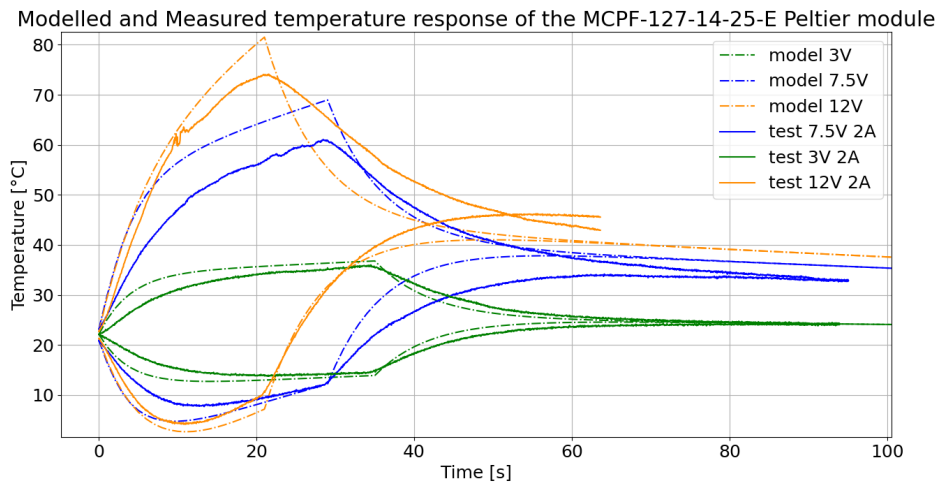


Figure C.10: Final model of the MCPF-127-14-25-E Peltier module for 3, 7.5 and 12 V and 2A.

As shown in Figure C.10, the model seems to overestimate the maximum temperatures and underestimate the minimum temperatures. Hence, the model overestimates the heat-pumping capacity of the module. This is due to the assumption that the Seebeck coefficient is constant as discussed in Section C.1.5, especially for the 7.5 V run. The errors on the hot side temperature are 0.78 K for 3V, 7.90 K for 7.5 V and 7.39 K for 12V. The cold side temperature errors are 1.04 K for 3V, 2.93 K for 7.5 V and 1.49 K for 12 V. As this model will be used to estimate the amount of PCM needed to adhere to ice, this model is accurate enough to provide a first order estimation.

In Figure C.11 the heat absorbed at the cold side of the Peltier module and the input power are modelled for the different power levels. The coefficient of performance (COP) of a Peltier module is described by Equation C.20 [77]. As shown in Figure C.11, the COP is larger than 1 for 8s with 3 V, 2.6 s with 7.5 V and 0.1 s with 12 V. When the temperature difference between the hot and cold side becomes significantly large, the heat flowing to the cold side is larger than the heat pumping. This results in a negative absorbed heat in Figure C.11 after 18.5 s for 3 V, 11 s for 7.5 V and 13 s for 12 V.

$$COP = \frac{Q_c}{W} = \frac{2N \cdot \alpha_{pn} \cdot I \cdot T_c - 0.5 \cdot I^2 \cdot R - K \cdot \Delta T}{I[2N \cdot \alpha_{pn} \cdot \Delta T + I \cdot R]} \quad (C.20)$$

²<https://docs.scipy.org/doc/scipy/reference/optimize.minimize-lbfgsb.html>, retrieved on 22-08-2023.

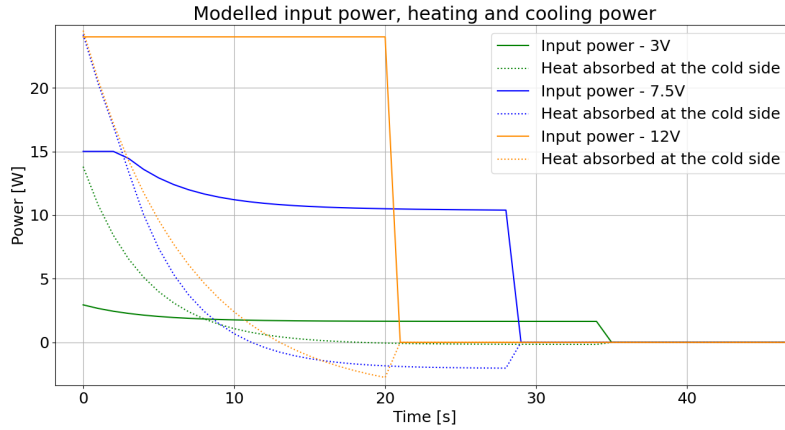


Figure C.11: Modelled heat absorbed at the cold side of the MCPF-127-14-25-E Peltier module and input voltage for 3V, 7.5 V and 12V.

This model is built with the estimation equations derived by Zhaoxia Luo 2008 [5]. This method ensures the developed model can be easily changed to describe a different module with the parameters provided by the developer. To create a more precise module the estimated physical characteristics should be measured as proposed by Huang et al. 2000 [34].

C.2. Model ice adhesion mechanism

Using the model developed in Section C.1, the temperature response of the ice adhesion mechanism designed in Section 4.3 can be modelled. First, the effect of the PCM container is modelled. Next, the temperature response of the adhesion pad is heated by the Peltier module. Finally, the sensible heat storage of water in the adhesion mechanism and the latent heat storage of coconut oil and octadecane are modelled. All measurements in this section are performed with the MCPF-127-14-25-E Peltier module and a power supply of 7.5 V and 2 A.

C.2.1. Model effect PCM container

To model the effect of the aluminium PCM container the mass and specific heat capacity of the container and the air inside of the container are added to the mass and specific heat of the hot side alumina plate. Using Equation C.14, the change in temperature of the container and the hot plate, dT_h , can be calculated as shown in Equation C.21. As the container and Peltier module are connected with the Due to the high thermal conductivity of 11.2 W/mK³ of the Prolimatech PK-3 thermal paste connecting the peltier and the container, the two temperatures can be assumed to be the same.

$$dT_h = \frac{Q_h - Q_{dissipation}}{c_{alumina} * m_{plate} + c_{alu} * V_{container} * \rho_{alu} + c_{air} * V_{air} * \rho_{air}} \quad (C.21)$$

Where, Q_h is the heat flow to the hot side as calculated by Equation C.22, $Q_{dissipation}$ the heat dissipating from the container to the surrounding air, $c_{alumina}$, c_{alu} & c_{air} are the specific heat coefficient for alumina (880 J/kgK [46]), aluminium (900 J/kgK [72]) and air (1006 J/kgK [71]), m_{plate} is the mass of the hot side plate and $V_{container}$ and V_{air} are the volume of the container (29.49 cm³) and the air inside the container (39.51 cm³).

$$Q_h = 2N\alpha_{pn}IT_c + 0.5 \cdot I^2R - K\Delta T \quad (C.22)$$

The heat is dissipated similarly as described in Section C.1.6 and can be calculated by Equation C.23.

$$Q_{dissipation} = h \cdot (A_{container} - A_{peltier}) \cdot (T_h - T_{ambh}) \quad (C.23)$$

³https://www.bol.com/nl/nl/p/prolimatech-pk-3-5g-heat-sink-compound-11-2-w-m-k/9200000034871734/?bltgh=tPAVIQuwtXy9XYqrteLCgw.2_22.26.ProductTitle, retrieved on 19-08-2023.

Where $A_{container}$ is the surface area of the container and T_{ambh} is the temperature of the heat pocket of 100 mm around the container.

This model does not consider a temperature gradient across the container. However, due to the high thermal conductivity of aluminium, the difference between the temperatures can be neglected [2]. Furthermore, the air in the container is assumed to be heated up together with the container, without modelling the heat transfer from the container to the air. This is justified by the large area of the aluminium in contact with the air due to the heat fins. A total area of 126.88 cm^2 is shown in green in Figure C.12.

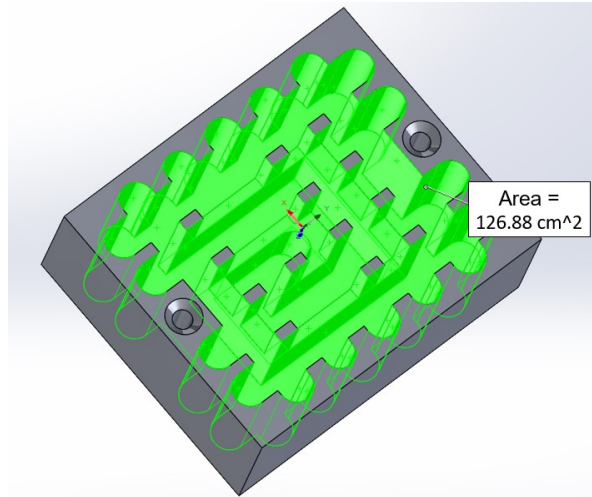


Figure C.12: Drawing of the PCM container showing the area inside the container in green.

In Figure C.13 the results of the measurements of the MCPF module with the empty container (green line) and the model (dashed line) described in this subsection are plotted.

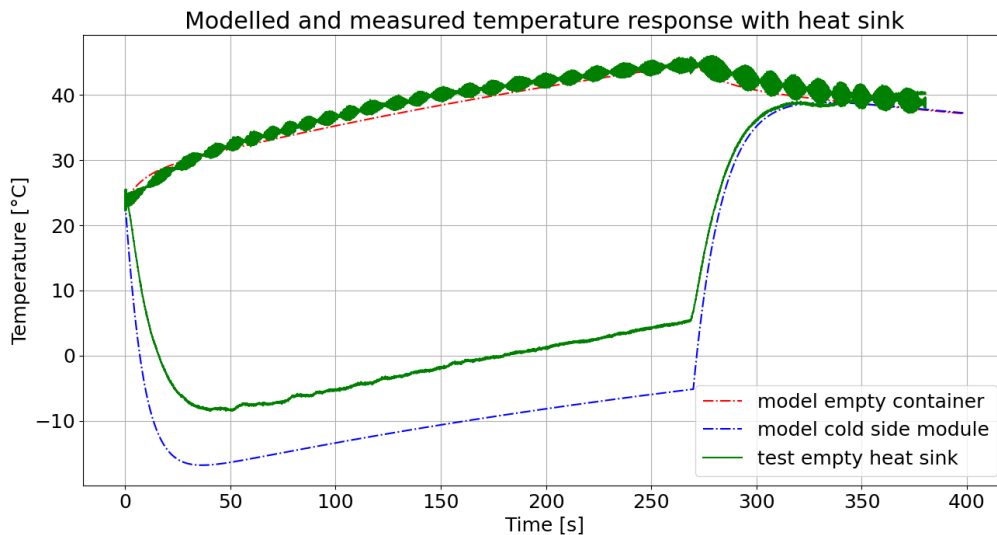


Figure C.13: Modelled and measured temperature response of the MCPF module with the empty aluminium container.

As shown in Figure C.13 this model provides a good fit, especially for the temperature of the container as shown by the red line. However, the temperature of the cold side is underestimated by the model as shown by the blue line. This model will be used to estimate the amount of PCM needed to create ice adhesion. Therefore, the cold side temperature must fit the experimental data well, as this temperature

must reach below zero to freeze the water to the adhesion pad. Hence, the model is fitted to the data by reducing the heat pumping capacity, calculated by $2N \cdot \alpha \cdot I \cdot T_c$. The best fit was found for a heat pump reduction of 20%. The resulting model is shown in Figure C.14. As shown this model provides a good fit for the temperature response of the Peltier module with the empty PCM container.

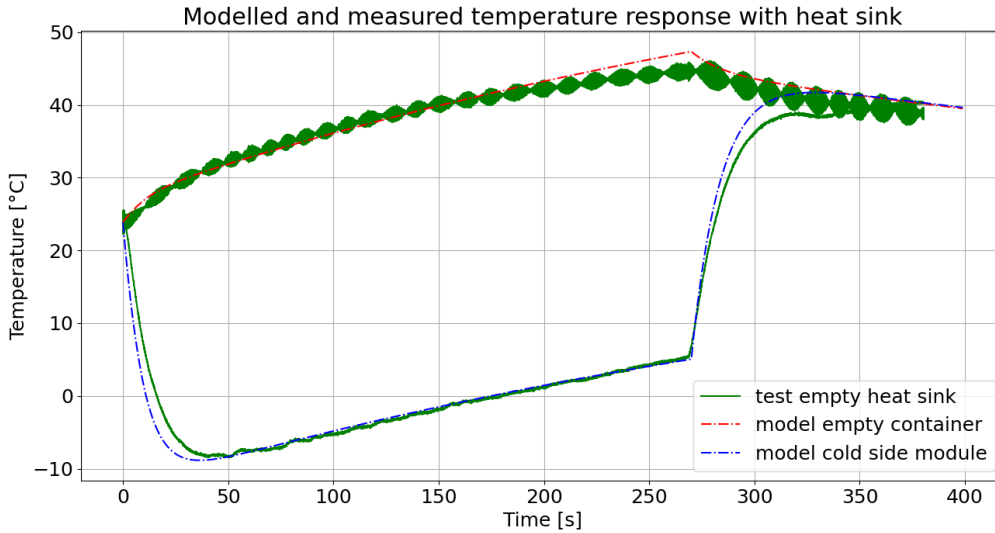


Figure C.14: Modelled temperature response of the MCPF module with a 20% reduced heat pumping power with the empty aluminium container compared to the measurements.

C.2.2. Model adhesion pad response

To model the temperature response of the ice adhesion pad, described in Section 4.4, the mass and specific heat coefficient of the pad are added to Equation C.14. Hence, using the same assumptions mentioned in Section C.2.2, the change in temperature of the adhesion pad and the cold side of the Peltier, dT_c , can be calculated with Equation C.24.

$$dT_c = \frac{-Q_c - Q_{disspad}}{c_{alumina} * m_{plate} + c_{alu} * V_{pad} * \rho_{alu}} \quad (C.24)$$

Where, Q_c is the heat pumping rate as calculated by Equation C.1, $Q_{disspad}$ the heat dissipation from the pad as shown in Equation C.25 and V_{pad} is the volume of the aluminium pad of 16 cm^3 .

$$Q_{disspad} = h \cdot (A_{pad} - A_{peltier}) \cdot (T_c - T_{ambc}) \quad (C.25)$$

Where A_{pad} is the area of the adhesion pad and T_{ambc} the temperature of the 100 mm pocket of air around the pad.

In Figure C.15, the modelled and measured temperature response of the Peltier module with the empty container and adhesion pad are shown. As shown the model fits the measurement results well, especially for the adhesion pad temperatures, which determine if ice adhesion is possible or not. The slight overestimation of the adhesion pad temperature will result in a more conservative estimate for the required PCM mass (more mass, less risk of no adhesion).

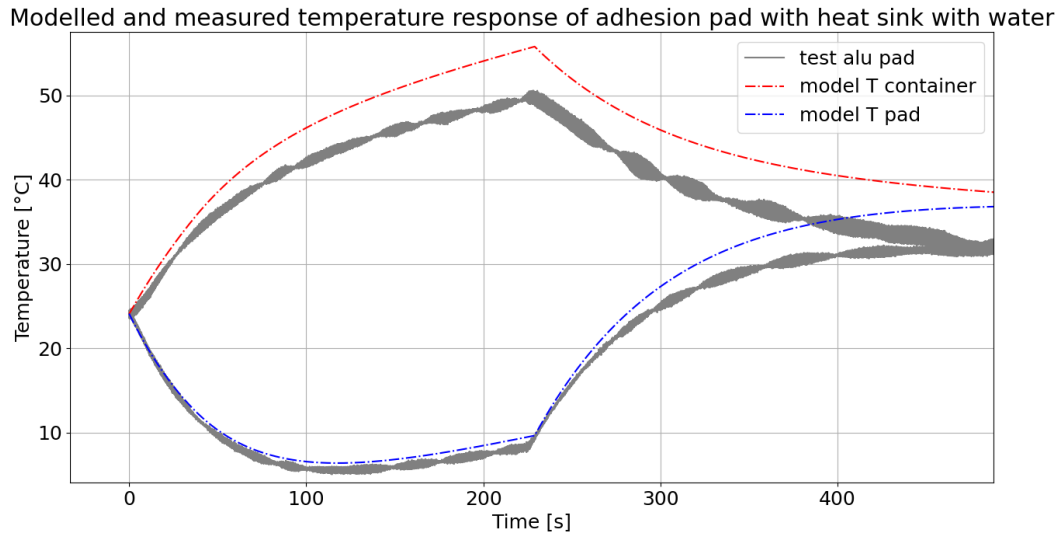


Figure C.15: Modelled and measured temperature response of the MCPF module with the aluminium adhesion pad and the empty container.

C.3. Conclusion and model limitations

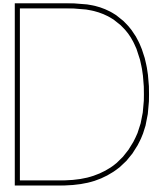
In this chapter, a theoretical model was built to estimate the effect of different PCMs, PCM containers and Peltier modules on the performance of the ice adhesion mechanism without performing tests. The model uses the method developed by Zhaoxia Luo 2008 [5] to estimate the temperature response of different Peltier modules, based on the I_{max} , U_{max} , ΔT_{max} provided by the manufacturer and the effect of the PCM container and adhesion pad was modelled. The model was fitted to and validated by the measurements done in Appendix E and Appendix D. The model was used to estimate the response of the TEC1-06308 module with a voltage of 4.35 V and the estimated required volume to obtain ice adhesion was 6.45 cm³ of octadecane. The integration of the PCM is described in Chapter 7.

The model of the TEC1-06308 with PCM cooling can be found in Appendix B and here:

<https://colab.research.google.com/drive/1TNSZa6nxz-4LL3EtUq4Gw15tNpZGsMis?usp=sharing>

To further improve the model the following limitations must be addressed:

- **Variable power function** The model can only estimate the behaviour of the PCM container for one power mode (power on and then off). Adding different power functions to the model (adding heating/cooling cycles or switching polarity), would allow for a better estimation of the behaviour of the link during operation and might influence the required PCM mass.
- **Temperature of the PCM** The model assumes the container with PCM as one mass that heats up. However, the PCM temperature remains constant around its melting temperature while melting. Hence, the container and the PCM temperature differ. Incorporation of this into the model will result in a more accurate description of the cooling effect of the PCM.
- **Solidification of PCM** The model does not consider solidification and assumes the PCM stays melted till the container cools to a temperature of less than the melting temperature. At this point, it instantaneously changes into a solid. In reality, the latent heat stored in the PCM will be released at this point.
- **Validation of the TEC1-06308 module model** The model of the TEC1-06308 uses the calibration parameters found for the MCPF-127-14-25-E module. The temperature response of TEC1-06308 must be measured, to calibrate the model to the measurements.
- **Model of ice** The model does not provide a definitive answer as to when ice adhesion will occur, as the ice is not included in the model. The temperature of the ice will influence the temperature of the adhesion pad and hence the adhesion itself. As shown by experiment 3 in Chapter 6 ice adhesion also occurs for a mechanism that does not reach subzero temperatures without the ice.



Phase Change Material Tests

To optimise the cooling mechanism of FLICK [76], the water cooling system should be replaced by a static solution as explained in Chapter 3. Phase change materials store the thermal energy from the heat source. This energy is released as the material cools. This means that the material can absorb the generated heat, which keeps the desired component cool. The question to be answered in this chapter is:

What is the optimal phase change material to absorb the energy from the adhesion mechanism?

In this chapter, solid-liquid PCMs and liquid-vapour PCMs are tested and the test results are analysed. Based on the analysis, a PCM is selected to use in the ice adhesion mechanism designed in Chapter 4. In Appendix A the short descriptions of the raw measurement files of the experiments performed in this chapter are listed.

D.1. Melting PCM experiments

Melting PCMs use their latent heat capacity of melting to absorb thermal energy. When the PCM melts the liquid part must be contained. The design process of this container is described in Section 4.3. In this section, the tests with GCS-104-PCM, coconut oil, paraffin wax and octadecane are described and analysed.

D.1.1. GCS-104-PCM

GCS-104-PCM is a thermal interface material. A thermal interface material is used to make heat transfer between components more effective by increasing contact between surfaces by filling the air gaps. The GCS-104-PCM uses phase change to absorb thermal energy and is thereby also a PCM.

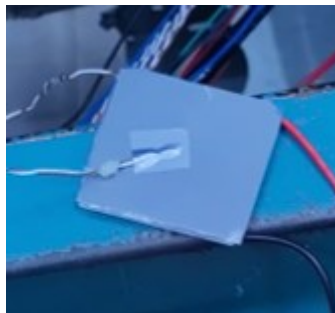


Figure D.1: Peltier module with GCS-104-PCM with a thermocouple measuring the temperature.

Experiment GCS-1

The first test was done with a thermal interface material GCS-104-PCM. The control or normal Peltier module response was compared with a Peltier covered with 0.12 mm GCS-104-PCM¹ on the hot side

¹<https://docs.rs-online.com/0784/0900766b81588592.pdf>, retrieved on June 2nd 2023

as shown in Figure D.1.

The latent heat capacity of this material is between 200 to 280 J/g (personal communication GCS Thermal, 2-6-2023). The comparison of the temperature response of the TEC1-12706 module with and with PCM is shown in Figure D.2.

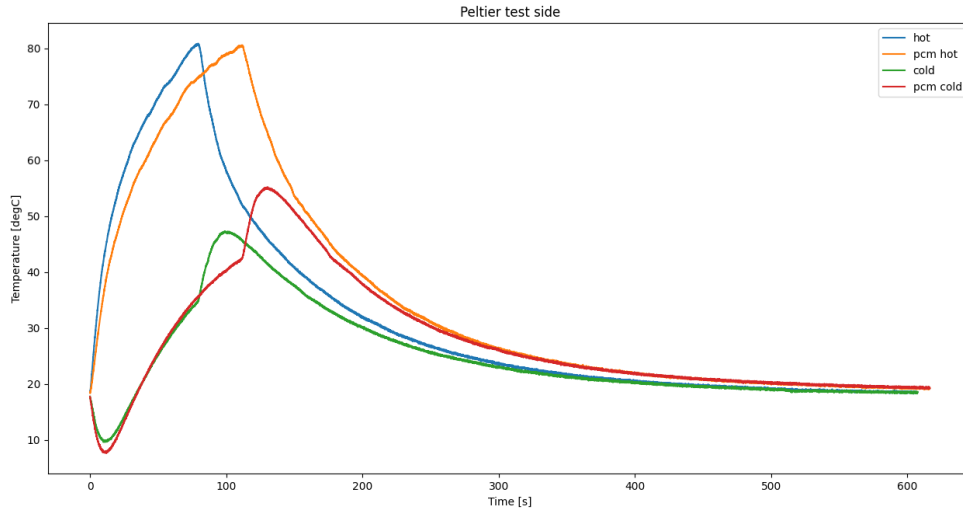


Figure D.2: Temperature response of the hot and cold side of the TEC1-12706 of KIWI electronics with and without GCS-104-PCM. Power supply: 2A, 7.5V

The Peltier was turned on till the hot side reached 80°C. As shown in Figure D.2 after the Peltier is turned off the hot side drops in temperature and the cold side first rises in temperature before it starts decreasing as well. The control (blue line in Figure D.2) reached 80.8°C after 79.6 s and the Peltier module with the PCM (orange line in Figure D.2) reached 80.6°C after 111.7 s. The cold side of the Peltier reached a minimum temperature of 9.6 °C without (green line in Figure D.2) and 7.6 °C with PCM (red line in Figure D.2). As expected due to the absorption of energy of the PCM changing phase, the application of the PCM resulted in a lower minimum temperature and it took longer for the hot side to heat up. However, due to the small volume of 224 mm³ of PCM, the hot side is not kept at a constant temperature as the PCM can absorb a limited amount of energy. The melting temperature of GCS-104-PCM is between 50 and 55 °C, hence the cold side could in the ideal circumstances reach subzero temperatures as the maximum temperature difference of the TEC1-12706 is 68 °C. However, due to the small thickness of the material, it cannot absorb a lot of heat energy and the hot side quickly exceeds this temperature and no plateau can be seen at the melting temperature of the PCM in Figure D.2.

Experiment GCS-2

By stacking the available GCS-104-PCM material, a thickness of 1.2 mm could be achieved (resulting in a volume of 1.92 cm³) and tested resulting in the results shown in Figure D.3. As shown a slight decrease in temperature was achieved with the PCM. However, not significant due to the small thickness of the PCM material and hence little absorbed heat.

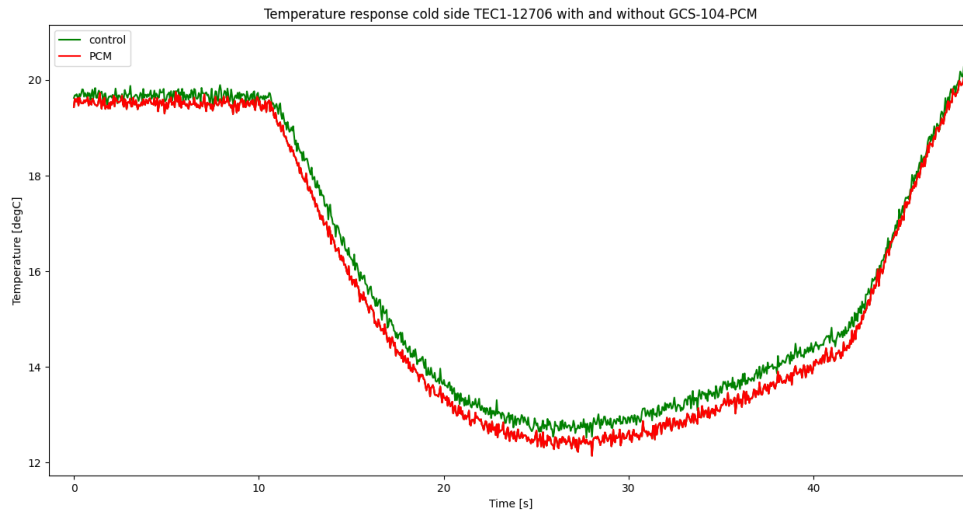


Figure D.3: Temperature response of the cold side of the TEC1-12706 of KIWI electronics with and without GCS-104-PCM with a thickness of 1.2 mm. Power supply: 2A, 7.5V

D.1.2. Coconut oil

Next to the GCS-104-PCM, coconut oil was tested as a possible PCM. The latent heat capacity of coconut oil is 105 J/g and the melting point is 24 °C [37].

Experiment Coco-1

The first test was performed as follows: 13 g of coconut oil was placed in a container made from duck tape on top of the Peltier module as shown in Figure D.4. To measure the temperature response, 2 thermocouples were placed on the cold side of the Peltier module.

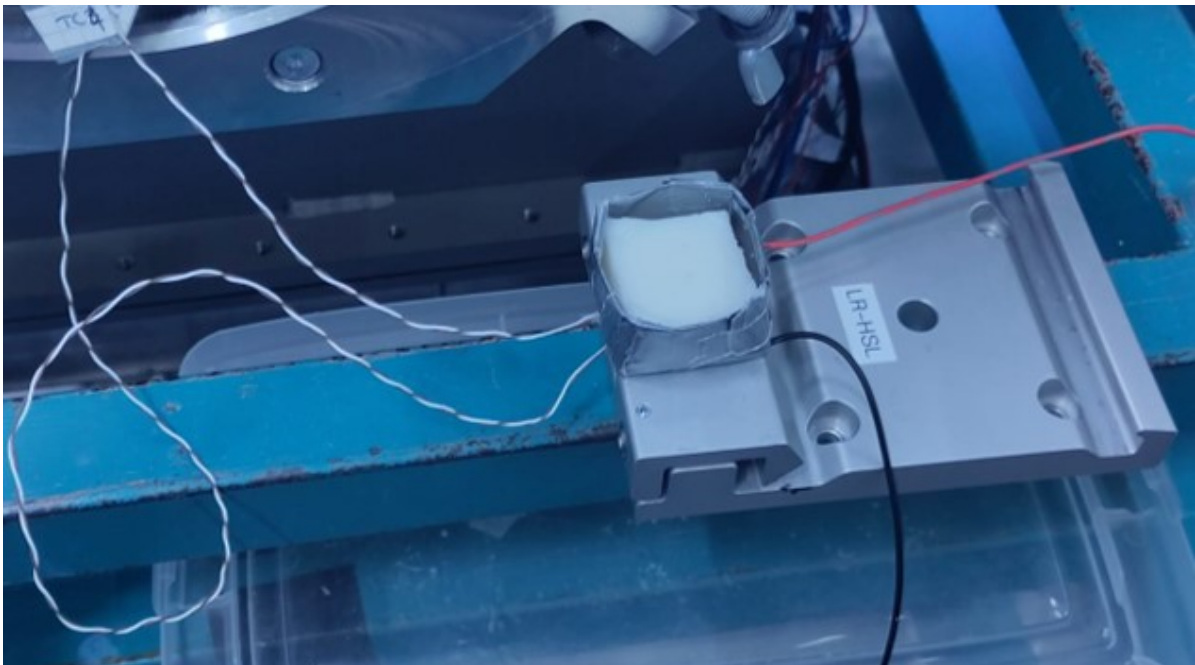


Figure D.4: Setup with 13 g coconut oil as PCM.

Comparing the temperature response of the cold side of the Peltier module with and without coconut oil

results in Figure D.5. As expected the cold side with the coconut oil PCM reaches lower temperatures as energy gets absorbed on the hot side. During this first test, the oil melted out of the setup after 150 seconds and therefore the peltier was turned off as shown by the steep increase in Figure D.5. As shown in Figure D.6 the hot side of the Peltier module reaches the melting point of coconut oil after 3 seconds, after which it slows down the heating rate resulting in a lower minimum temperature compared to the naked Peltier module. Furthermore, no plateau is observed in the measured temperature response in Figure D.5, which is expected due to the latent heat storage when the coconut oil starts melting. However, due to the low latent heat capacity (105 J/g) and boiling point ($24 \text{ }^\circ\text{C}$), the coconut oil melts fast. Hence, the cooling effect shows a lower minimum temperature and heating rate compared to the Peltier module without PCM cooling, but no maintained cold temperature.

Due to the promising cooling results and harmless nature of coconut oil, multiple cooling configurations were tested with this oil, as described in Section 4.3, to design the PCM container.

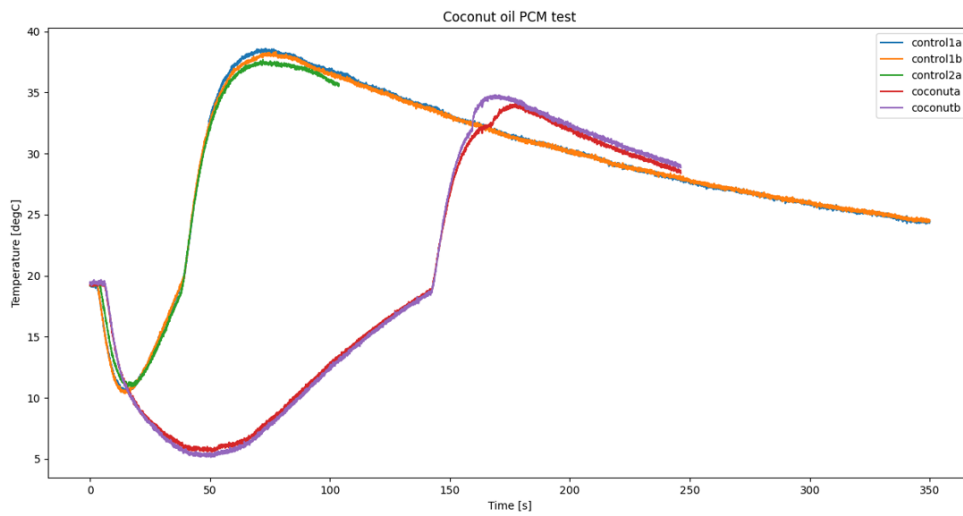


Figure D.5: Temperature response of the Peltier cold side with and without coconut oil PCM.

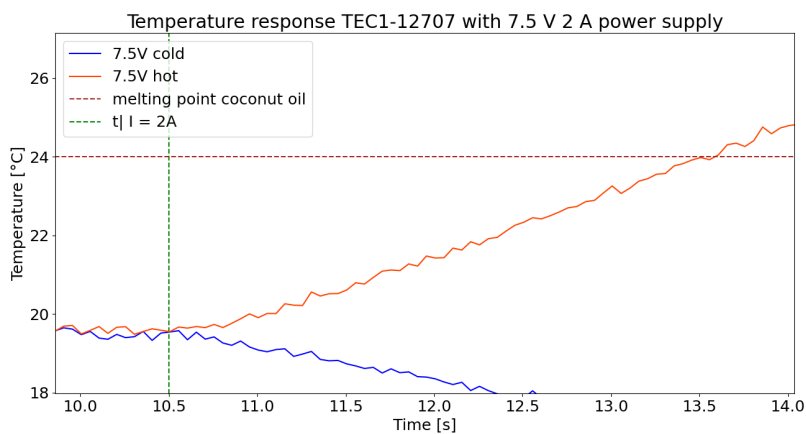


Figure D.6: Temperature between the start of operation for the Peltier module and the melting temperature of the coconut oil.

Experiment Coco-final

Using the aluminium PCM holder, shown in Figure D.7, as designed in Section 4.3 with the MCPF-127-14-25-E module, subzero temperatures of the 1 cm aluminium adhesion pad (see Section 4.4) could be reached with coconut oil as shown in Figure D.8.

Where the top lines show the temperature of the aluminium holder and the bottom lines the temperature of the adhesion pad. The container ensures proper contact with the PCM, by transferring the heat inside the PCM with aluminium fins (see Figure D.7 and Section 4.3) and can hold 34 g of coconut oil.

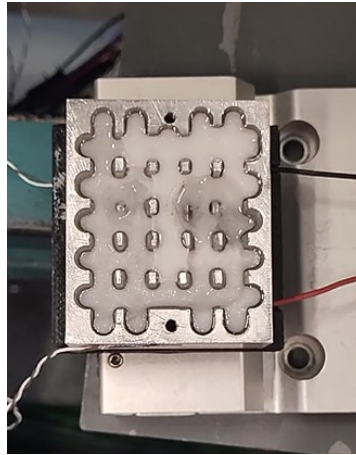


Figure D.7: Test setup with the aluminium container with 34 g coconut oil.

As shown by the orange lines in Figure D.8, the adhesion mechanism cooled by coconut oil reaches subzero temperature with the new container. The results in blue show the test with cooled coconut oil in the freezer, which gives the lowest temperatures. The test in red shows the temperature response with melted coconut oil, which performed similarly to the empty container. This can be explained by the fact that the melted oil cannot store energy by latent heat storage and thereby rises in temperature according to its specific heat capacity. As the test with coconut oil obtained subzero temperatures, this PCM can be used to create ice adhesion.

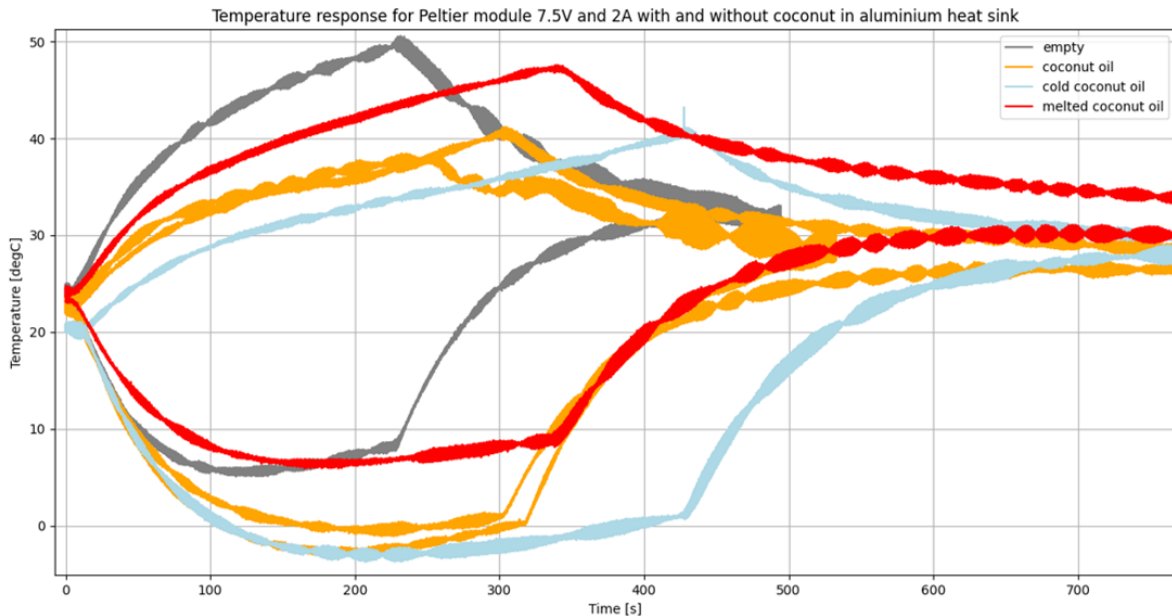


Figure D.8: Temperature response MCPF-127-14-25-E with 34 g coconut oil PCM.

D.1.3. Paraffin wax

Next to the GCS-104-PCM and coconut oil, a low-grade paraffin wax was tested as a possible PCM. The latent heat capacity of paraffin wax is 176 J/g [3] and has a melting point of 54 °C.

Experiment Para-1

The first test is shown in Figure D.9. Where the 13.7 g of paraffin wax was taped to the top of the TEC1-12706 Peltier module.

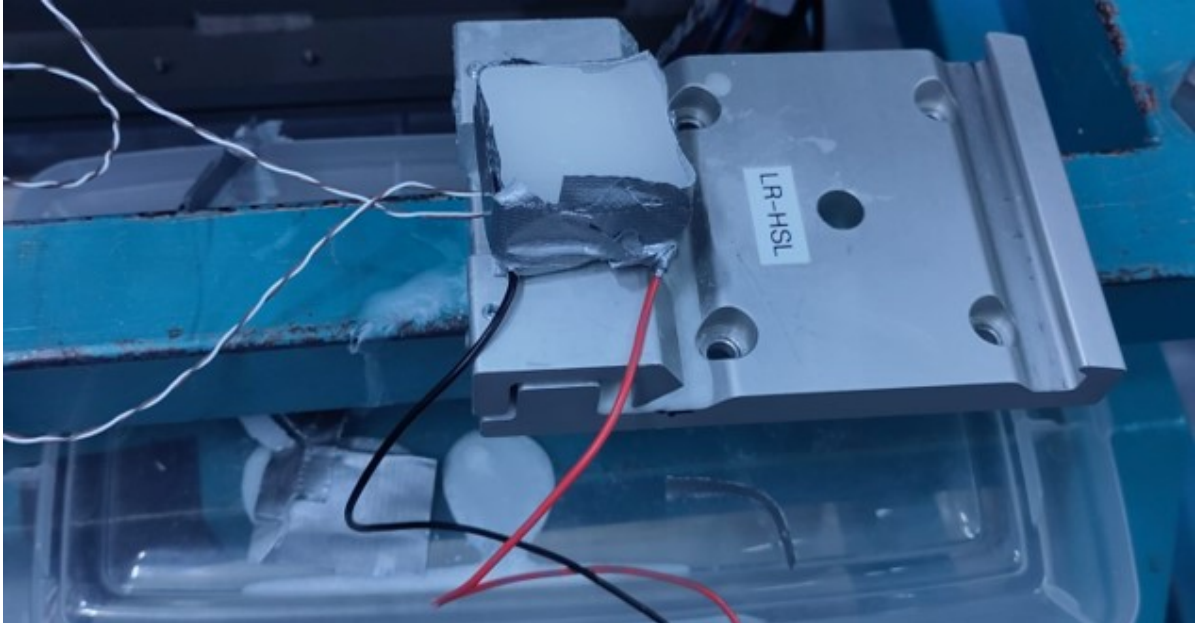


Figure D.9: Setup with 13.7 g paraffin wax as PCM.

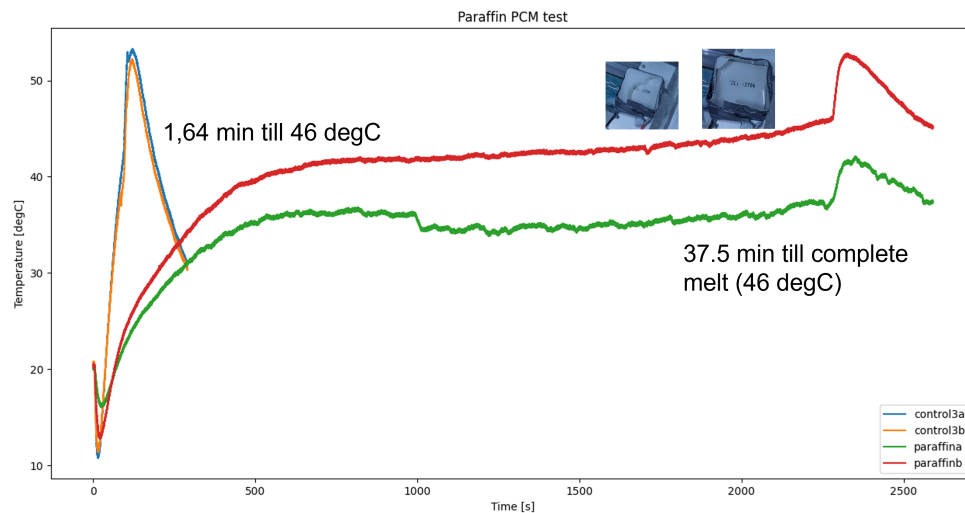


Figure D.10: Temperature response of the TEC1-12706 Peltier cold side with and without paraffin wax PCM.

The comparison with and without this PCM is shown in Figure D.10. Here, the minimum temperatures are higher with the PCM than without it, due to the higher melting point of paraffin wax. As shown in Figure D.11 the time between the activation of the TEC1-12706 module and when the module reaches

the melting point of the paraffin wax is around 20 seconds after the module is turned on (start at 7 s). This results in a higher heating rate, as the heat can dissipate slower through the wax than through air, and therefore higher minimum temperatures. However, when the top side reaches the melting point of the paraffin wax most of the energy gets used to melt the wax instead of increasing the temperature of the system. This effect is visible by the constant temperature of the cold side after 500 s.

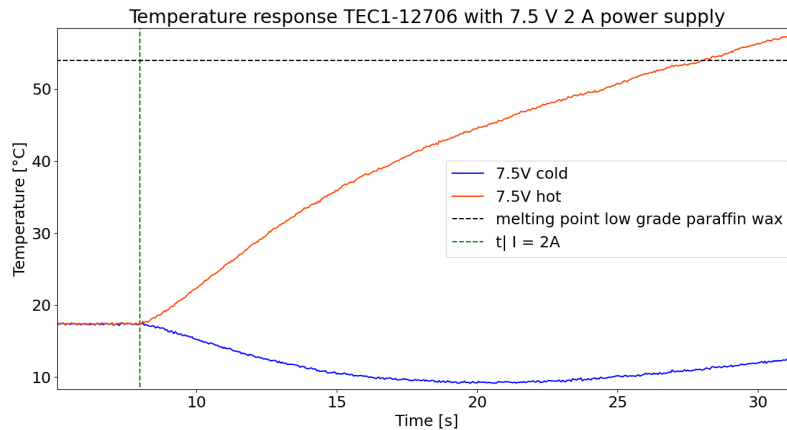


Figure D.11: Temperature between the start of operation for the TEC1-12706 Peltier module and the melting temperature of the paraffin wax.

The wax melted as shown in the top right corner of Figure D.10 and was completely melted after 37.5 min. This shows that the concept of using a PCM works to maintain a constant temperature on the cold side. However, a PCM with a lower melting point must be chosen to maintain a constant subzero temperature.

D.1.4. PCM selection - Octadecane

In this subsection, the test results of GCS-104-PCM, coconut oil and paraffin wax are analysed and the selection of the PCM for this project is described. Finally, the performance of the selected Octadecane is tested and described.

Analysis

To select the PCM to use in FLICK 2.0, the selection criteria that followed from the previously described test with GCS-104-PCM, coconut oil and paraffin wax were used. The performance of all the TEC1-12706 tests without adhesion pad are shown in Figure D.12.

In this figure, the minimum temperature of the cold side, the start temperature and the difference between these two temperatures are plotted. Here, the correlation between the minimum temperature and the maximum temperature difference on the cold side is shown by the diagonal in the corresponding plot. This is expected as the test with more effective cooling will cool to lower temperatures, thereby creating the biggest difference between the start and minimum temperature.

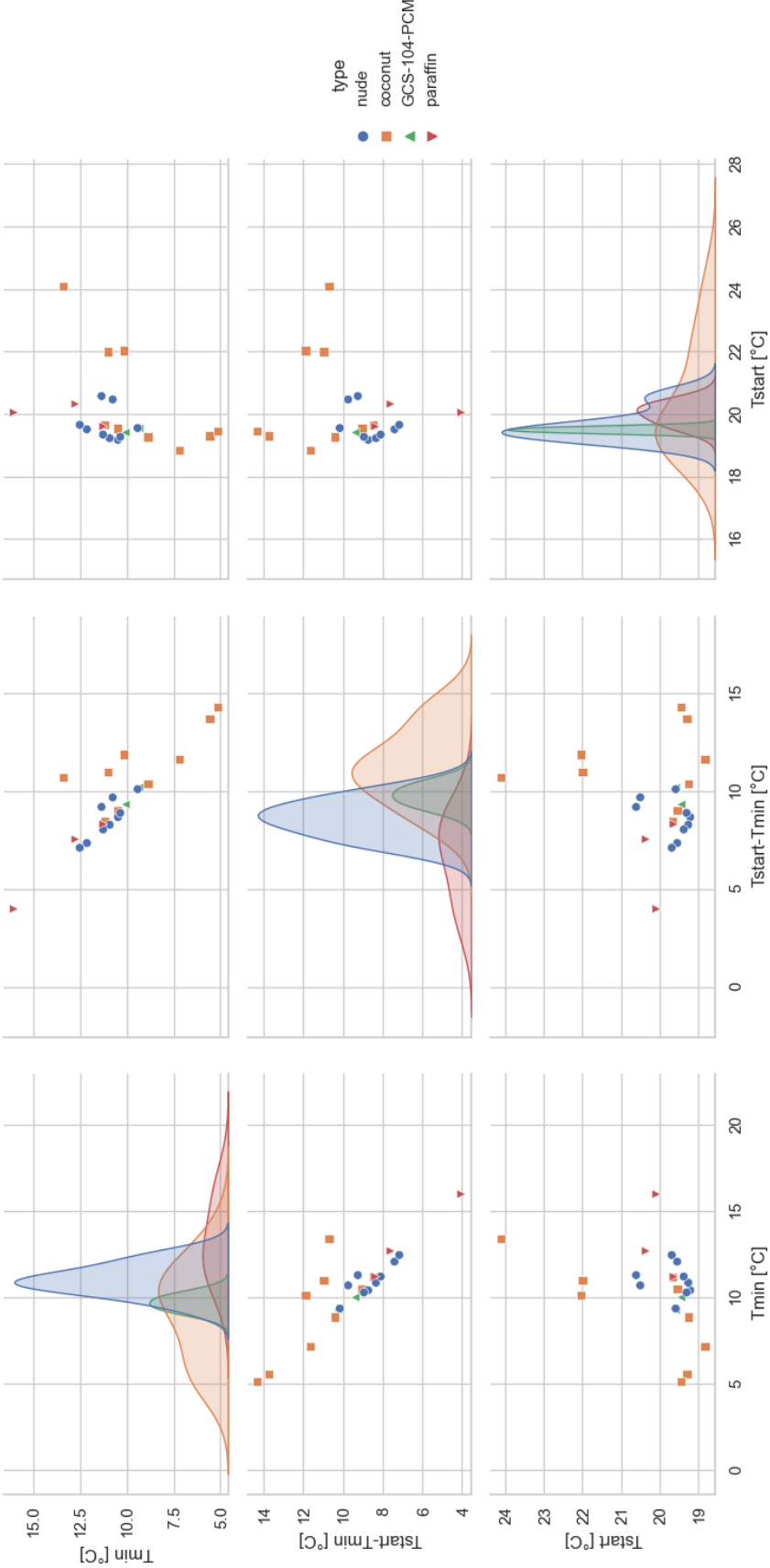


Figure D.12: Correlation between the start and minimum temperature of the cold side of the TEC1-12706 7.5 V 2 A, the hot side was cooled by various solid-liquid PCMs.

As shown by the plots the starting temperature does not have a clear correlation with the two chosen performance parameters, which justifies comparing the PCM cooling by these parameters. The distribution plot of the minimum temperature in the top left corner shows the coconut oil reaches the lowest temperatures and the paraffin wax the highest. The centre distribution plot of the temperature difference shows the coconut oil reaches the largest difference and the paraffin wax the smallest. In both plots, the GCS PCM performs in the upper-performance range of the naked Peltier.

The performance of a PCM depends on the latent heat capacity as well as the amount of PCM available. The available latent energy is added to the performance graphs of the tested solid-liquid PCMs in Figure D.13 (middle left graph in Figure D.12), where the energy ranges from blue (low) to yellow (high). The dotted lines indicate the mean minimum temperature and temperature difference for all measurements. The closer the data points are to the top left corner the better the performance.

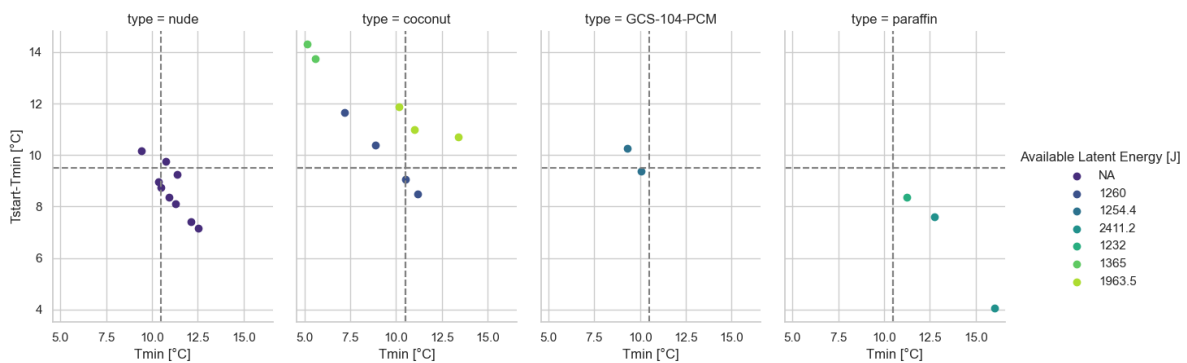


Figure D.13: Performance of PCM cooling of TEC1-12706 for 7.5 V 2 A power supply and different PCM types.

Figure D.13 shows the coconut oil results in the best cooling and the paraffin was in the worst cooling. This is expected as the boiling point of coconut oil is around 24 °C compared to 54 °C. Hence, a PCM should be selected with a boiling point between 20 and 30 °C as proposed in Chapter 3.

The GCS-104-PCM has a boiling point between 50-55 °C but shows better performance than the paraffin wax. This can be explained by the thermal conductivity of the PCM. The higher the thermal conductivity the lower the temperature of the hot side of the Peltier module as described by Equation 4.10. As the thermal conductivity of the GCS PCM is 4 W/mK compared to 0.21 W/mK for paraffin wax, this explains the observed results. Hence, the thermal conductivity of the PCM should be large.

As described by Figure 4.14 the melting velocity of the PCM and hence the hot side temperature is influenced by the density and the latent heat capacity of the PCM. The more mass and higher the latent heat capacity the slower the PCM will melt, and the lower the temperature of the Peltier module's hot side and hence the cold side. However, as this cooling mechanism is developed for an icy moon exploration robot, the mass must be as low as possible. The mass of space mission probes must be minimised, to reduce the cost of launching the mission into space. Therefore, a PCM must be selected with a large latent heat capacity and a low density.

Figure D.14 show the stored energy of water and coconut oil over the temperature range between 0 and 50 °C. As shown the latent heat storage of coconut oil only outperforms the sensible heat storage of water for a small temperature range. This is due to the high specific heat capacity of water. Hence, the specific heat capacity of the PCM must be high as this determines how much heat can be absorbed before the point of phase change.

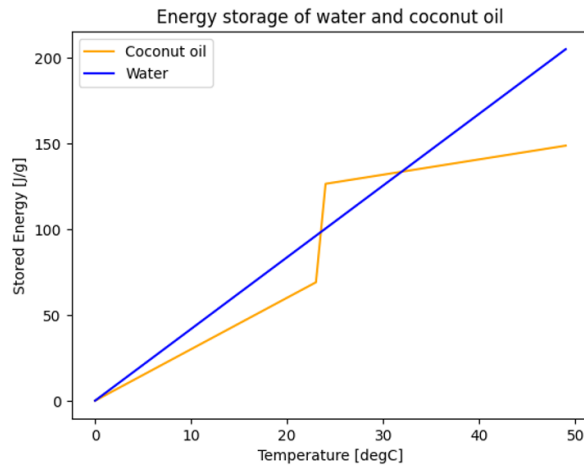


Figure D.14: Comparison of stored energy by liquid water and coconut oil between 0 and 50 °C

PCM selection

The considered PCMs are listed in Table D.1 and octadecane was found to be the best option for this project because it had the highest latent heat capacity of the PCMs with a melting temperature between 20 and 30 °C and the lowest density of all considered PCMs in Table D.1. Octadecane (CH₃(CH₂)₁₆CH₃) is a paraffin wax with a melting temperature of 28 °C and a latent heat capacity of 237 J/g [22]. Octadecane is comparable to the commercially available HS24 PCM, which has a lower melting point and might be less toxic. However, as octadecane outperforms HS24 PCM for most selection criteria, and is more easily available, it was chosen as the PCM for this research.

As shown in Figure D.15 the time between the activation of the MCPF-127-14-25-E module and when the module reaches the melting point of octadecane is around 2.5 seconds. This together with the high latent heat capacity makes this material a good fit to use in the PCM cooling mechanism.

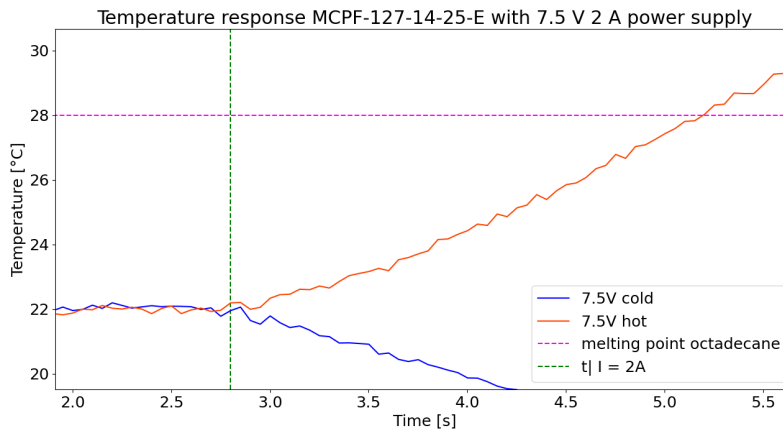


Figure D.15: Temperature between the start of operation for the MCPF-127-14-25-E Peltier module and the melting temperature of octadecane.

Experiment Oct-1

In Figure D.16 the temperature response of the MCPF-127-14-25-E with 25 g of Octadecane as PCM is compared to the empty container and the container filled with water. The bottom lines show the temperature of the adhesion pad and the top lines show the temperature of the wall of the container. As shown the use of octadecane as PCM results in lower temperatures that are sustained for longer. A minimum temperature of -7.71 °C of the adhesion pad and sustained subzero cooling for 10 minutes and 15 seconds was obtained. These results show that the latent heat storage of octadecane outperforms the sensible heat storage of water and is therefore a good choice to use in the adhesion mechanism

Table D.1: Properties of PCMs with a melting point between 17 and 33 °C.

PCM Type	T _{melt} [degC]	Latent heat capacity [kJ/kg]	Specific heat capacity [kJ/kgK]	Thermal Conductivity [W/mK]	Density [kg/m ³]	Corrive/ Toxic	Price (on Merck)
Coconut oil [18] [37]	24	105	2.7	0.165	900	no/no	80.70 EU/kg
Octadecane [22]	28	237	1.8 solid 2.3 liquid	0.335	868	no/ irritating to eyes, respiratory system and skin	76.60 EU/100 g
Lauric acid/ Methyl Palmitrate (40:60) [60]	25.6	205.4	1.5	0.1802	888	no/ yes no/ toxic to fish	LA: 29.20 EU/100g MP: 62.50 EU/100g
Glycerol [51]	17.8	200	2.43	0.285	1261	no/no	43.90 EU/100ml
Potassium Fluoride Tetrahydrate [30]	18.7	200-246	1.5 solid 2.47 liquid	0.49	1440	yes/yes [74]	NA
Calcium Chloride Hexahydrate [30]	29	140-172	2.78 [80]	3.359 [80]	1567	no/irritating to eyes	31 EU/kg
HS24 PCM [56]	24	218	2.07 solid 2.42 liquid	1.05 solid 0.55 liquid	1621 solid 1510 liquid	no/no	NA

of the ice climbing robot at room temperature.

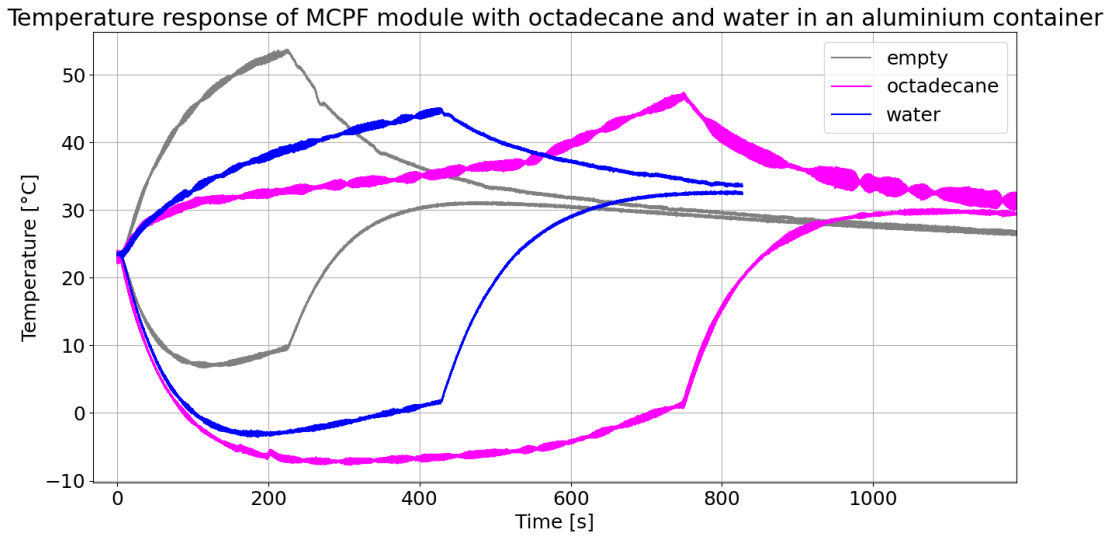


Figure D.16: Temperature response of the MCPF-127-14-25-E with Octadecane compared to water and the empty container, supplied power: 7.5 V and 2 A.

D.2. Vaporising PCM experiments

As the latent heat of evaporation is generally higher than the latent heat of melting, this could be an option to cool the Peltier module as described in Section 3.4. In this section, the results of the cooling performance tests of acetone and the NOVEC7000 engineering fluid are described.

D.2.1. Acetone

The first liquid to be tested was acetone. Acetone has a boiling point of 56 °C and a latent heat of evaporation of 534 kJ/kg.

Experiment Ac-1

The first test was performed by applying acetone directly, resulting in cooling of the hot side as shown in Figure D.17 and lower temperatures on the cold side as shown in Figure D.18.

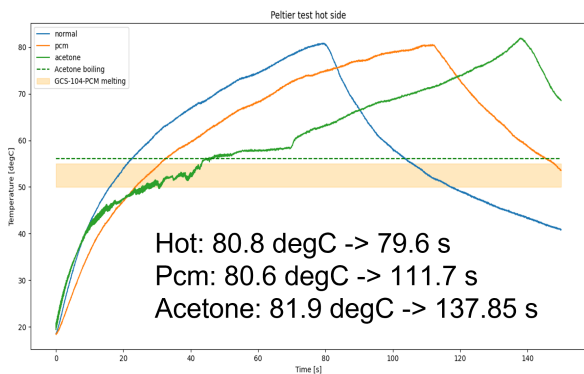


Figure D.17: Temperature over time of TEC1-12706 peltier hot side, with acetone and GCS-104-PCM.

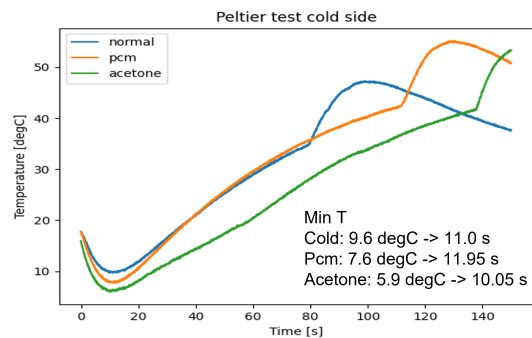


Figure D.18: Temperature over time of TEC1-12706 peltier cold side, with acetone and GCS-104-PCM.

Experiment Ac-2

Due to these promising results a balloon containing 40 ml of acetone was connected to the Peltier module with glue as shown in Figure D.19. This balloon is needed to contain the vapour as the acetone

evaporates. Due to the volume change of the acetone the balloon inflates as shown in Figure D.19. The temperature response of the cold side of the Peltier module with acetone as PCM is shown in Figure D.20 in green. It shows the temperature only rises 3 °C in 200 s due to the high latent heat capacity of acetone. Zooming in gives Figure D.21 which shows the minimum temperature obtained with acetone as PCM is similar to for the coconut oil. However, as the initial temperature of the test with acetone was higher, it outperformed the coconut oil.

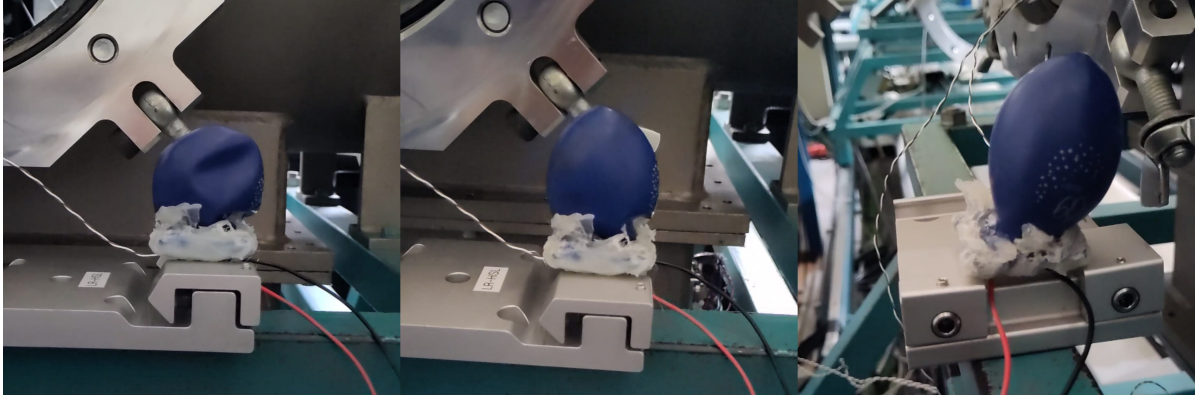


Figure D.19: Balloon with acetone heated by TEC1-12706.

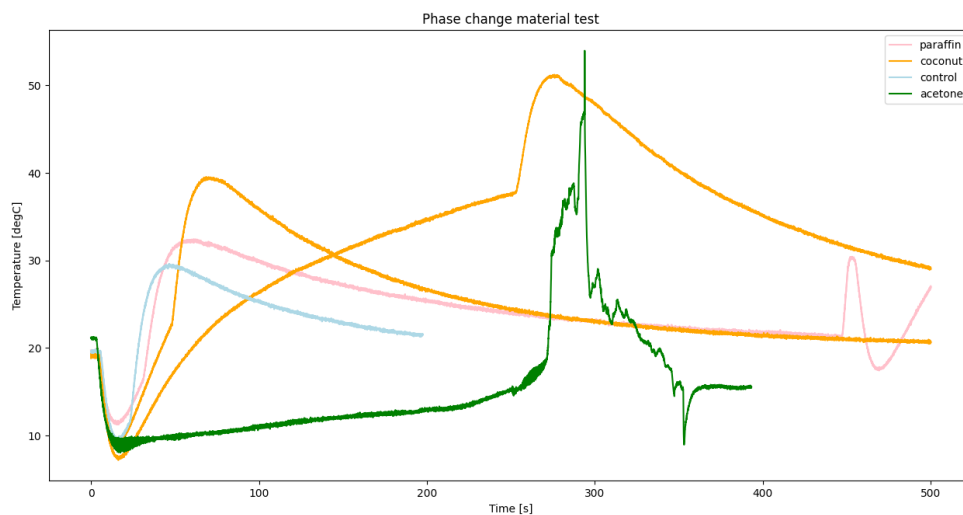


Figure D.20: Cold side temperature response of TEC1-12706 for different PCMs.

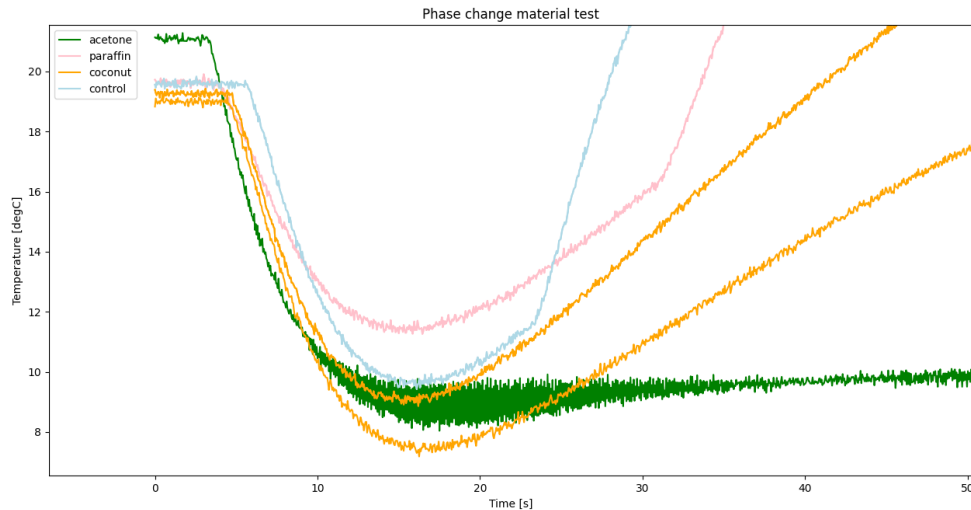


Figure D.21: Minimum temperature of TEC1-12706 for different PCMs.

However, due to the corrosive nature of acetone, the glue degraded and the setup started to leak.

Experiment Ac-3

The setup was redesigned by 3D printing a container from PETG which will only be slightly attacked by acetone but performs well enough for these experiments. Adding 40 ml of acetone to the setup shown in Figure D.22 and testing the temperature response of the cold side of the QC-127-1.4-6.0A Peltier module for 7.5, 9 and 12 V and a current of 2 A, resulted in Figure D.24.

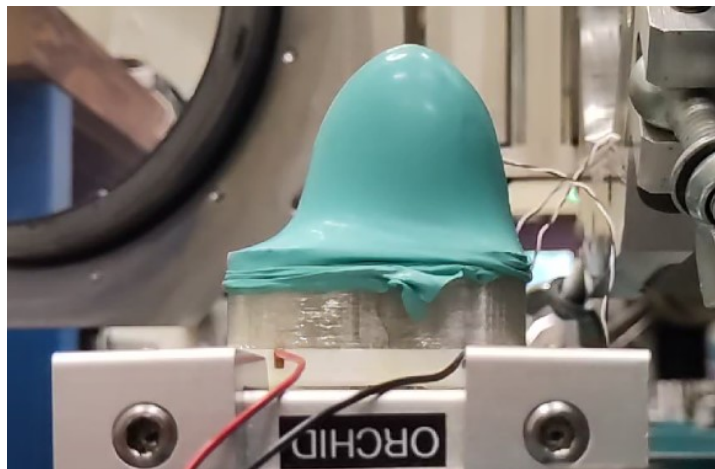


Figure D.22: Balloon with acetone holder heated by QC-127-1.4-6.0A.

As shown in Figure D.23 the QC-127-1.4-6.0A module reaches the boiling temperature of acetone after 17 seconds. After, this the hot side is cooled by latent heat storage and the heating rate of the cold side is decreased.

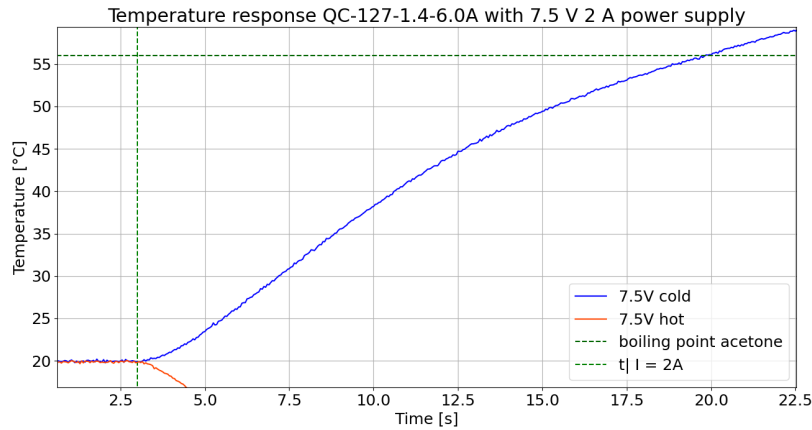


Figure D.23: Temperature between the start of operation for the QC-127-1.4-6.0A Peltier module and the boiling temperature of acetone.

As expected the test shown in Figure D.24 with acetone reaches lower minimum temperatures, than the Peltier module alone. The higher voltages result in higher minimum temperatures due to the extra heat that is produced when more power is supplied to the module.

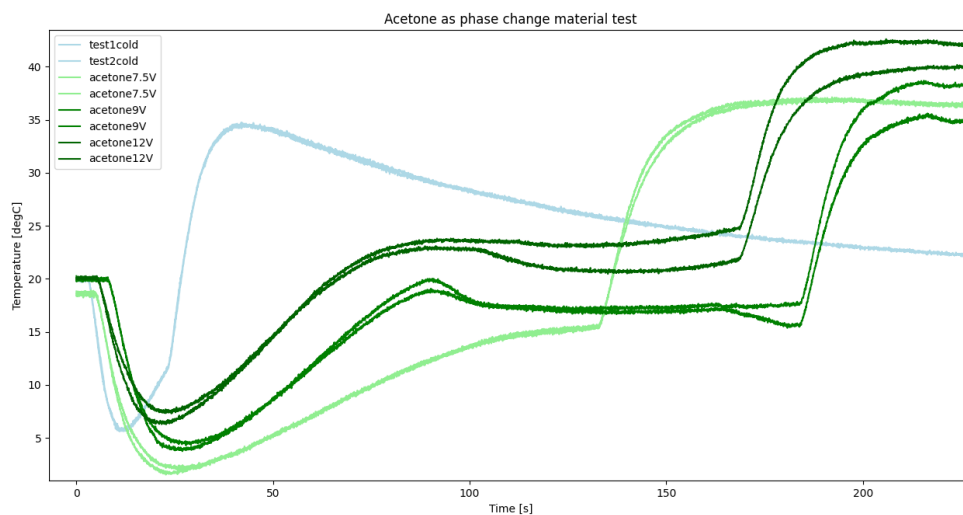


Figure D.24: Cold side temperature response of QC-127-1.4-6.0A with acetone for different voltages.

Figure D.24 clearly shows the working principle of the PCM. As the top side touching the acetone reaches the boiling temperature of acetone after 90 seconds, the thermal energy is absorbed by the boiling process and hence the temperature stays constant which results in a constant cold side temperature. However, to obtain a constant subzero temperature to boiling point of the cooling liquid should be lower.

Conclusion

In conclusion, acetone cools the hot side of a Peltier enough to keep the cold side temperature constant at around 20 °C due to its high latent heat capacity of 534 kJ/kg. However, as subzero temperatures are needed for the ice adhesion mechanism, a liquid with a lower boiling temperature must be found. Furthermore, the corrosive nature of acetone makes it hard to contain and it is toxic. Hence, acetone is discarded as a viable option.

D.2.2. NOVEC7000 Engineering Fluid

Other liquids with a lower boiling point are pentene, pentane, cyclopentene, diethyl ether, ammonia solution, Trichlorofluoromethane and NOVEC7000 engineering fluid. The pentenes are more corrosive than acetone and toxic and hence will not be used in this research. Di-ethyl ether is sensitive to electrical currents and highly flammable and is therefore not an option (personal communication Baris Kumru, 25-5-2023). The ammonia solution would be a good option due to the high latent heat capacity of ammonia however a 25% solution is toxic and can only be used in a chemical fume hood (personal communication Roy Awater, 20-6-2023). Trichlorofluoromethane is a common refrigerant but depletes the ozone layer. Hence, the only suitable solution would be the NOVEC7000 engineering fluid. This fluid is non-toxic, non-corrosive and has a boiling point at 34 °C and a latent heat of evaporation of 142 kJ/kg [54].

Experiment No-1

The holder designed to contain the NOVEC7000 engineering fluid is shown in Figure D.25. This setup is designed to contain both the liquid phase of the PCM and the vapour. The o-ring on the round edge and the balloon clamped over the setup as shown in Figure D.26 ensure minimal leaking. This balloon ensures the containment of the vapour phase. The QC-127-1.4-6.0A is connected to the 1 mm aluminium plate with FCT-730 thermal tape, which is connected with 2-component epoxy on the bottom of this container. Testing the setup as shown in Figure D.27 resulted in the inflation of the balloon.

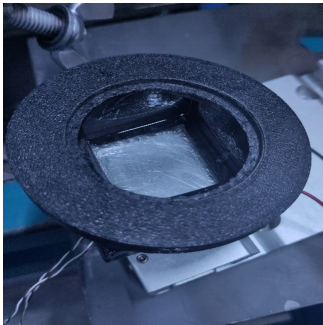


Figure D.25: Liquid PCM holder with NOVEC7000.

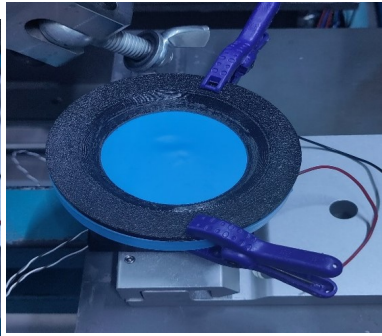


Figure D.26: Liquid container with elastic membrane (balloon) clamped to the setup.



Figure D.27: Inflated balloon during test of setup with NOVEC7000.

The QC-127-1.4-6.0A Peltier module reaches the boiling temperature of the NOVEC7000 liquid after 5.5 seconds as shown in Figure D.28

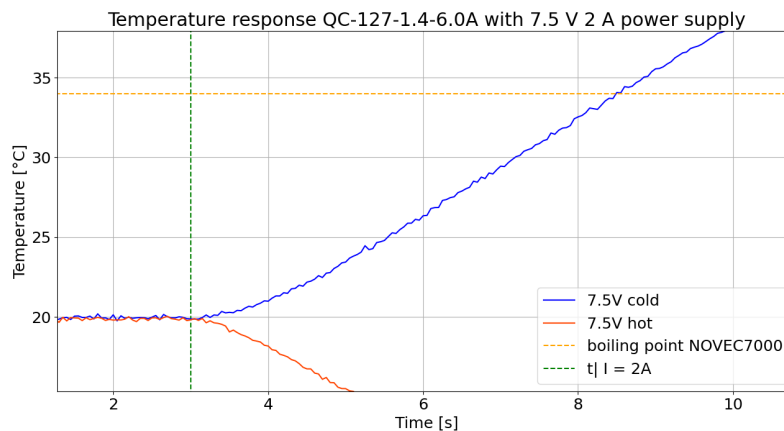


Figure D.28: Temperature between the start of operation for the QC-127-1.4-6.0A Peltier module and the boiling temperature of the NOVEC7000 engineering fluid.

The comparison of the temperature response of the cold side of the QC-127-1.4-6.0A Peltier module between an empty container, the container with 20 ml NOVEC7000 and with 20 ml water is shown in Figure D.29 and Figure D.30 for a voltage of 14 V and a current of ~ 3.5 A. Figure D.29 shows the lowest minimum temperature is obtained by the empty container. This is likely because the ambient temperature was 21 °C, while the tests started at 24 °C, therefore the air might have cooled down the hot side more at the beginning of the tests.

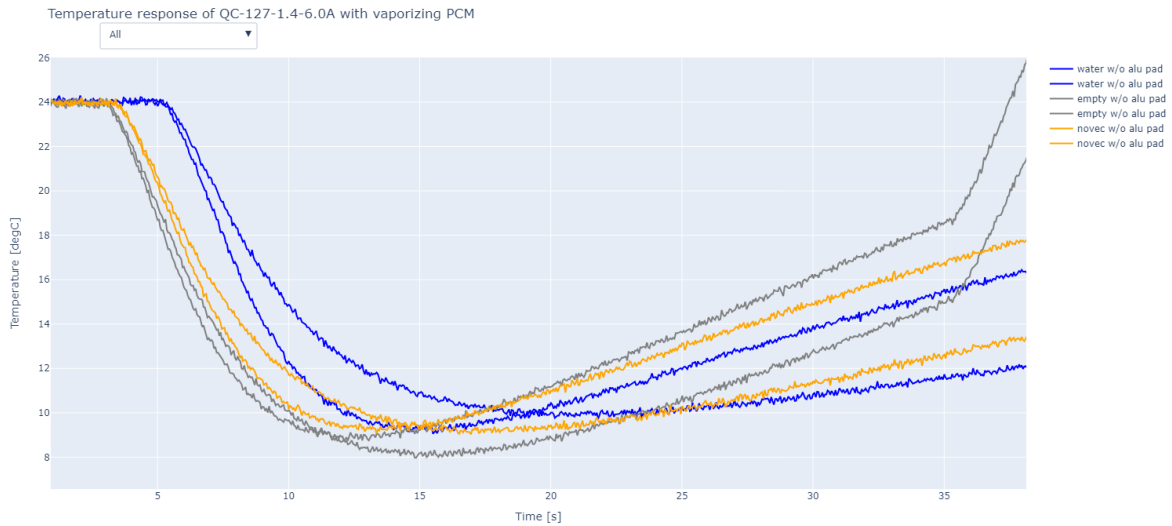


Figure D.29: Minimum temperature cold side QC-127-1.4-6.0A with and without NOVEC7000 and water.

Figure D.30 shows water reduces the heating rate of the Peltier module more than the NOVEC7000 fluid does. This means that the specific heat capacity of water (4.1813 J/gK) results in more energy absorption than the latent heat capacity of NOVEC7000 (142 kJ/kg). This can be explained by the fact that the whole body of water is used in the energy absorption to heat the water, while only a small layer of NOVEC7000 touching the Peltier module absorbs energy to evaporate. Due to the small thermal conductivity of the NOVEC liquid of 0.075 W/mK, the heat cannot transfer far through the liquid and hence less of the available latent heat storage can be used at any instance in time.

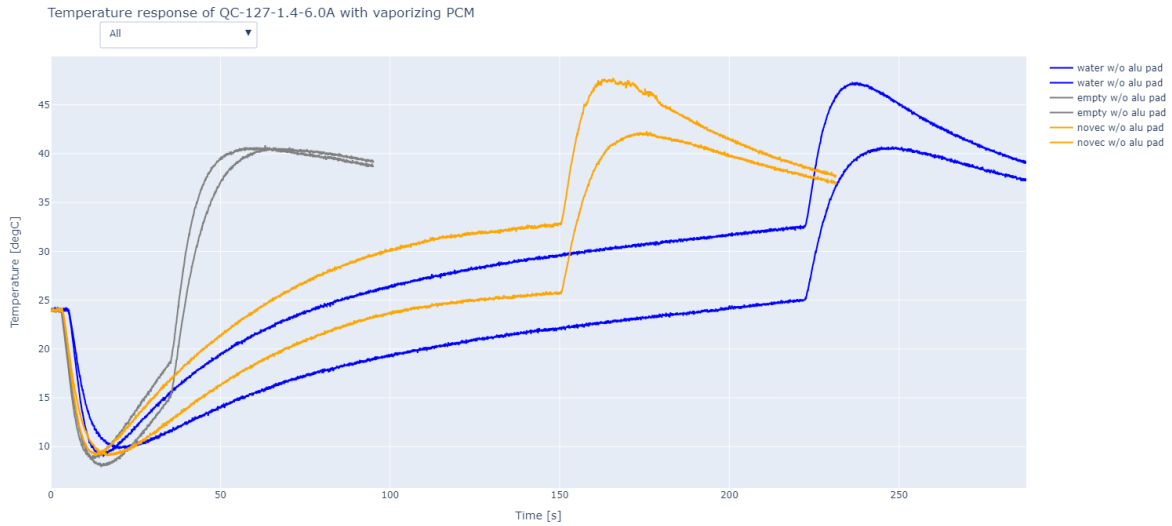


Figure D.30: Temperature response cold side QC-127-1.4-6.0A with and without NOVEC7000 and water.

Experiment No-2

Measuring the 1 cm aluminium pad temperature response for a power level of 15 W and ~50 W, resulted in a lower heating rate of the system as shown in Figure D.31. Furthermore, the lower power tests resulted in lower temperatures of the aluminium pad. The water outperformed the NOVEC7000 liquid.

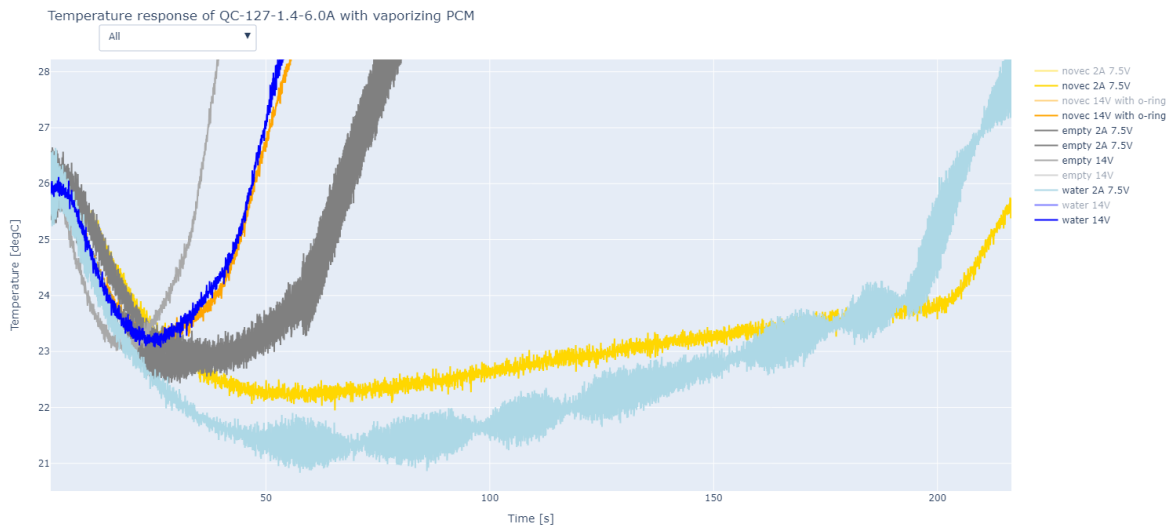


Figure D.31: Temperature response 1 cm aluminium pad connected to the cold side of QC-127-1.4-6.0A with and without NOVEC7000 and water. Tested at 15 W (7.5V 2A) and 50 W (14V).

Experiment No-3

In Figure D.32 the temperature response of the adhesion pad cooled with NOVEC7000 in the aluminium container designed in Section 4.3 is shown. As shown the cooling with NOVEC7000 does not result in subzero temperatures needed to freeze water. However, by placing the adhesion pad on the ice the cooling effect might be enough to create adhesion as will be discussed in Chapter 7.

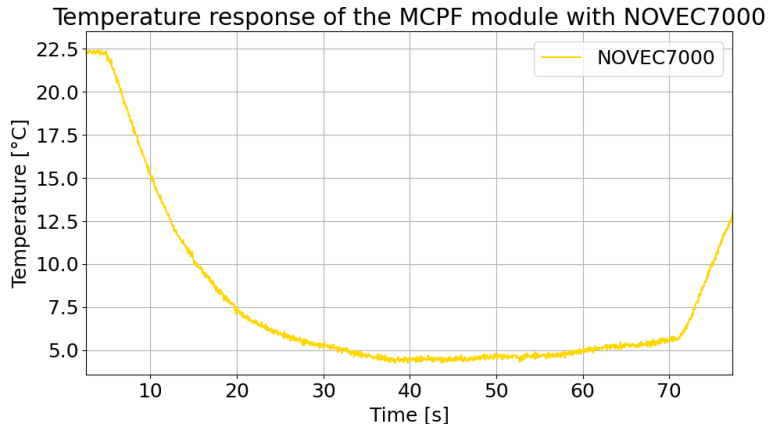


Figure D.32: Temperature response of the MCPF-127-14-25-E with NOVEC7000 engineering liquid, supplied power: 7.5 V and 2 A.

Conclusion

In conclusion, testing the NOVEC7000 fluid showed liquid water outperformed the liquid in cooling performance. The test with NOVEC7000 did not reach subzero temperatures, due to its low thermal conductivity and relatively low latent heat capacity for a vaporising PCM.

D.3. Conclusion

In conclusion, this chapter aimed to answer the question:

What is the optimal phase change material to absorb the energy from the adhesion mechanism?

To answer this question both solid-liquid (melting) and liquid-vapour (vaporising) PCMs were tested. In Table D.2 the properties of tested PCMs in this chapter are listed.

Table D.2: Properties of tested PCMs

PCM	Phase Change Temperature [°C]	Latent Heat Capacity [kJ/kg]	Specific Heat Capacity [J/gK]	Thermal Conductivity [W/mK]	Density [kg/m ³]	Corrosive/ Toxic
GCS-104-PCM	50-55 [25]	200-280 (from supplier)	NA	4 [25]	2800 [25]	No/No
Paraffin Wax	54 (from supplier)	176 [3]	2.14-2.9 [19]	0.21 [11]	930 [11]	No/No
Coconut Oil	24 [37]	105 [37]	1.33 solid 2.71 liquid [18]	0.165 [18]	900 [37]	No/No
Acetone	56 [70]	542 [70]	2.21 [19]	0.18 [70]	785 [70]	Yes/Yes
NOVEC7000 [1]	34	142	1.3	0.075	1400	No/No
Octadecane [22]	28	237	1.8 solid 2.3 liquid	0.334	868	No/Yes

The selected PCM material for this project is octadecane, because of its high latent heat capacity and low melting point, which resulted in a minimum temperature of -7.71 °C of the adhesion pad and sustained subzero cooling for 10 minutes and 15 seconds (see Figure D.16). In Figure D.33 the temperature difference of the cold side is plotted over the minimum temperatures of the adhesion pad cooled by the MCPF-127-14-25-E module cooled by different PCMs in an aluminium container. As expected the octadecane, indicated by the pink star, outperforms all other tested PCMs. Furthermore, the temperature of the PCM influences its cooling performance as the cold coconut oil resulted in a lower minimum temperature than the melted oil. Therefore, the mechanism should allow the PCM to

dissipate its heat to the surroundings and cool down.

PCM cooling performance with MCPF-127-14-25-E module, aluminium holder and adhesion pad

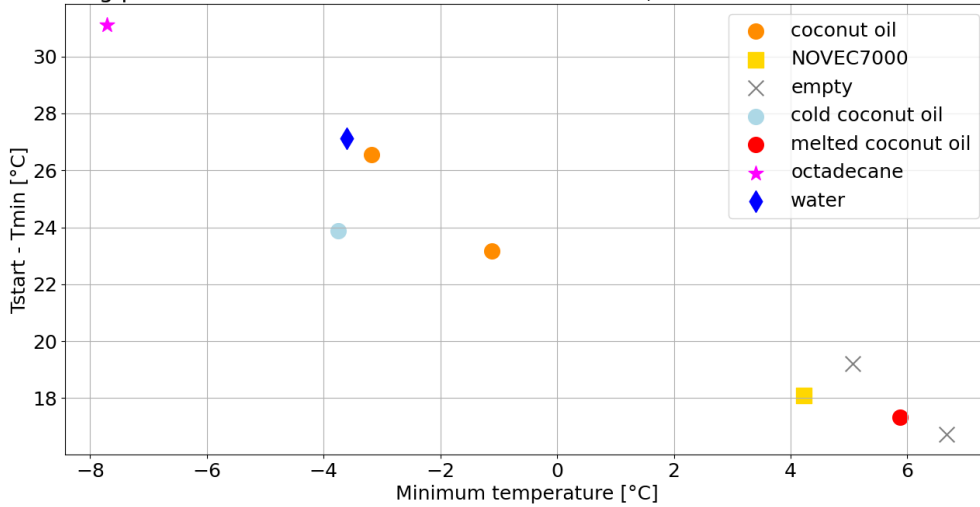
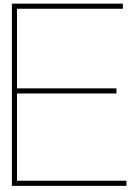


Figure D.33: Performance of PCM cooling of the adhesion pad with the MCPF-127-14-25-E module for 7.5 V 2 A power supply and different PCM types in the aluminium container.

In Section 4.3 the design process of the container to hold the selected solid PCM is described and integrated into an ice adhesion mechanism. The container transfers the heat from the Peltier module into the PCM to increase the contact area with the heating element and thereby the cooling effect. Furthermore, the container is made from a material that increases the dissipation of heat from the PCM (aluminium), to ensure the PCM can cool down. This ensures the PCM can keep using latent heat storage instead of sensible heat storage.

The tests on ice with the adhesion mechanism with octadecane are described in Chapter 6. In Appendix C the required octadecane mass for ice adhesion is estimated and this volume is integrated into the design of FLICK in Chapter 7.

Finally, the observed expansion of the liquid-vapour PCMs can be used for locomotion. However, the test with the NOVEC7000 inside the PCM container resulted in a slightly better performance compared to the empty aluminium container (yellow square in Figure D.33). This is due to the low thermal conductivity of the engineering fluid. Therefore, another fluid with a higher thermal conductivity and latent heat capacity should be selected or engineered to obtain subzero temperatures.



Peltier module tests

Peltier modules convert electricity to heating and cooling by using the thermoelectric effect as described in Section 3.2. In this section, the performance of the three types of modules used in the experiments is tested and the temperature response of the selected MCPF-127-14-25-E is modelled.

E.0.1. TEC1-12706

The TEC1-12706 Peltier module uses 127 semi-conductor couples and has a maximum current of 6 A. In Figure E.1 the temperature response of the TEC1-12706 Peltier module from KIWI electronics¹ was measured with two thermocouples (the red-white wires) on the top and bottom. Both the top and the bottom sides of the Peltier module are in contact with the ambient air. The current flows from the red to the black wire through the Peltier module. This Peltier module was selected and used in the first experiments, because of the low price and easy availability.



Figure E.1: Set up to measure the temperatures on the hot and cold side of the TEC1-12706 Peltier module.

Figure E.2 shows the temperature response of the hot and cold side of the TEC1-12706 for different voltages and a current of 2A. The red lines indicate the hot side temperatures and the grey lines the cold side. The darker the color the lower the voltage. As shown the temperature difference between the hot and cold increases with voltage and the lower the voltage the longer it takes for the system to heat up. The minimum temperature decreases with increasing voltage as shown in Figure E.3 till a temperature of 11.5 °C is reached by supplying 9 or 12 V. This can be explained by the fact that a higher voltage results in both more heating and cooling, as a higher power supply results in more heating (see 12 V hot line in Figure E.2) and in a higher heat pumping rate as it influences the Seebeck coefficient. As some of the produced heat seeps from the hot to the cold side, this heat can outweigh the added cooling power. This explains the similar minimum temperature between 9 and 12 V.

¹<https://www.kiwi-electronics.com/en/40x40mm-thermoelectric-peltier-module-12v-60w-3623?search=peltier>, retrieved on June 2nd 2023

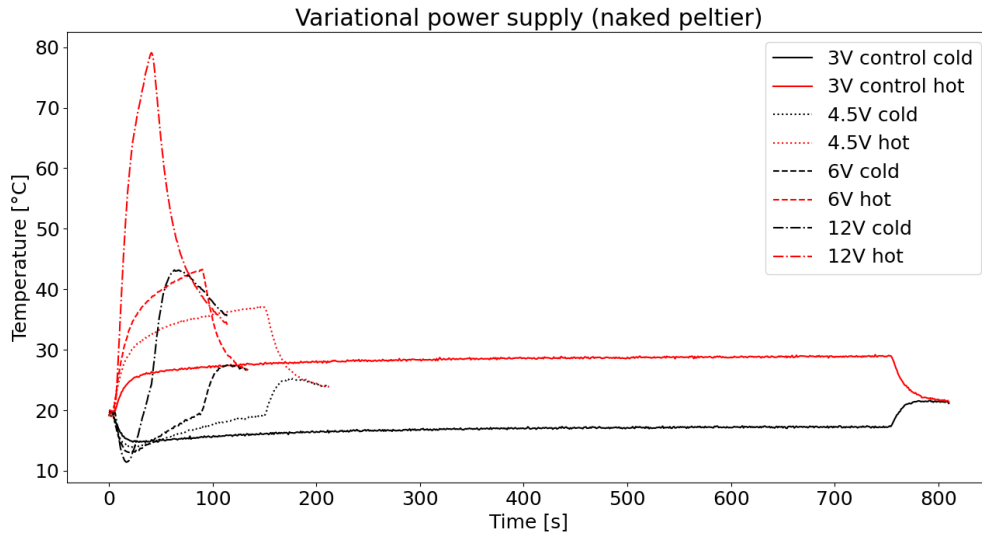


Figure E.2: Temperature response of TEC1-12706 for different voltages, $T_{amb} = 18.5\text{ }^{\circ}\text{C}$.

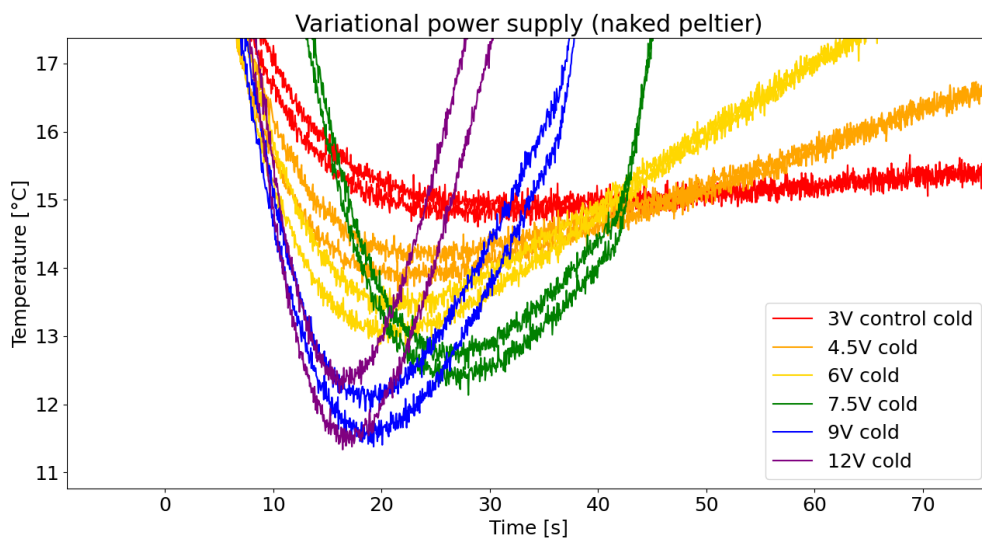


Figure E.3: Minimum temperature of TEC1-12706 for different voltages, $T_{amb} = 18.5\text{ }^{\circ}\text{C}$.

However, the quality of these peltier modules was low as some would break in between the test days. In previous research, TEC1-12706 modules from different manufacturers were compared and the modules from KIWI showed the worst behaviour [76], as shown in Figure E.4 as shown by the red line. As shown the Generic-1 (which was bought from KIWI Electronics) uses the most power and cools the least.

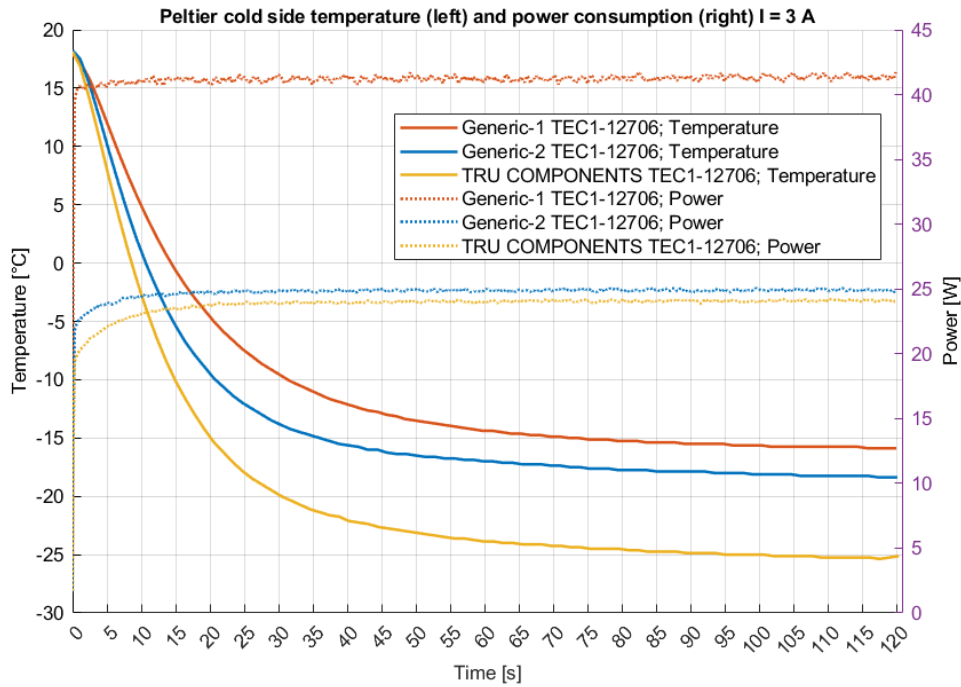


Figure E.4: Temperature response and power consumption over time of TEC1-12706 with water cooling as shown in T. Mooijman 2023 [76]. $T_{amb} = 18\text{ }^{\circ}\text{C}$.

E.0.2. QC-127-1.4-6.0A

A better-performing, more expensive Peltier module was bought: QC-127-1.4-6.0A. This Peltier module has similar performance as the TRU COMPONENTS TEC1-12706 (yellow line in Figure E.4), but can theoretically obtain a higher temperature difference between the cold and hot sides ($71\text{ }^{\circ}\text{C}$ compared to $60\text{ }^{\circ}\text{C}$). The temperature response of this module is shown in Figure E.5 for a current of 2 A (dashed line) and 3 A (solid line). As shown the 2 A line reaches $11\text{ }^{\circ}\text{C}$ instead of the $13\text{ }^{\circ}\text{C}$ reached in Figure E.3 for similar power levels. The horizontal dashed lines show when the power supply was turned off. Furthermore, the test with a higher current results in a slightly lower minimum temperature and an increased heating rate of the system.

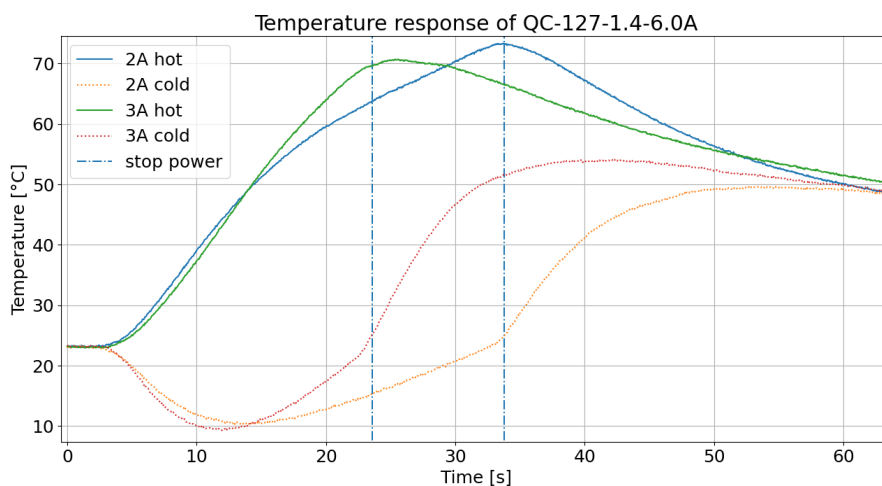


Figure E.5: Temperature response of QC-127-1.4-6.0A, $T_{amb} = 20.7\text{ }^{\circ}\text{C}$.

As shown the lower power levels result in a lower heating rate, as less heat is produced (see Equa-

tion 3.1). Therefore, a Peltier module with a lower maximum current and hence heat production should be selected. This module could reach a similar maximum temperature difference while producing less heat.

E.0.3. MCPF-127-14-25-E

The MCPF-127-14-25-E Peltier module from Farnell produces a large maximum temperature difference of 73 K with low power consumption and hence produces less heat. Table E.1 shows the properties of the peltier modules. The MCPF-127-14-25-E is more expensive and thicker but reaches a larger temperature difference for less supplied power than the other modules. For this research, the standard module dimensions of 40 by 40 mm were chosen. The recommended operation current is lower than 0.7 of I_{max} , which is 2.73 A in this case. Hence, this Peltier was tested with the 2 A power supply.

Table E.1: Properties of the Peltier modules.

name	max temperature difference	max voltage	max current	max power	price	dimensions
QC-127-1.4-6.0A	71 K	14.4 V	6 A	55.2 W	33.99 EU	40x40x3.8 mm ³
TRU COMPONENTS TEC1-12706	60 K	15 V	6.4 A	65 W	30.99 EU	40x40x3.8 mm ³
Kiwi electronics TEC1-12706	68 K	14.9 V	6.4 A	60 W	5.95 EU	40x40x3.8 mm ³
MCPF-127-14-25-E	73 K	15.7 V	3.9 A	37 W	65.54 EU	40x40x4.8 mm ³

In Figure E.6 the temperature response of the MCPF-127-14-25-E is shown. As expected the higher voltage results in lower minimum temperature and a larger temperature difference due to the larger heating and heat pumping power.

Maximum temperature difference between hot and cold side of MCPF-127-14-25-E peltier module

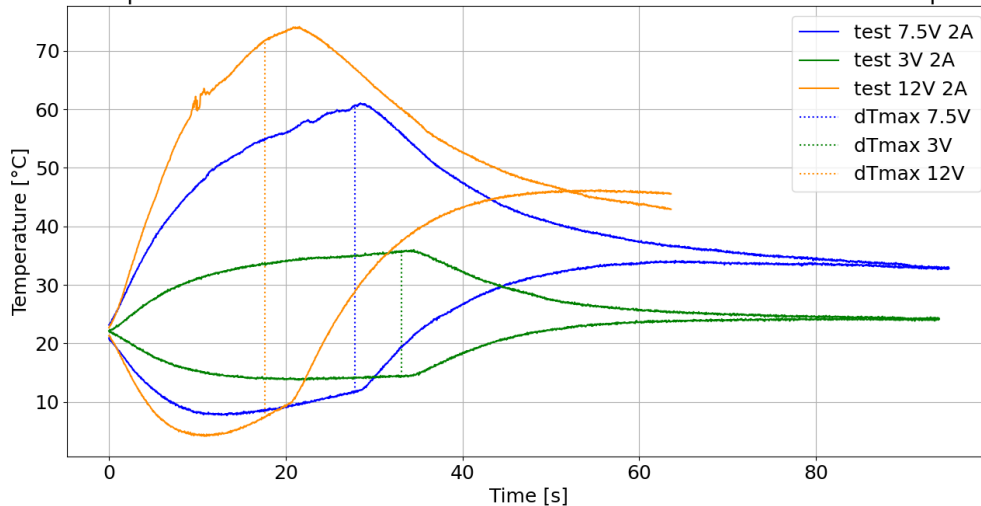


Figure E.6: Temperature response for the MCPF-127-14-25-E for 3, 7.5 and 12 V, $T_{amb} = 20.2$ °C.

Comparing Figure E.6 to Figure E.3 the better performance is shown by the lower minimum temperatures obtained by the MCPF compared to the TEC1 module, even though the MCPF module was tested in a higher ambient temperature (20.2 °C compared to 18.5 °C). The measured maximum temperature differences between the hot and cold side of the MCPF module are 21.56 °C for 3 V, 49.11 °C for 7.5 V and 64.47 °C for 12 V indicated by the vertical dashed lines. As these maximum temperature differences were found before the point of maximum temperature (the point at which the power supply was turned off, and the top line starts decreasing in Figure E.6), this is the maximum temperature

difference for the corresponding operational mode of the Peltier module. After the point of maximum temperature difference (vertical dashed line in Figure E.6), the cold and hot sides do not start diverging, as the heating effect is larger than the heat pumping effect after the maximum temperature difference. Hence, the whole system will heat up after this point.

E.1. Power supplies

The power supplies used in this research are described in this section:

A 2 amperes-regulated direct current power supply was used to control the Peltier modules used in the experiments. This power supply could supply a voltage of 3, 4.5, 6, 7.5, 9 and 12 V. To switch the polarity of the power supply the red and black wires were switched manually.

Furthermore, a GLPS 3003E 0-30V 0-3A power supply (see Figure E.7) was used with a maximum current of 3.26 A. The current in the supply could be changed and the corresponding voltage would be provided to the Peltier module. Lastly, an ES015-10 power supply (see Figure E.8) was used to supply a voltage of 14 V with a free current up to 10 A.



Figure E.7: GLPS 3003E 0-30V 0-3A power supply



Figure E.8: ES015-10 power supply